Instability and transport phenomena in oscillating suspensions of non-Brownian particles in confined geometries

Instabilité et transport dans des suspensions de particules non Browniennes oscillantes dans des géométries confinées

Thèse de doctorat de l'université Paris-Saclay
et de l'université de Buenos Aires

École doctorale n° 579 : sciences mécaniques et énergétiques, matériaux et géosciences (SMEMaG)
Spécialité de doctorat : Mécanique des fluides
Graduate School : Sciences de l'ingénierie et des systèmes.
Référent : Faculté des sciences d'Orsay

Thèse préparée dans les unités de recherche **FAST (Université Paris-Saclay, CNRS)** et **Grupo de Medios Porosos (Universidad de Buenos Aires)**, sous la direction de **Georges GAUTHIER**, enseignant chercheur, la direction de **Irene IPPOLITO**, professeur, et le co-encadrement de **Y. Lucrecia ROHT**, professeur

Thèse soutenue à Buenos Aires, le 27 novembre 2025, par

Alejandro Adrián GARCÍA

Composition du jury

Membres du jury avec voix délibérative

Fernando MINOTTI Professeur, Universidad de Buenos Aires (Argentina)	Président
Adolfo BANCHIO Professeur, Universidad Nacional de Córdoba (Argentina)	Rapporteur & Examinateur
François PETERS Maître de conférences (HDR), INPHYNI Université de Cote d'Azur	Rapporteur & Examinateur
Luciana BRUNO Chercheuse, CONICET (Argentina)	Examinatrice
Pablo COBELLI Professeur, Universidad de Buenos Aires (Argentina)	Examinateur
Emmanuelle RIO Professeur, Université Paris-Saclay, CNRS	Examinatrice
Daniel BONAMY Directeur de recherche, CEA, CNRS, Université Paris-Saclay	Examinateur

THESE DE DOCTORAT

NNT : 2025UPAST160

ÉCOLE DOCTORALE
Sciences mécaniques et
énergétiques, matériaux
et géosciences (SMEMAG)

Titre : Instabilité et transport dans des suspensions de particules non Browniennes oscillantes dans des géométries confinées

Mots clés : suspensions macroscopiques, instabilité, experimental.

Résumé : Cette thèse étudie les écoulements oscillants de suspensions de sphères non browniennes dans des canaux étroits. Les écoulements de suspensions sont répandus dans la nature et les systèmes industriels et biologiques, et les écoulements oscillants sont intéressants en raison de l'influence des inversions de flux. Des expériences antérieures au laboratoire FAST et au Grupo de Medios Porosos ont montré que l'écoulement oscillant de suspensions dans des cellules de Hele-Shaw peut être instable, entraînant une modulation de la concentration en particules le long du canal. Un tel comportement était nouveau et a motivé la présente étude.

Notre objectif dans ce travail a été de comprendre cette instabilité à partir des variations temporelles des champs de vitesse et de concentration, ainsi que de la microstructure de la suspension, à la fois à l'échelle d'une période d'oscillation et à celle du développement de l'instabilité. À cette fin, nous avons utilisé une technique optique permettant de suivre les particules individuelles à l'intérieur de la suspension et d'obtenir à la fois des statistiques microscopiques (distributions de paires) et des grandeurs macroscopiques (concentration locale et vitesse des particules).

Nous avons utilisé des sphères de PMMA (acrylique) en suspension dans un liquide newtonien avec des fractions volumiques moyennes de particules $\phi_b =$ 0,2−0,4. Les particules, de diamètre 40 et 85 µm, étaient non-browniennes. Le fluide suspendant était une solution aqueuse de même densité et indice de réfraction que les particules, afin d'annuler la sédimentation et de rendre la suspension transparente. L'écoulement avait lieu dans des canaux rectangulaires saturés par la suspension (longueur = 150 mm, épaisseur $2b = 1$ ou 2 mm, largeur = 10 mm correspondant respectivement aux directions x, y et z). Une pompe à seringue induisait des variations périodiques de débit en onde carrée (période $T = 2 - 20$ s) entraînant des amplitudes de déplacement $A = 2\,b - 20\,b$ et des nombres de Reynolds inférieurs à 1. L'utilisation d'un fluide fluorescent et l'éclairage du canal par un plan laser mince, parallèle à sa longueur et à son épaisseur, permettaient d'observer les particules et de déterminer leur position, vitesse et concentration locale.

Au début de chaque expérience, la fraction volumique locale ϕ et la composante de vitesse V_x étaient constantes avec x et la composante transversale V_y était ≈ 0. Après quelques oscillations, et toujours avec $V_y \approx 0$, la fraction locale ϕ devenait plus grande au centre ($y = 0$) qu'à proximité des parois ($y = \pm b$) en raison de la migration des particules induite par le cisaillement, entraînant une viscosité plus élevée dans cette région et un profil de vitesse aplati. Ensuite, ϕ cesse de croitre et une composante d'écoulement secondaire transverse V_y périodique d'une longueur d'onde $\approx 7\,b$ apparaît le long de x : elle correspond à une séquence de cellules de recirculation de directions alternées changeant aux inversions du flux moyen et convectées par celui-ci. Simultanément, la bande de haute concentration près de $y = 0$ développe des distorsions transversales de même longueur d'onde qui, elles aussi, sont convectées par les oscillations du flux moyen.

L'amplitude à la fois de la vitesse d'écoulement secondaire et des distorsions de la bande de haute concentration augmente à peu près exponentiellement jusqu'à saturer. Le taux de croissance correspondant augmente avec la fraction volumique moyenne ϕ_b et devient nul en dessous d'une valeur seuil $A/b \approx 1$ de l'amplitude de déformation. Ces deux observations suggèrent que l'instabilité résulte des interactions irréversibles entre particules, probablement par des contacts solides, et que l'inversion de flux joue un rôle important dans son développement. La microstructure de la distribution de paires de particules avant l'apparition de l'instabilité montre une asymétrie avec un excès transitoire de paires se séparant après chaque inversion de flux.

Title: Instability and transport phenomena in oscillating suspensions of non-Brownian particles in confined geometries

Keywords: macroscopic suspension, instability, experimental.

Abstract: This thesis studies oscillatory flows of neutrally-buoyant non-Brownian spherical particles suspensions in narrow channels. Flows of suspensions are widespread in nature, and industrial and biological systems, and the case of oscillatory flows is particularly interesting in view of the possible influence of flow reversals. Previous experiments in our laboratory have shown that the oscillatory flow of suspensions inside Hele-Show cells can be unstable, resulting in a modulation of the particle concentration along the length of the channel. Such a behavior was novel and motivated the present study.

Our objective in this work has been to understand this instability from the time variations of the velocity and concentration fields and from those of the microstructure of the suspension both at the time scale of an oscillation period and at that of the development of the instability to determine the parameters controlling this onset. For this purpose, we used an optical technique allowing us to track individual particles inside the suspension and calculate both microscopic statistics (pair distributions) characterizing spatial correlations of the particle distribution and macroscopic quantities (local concentration and velocity) and their spatial variations and time dependence.

We used PMMA (acrylic) spheres suspended in a Newtonian liquid with bulk particle volume fractions ϕ_b between 0.2 and 0.4. The particles were spherical with diameters of 40 and 85 µm and, therefore, non-Brownian. The suspending fluid was an aqueous solution of same density and refractive index as the particles, in order to cancel sedimentation and render the suspension transparent. Flow took place in rectangular channels saturated with the suspension (length = 150 mm, thickness $2b = 1$ or 2 mm, width = 10 mm corresponding respectively to the x, y and z directions). A programmable syringe pump induces periodic square wave flow rate variations (periods $T = 2$–$20\,$s) resulting in displacement amplitudes $A = 2\,b$–$20\,b$ and Reynolds numbers below 1. Using a fluorescent fluid and illuminating the channel by a thin laser plane (20 µm) parallel to its length and thickness and located in the middle of the thickness allows us to observe the particles as dark circles and determine their individual location and velocity and their local concentration.

At the beginning of each experiment, the average local volume fraction ϕ and the velocity component V_x are constant with x and the transverse component V_y is ≈ 0. Then, after a few oscillations, and still with $V_y \approx 0$, the local fraction ϕ becomes larger in the center ($y = 0$) than near the walls ($y = \pm b$) due to shear-induced particle migration, resulting in a higher viscosity in this region and a blunted velocity profile. The rate of migration appears to be strongly related to the development of the instability. Then, the increase of ϕ levels off and a periodic transverse secondary flow component V_y of wavelength $\approx 7\,b$ along x appears: it corresponds to a sequence of recirculation cells of alternating directions changing at mean flow reversals and convected by it. Simultaneously, the band of high particle concentration near $y = 0$ develops transverse distortions of same wavelength which, too, are convected by the oscillations of the mean flow.

The amplitude of both the secondary flow velocity and the distortions of the high ϕ band increase roughly exponentially until a saturation is reached. The corresponding growth rate increases with the bulk volume fraction ϕ_b and becomes zero below a threshold value $A/b \approx 1$ of the strain amplitude. Both observations suggest that the instability is driven by irreversible particle interactions, most probably by solid contacts, and that the flow reversal plays an important part in its development. The microstructure of the particle pair distribution before the onset of the instability is shown to be asymmetric with a transient excess of separating pairs after each flow reversal.

Título: Transporte, dispersión y reversibilidad de un trazador en un flujo oscilante de suspensiones

Palabras cláves: suspensión macroscópica, inestabilidad, experimental.

Resumen: Esta tesis estudia el flujo oscilante de suspensiones de partículas no brownianas en canales estrechos. El flujo de suspensiones está presente en una gran variedad de situaciones naturales e industriales, y los flujos oscilantes son interesantes, en particular, por la influencia de las inversiones del flujo. Los experimentos previos realizados en nuestros laboratorios mostraron que los flujos oscilantes de suspensiones dentro de celdas de Hele-Shaw pueden ser inestables, resultando en una modulación de la concentración de partículas a lo largo de la celda. Este comportamiento resultó novedoso y motivó el presente estudio.

Nuestro objetivo en este trabajo es entender esta inestabilidad a partir de las variaciones espaciales y temporales de variables macroscópicas (campos de velocidad y de concentración de partículas) y microscópicas (distribución de pares de partículas), tanto a la escala temporal de una sola oscilación, como durante el desarrollo de la inestabilidad, determinando así los parámetros que la controlan. Utilizamos técnicas experimentales que nos permitieron observar y rastrear partículas individuales dentro de la suspensión, calculando las variables antes mencionadas mediante procedimientos estadísticos.

Las suspensiones se componen de partículas esféricas de PMMA (acrílico) suspendidas en líquidos newtonianos. Las partículas ocupan una fracción ϕ_b de entre 0,2 y 0,4 del volumen total. Se utilizaron partículas con diámetros de 40 y 85 µm, lo suficientemente grandes para considerarlas no brownianas. Los líquidos son soluciones acuosas con la misma densidad e índice de refracción que las partículas, evitando así efectos de sedimentación y obteniendo suspensiones transparentes. Se estudia el flujo dentro de canales rectangulares cerrados con largo de 150 mm, espesor $2b$ de 1 o 2 mm y ancho de 10 mm (respectivamente, direcciones x, y, z). Una bomba de jeringas induce flujos periódicos con forma de onda cuadrada en el caudal (periodos entre 2 y 20 s), resultando en amplitudes de desplazamiento A entre $2\,b$ y $20\,b$ y números de Reynolds menores a 1. Mediante el uso de fluorescencia y un plano láser más fino que las partículas, observamos a las mismas en un corte ubicado en el medio del ancho, paralelo al largo y el espesor.

Al comienzo de cada experimento, la fracción de volumen local ϕ (concentración de partículas) y la velocidad longitudinal V_x son uniformes en la dirección x, mientras la velocidad transversal V_y es ≈ 0. Luego de algunas de oscilaciones, y todavía con $V_y \approx 0$, observamos que la fracción local ϕ se ha vuelto marcadamente más grande en el centro del espesor ($y = 0$) como consecuencia de la migración de partículas hacia allí inducida por el flujo de corte. Esto resulta en una mayor viscosidad en el centro y perfiles de velocidad más planos. Luego, el incremento de ϕ en el centro se detiene y aparece un flujo secundario con velocidades transversales V_y no nulas y periódicas en x con una longitud de onda $\approx 7\,b$: el mismo corresponde a una secuencia de celdas de recirculación que son arrastradas por el flujo principal y cambian de dirección con el mismo. Simultáneamente, la región de alta concentración de partículas cerca de $y = 0$ adquiere una forma ondulante con la misma longitud de onda. Este patrón también es arrastrado por el flujo principal.

Las amplitudes del flujo secundario y del patrón ondulante en ϕ aumentan en forma aproximadamente exponencial hasta saturar. La correspondiente tasa de crecimiento aumenta con la fracción volumétrica promedio ϕ_b y disminuye hasta cero al reducir la amplitud de oscilación a $A \approx b$. Estas observaciones nos sugieren que la inestabilidad está inducida por interacciones irreversibles entre las partículas, probablemente contactos sólidos, y que la inversión periódica de la dirección de flujo juega un papel importante. Observaciones a la escala de las partículas muestran una microestructura anisotrópica que debe reorganizarse cada vez se invierte la dirección de flujo.

Agradecimientos

A Irene, por haberme abierto las puertas a la investigación tanto en Argentina como en Francia.

A Lucrecia, por tener paciencia con mis rezongos, atender toda clase de consultas y ayudarme a ser mejor docente.

A todos en el GMP, por ser amigables y haberme invitado a partidos de fútbol y torneos de ajedrez.

A la facultad de ingeniería, por prestar sus instalaciones, y a la universidad de Buenos Aires, por la beca que hizo posible este doctorado.

A Georges, por las discusiones sobre artículos y sobre la física de suspensiones.

A Dominique, por su participación en las reuniones mensuales y sus aportes a nuestros artículos.

Al FAST, por ser un lugar tan agradable donde trabajar, y todos sus miembros, por el esfuerzo para integrar a cada uno de los llegamos y luego nos vamos.

A la universidad de Paris-Saclay, por la beca que hizo posible que conozca un país tan hermoso.

A Germán (con tilde), por estar ahí casi desde el comienzo para tratar de darle sentido a todo lo que medía en los experimentos.

A Facundo Zaldivar, por el diseño inicial del sistema de lentes que finalmente armé años después en el FAST.

A Valentino Schmidt, por la caracterización de las partículas en la universidad de San Luís. Llevé las muestras durante la reunión de Fluidos de 2023, donde la pasé muy bien.

A todos los técnicos del FAST. A Christophe Manquest, por la ayuda en la caracterización de partículas. A Lionel Auffray, por las piezas en la impresora 3D. A Rafaël, por que, además de ayudarme cortando piezas de plástico y metal, fuiste una persona muy divertida con la que poder hablar en español.

A todos los miembros del jurado, por tomar parte de su tiempo para leer mi tesis, evaluarla y escuchar mi defensa.

A mi padre, por escuchar atentamente mis idas y venidas mientras tomamos un café los fines de semana. Gracias por creer en mi y alentarme a seguir adelante.

A mi madre, por todas las comidas ricas, los libros y las películas para pensar.

Y muy especialmente, a Jean-Pierre. Por haber ido más allá de cualquier obligación y acompañarme no solo como investigador, leyendo todo lo que escribía y tratando de entenderlo y mejorarlo, si no también como persona, por ayudarme a establecerme en Francia cuando recién llegué y presentarme con todos. Gracias.

Contents

Chapter 1

Introduction

The topic of this thesis is the study of particle *suspensions* in oscillatory flows through small channels. A particle suspension can be defined as a fluid with particles dispersed in its volume. Usually, this means small solid bodies in a liquid, although drops of an immiscible liquid or even gas bubbles may result in a system with similar characteristics. A household example is the mixture of flour with a large proportion of water (Létang, Piau, and Verdier 1999). Another example can be found inside ourselves: our blood is composed of different cells (the solid bodies) in a liquid called plasma (Baskurt and Meiselman 2003). Going towards one of the original motivations of this work, we have the mixtures of soil and water. Understanding the downhill flow of mud after heavy rain can be very important for people living in some regions (Kostynick et al. 2022). At a smaller scale, water can flow underground through networks of small crevices called *fractures*, dragging solid particles from the surrounding soil. Such situations are of practical relevance for the extraction of geothermal energy, oil, and gas from the ground (Yang et al. 2022).

All the mentioned cases have in the common the presence of a large fraction of solid particles in the fluid, resulting in significant departures from the behavior of the base fluid. Another characteristic of such suspensions is that they can be very complex to study because the fluid or the particles alone already present complex behaviors on its own: flour particles are porous and absorb water, blood cells are deformable, and underground, oil, water and solids may form a three-phase system flowing through a complex network of fractures. The objective of this work is to answer questions relevant to all suspensions by studying a model system which retains only the most prominent characteristics.

During the course of this doctorate, experiments were performed using micrometric plastic spheres as particles, and a fluid of same density and optical index as the particles so that the mixture is transparent and the particles remain suspended indefinitely. We studied the resulting suspension flow inside transparent, straight channels with apertures of a few millimeters and lengths of a few tens of centimeters. Such an artificial preparation may seem too remote from the previous natural and industrial examples, but nevertheless, it presents the most distinctive attributes of suspensions, while allowing us to control, visualize and understand its behavior during the experiments.

Specifically, we observed the trajectories of individual particles in order to obtain simultaneously information on the particle organization at their scale (*microstructure*), and macroscopic measurements of particle concentration and velocity fields. Another important characteristic of our experiments is the use of oscillatory flows. The reason is two fold. First, suspensions flowing over long distances in channels are notorious for inducing an inhomogeneous particle distribution, then, in order to reach a (quasi) steady state in short channels, we used oscillatory flows where a suspension can accumulate arbitrarily long displacements in a confined space. Second, the behavior of suspensions may be altered in several ways depending on the oscillation amplitude, including a transition from irreversible to reversible particle trajectories. An understanding of these changes can help in the modelling of more general transient behaviors, and may have direct applications such as improving the mixing of substances (Souzy, Pham, and Metzger 2016) or reducing the energy requirements for the flow of suspensions (Ness, Mari, and Cates 2018).

In the course of this chapter, the main characteristics of suspensions will be introduced along with some theoretical frameworks when needed. In Chapter 2, a detailed description of the experimental setup and how it was realized will be given. In Chapters 3-5, the results will be presented divided in several parts: steady flow characterization, response to flow reversal and unstable oscillatory flow. Finally, in Chapter 6, the main conclusions and future lines of work will be summarized.

1.1. Particles

There are a wide variety of particle types. The material may be deformable, like liquid drops and the red blood cells, or it may be rigid. Restricting ourselves to the latter case, they may be porous and allow the fluid to penetrate inside (like coffee grains), or be impermeable (like sand grains). We will focus on the rigid, impermeable case. Then, we may consider the particle shape. Particles with elongated forms, like fibers, tend to align with the flow, and introduce a time-varying behavior in the suspension (Stover, Koch, and Cohen 1992). Here, we study instead the case of highest symmetry, spheres, greatly simplifying the behavior while retaining similarities to irregular particles with aspect ratio close to one, like sand grains (D. Leighton and Acrivos 1986). Even if all the particles share the same shape, they may have different sizes, in which case segregation can be observed in certain flows (Lyon and Leal 1998b). We choose again the simplest case: monodisperse particles, that is, all with roughly the same size. More concretely, we will present results for monodisperse spherical particles with diameters of 40 and 85 µm.

1.2. Fluid

For this work, we are interested in incompressible Newtonian liquids as suspending fluids. Those can be modelled by continuity and Navier-Stokes equations, but here we will consider more general equations that can be used to model also non-Newtonian fluids, since particle suspensions can behave like those. First, we have the continuity of the velocity field $\boldsymbol{u}$,[1]

$$\nabla \cdot \boldsymbol{u} = \partial_x u_x + \partial_y u_y + \partial_z u_z = 0, \tag{1.1}$$

where ∂_i is the spatial derivative operator along the direction i. Second, the balance of momentum or Cauchy equation,

$$\rho \left(\partial_t \boldsymbol{u} + \boldsymbol{u} \cdot \nabla \boldsymbol{u} \right) = \boldsymbol{b} + \nabla \cdot \boldsymbol{\sigma}, \tag{1.2}$$

---

[1] Bold letters represent vectors and tensors in this work. For example, $\boldsymbol{u}$ has three Cartesian components: u_x, u_y, and u_z.

where ρ is the fluid density, ∂_t is the temporal derivative, $\boldsymbol{b}$ is the sum of the bulk (volume) forces on the element of fluid, and $\boldsymbol{\sigma}$ is the second-order stress tensor which corresponds to the surface forces between adjacent elements of fluids. Both $\boldsymbol{b}$ and $\boldsymbol{\sigma}$ may depend on $\boldsymbol{u}$, ρ or any other property of the fluid or the environment.

An important class of fluids are those called *Newtonian*, for which the stress tensor takes the form

$$\sigma_{ij} = -p\,\delta_{ij} + 2\eta\,E_{ij}, \tag{1.3}$$

where p is the fluid pressure, $\boldsymbol{\delta}$ is the Kronecker delta, η is the fluid viscosity, and $\boldsymbol{E}$ is the strain-rate tensor,

$$E_{ij} = \tfrac{1}{2}(\partial_i u_j + \partial_j u_i). \tag{1.4}$$

Then, Eq. (1.2) takes the form of the Navier-Stokes equation for an incompressible fluid:

$$\rho\,(\partial_t \boldsymbol{u} + \boldsymbol{u}\cdot\nabla\boldsymbol{u}) = \boldsymbol{b} - \nabla p + \nabla\cdot(\eta\nabla\boldsymbol{u}). \tag{1.5}$$

In Sec. 1.3, we will see that it is possible to model the whole suspension as a continuous fluid with the previous equations, although Eq. 1.3 will have to be modified to account for the non-Newtonian behavior of suspensions.

Simple shear flow

Locally, any incompressible flow can be described by a velocity field $\boldsymbol{u}$ which depends linearly on the position vector $\boldsymbol{x}$, with symmetric and anti-symmetric components proportional to the strain rate tensor and the local vorticity, respectively (Batchelor 1967, chapter 2). A particularly important case, in part because it is simple to set up in experiments, is that of simple shear flows where

$$\boldsymbol{u}(y) = \dot{\gamma} y \hat{\boldsymbol{x}}. \tag{1.6}$$

Here, the directions x, y, z are the flow, gradient, and vorticity directions respectively; $\hat{\boldsymbol{x}}$ is the unit vector pointing in the x direction, and $\dot{\gamma}$ is called shear rate (see Fig. 1.1). In most of our studies, it is not so important how fast the fluid is travelling with respect to a fixed frame of reference (u_x), but how large the local velocity gradient $\dot{\gamma}$ is.

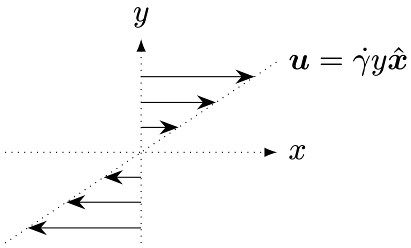

Figure 1.1: Simple shear flow.

1.2.1. Inertia, Reynolds number and Stokes equation

The ratio of magnitudes between the left hand side of Eq. (1.5) (inertial term) and the last term on the right (viscous term) can be estimated with the Reynolds number

$$\mathrm{Re} = \frac{\rho U^2/L}{\eta U/L^2} = \frac{\rho U L}{\eta}, \tag{1.7}$$

where U and L are velocity and length scales characteristic of the system under study.

When there are particles inside the fluid, they introduce an additional length scale (e.g. particle radius a), and we may be interested both in a *flow* Reynolds number Re and a *particle* one $\mathrm{Re_p}$. Given a characteristic shear rate $\dot\gamma$, we can use $L = a$ and $U = \dot\gamma a$ to obtain

$$\mathrm{Re_p} = \frac{\rho \dot\gamma a}{\eta} \tag{1.8}$$

In suspensions, the particles tend to be small compared to other relavant distances and $\mathrm{Re_p} < \mathrm{Re}$ is the most common situation.

When both Re and $\mathrm{Re_p}$ are small, one can consider the flow to be inertialess and disregard the corresponding term in Eq. (1.5), reducing it to the Stokes equation:

$$0 = \boldsymbol{b} - \nabla p + \nabla \cdot (\eta \nabla \boldsymbol{u}). \tag{1.9}$$

This equation has two interesting properties. First, it is linear in its variables ($\boldsymbol{u}$, p), making its resolution much easier. Second, the resulting flows are reversible: if we invert instantaneously the velocity and the bulk forces ($\boldsymbol{u} \to -\boldsymbol{u}$, $\boldsymbol{b} \to -\boldsymbol{b}$), the evolution of a fluid that follows this equation will exactly retrace its steps. In the following sections, we will see that, altought the Stokes equation remains useful to model the fluid phase of suspensions, direct interactions between the particles can break this temporal symmetry, resulting in some of the most striking behaviors of suspensions.

1.3. Suspensions as effective fluids

A suspension may be modeled as a Newtonian fluid with an effective viscosity η_s that depends on the particle concentration, usually defined by the fraction ϕ of the suspension volume occupied by particles. Of course, this makes sense only at length scales much larger than the particle size. For dilute suspensions ($\phi \lesssim 0.04$),

$$\eta_\mathrm{s}(\phi) = \eta_\mathrm{f}\,(1 + \tfrac{5}{2}\phi), \tag{1.10}$$

where η_f is the viscosity of the suspending fluid, assumed to be Newtonian. This expression was reached by Einstein (1905) considering the perturbation to the flow made by each particle independently and, then, multiplying by the concentration. Corrections of higher order in ϕ require knowledge of the relative positions of the particles, which in turn are affected by the type of bulk flow (Batchelor and Green 1972). The dependence of the parameters on the flow type is characteristic of non-Newtonian fluids, and this is the first sign that a more complex model will be required to fully capture the suspension behavior.

Nonetheless, the viscosity under steady shear flow is well characterized and several empirical formulas have been proposed (see the review of Guazzelli and Pouliquen 2018). In particular, the relation proposed by Maron and Pierce (1956) is simple and fits well the available data:

$$\eta_\mathrm{s}(\phi) = \eta_\mathrm{f}\,(1 - \phi/\phi_J)^{-2}. \tag{1.11}$$

Here, ϕ_J is the jamming fraction: the volume fraction at which the particles cannot move relative to each other, making the suspension flow essentially impossible and, hence, the viscosity diverges. Figure 1.2 shows a plot of this formula along with different measurements and other estimations.

The jamming fraction can be defined by geometrical constraints, for example, rigid monodisperse spheres at the random-close-packing fraction ($\phi_\mathrm{RCP} \approx 0.64$) do not have enough physical space between them to move under a shearing flow. On the other hand, ϕ_J can take

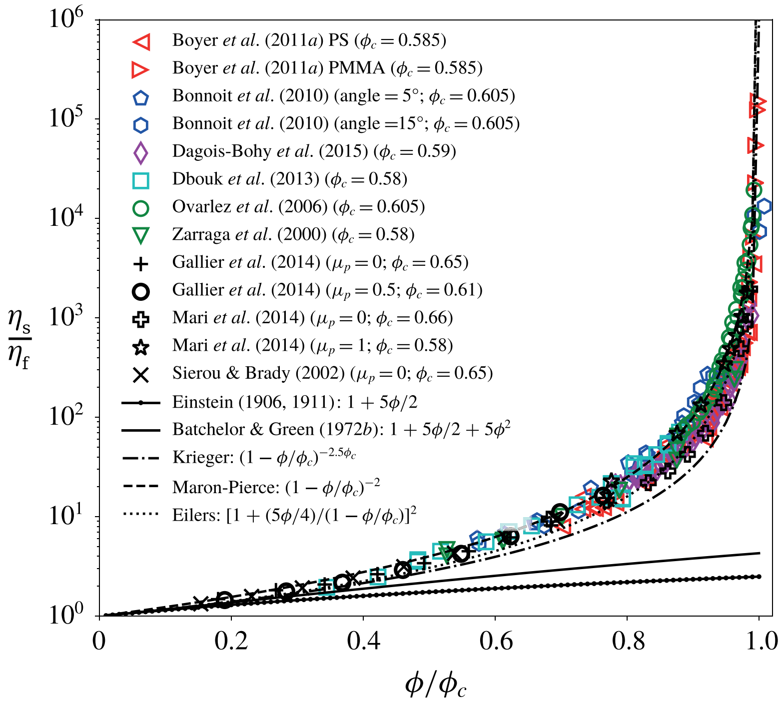

Figure 1.2: Comparison of measurements, simulations and laws for the suspension relative viscosity $\eta_\mathrm{s}/\eta_\mathrm{f}$ as a function of the relative volume fraction ϕ/ϕ_J ($\phi_\mathrm{c} = \phi_\mathrm{J}$). Taken from Guazzelli and Pouliquen (2018), figure 4b.

smaller values if the particles get jammed due to the frictional interaction between them (see Sec. 1.4.2). In this case, the value of ϕ_J may decrease with the shear stress as more particles form contacts, making the suspension shear thickening (η_s grows with increasing σ_{xy}, see next section).

1.3.1. Non-Newtonian behavior

The behavior of flowing suspensions is not fully described just by the previous viscosity function $\eta_\mathrm{s}(\phi)$, instead, measurements show some departures from Eq. 1.3 corresponding to non-Newtonian behavior.

Shear thinning and thickening

Suspensions can be both shear thinning and shear thickening, that is, η_s might decrease or increase with increasing shear rate $\dot{\gamma}$, respectively. For colloidal suspensions (particle size $\lesssim 10\,\mu\mathrm{m}$), the shear thinning and thickening behavior can alternate as the shear rate increases, like in the curves $\eta_\mathrm{s}(\dot{\gamma})$ displayed in Fig. 1.3a. For very high concentrations ($\phi \geq 0.51$ in this case), a discontinuous increase of the viscosity with the shear rate is observed, while at smaller

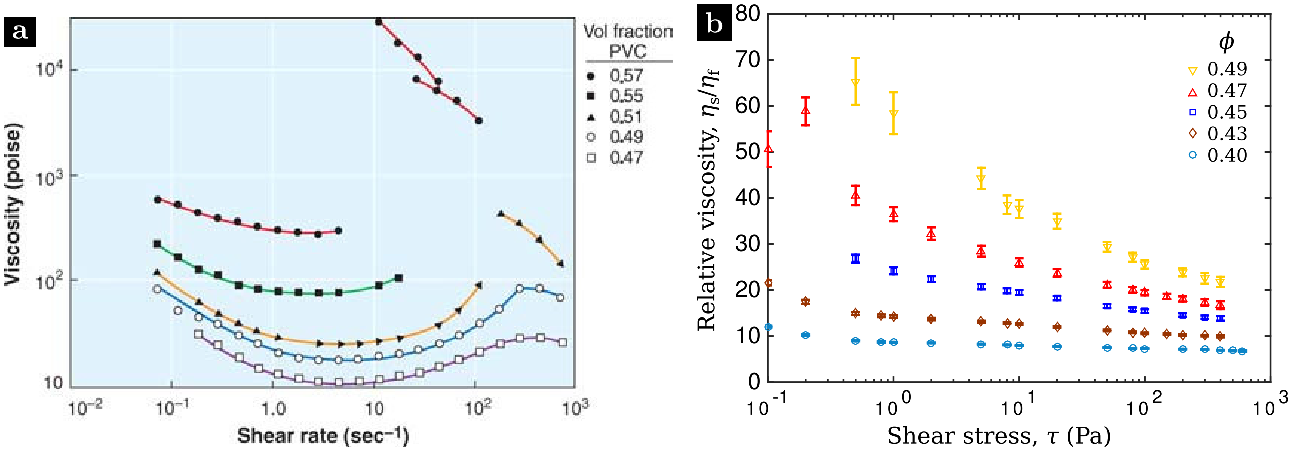

Figure 1.3: a) Suspension viscosity η_{s} as a function of shear rate $\dot{\gamma}$ for suspensions of 1.25 µm PVC spheres suspended in dioctyl phthalate. Measurements from Hoffman (1972), figure from Stickel and Powell (2005). b) Relative viscosity $\eta_{\mathrm{s}}/\eta_{\mathrm{f}}$ versus the shear stress $\tau = \eta_{\mathrm{s}}\dot{\gamma}$ for suspensions of 40 µm polystyrene (PS) spheres in silicon oil. From Lobry et al. (2019).

concentrations the change is continuous. Given the shear stress $\tau = \eta_{\mathrm{s}}\dot{\gamma}$, a critical stress τ_{c} can be defined for both forms of shear thickening behavior and, from an analysis of previous works, Barnes (1989) concluded that $\tau_{\mathrm{c}} \propto a^{-2}$, where a is the radius of monodisperse spheres. For this reason, shear thickening is usually not observed for larger particles (most flows will have $\tau > \tau_{\mathrm{c}}$), instead, only shear-thinning behavior can be seen, as show in Fig. 1.3b for spheres of diameter $2a = 40$ µm. Possible explanations for these phenomena usually consider short range interactions between particles, like repulsive forces for colloidal particles and solid contacts for large particles (Lemaire et al. 2023). More on these interactions will said in Sec. 1.4.

In our experiments with channel flows, both the shear rate and the volume fraction vary in space so, even if our suspensions (PMMA spheres with diameters of 40 and 85 µm) might be slightly shear thinning like other similar ones (Blanc, Peters, and Lemaire 2011; Gamonpilas, Morris, and Denn 2016), in practice, the variations of viscosity with the shear rate would be negligible compared to those induced by the variations of the volume fraction (see Sec. 1.6.2 for more details on the kind of flow conditions we study).

Normal stress differences

For incompressible Newtonian fluids, Eq. 1.3 implies that the diagonal components of the stress tensor (σ_{xx}, σ_{yy}, σ_{xx}) are all equal to $-p$, an isotropic pressure applied on the fluid element under analysis. These components are called *normal stresses*, and it has been found that in various complex fluids they may be different from each other, meaning that those fluids exert an anisotropic stress while flowing. In order to study the non-Newtonian behavior of a fluid, we are interested in the *normal stress differences*:

$$N_1 = \sigma_{xx} - \sigma_{yy}, \quad N_2 = \sigma_{yy} - \sigma_{zz}. \tag{1.12}$$

Here x, y, and z correspond to the flow, gradient, and vorticity directions of the simple shear flow displayed in Fig. 1.1.

A well-studied example is solutions of elastic polymers. Those tend to elongate with the flow, providing an additional tension in the flow direction which results in a positive N_1 and a small N_2 (Bird, Armstrong, and Hassager 1987). A consequence of this can be observed directly in experiments where a rod is partially submerged into a polymeric solution and rotated: the solution climbs up the rod and the free surface becomes curved (Weissenberg effect). From experiments like this and other rheological measurements, it is possible to measure linear combinations of N_1 and N_2 and, finally, infer their separate values as functions of the shear rate and other relevant parameters.

Zarraga, Hill, and Leighton Jr (2000) performed the above experiment with a suspension of spheres and found that the free surface depressed around the rod, a feature corresponding to a negative value of $N_1 + \frac{1}{2}N_2$. From this experiment, along with multiple other rheological experiments, they concluded that the suspension viscosity η_s decreases slightly with the shear rate $\dot{\gamma}$ (shear thinning behavior) and increases sharply with the volume fraction ϕ, like in Fig. 1.2. Moreover, they found that both N_1 and N_2 are negative, roughly proportional to the absolute value of the shear stress $\sigma_{xy} = \eta_s\dot{\gamma}$, and decrease with the volume fraction. Similar results were found by Dai et al. (2013), who complemented their rheological measurements with the observation of the curvature of the free surface of a suspension flowing down a trough. Figure 1.4 displays measurements of $-N_1/|\sigma_{xy}|$ and $-N_2/|\sigma_{xy}|$ as functions of ϕ obtained from multiple sources.

To incorporate the above observations into the suspension rheology, both Morris and Boulay (1999) and Zarraga, Hill, and Leighton Jr (2000) proposed similar phenomenological

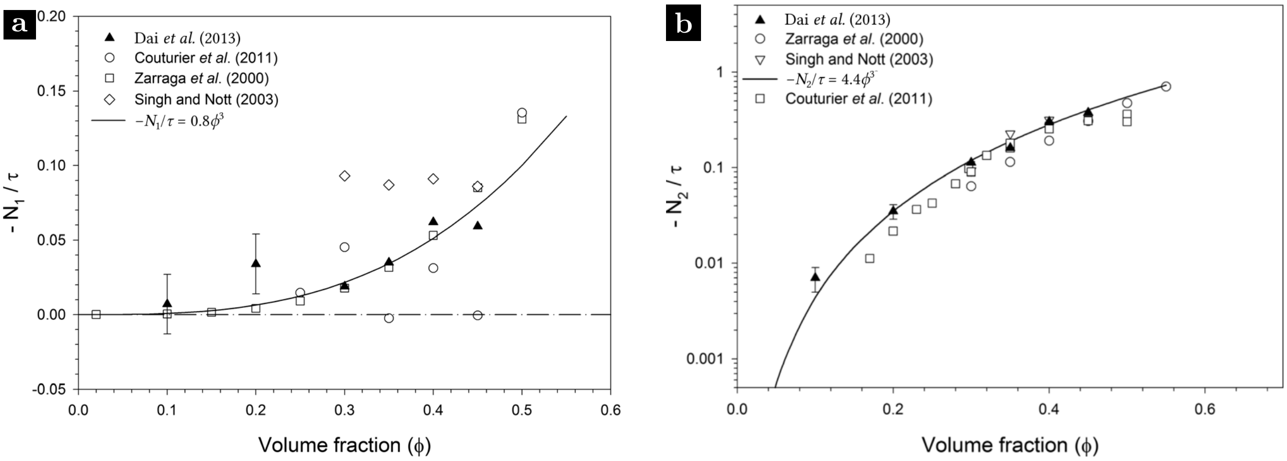

Figure 1.4: Normal stress differences N_1 (a) and N_2 (b) obtained in different experiments and simulations. Both are shown with the sign inverted and normalized by the absolute shear stress $\tau = |\sigma_{xy}|$. Taken from Dai et al. (2013).

models where the suspension stress has the form

$$\sigma^s_{ij} = -p\delta_{ij} + 2\eta_\mathrm{s}(\phi)\, E_{ij} - \eta_\mathrm{f}\eta_\mathrm{n}(\phi)\, |\boldsymbol{E}|\, Q_{ij}. \tag{1.13}$$

The first two terms are equivalent to those found for Newtonian fluids, with p, the fluid dynamic pressure, and η_s, the suspension viscosity which may take the form of an expression like Eq. 1.11. The last term accounts for the particle contribution to the pressure and the normal stress differences. Here $|\boldsymbol{E}| = (E_{ij}E_{ji})^{1/2}$ is a measure of the shear rate, and $\boldsymbol{Q}$ is the tensor

$$\boldsymbol{Q} = \begin{pmatrix} 1+\alpha_1 & 0 & 0 \\ 0 & 1 & 0 \\ 0 & 0 & 1-\alpha_2 \end{pmatrix}, \tag{1.14}$$

where α_1 and α_2 are constants of the order of 0.3 which account for the relative strengths of N_1 and N_2. Finally, η_n is an increasing function of the volume fraction that diverges at the jamming fraction ϕ_J and has a zero value in the absence of particles $[\eta_\mathrm{n}(0) = 0]$. Concretely, Morris and Boulay (1999) proposes $\eta_\mathrm{n} = C[\phi/(\phi_\mathrm{J} - \phi)]^n$ with $C = 0.6$ and $n = 2$, while Zarraga, Hill, and Leighton Jr (2000) uses $C = 2.17\,\phi_\mathrm{J}^3 \approx 0.5$ and $n = 3$.

The normal stress differences are closely connected with the fact that particles suspended in shearing flows are not distributed randomly inside the volume, but instead, form a *microstructure*. We will discuss this in greater detail in Sec. 1.5. For now, we want to highlight that the presence of elements that may alter this microstructure, like walls, can also directly affect N_1 and N_2. Gallier, Lemaire, Lobry, et al. (2016) performed simulations of suspensions in wall-bounded channel flow and found that N_1 is positive near the walls (up to a distance of roughly one particle diameter), and negative, far from them.

1.4. Interactions

The macroscopic behavior of the suspension is defined by the way the particles interact with the surrounding fluid and between themselves. Here, we present the most common mechanisms.

1.4.1. Hydrodynamic forces

One particle moving relative to the surrounding fluid will experience a *drag force* which, for a sphere of radius a and with $\mathrm{Re} = 0$, takes the form

$$\boldsymbol{F}_{\mathrm{d}} = -6\pi\eta_{\mathrm{f}} a\,(\boldsymbol{u}^p - \boldsymbol{u}), \tag{1.15}$$

where $\boldsymbol{u}^p$ is the particle velocity, and $\boldsymbol{u}$ is the bulk velocity of the fluid which can be estimated by calculating the average fluid velocity in a suitably large volume centered on the particle.

In general, the drag force will oppose any relative displacement, making the particles and the fluid move mostly together in viscous fluids. In a simple shear flow of the form $\boldsymbol{u} = \dot{\gamma} y \hat{x}$, a force-free sphere will move with the velocity corresponding to its position, i.e. $\boldsymbol{u}^p = \dot{\gamma} y_p \hat{x}$ for a particle with its center located at (x_p, y_p, z_p). Furthermore, such a sphere will introduce a perturbation of the velocity field that extends to a considerable distance due to its slow decay as $1/r^2$ far from the sphere, with r being the distance from the center of the particle (Batchelor 1967, chapter 4).

When multiple particles are present, the perturbations may reach each other and generate long-range interactions. In the limit $\mathrm{Re} \to 0$, the hydrodynamic forces and torques exerted on the particles can be calculated as the multiplication of a resistance matrix and a vector made from the translational and rotational velocities of the particles. The resistance matrix is a function only of the relative particle positions, their radii, and the fluid viscosity (any non-viscous force has to be considered separately). This approach is the basis of the Stokesian dynamics simulations (Brady and Bossis 1988).

Of special interest is the hydrodynamic interaction between two nearly touching particles since it is dominated by the *lubrication force*. For two spheres with same radius a, its normal component is

$$\boldsymbol{F}_{\mathrm{l}} = -\frac{6\pi\eta_{\mathrm{f}} a^2 U_r}{r - 2a}\hat{\boldsymbol{r}}, \tag{1.16}$$

where $\hat{\boldsymbol{r}}$ is the unit vector pointing from one particle to the other, and U_r is the radial component of the relative pair velocity $\boldsymbol{U}$ (see Fig. 1.5).

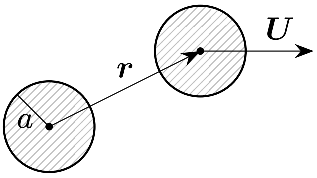

Figure 1.5: Interacting pair of spheres.

The lubrication force opposes any change in the relative distance r between the spheres and diverges as they come closer. Similar characteristics can be found for particles of (almost) any shape and also for the interaction between particles and walls (effectively a sphere of infinite radius). The fact that $\boldsymbol{F}_{\mathrm{l}}$ diverges as $r \to 2a$ suggests that any direct contact between two sphere would be impossible but, in practice, this is not the case as real surfaces are rough and have asperities (see next section).

Notice that for the lubrication force we have to consider only two particles at a time, and not the interactions between all of them like in the resistance matrix formulation. Both approaches may be combined to efficiently simulate concentrated suspensions.

1.4.2. Contact forces

When a suspension of spheres is subject to a shearing flow like that shown in Fig. 1.1, a sphere far from others and at a transverse position y will move with the velocity $\boldsymbol{u} = \dot{\gamma} y \hat{\boldsymbol{x}}$ of the streamline, due to the drag force. Then, spheres in different streamlines may collide in the sense that they approach, have strong short-range interactions and, then, separate (see Fig. 1.6). At zero Re, the reversibility of the Stokes equation (1.9) and the symmetry of the bulk flow, would make the trajectories fore-aft symmetric (i.e. in the flow direction x, see the black curve in Fig. 1.6b).

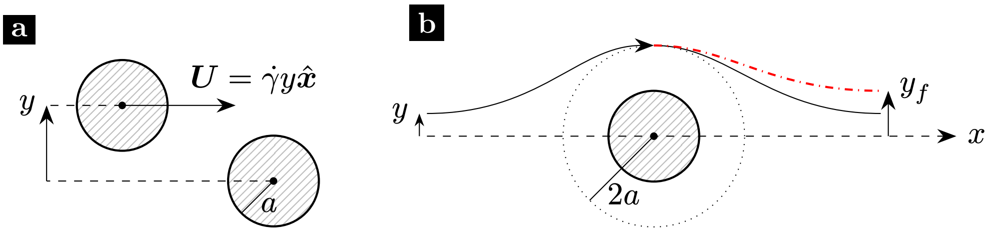

Figure 1.6: Particle collision in bulk shear flow. a) Two spheres approaching. b) Possible trajectories of the top sphere in a reference frame following the bottom one. Black curve: hydrodynamic forces only. Red dash-dotted curve: hydrodynamic and contact forces.

Contrary to this, experiments with shear flow shows that suspended spheres have a transverse self diffusivity D_y proportional to $a^2\dot{\gamma}$ and increasing with ϕ (D. Leighton and Acrivos 1987a). This means that after a time t, a sphere will end up at a transverse distance $\sqrt{D_y t}$ from its original streamline, on average. Then, it must be able to change streamlines by a mechanism not considered above. Possible mechanisms include interactions of more than two spheres, and non-hydrodynamic interactions like Brownian motion (Sec. 1.4.3), colloidal forces (Sec. 1.4.4), and solid contacts. Of those, only solid contacts was shown to be relevant for larger particles ($2a > 10\,\mu\mathrm{m}$), and for all volume fractions, down to the case of only two particles (Firouznia et al. 2018; Popova et al. 2007).

When two spheres approach each other, their surface separation may become exceedingly small ($\sim 10^{-4}a$) and, while the lubrication force guarantees that smooth surfaces will not touch, real spherical particles have rough surfaces with asperities of comparable size (Lemaire et al. 2023). Accordingly, two rough spheres close enough can make contact through their asperities and an additional normal force appears, halting their approach. The *contact force* only acts when particles approach, but not when they separate, and this results in fore-aft asymmetric trajectories, like that illustrated by the red dash-dotted curve in Fig. 1.6b (Da Cunha and Hinch 1996). This behavior is irreversible under flow reversal: a sphere starting with the separation y_f shown in the figure, and going to the left, would not end with a separation $|y| < |y_f|$, but even farther apart.

Besides a normal component, the contact force may have a tangential component that hinders or prevents sliding motion between particles. This *frictional force* is crucial to reproduce in simulations the experimentally measured viscosities (Gallier, Lemaire, Peters, et al. 2014). These restrictions on the particles motion may jam the suspension for particle configurations where it would otherwise flow, effectively reducing the jamming fraction ϕ_J (Wyart and Cates 2014).

1.4.3. Brownian motion

Very small particles ($2a \lesssim 1\,\mu\text{m}$) can be significantly displaced by the random collisions with the molecules of the fluid. The accumulation of these displacements results in a random walk first described by Robert Brown in 1827, and can be characterized by a diffusivity

$$D_{\mathrm{B}} = \frac{k_{\mathrm{B}}T}{6\pi\eta_{\mathrm{f}}a}, \tag{1.17}$$

where k_{B} is the Boltzmann constant, T is the temperature, and a is the particle radius. The Péclet number $\mathrm{Pe} = UL/D_{\mathrm{B}}$ compares the convective and diffusive transport rates, with U and L being characteristic velocity and length scales. Considering again the case of particle shear flows with $U = \dot{\gamma}a$ and $L = a$, we obtain the particle Péclet number

$$\mathrm{Pe}_{\mathrm{p}} = \frac{\dot{\gamma}a^2}{D_{\mathrm{B}}} = \frac{6\pi\eta_{\mathrm{f}}\dot{\gamma}a^3}{k_{\mathrm{B}}T}. \tag{1.18}$$

It is clear now why the particles must be small for the Brownian motion to have a significant impact. In practice, this means that small particles in a static fluid will eventually reach an equilibrium distribution, while large particles will remain in their positions for very long times in the absence of external forces (e.g. gravity). In our study, we do not need to consider Brownian forces since the spheres used have diameters $2a \geq 40\,\mu\text{m}$, and can be safely considered as *non-Brownian.*

1.4.4. Colloidal forces

Another interaction relevant for small particles is the colloidal forces between pairs of them. One considers as colloidal any short-range (nanometric scale) force between the surfaces of two adjacent particles. The most common cases are Van-der-Waals forces, which are attractive, and electrostatic forces between equally-charged particles, which are repulsive. Colloidal forces affect significantly the motion of the particles when the ratio between their surface and volume is large enough, in practice, this applies for particles with $2a \lesssim 10\,\mu\text{m}$, otherwise, they are called *noncolloidal.* As in the case of Brownian forces, the relatively large size of our particles ($2a \geq 40\,\mu\mathrm{m}$) means that colloidal forces will not play an important role in our experiments.

1.4.5. Gravity and sedimentation

One particle submerged and under the effect of gravity will be subject to a *buoyancy force*

$$\boldsymbol{F}_\mathrm{b} = (\rho_\mathrm{p} - \rho_\mathrm{f}) V_\mathrm{p}\, \boldsymbol{g}, \tag{1.19}$$

where ρ_p is the particle density, ρ_f is the fluid density, V_p is the particle volume, and $\boldsymbol{g}$ is the gravity acceleration. Spherical particles of radius a and denser than the fluid will settle with a velocity

$$U_\mathrm{S} = \tfrac{2}{9}(\rho_\mathrm{p} - \rho_\mathrm{f}) a^2 g / \eta_\mathrm{f} \tag{1.20}$$

in the Stokes regime ($\mathrm{Re} = 0$), as a result of the balance of $\boldsymbol{F}_\mathrm{b}$ and the drag force $\boldsymbol{F}_\mathrm{d}$.

With multiples particles in suspension, the settling, also called *sedimentation*, is hindered by the interactions between each other, and U_S must be corrected by a factor which has been estimated as (Richardson and Zaki 1954)

$$f_\mathrm{hs}(\phi) = (1 - \phi)^\alpha, \tag{1.21}$$

with exponents α between 2 and 5.1 found in the literature (Chapman and Leighton Jr 1991; Miller and Morris 2006). As for the suspension viscosity, an exact calculation of f_hs would require a knowledge of the particle distribution (Davis and Acrivos 1985).

In order to study the effects of the flow on our suspensions separately from any buoyancy effects, we matched both densities ($\rho_\mathrm{f} = \rho_\mathrm{p}$), rendering the particles *neutrally buoyant.*

1.5. Microstructure: particle self-organization at the microscale

In the previous section, we have seen different ways in which the particles can interact between themselves and with the fluid, especially in straining flows which make the particles approach one another. In principle, the knowledge of the particle configuration (e.g. position of the centers) and the boundary conditions for the fluid might allow us to calculate macroscopic properties of a suspension (e.g. viscosity). Given that the particles can have significant long-range interactions, it is necessary to consider how each particle influences the motion of every other one, an exceedingly difficult task to perform analytically, and a computationally demanding one for simulations.

Batchelor and Green (1972) approached this problem by considering that in low-concentration ($\phi \lesssim 0.1$) non-Brownian sphere suspensions, only pairwise hydrodynamic interactions between the spheres need to be taken into account to calculate the suspension viscosity $\eta_{\mathrm{s}}(\phi)$ up to an order ϕ^2. In the other extreme, for very high concentrations ($\phi \gtrsim 0.45$), Mari et al. (2014) have shown that simulations using only pairwise forces between the particles can qualitatively reproduce several characteristics of suspensions near jamming. This is so because in this case most of the suspension stress results from short-range lubrication or contact forces between nearby particles. For intermediate concentrations, the long-range multi-body hydrodynamic interactions must be incorporated using simulation methods like *Stokesian Dynamics* (Brady and Bossis 1988), *force coupling* (Yeo and Maxey 2010), or *fictitious domain* (Gallier, Lemaire, Peters, et al. 2014) and, even in these more complete simulations, limitations in the spatial resolution usually require that short-range hydrodynamic interactions forces are complemented with additional forces between pairs of neighboring particles.

For the above reasons, it is very important to know about the spatial distribution of neighboring particles in suspensions, usually through the statistical properties of their relative positions. Consider a volume V containing N ($\gg 1$) particle centers in a suspension undergoing a simple shear flow like that shown in Fig. 1.1, induced, for example, by moving walls far from the volume under analysis. During the shearing, particles will keep moving and colliding each other but, eventually, the statistical properties of the suspension will stop changing meaningfully and it can be said to be in a *steady state.*

One such property is the probability density $P(\boldsymbol{x}_0+\boldsymbol{r}|\boldsymbol{x}_0)$ of finding a particle at a position $\boldsymbol{x}_0 + \boldsymbol{r}$ when a reference particle is at position $\boldsymbol{x}_0$. Far from the reference particle ($|\boldsymbol{r}| \to \infty$), the particle positions are uncorrelated and $P(\boldsymbol{x}_0 + \boldsymbol{r}|\boldsymbol{x}_0)$ is simply $P(\boldsymbol{x}_0 + \boldsymbol{r}) = n$, where $n = N/V$ is the particle number density. Here we assume that there are no inhomogeneities in the particle concentration. On the other hand, near the reference particle, the distribution of neighboring particles is usually not uniform and it gives us information about the way in which particles interact.

In particular, we will take

$$P(\boldsymbol{x}_0 + \boldsymbol{r} | \boldsymbol{x}_0) = n\, g(\boldsymbol{r}), \tag{1.22}$$

where g is the *pair-distribution function* which in general may depend on time t, position $\boldsymbol{x}_0$, radii of the particles, and other properties of them. Here, we will concentrate on the simpler case where the suspension properties are constant and homogeneous, and all the particles are identical spheres of the same radius a.

1.5.1. Steady pair-distribution function

Several measurements of $g(\boldsymbol{r})$ in experiments and simulations may be found in the literature about suspensions, of which Parsi and Gadala-Maria (1987) seems to be the earliest. Here, we want to highlight the work of Blanc, Lemaire, et al. (2013) due to the clarity of their results and the wide range of particle volume fractions studied. They performed experiments in which a suspension of monodisperse spheres ($2a = 86\,\mu\mathrm{m}$) is continuously sheared inside a wide-gap Couette device, with very small Reynolds numbers and very large Péclet ones. Using fluorescence, they were able to observe the particles in a plane inside the device, as shown in Fig. 1.7a. This plane corresponded to the velocity (x) and gradient (y) directions. Inside the region of interest (white box in Fig. 1.7a), the volume fraction ϕ and the shear rate $\dot{\gamma}$ are approximately uniform. These authors tracked the particles and accumulated enough statistics to obtain the twodimensional pair-distribution functions (pdf) displayed in Figs. 1.7b-f, each corresponding to a different volume fraction. In all cases, the results correspond to the steady state reached after enough shearing.

All the pdf's present their largest probability for pairs of particles nearly in contact (red rings at $r \approx 2a$ in the images). Looking at the smallest volume fraction ($\phi = 0.05$ in Fig. 1.7b), we observe that $g(r_x, r_y)$ is roughly symmetric with respect to a reflection along the horizontal direction, and has depletions of pairs near $r_y = 0$. This is called fore-aft symmetry since inverting the flow direction (horizontal) would result in a similar pdf. That said, it is clear that this pdf is not completely symmetric and, as the volume fraction increases, the pdf's become more asymmetric with respect to a flow inversion. Figure 1.7d ($\phi = 0.35$) is a clear example: now the depleted regions are off axis at what are called the extensional

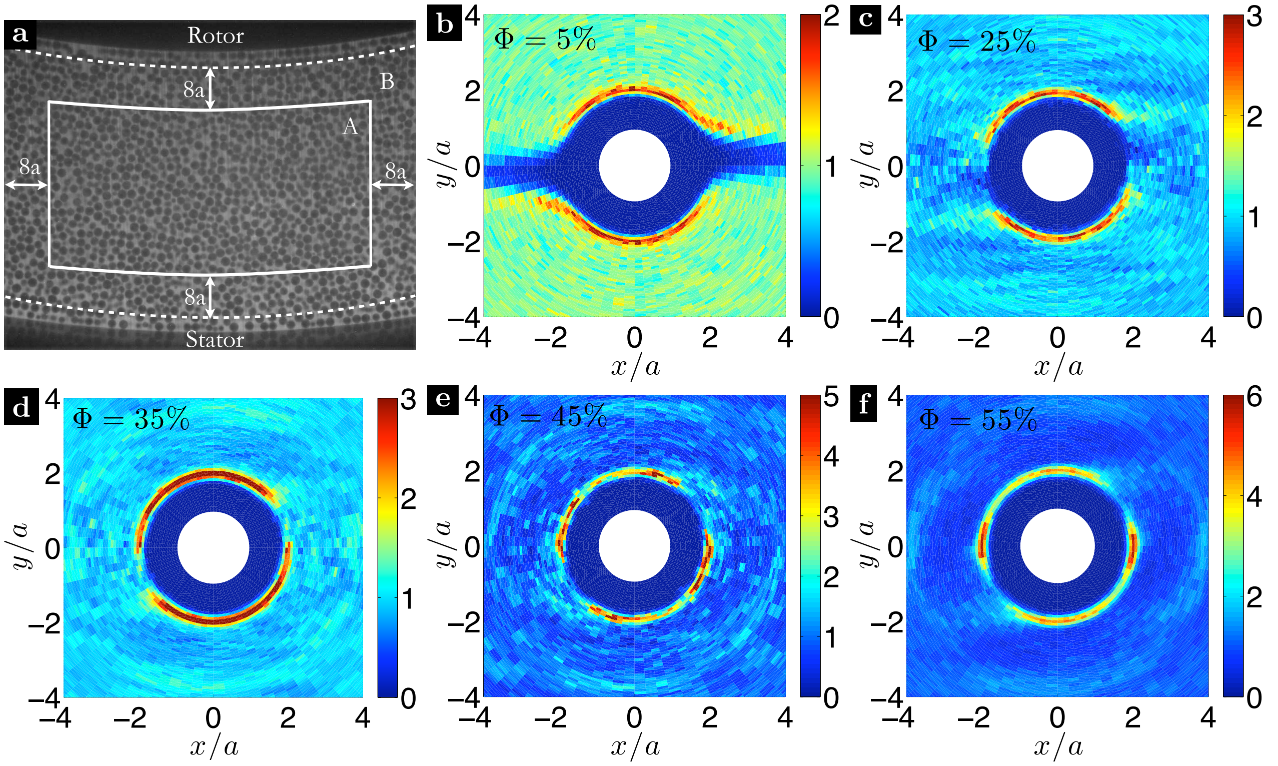

Figure 1.7: Figures taken from Blanc, Lemaire, et al. (2013). a) Example image from their experiments. The dark disks correspond to spherical particles with diameters $2a \approx 86\,\mu\mathrm{m}$. The inner radius rotates to the right to induce an approximately uniform shear inside the white box, where the data is collected. b-f) Pair-distribution function $g(r_x, r_y, r_z)$ for $r_z \approx 0$, as a function of r_x/a (horizontal axis) and r_y/a (vertical one). The colors indicate the values of g. Each plot corresponds to a different particle volume fraction ϕ.

quadrants ($r_x r_y > 0$).

This is an important characteristic of the pdf's of suspensions. The reversibility of the Stokes equation (Eq. 1.9) with respect to an inversion of the flow direction results in trajectories for the collision of two particles which are symmetric in the flow direction, when only hydrodynamic forces are considered (see black curve in Fig. 1.6b). In turn, this results in a symmetric pdf similar to that shown in Fig. 1.7b. As the particle concentration increases, the short-range interactions which are not reversible become important, most prominently the direct contacts between the particle surfaces. The normal contact force keeps the particles in a pair separated during their approach in the compressional quadrant ($r_x r_y < 0$), but does not have an impact during their separation in the extensional quadrant ($r_x r_y > 0$); this results in irreversible trajectories (red curve in Fig. 1.6b) and the asymmetry observed in Fig. 1.7d. Moreover, it leads to a particle self-diffusivity that will be discussed in Sec. 1.6.1 and to the normal stress differences shown in Sec. 1.3.1 (Brady and Vicic 1995; Seto and Giusteri 2018).

For even larger volume fractions ($\phi = 0.45$ and 0.55 in Figs. 1.7e,f), secondary depletion zones appears in the compressional quadrants, and the pdf becomes roughly symmetric with respect to inversions in either x or y directions. This increased ordering as the volume fraction approaches its jamming value ($\phi \approx 0.6$), may reduce effects associated with the fore-aft asymmetry of g, like self-diffusivities (Zhang, Kopelevich, and Butler 2024) and normal stress differences (Seto and Giusteri 2018).

1.5.2. Reorganization after flow reversal

The fact that neighboring particle positions are correlated in space is interpreted as a shear-induced *microstructure* of suspensions. In general, this structure is not symmetric and depends on the type of flow. The pdf's observed in Figs. 1.7b-f correspond to a shearing flow where the particles move from left to right in the top ($r_y > 0$) and, opposite, below ($r_y < 0$). If the flow direction were to reverse, the particles would have to rearrange such that the pdf's become reflected along the flow direction (x). During this transient situation, most particles lose contacts and the suspension viscosity is sharply reduced, as first shown by Gadala-Maria and Acrivos (1980).

Figure 1.8a shows measurements of the relative suspension viscosity $\eta_\mathrm{s}/\eta_\mathrm{f}$ as functions of the strain $\dot{\gamma}t$ accumulated after a shear reversal (Blanc, Peters, and Lemaire 2011). Immediately after reversal ($t = 0$), there is a sharp decrease of the viscosity in all cases, which then continues to decrease a little more before starting to recover until it reaches its pre-reversal (steady) value after a strain $\dot{\gamma}t$ of the order of one.

In order to understand better this process, Peters et al. (2016) performed simulations where they distinguish between the contributions of hydrodynamic and contact forces to the viscosity. Figure 1.8b displays the suspension viscosity η^S, the hydrodynamic contribution η^H and the contact one η^C as functions of the accumulated strain $\dot{\gamma}t$ before and after a reversal at $t = 0$, for a suspension of spheres with volume fraction $\phi = 0.45$. Note that $\eta^S = \eta^H + \eta^C$. Looking at the components (middle and bottom plots), we observe that the sharp decrease in η^S is a consequence of the drop to zero of the contact contribution, while the hydrodynamic one increases moderately. After these sudden changes, both components slowly relax to their previous values. Since η^C takes on values about twice those of η^H in the steady state (for

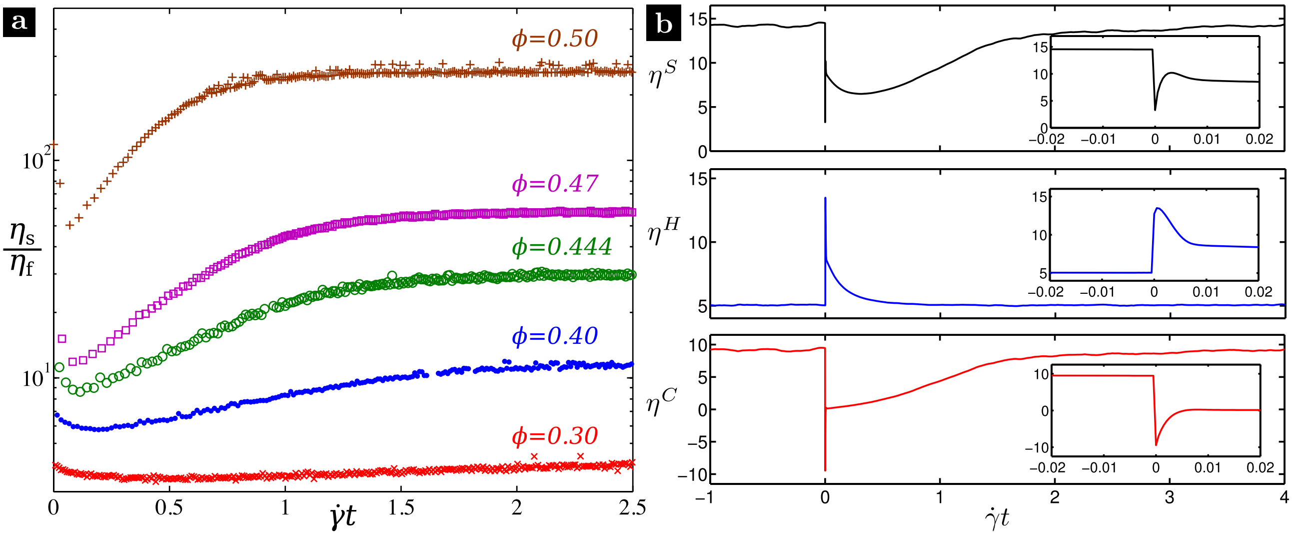

Figure 1.8: a) Relative suspension viscosity η_s/η_f versus accumulated strain $\dot{\gamma}t$ after a shear reversal ($t = 0$). Measurements by Blanc, Peters, and Lemaire (2011) using various volume fractions ϕ. b) Suspension viscosity (η^S), and its hydrodynamic (η^H) and contact (η^C) components for a simulated suspension with $\phi = 0.45$ in a similar situation. From Peters et al. (2016).

this particular volume fraction), the loss of contacts induces a strong reduction of the total suspension viscosity.

A study of the previous variations for different volume fractions shows that the viscosity drop $[\max(\eta^S) - \min(\eta^S)]$ increases monotonically with the volume fraction ϕ, and the characteristic strain required for relaxation, decreases monotonically with ϕ. The first observation can be explained by the contribution of contacts to the suspensions stress increasing as the particles are forced into a closer proximity of each other. The second observation is a consequence of the increased rate of particle collisions, which accelerates the irreversible evolution of the suspension.

The above results show that, in order to fully explain time-dependent flows of suspensions, we need to know not only the particle volume fraction at each position, but also the instantaneous state of the particle microstructure. Various models were proposed along the years for capturing its salient characteristics with a reduced number of degrees of freedom, usually taking the form of a second-order fabric tensor $\langle p_i p_j \rangle$ where $\boldsymbol{p} = \boldsymbol{r}/|\boldsymbol{r}|$ and the average is calculated over all the particle pairs with the help of an estimation of g (Phan-Thien 1995; Chacko et al. 2018; J. Gillissen and H. Wilson 2018).

1.6. Shear-induced self-diffusion and migration of particles

In section 1.4.2, we explained that two particles approaching each other in a simple shear flow could experience solid contacts through asperities on their surfaces, with the end result that particles accumulate displacements transverse the flow direction after each of those close encounters. These displacements induce a random walk of the particles, happening simultaneously with the shearing motion, which can be characterized by a self-diffusivity increasing with the shear rate and the volume fraction (Drazer et al. 2002). Then, in inhomogeneous situations where the shear rate or the volume fraction vary with the position, this otherwise random motion can give rise to net flows of particles moving from regions where the diffusivity is larger to ones where it is smaller. This phenomenon is called *shear-induced migration* of the particles (D. Leighton and Acrivos 1987b), and it is an irreversible process happening in suspensions with $\mathrm{Re} = 0$ and $\mathrm{Pe} \to \infty$, since reversing the flow direction would not bring the suspension back to its previous state, but further increase the lateral deviations of the particles.

The phenomena discussed in this section are essential to our work since we study pressure-driven flows of suspensions through channels, one of the most common situations where the particle migration can be observed. Moreover, knowledge of the particle self-diffusivity can be useful to estimate the characteristic lengths and times of other irreversible processes in suspensions. Later, in Sec. 1.7, we will consider how the oscillatory flows used in our experiments may be affecting the diffusion and migration processes explained here.

1.6.1. Particle self-diffusion

Simulations and experiments tracking individual particles can provide transverse positions $y(t)$ and $z(t)$ of the particles. Here x is the flow direction, y is the velocity gradient direction, and z is the vorticity direction (refer to Figs. 1.1 and 1.6). Then, it is possible to calculate the accumulated displacements $\Delta y(t) = y(t) - y(0)$ and $\Delta z(t) = z(t) - z(0)$ resulting from the multiple collisions that each particle experienced up to time t. For simple shear flows (i.e. uniform and constant $\dot{\gamma}$ and ϕ), and assuming that the experiments start from a steady state at time $t = 0$, the average over multiple particles and experiments results in curves of $\langle(\Delta y)^2\rangle/a^2$ and of $\langle(\Delta z)^2\rangle/a^2$ versus $\dot{\gamma}t$ like those shown in Fig. 1.9a. After an initial transient behavior (up to $\dot{\gamma}t \approx 5$ here), the curves become linear and diffusion coefficients D_{yy} and D_{zz} can be obtained using the following relations:

$$\langle(\Delta y)^2\rangle \sim 2D_{yy}t, \quad \langle(\Delta z)^2\rangle \sim 2D_{zz}t. \tag{1.23}$$

Considering a zero particle Reynolds number, and excluding the influence of the walls or external forces (e.g. gravity), the only characteristic scales are given by the particle radius a (assuming monodisperse particles) and by the inverse of the shear rate $1/\dot{\gamma}$. Then, the dimensionless diffusivities $D^*_{yy} = D_{yy}/(a^2\dot{\gamma})$ and $D^*_{zz} = D_{zz}/(a^2\dot{\gamma})$ can be used to compare the results from different works.

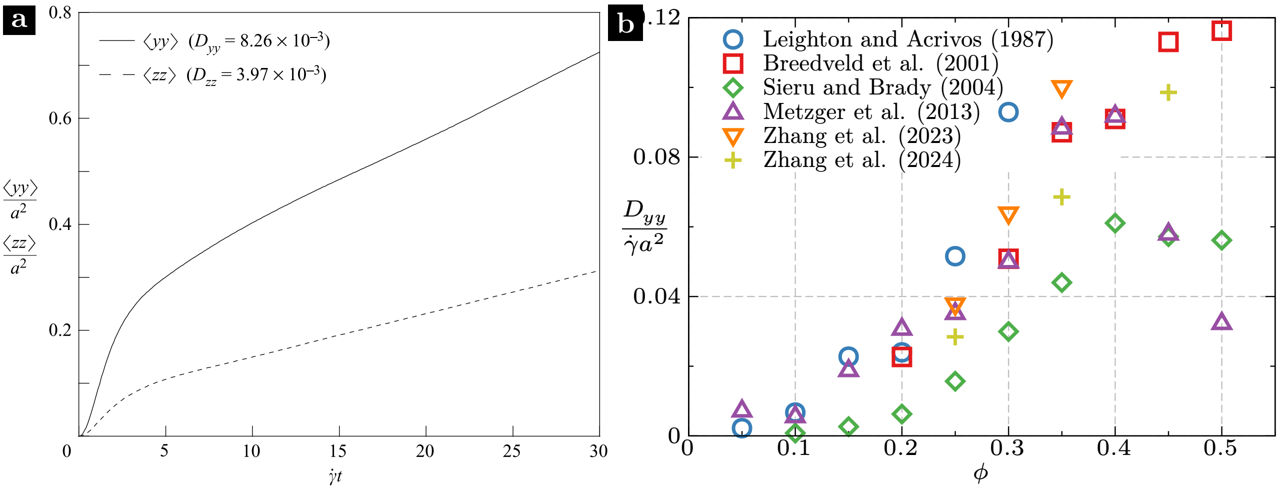

Figure 1.9: a) Representative mean-square displacement curves $\langle yy\rangle = \langle(\Delta y)^2\rangle$ and $\langle zz\rangle = \langle(\Delta z)^2\rangle$ as functions of strain $\dot{\gamma}t$ for suspensions with volume fraction 0.2 in simulations from Sierou and Brady (2004). b) Self-diffusion coefficient in the gradient direction $D^*_{yy} = D_{yy}/(\dot{\gamma}a^2)$ as a function of the volume fraction ϕ. Taken from various experiments (D. Leighton and Acrivos 1987a; Breedveld et al. 2001; Metzger, Rahli, and Yin 2013; Zhang, Pham, et al. 2023) and simulations (Sierou and Brady 2004; Zhang, Kopelevich, and Butler 2024).

Figure 1.9b displays values of D^*_{yy} as a function of ϕ obtained by multiple authors. Values for D^*_{zz} are less frequently found in the literature as they are more difficult to measure in experiments, but generally, they show similar trends but smaller values. In all cases, the diffusivity D^*_{yy} increases greatly with volume fractions from $\phi = 0.1$ to ≈ 0.4. For larger values of ϕ, the diffusivity may continue to increase, may remain flat or it may even decrease.

It seems that at higher concentrations, factors related to the details of the contact forces and the ordering of the particles become important. For example, Metzger, Rahli, and Yin

(2013) observed that the particles got organized into layers parallel to the flow direction in their experiments using large volume fractions ($\phi > 0.4$). Similarly, Zhang, Pham, et al. (2023) found that particles with larger surface roughness got organized into layers, and their measured diffusivities were approximately a 20% smaller than those of smoother particles, contrary to expectations of the opposite. They hypothesize that particles moving inside layers may be able to avoid collisions, or they may bounce back to their original layer after one, reducing the opportunities to accumulate large displacements. Continuing this work, Zhang, Kopelevich, and Butler (2024) performed simulations with and without friction during contacts (i.e. the tangential component of the contact force), and found that the addition of friction significantly increased the diffusivity, improving the agreement with experimental data (see the yellow crosses in Fig. 1.9b) compared to previous simulations from Sierou and Brady (2004) (green diamonds) which do not account for friction. Consistently, they show that in simulations with frictional contacts, the particles are less prone to form layers.

In summary, measurements of the particle self-diffusivity provide a macroscopic characterization of the effect of particle-particle contacts, which is otherwise very difficult to observe directly, and the trends shown here (increase with ϕ, influence of surface characteristics and ordering of the particles), will remain relevant to analyze more complex situations with gradients in the strain rate and the volume fraction directly influencing the motion of the particles.

1.6.2. Shear-induced migration

Gadala-Maria and Acrivos (1980) observed a long-term decrease of the viscosity of a suspension in a Couette device. It turned out that the particles were escaping from the gap where the shear is imposed to a connected reservoir which was stationary, decreasing the particle volume fraction in the gap. D. Leighton and Acrivos (1987b) explained this phenomenon as the migration of particles from regions of high to low shear stress $\eta\dot{\gamma}$ (gap to reservoir), as a result of their shear-induced diffusive motion.

Pressure-driven flows inside tubes or channels are important situations where particle migration is also observed. Figure 1.10 illustrates the flow induced in a fluid filling the space between two parallel planes by a uniform pressure gradient parallel to the planes (x direction).

The planes correspond to fixed walls and the no-slip boundary condition imposes $\boldsymbol{u}(\pm b) = 0$. For a Newtonian fluid with viscosity η and Re = 0, Eq. (1.9) predicts a shear stress linear in y:

$$\eta \frac{\partial u_x}{\partial y} = -Gy, \tag{1.24}$$

where G is the magnitude of the pressure gradient. Assuming a uniform viscosity η, the integration of the previous equation results in a parabolic velocity profile

$$\boldsymbol{u}(y) = u_{\max}\left[1 - \left(\frac{y}{b}\right)^2\right]\hat{\boldsymbol{x}}, \quad u_{\max} = \frac{Gb^2}{2\eta}. \tag{1.25}$$

Such profiles can be observed in channels where the previous situation is approximated by a rectangular cross section with a large aspect ratio, assuming the observations are performed far enough from the lateral walls.

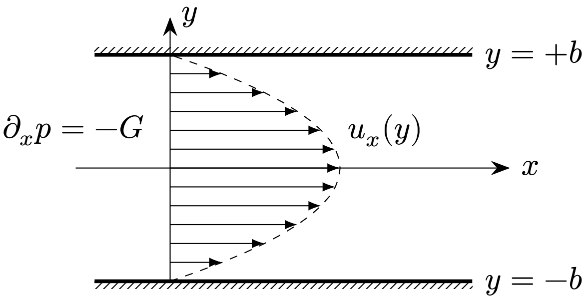

Figure 1.10: Flow between two parallel planes at $y = \pm b$ induced by a pressure gradient $-G$ in the x direction.

If instead of a Newtonian fluid, we have a suspension between the planes, the inhomogeneity of the shear stress will make the particles migrate towards the center where $\dot{\gamma} = 0$. Rashedi et al. (2020) performed steady channel flow experiments in a 4 m-long rectangular channel with a width of 40 mm and a gap $2b = 2$ mm. Particles with diameter $2a \approx 80$ µm were suspended in a very viscous fluid, resulting in a Reynolds number close to zero (Re $< 10^{-5}$). The suspension entered the channel with an almost uniform particle concentration, and reached the outlet with a significantly larger concentration in the center of the gap. Figure 1.11 shows images and volume fraction profiles taken near the inlet and the outlet for a suspension with average volume fraction $\phi_{\text{bulk}} = 0.4$.

Another consequence of the particle migration is a nonuniform viscosity. Remember that the suspension viscosity increases with the volume fraction and diverges near the jamming

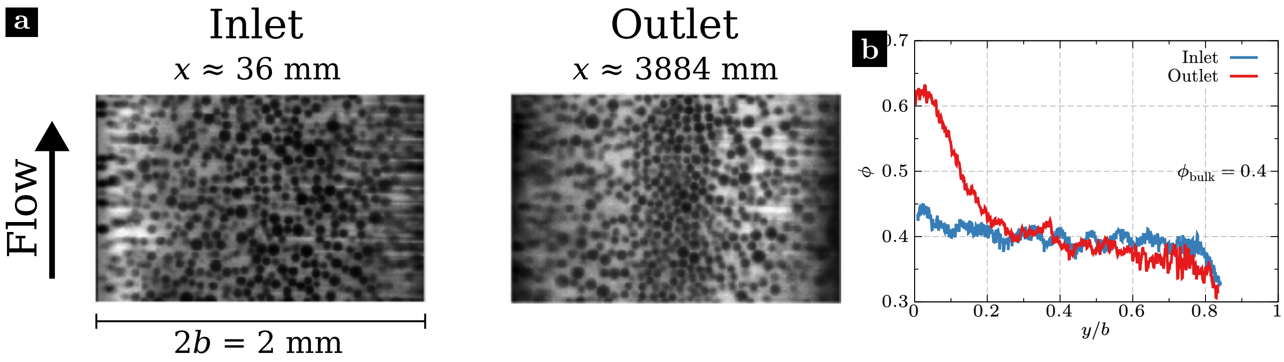

Figure 1.11: a) Images showing a slice of a suspension of spheres ($\phi_{\text{bulk}} = 0.4$) in a straight channel. The slice shows the flow and gap directions, and is located far from the lateral walls. Left: near the inlet. Right: near the outlet. b) Particle volume fraction profiles across one half of the gap (center at $y = 0$, wall at $y = b$). From Rashedi et al. (2020), figures 2 and 6.

fraction (see Sec. 1.3). After migration, the local volume fraction ϕ increases monotonically from the walls ($y = \pm b$) to the gap center ($y = 0$), reaching values near its jamming fraction (≈ 0.6) close to the later, as seen in the red curve in Fig. 1.11b. Consequently, the suspension viscosity η_{s} will also increase from the walls to the center, and replacing η with $\eta_{\text{s}}(\phi)$ in Eq. (1.24) will result in non-parabolic velocity profiles.

Figure 1.12 displays profiles across the gap of the particle volume fraction $\phi(y)$ and the particle longitudinal velocity $u_x^{\text{p}}(y)$ for mean volume fractions ϕ_{bulk} between 0.1 and 0.5.[2] On the left, we observe that all the concentration profiles show the effects of particle migration, although the maximum volume fraction reached in the center increases with ϕ_{bulk}. On the right, the velocity profiles become progressively more *blunted* in the center with increasing ϕ_{bulk}, that is, with smaller maximum velocities in the center ($y = 0$) and larger ones near the walls ($y = \pm b$). This is a consequence of the nonuniform viscosity which is larger in the center and smaller near the walls. For the larger concentrations ($\phi_{\text{bulk}} \geq 0.30$), the volume fraction near the center approaches the maximum packing (≈ 0.6), resulting in very large viscosities there and a region where the suspension moves almost like a solid block, with nearly constant velocity and zero shear rate.

Rashedi et al. (2020) also measured volume fraction profiles at intermediate positions between the inlet ($x = 0$) and the outlet ($x = 4000\,b$). Looking at the volume fraction ϕ_{center} in the center ($y = 0$) of those profiles, it is possible to track the progress of the particle

---

[2] The particle velocity $\boldsymbol{u}^{\text{p}}$ is measured from the average motion of the particles and, in principle, it could differ from the fluid-averaged velocity. Nonetheless, this is a very viscous fluid and $\text{Re} \approx 0$, then, we can assume that the drag force makes the velocity slip between the particles and the fluid minimal and both velocities are identical for our current purposes.

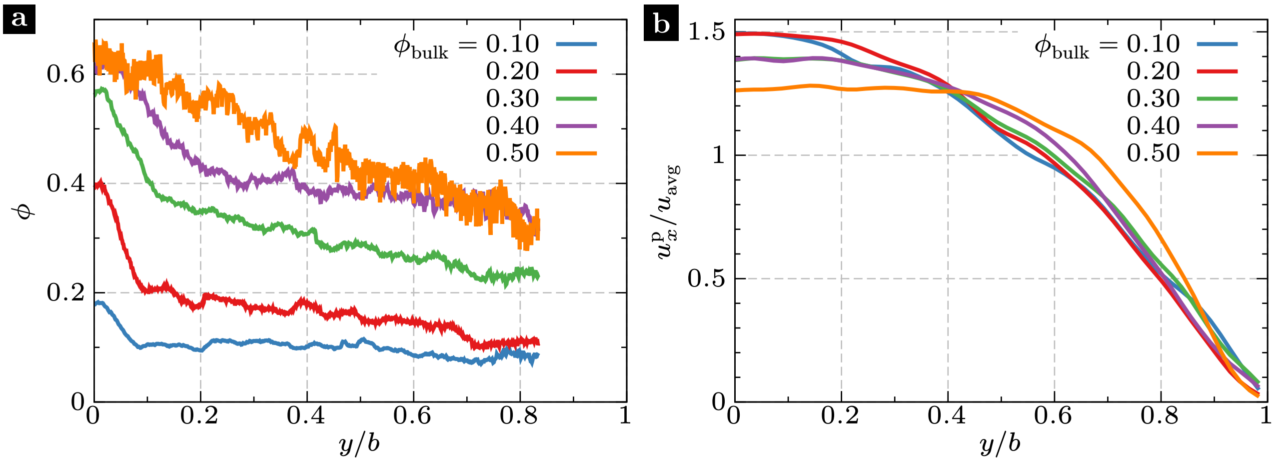

Figure 1.12: Profiles near the channel outlet and across the gap for different average volume fractions ϕ_{bulk}. a) Particle volume fraction. b) Particle velocity divided by its average. Taken from Rashedi et al. (2020), figures 6 and 9.

migration along the channel length, as displayed in Fig. 1.13. In the figure, we observe that ϕ_{center} increases with x up to $x \approx 2000\,b$, except for $\phi_{\text{bulk}} = 0.10$, for which it is unclear whether an equilibrium value of ϕ_{center} is reached inside this channel.

In the above study, the suspension was required to travel large distances in order for the particle migration to become apparent, but it is also possible to observe migration in oscillatory flows where the suspension accumulates large displacements (and strains) without any net one (Snook, Butler, and Guazzelli 2016). This is so because the migration is an irreversible process and the particles move toward the channel's center irrespective of the direction in which the suspension is flowing. In Sec. 1.7.2, we will discuss in more detail the influence of the oscillations on the particle migration.

The migration process in channels (and tubes) has been modelled using shear-induced

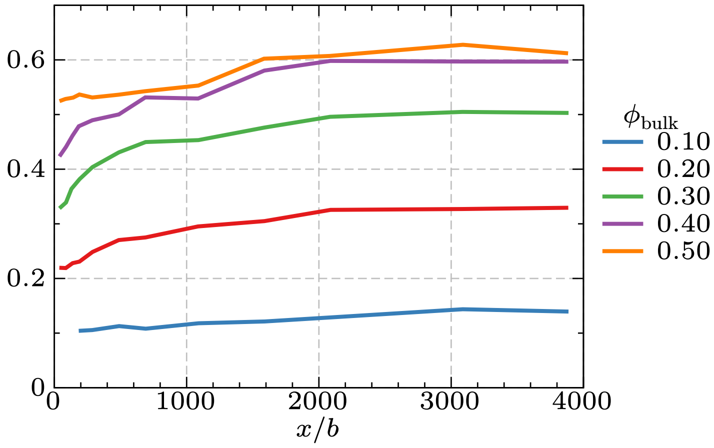

Figure 1.13: Particle volume fraction in the centerline of the channel as a function of the position along its length for different mean volume fractions. Taken from Rashedi (2019), figure 2.12.

diffusivities by Phillips et al. (1992). They consider two balancing particle fluxes: one due to the gradient of the collision frequency, which is taken proportional to $a\nabla(\dot{\gamma}\phi)$; and another due to the gradient of the viscosity, proportional to $(a/\eta)\nabla\eta$. This model, usually called *diffusive flux model*, successfully predicts the accumulation of particles in the center, and the blunted velocity profiles, but the profiles obtained do not match the profiles from experiments.

An alternative interpretation is provided by the *suspension balance model* of Nott and Brady (1994). Here the particle fluxes that induce the migration are a consequence of an imbalance of the normal stresses produced (and felt) by the particles. Concretely, the particle flux at $\mathrm{Re} = 0$ is calculated as

$$J_i^{\mathrm{p}} = \frac{2a^2}{9\eta_{\mathrm{f}}}\, f_{\mathrm{hs}}(\phi)\, \partial_j \sigma_{ij}^{\mathrm{p}}. \tag{1.26}$$

Here, f_{hs} is the hindered settling function from Eq. (1.21) and $\boldsymbol{\sigma}^{\mathrm{p}}$ is the particle contribution to the stress tensor, that is, the total suspension stress minus the stress induced by the fluid alone. One advantage of this model is that normal stress differences (see Sec. 1.3.1) can be incorporated using Eq. 1.13, resulting in a model that can explain better the particle migration in certain curvilinear shear flows, like inside a cone-and-plate rheometer (Morris and Boulay 1999). In the end, both the particle diffusivity and their contributions to the normal stresses are a consequence of the particle contacts, so, both models capture the same intrinsic phenomenon.

1.7. Irreversibility in oscillatory shear flows

Given that we use flow oscillations in our experiments, it is important to know more about their possible effects on the irreversible processes described in the previous section for steady flows. In Sec. 1.5.2, we have seen that, after a reversal of the flow direction, the particles transiently lose contacts and the viscosity decreases until a microstructure corresponding to the new flow direction is formed. Given that solid contacts between particle have been associated with irreversible behavior in suspensions, like particle self-diffusion and migration, we may expect some degree of reversibility in the trajectories of the particles after reversal and before new contacts are established.

1.7.1. Uniform oscillatory shear flows

In order to validate the previous hypothesis, Pine et al. (2005) performed experiments using oscillatory shearing of suspensions between two concentric cylinders (Couette device) with $\mathrm{Re} \approx 0$ and $\mathrm{Pe}^{-1} \approx 0$. During each oscillation cycle, the inner cylinder is made to rotate in one direction, uniformly straining the suspension by an amount γ_0 and, then, the opposite rotation is performed, counteracting the previous strain.[3] Then, they studied the trajectories of the particles for different values of the strain amplitude γ_0, observing that for amplitudes below a critical value of γ_c, the particles returned to their initial positions after each oscillation while, for amplitudes above the critical value, the particles accumulated random displacements after each cycle.

This random motion can be characterized by a diffusivity which depends on the strain amplitude γ_0, as shown in Fig. 1.14a. There, we see that the diffusivity increases linearly with γ_0 above a threshold value (γ_c) that depends on the volume fraction ϕ and, below that value, the diffusivity is negligible, presenting a clear transition from reversible to irreversible behavior as the strain amplitude increases. Figure 1.14b shows that γ_c is a decreasing function of the volume fraction ϕ, of the order of 2 for $\phi = 0.30$ and 0.40. This is consistent with the results of Peters et al. (2016) where the strain required for the viscosity to recover its steady value has a similar dependence on ϕ (see their figure 12). Then, a plausible explanation is that for strain amplitudes $\gamma_0 < \gamma_c$, the particles do not come into contact frequently during the oscillations, and their interactions are (almost) purely hydrodynamical, resulting in reversible trajectories during close approaches, as represented by the black trajectory in Fig. 1.6b.

A stronger connection between the critical strain amplitude γ_c and the particle contacts is established in the work of Pham, Butler, and Metzger (2016), where they measured γ_c for two sets of spherical particles differing only in their surface roughness. First, they took “smooth” spheres of PMMA (acrylic) with a radius $a = 1\,\mathrm{mm}$, and measured the average size of the asperities on their surfaces using images from a scanning electron microscope (SEM). It was found to be $\epsilon \approx 0.002\,a$. Then, they increased the roughness of a second batch of these particles by making them rotate on sandpaper, resulting in an average asperity size $\epsilon \approx 0.005\,a$. Finally, experiments performed with both sets of particles showed that γ_c was

---

[3] In their article, γ_0 is the strain over one quarter cycle, here, it is defined as twice that value.

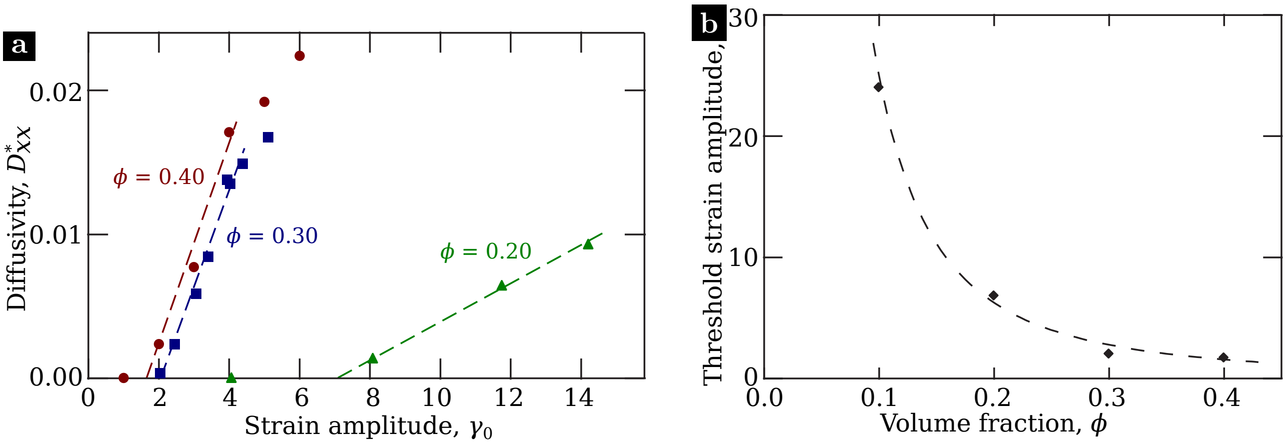

Figure 1.14: a) Dimensionless particle self-diffusivity in the flow direction, $D^*_{xx} = D_{xx}/(\dot{\gamma}a^2)$, as a function of the oscillation strain amplitude γ_0, for three different volume fractions ϕ. b) Threshold (also called critical) strain amplitude γ_c as a function of the volume fraction ϕ. The dashed line is a power law $C\phi^{-\alpha}$ fitted to the data points: $C = 0.28$, $\alpha = -1.93$. Taken from Pine et al. (2005).

smaller for the rougher particles (volume fractions $0.25 < \phi < 0.50$). Using geometrical arguments, the authors explain this result by showing that the number of configurations in which the particles can avoid contacts during a strain of γ_0 decreases with ϵ, reaching zero for a critical strain

$$\gamma_c = \frac{C}{(\epsilon/a)^{1/2}} \left(\frac{\phi_\mathrm{m}}{\phi} - 1 \right), \tag{1.27}$$

which was found to fit well their experimental results with $C = 0.22$ and $\phi_\mathrm{m} = 0.58$.

1.7.2. Pressure-driven oscillatory shear flows

In Sec. 1.6.2, we described the shear-induced migration of particles away from the walls in steady pressure-driven flows through pipes and channels, and mentioned that it is an irreversible process occurring due the nonuniform shear rate. Following the previous section, one might wonder if a suspension oscillating in those geometries could also have a critical oscillation amplitude below which it would behave reversibly without any particle migration. In this case, the analysis is complicated by the fact that the strain induced during one oscillation cycle varies with the position. Consider a velocity profile $u(y)$ like those seen in Fig. 1.12b for channel flow: it is clear that the shear rate $\dot{\gamma}(y) = |\partial u/\partial y|$ is maximum near the walls ($y = \pm b$ in this case), and zero at the centerline ($y = 0$). Consequently, for oscillations with period T, the strain induced during one half period is $\gamma_\mathrm{osc}(y) = \dot{\gamma}(y)\,T/2$ and has the same dependence on position as the shear rate. Then, one might wonder if it possible for a suspension to behave reversibly near the center and irreversibly near the wall for a given oscillation amplitude.

In other to answer these questions, Guasto, Ross, and Gollub (2010) performed experiments with a suspension of spheres ($2a = 220\,\mu\text{m}$, $\phi_{\text{bulk}} = 0.4$) oscillating in a channel with a gap $2b = 5\,\text{mm}$. Figure 1.15a displays the steady-state volume fraction profiles $\phi(y)$ reached after enough oscillations for different maximum strain amplitudes $\gamma_{\text{max}} = \gamma_{\text{osc}}(b)$.[4] For the smallest amplitude used ($\gamma_{\text{max}} = 1.97$), no significant migration was observed while, as γ_{max} increases, the profiles become progressively more concentrated in the center, resembling those seen for steady flows in Fig. 1.12a. After the corresponding steady-state is reached, they measured the particle self-diffusivity in the direction of the flow, D_{xx}.[5] In Fig. 1.15b, we see that D_{xx} strongly increases all across the gap with the strain amplitude, although it reaches larger values near the walls that in the center. The above results show that for certain small strain amplitudes ($\gamma_{\text{max}} \lesssim 3$ in this case), the suspension behaves reversibly (no migration, very low diffusivity) and, as the strain amplitude increases, the suspension behavior becomes progressively more irreversible everywhere.

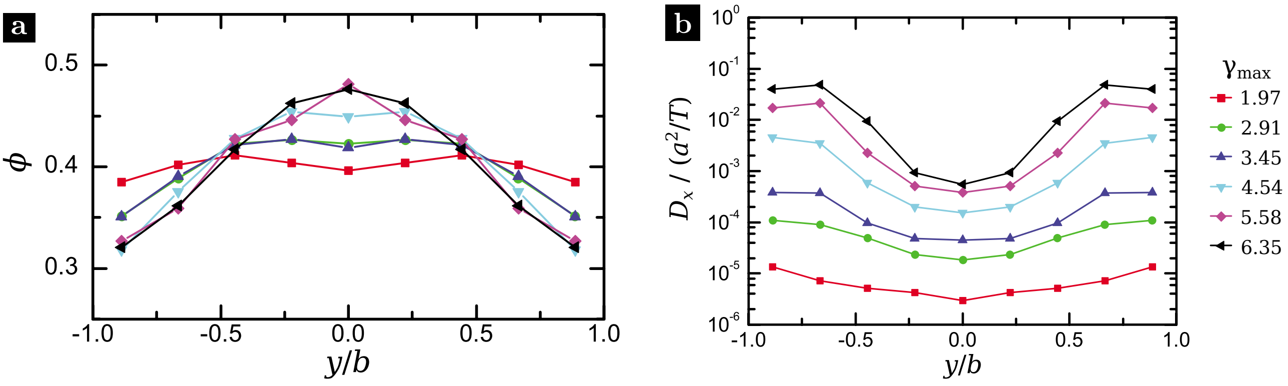

Figure 1.15: a) Steady-state particle volume fraction profiles across the gap of a channel for different oscillation strain amplitudes γ_{max} (legend on the right). b) Particle self-diffusivity in the flow direction D_{xx} normalized by a^2/T, with $13\,\text{s} < T < 36\,\text{s}$, the oscillation period (increases with γ_{max}). From Guasto, Ross, and Gollub (2010).

A broader range of strain amplitudes was investigated by Butler, Majors, and Bonnecaze (1999) for experiments in which a suspension ($\phi_{\text{bulk}} = 0.4$, radius $a \approx 65\,\mu\text{m}$) oscillates inside pipes with radii $R = 10\,\text{mm}$ and $4.4\,\text{mm}$. They measured the resulting particle distributions

---

[4] Guasto, Ross, and Gollub (2010) measured profiles $\gamma(y)$ and used their maximum values (found near the wall) as a reference strain amplitude. In other works, and our own, the strain amplitude is characterized by $\bar{\gamma}_0 = A/b$, where A is the average distance travelled by the suspension during half of an oscillation and b is the channel half thickness or the radius of a pipe. For channel flow, both strain values can be related if we approximate the velocity profile as a parabola: $\gamma_{\text{max}} \approx 3\bar{\gamma}_0$.

[5] Like in Pine et al. (2005), D_{xx} is measured by observing the positions of the particles after each oscillation.

$\phi(r)$ for different oscillation amplitudes A, where r is the distance from the pipe center line, and A is the average distance travelled by the suspension during the first half of each oscillation. In the largest pipe, they found that the particles migrated toward the center for large amplitudes ($A \geq 2\,R$) while, for small amplitudes ($A = 0.03\,R$), they found an anomalous migration toward the walls. In the smaller pipe, the migration was always toward the center, but for the smaller amplitudes, the gradient in $\phi(r)$ was much smaller, meaning a weaker migration.

A similar phenomenon was observed in the two-dimensional simulations by Morris (2001). Here, a suspension of disks occupying 40% of the available area was made to oscillate between two parallel walls separated by a distance $2b$. The final distribution of the disks (after enough oscillations) depends on the oscillation amplitude A, with a critical value $A_\mathrm{c} = 1.5\,b$: above this value, the disks migrated toward the centerline, below, toward the walls, and when $A = A_c$, they remained homogeneously distributed. It is noted that during the anomalous migration (toward the walls), disks that were initially nearby tend remain so during the whole process, suggesting that the process is nondiffusive since the particles do not wander around randomly. See Fig. 1.16 for some examples of the disk distributions observed.

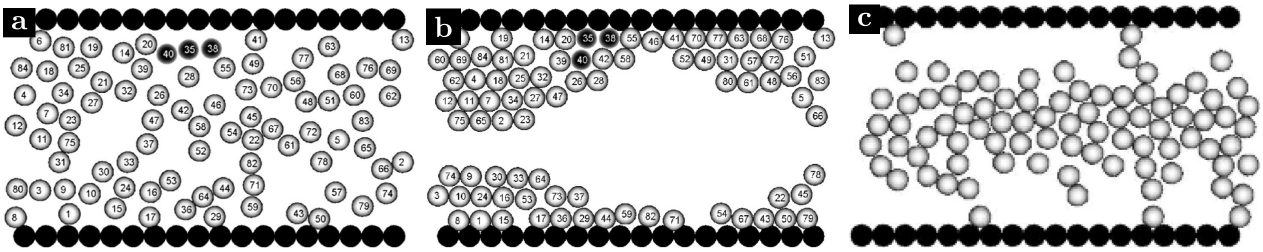

Figure 1.16: Snapshots taken from simulations of a suspension of disk of radius a confined between two walls separated by a distance $2b = 18.3\,a$. The walls are made of fixed particles (black disks at the top and bottom). Periodic boundary conditions apply in the horizontal direction. From Morris (2001). a) Initial state. b) State after 500 oscillations with amplitude $A = 0.2\,b$. The disks migrated toward the walls. Notice that the disks numbered 35, 36, and 40 remain nearby as in the initial state. c) Typical distribution reached with a steady flow ($A \to \infty$) where the disk migrated toward the centerline.

A possible explanation is provided by Ingber and Vorobieff (2013) considering trajectories of just two rough spheres in simulated oscillatory Poiseuille flow. They predict that when the two spheres get closer, the position of their center of mass (CM) moves toward the region with low shear rate (e.g. center of a pipe); while during their separation, the CM moves back toward the high shear rate region (e.g. walls). The sphere roughness ($\epsilon > 0$) introduces an asymmetry in this process which results in a net transverse displacement of the center of mass. Interestingly, for small enough oscillation amplitudes ($A \lesssim 13\,b$ in their case), the spheres have a net migration toward the region of high shear rate, in qualitative agreement with experiments of Butler, Majors, and Bonnecaze (1999).

The above results suggest that suspensions might develop a microstructure different from that shown in Fig. 1.7 when they are subjected to oscillations, especially during the proposed loss of contacts after each flow reversal. This alternative microstructure would have more pairs in expansion (separating) than in compression (approaching), resulting in a tensile contribution of the particles to the normal stress ($\sigma^{\mathrm{p}}_{yy} < 0$) that could explain the anomalous migration using the suspension balance model (see Eq. 1.26). Such a tensile normal stress during oscillations was observed in the simulations of Bricker and Butler (2007), although with an absolute value much smaller than those of the steady normal stresses.

We will continue the present discussion about the effects of oscillations in suspensions in Chapter 6, after we have presented our results concerning an instability in oscillatory channel flow, first observed in the experiments summarized in the following section.

1.8. Instability in the oscillatory channel flow of suspensions

In our laboratory, Roht (2017) and Roht et al. (2018) reported experiments with sphere suspensions oscillating inside narrow channels (Hele-Shaw cells). Measuring the light transmitted across the channel thickness, they measured the relative particle concentration along the flow (x) and width (y) directions, as shown in Fig. 1.17a, and found that the particles can get organized into patterns of periodic stripes perpendicular to the flow direction (see the image in Fig. 1.17a). They observed this phenomenon for a broad range of experimental parameters: bulk particle volume fractions ϕ_{bulk} between 0.25 and 0.37, particle diameters $2a = 40\,\mu\mathrm{m}$ and $60\,\mu\mathrm{m}$, channel thicknesses $2b$ between 0.4 mm and 1 mm, oscillation strain amplitudes A/b between 1 and 20, and oscillation periods T between 1 s and 10 s. In all cases, the particle and fluid densities ($\rho \sim 1$) were matched to prevent buoyancy effects and, for an average flow velocity $U = 2A/T$, the Reynolds number $\mathrm{Re} = Ub\rho/\eta_{\mathrm{f}}$ ranged between 0.01 and 5.

The wavelength λ of the pattern was found to be proportional to the channel thickness $2b$,

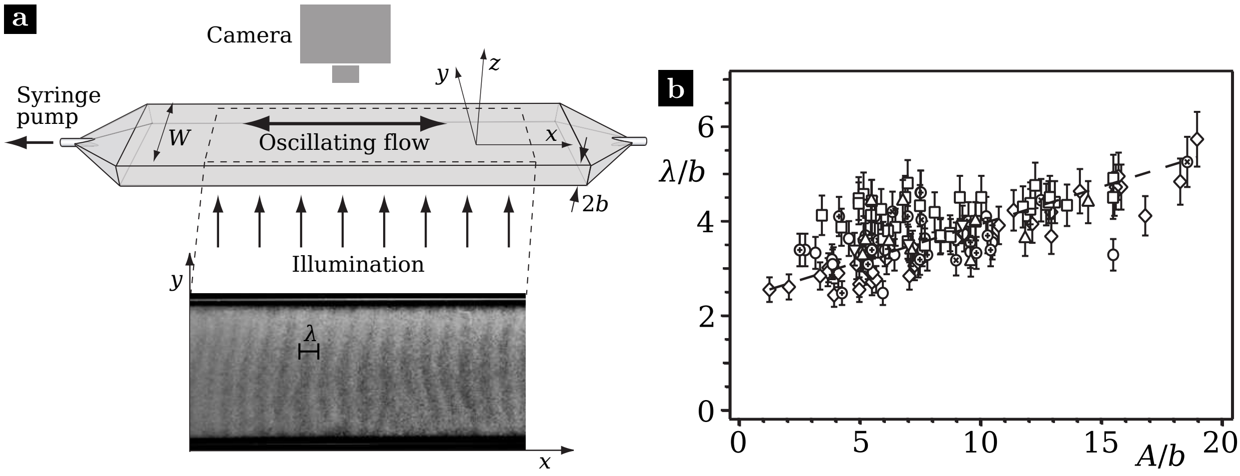

Figure 1.17: a) Experimental setup from Roht et al. (2018) with an example of the captured images below. b) Pattern wavelength λ versus the oscillation amplitude A, both normalized by the channel half thickness b. Each marker type corresponds to a different combination of the experimental parameters a, b, and ϕ_{bulk}. See Roht et al. (2018) for details.

and to increase with the strain amplitude A/b from $\lambda \approx 2\,b$ to $6\,b$, as shown in Fig. 1.17b. The observed pattern does not form instantaneously, but instead requires a certain time lapse t_{onset} to become visible (onset) and, afterwards, its contrast increases with time until a maximum is reached. For a given time t measured from the beginning of the oscillations, a characteristic accumulated strain $\bar{\gamma}$ can be calculated by multiplying the number of oscillations t/T by twice the strain amplitude $2A/b$ (remember that A is the average distance traveled during a half oscillation), resulting in $\bar{\gamma} = 2At/(bT)$. Then for $t = t_{\text{onset}}$, the strain accumulated before the onset was found to be $\bar{\gamma}_{\text{onset}} \approx 400$ for $\phi_{\text{bulk}} = 0.35$, without any clear trend regarding its dependence on A/b.

Finally, complementary experiments were performed using fluorescence and illuminating with a laser sheet to observe the particle distribution in a plane oriented parallel to the thickness of the channel (z direction) and to its length (x direction), and located roughly at half distance across its width (y direction). A version of this technique improved for the present doctoral thesis will be described in greater detail in Chapter 2. Figure 1.18 displays a sequence of images obtained from one of these experiments, where the bright and dark regions correspond to higher and lower particle concentrations, respectively. Initially ($t = 0$), the particles appear to be concentrated in the centerline, probably as a consequence of shear-induced migration occurring in an earlier phase of the experiments. After a number of oscillations ($t/T = 50$), we observe that the central band of high concentration deformed into a wavy pattern with a wavelength $\approx 7\,b$. With even more oscillations ($t/T = 83$), we find a new pattern formed by series of regions with high concentration (“dots”) located near the center of the thickness, each separated by roughly half the value of the previous wavelength.

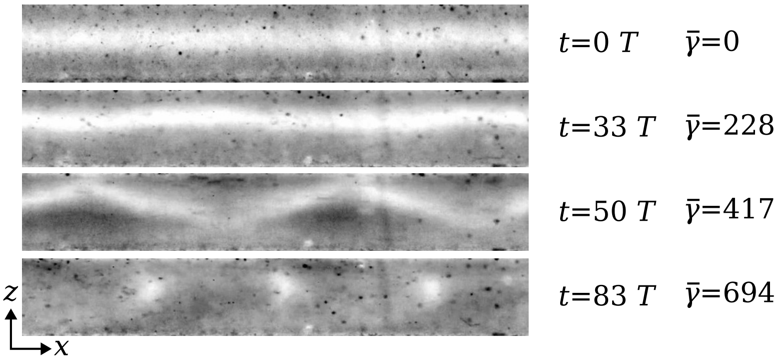

Figure 1.18: Sequence of images showing the particle distribution in a length-thickness plane inside a channel for one example experiment with oscillations ($\phi_{\text{bulk}} = 0.35$, $2a = 40\,\mu\text{m}$, $2b = 1.2\,\text{mm}$, $A = 5\,\text{mm}$, $T = 1.2\,\text{s}$). The flow direction is horizontal, with walls above and below each image. The bright zones correspond to a high particle concentration. From Roht et al. (2018)

It seems logical to conclude that the pattern previously observed as stripes in the plane xy (image in Fig. 1.17a), corresponds the pattern seen in the plane xz as a sequence of “dots” (bottom image in Fig. 1.18). A comparison of the second ($t = 33\,T$) and third images ($t = 50T$) in Fig. 1.18 suggests that the particles moved transversally to the main flow in some locations along the x direction, toward to top or bottom walls. The exact mechanism responsible for this phenomena was not clearly identified at the end of the previous work, and it remains an open question whether it might be similar to that responsible for the anomalous migration toward the walls discussed in Sec. 1.7.2, or maybe the mechanism is more general and not exclusive to suspensions, like the instabilities proposed by Hinch, Harris, and Rallison (1992) and Brady and Carpen (2002) for fluids with nonuniform normal stress differences.

The observed behavior does not match any of the instabilities previously seen in suspensions. For example, Moosavi et al. (2014) studied the oscillatory channel flow of sphere suspensions and found filament-like irregular stripes aligned in the vorticity direction (like the above ones), but their particles were less dense than the fluid and showed signs of re-suspension during the oscillations. Moreover, the particles were more confined ($b/a = 0.5$, $2a = 80\,\mu\text{m}$) and they only observed the pattern for suspensions with $\phi_{\text{bulk}} \leq 0.14$ and periods $T \leq 0.17$ ($A = 0.42\,\text{mm}$ fixed), out of the ranges of parameters studied by Roht. Another example is the work of Varga et al. (2019) which shows how particles that attract each other in dilute suspensions ($\phi_{\text{bulk}} < 0.1$, $2a < 10\,\mu\text{m}$) segregate into periodic stripes formed by log-like structures aligned along the vorticity direction in simple shear flows, leaving clear fluid in between. They found that the pattern only forms for shear rates below a critical value that increases with the strength of the attractive interparticle force and decreases with the viscosity. On the other hand, Roht (2017) shows that the stripe formation is not significantly affected by changes in the viscosity between 9 and 26 mPa s and, moreover, there is no reason to expect large effects from non-hydrodynamic attractive forces between their particles as they are large in size. More importantly, Roht tested suspensions with ϕ_{bulk} between 0.15 and 0.40 and only found the stripes pattern for $\phi_{\text{bulk}} \geq 0.25$ while, on the contrary, the above two examples used dilute suspensions with much lower concentrations. In the case of concentrated suspensions, periodic perturbations of the particle concentration and velocity were found for shear-thickening suspensions near jamming, both in simple shear flows (Ovarlez et al. 2020; Saint-Michel, Gibaud, and Manneville 2018) and steady pipe flow (Bougouin et al. 2024). These perturbations occur due to a transient jamming of the suspension in some regions while it flows in others. Shear thickening in suspensions is commonly seen with particles like cornstarch which have polymers on their surfaces or in particles small enough that colloidal forces have a significant role, neither of which is the case for the PS and PMMA spheres used by Roht which are large ($2a \geq 40\,\mu\text{m}$) and have (relatively) smooth surfaces.

In order to better understand the unique phenomena shown by Roht el al., the work presented in this manuscript extends of these experiments using different, more local, types of measurements. The objective is to obtain a detailed knowledge at the particle scale of the behaviour of the velocity field of the particles and their spatial statistical distribution in the oscillation flow and during the development of the instability. In the following chapter, the experimental setup used will be explained in detail and, in Chapters 3-6, the results obtained will be presented. At the conclusion of this thesis, in Chapter 6, we will pursue the discussion started here using the new information.

Chapter 2

Experimental setup and procedure

At the end of the last chapter, we presented an instability of the oscillatory flow of suspensions inside Hele-Shaw cells, that is, inside narrow channels made from two parallel plates separated by a gap $2b$ much smaller than their other dimensions (length L and width W). In experiments measuring the light transmitted across the gap, Roht (2017) observed the formation of a pattern of periodic stripes aligned to the vorticity direction (width) and perpendicular to the flow direction (length). On the other hand, their experiments looking at a view of the channel rotated by 90° show that, in a plane parallel to the length and gap directions, the particles can get organized in a wave-like pattern first and, then, in a pattern with periodic pockets of high particle concentration separated along the length by a wavelength similar to that of the striped patterns.

The second experiment suggested that the particles moved in both the directions of the gap and the length to form the striped pattern, but limitations in the visualization technique precluded the observation of particle trajectories or velocity fields. For the present thesis, we improved the technique to track individual particles and their neighbors as the instability develops, allowing us to connect this latter macroscopic behavior with the microscopic descriptions of the particle interactions given in the previous chapter.

Consequently, we used transparent materials for the channels, the particles, and the fluids in order to enable the optical observation of particles inside. We choose PMMA (i.e. acrylic) for the particles since those are widely available and fluids matching the density and the index of refraction of PMMA are well characterized and safe to handle. Index matching is important to prevent the distortion of the light as it crosses multiple particle-fluid interfaces, resulting in a blurry view of the interior. Moreover, rectangular channels of PMMA with the desired dimensions could be constructed, removing any light distortion at the walls. Some of the particles inside were made visible by dyeing with a fluorescent dye either the fluid or a fraction of the particles, and illuminating the channel with a laser sheet parallel to the length and gap directions. In the illuminated region, the dye (either in the fluid or the particles) shines in a specific wavelength which is observed preferentially using optical filters. With this technique, we can differentiate between both phases (fluid and particles) in a plane located at a position of our choosing inside the channel (usually in the middle of the width), and we can reconstruct the trajectories of the particles present there using images recorded with a video camera. Figure C.2 displays a simplified diagram of the experimental setup.

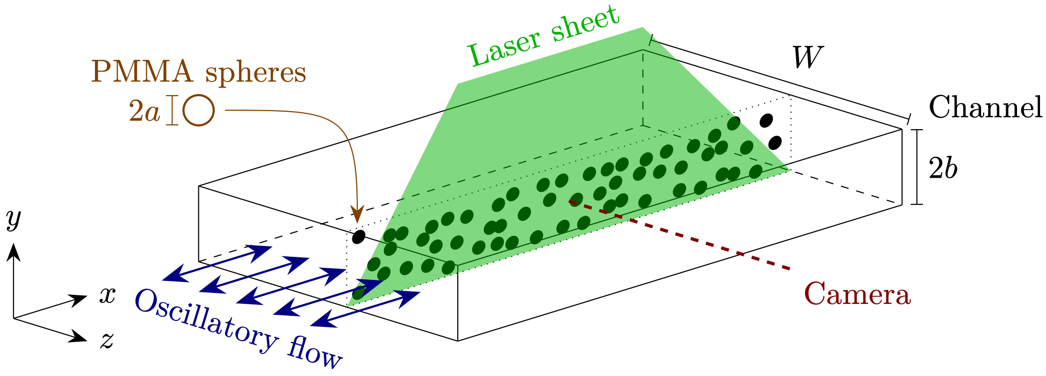

Figure 2.1: Simplified diagram of the experimental setup.

The following sections provide detailed descriptions of the particles, fluids and channels used, as well as of how the flow was set up and the laser sheet was obtained. By the end, we will go into the details of the particle tracking in the images and the processing of this information to obtain macroscopic quantities like concentration and velocity fields.

2.1. Particles

The particles used were always spherical, made from poly(methyl methacrylate), i.e. PMMA, and with nominal diameters $2a$ of 40, 60, and 85 µm. In all cases, the size distribution was roughly monodisperse. At 20ºC, PMMA has a density $\rho_\mathrm{p} \approx 1.19\,\mathrm{g/cm^3}$ and refractive index $n_\mathrm{p} \approx 1.49$, both small enough to be matched by the aqueous solutions utilized (see Sec. 2.2). Other transparent materials, like glass, require difficult-to-handle liquids to match both density and the refractive index simultaneously (Dijksman et al. 2012). We used spheres from two manufacturers, *Microbeads* and *Arkema*, and although both were made from PMMA, there were some practical differences in the way we had to deal with them.

2.1.1. Microbeads spheres

We used batches of spheres branded as *Spheromers CA40* and *CA60*. Per granulometric measurements, they have narrow size distributions with diameters 40.8 ± 0.6 µm and 63.7 ± 0.6 µm, respectively (see the distributions in Fig. 2.2a and 2.3a). Figures 2.2b and 2.3b show images of the spheres captured with a scanning electron microscope (SEM). Some roughness on the surfaces can be perceived, but no quantification is possible at this scale.[1]

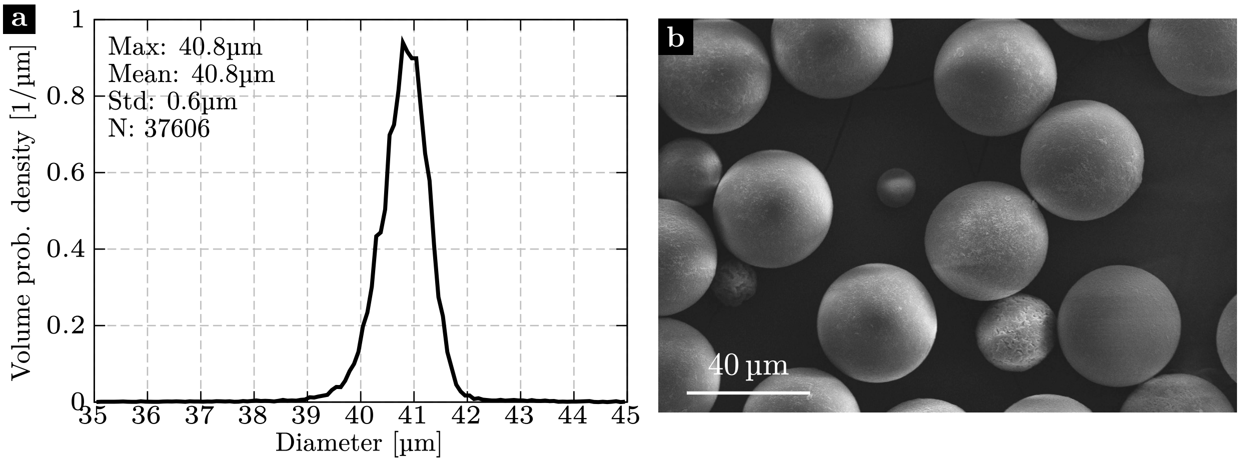

Figure 2.2: Microbeads spheres CA40. a) Size distribution by volume. b) SEM image.

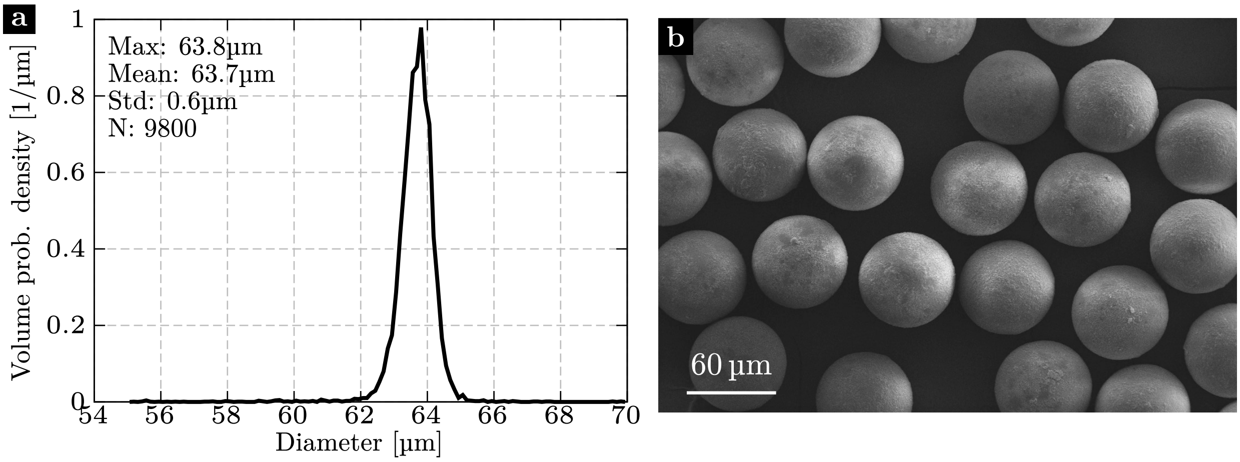

Figure 2.3: Microbeads spheres CA60. a) Size distribution by volume. b) SEM image.

In our first experiments, a small fraction of the particles could not be index matched with the fluid and looked like black disks in the experimental images. Moreover, they were less

---

[1] We thank C. Manquest from the FAST laboratory (France) for the granulometric measurements, and V. Schmidt from the INFAP (San Luis, Argentina) for the SEM images.

dense and tended to float, so, a possible explanation could be the presence of a gas bubble inside. To filter out these spheres, we suspended a batch of spheres in an aqueous solution with 23.5% NaCl (density 1176 $\mathrm{Kg/m^3}$), and used a centrifuge to accelerate the segregation. The problematic spheres clustered on the surface, while the rest, settled on the bottom. We discarded the spheres on the top, rinsed the remaining ones with distilled water, and let them dry before using in experiments.

In most of the experiments using these spheres, a fraction of them ($\approx 2\%$) were previously painted with rhodamine, a fluorescent dye used for visualization purposes (see Sec. 2.5). We painted spheres by immersion in a solution of ethanol and rhodamine at 40ºC for roughly thirty minutes and, then, we rinsed and dried them (Lenoble, Snabre, and Pouligny 2005). We also performed experiments where we put the rhodamine in the suspending fluid instead of the spheres, but the dye slowly penetrates the surfaces of these Microbeads spheres and makes them shine with the laser light. In Sec. 2.5.2, we will see that this results in experimental images where the particles visually overlap, making their individual detection difficult.

2.1.2. Arkema spheres

These spheres came in a polydisperse batch with diameters up to $\approx 200\,\mu\mathrm{m}$. We divided this batch into several ones with narrower size distributions using sieves with hole sizes equal to 80, 90, 100, 125, 150 and 160 µm. Figure 2.4 shows the characterization of the spheres obtained between the sieves of 150 and 160 µm. Notice that these spheres have larger surface irregularities (relative to their sizes) than those from Microbeads.

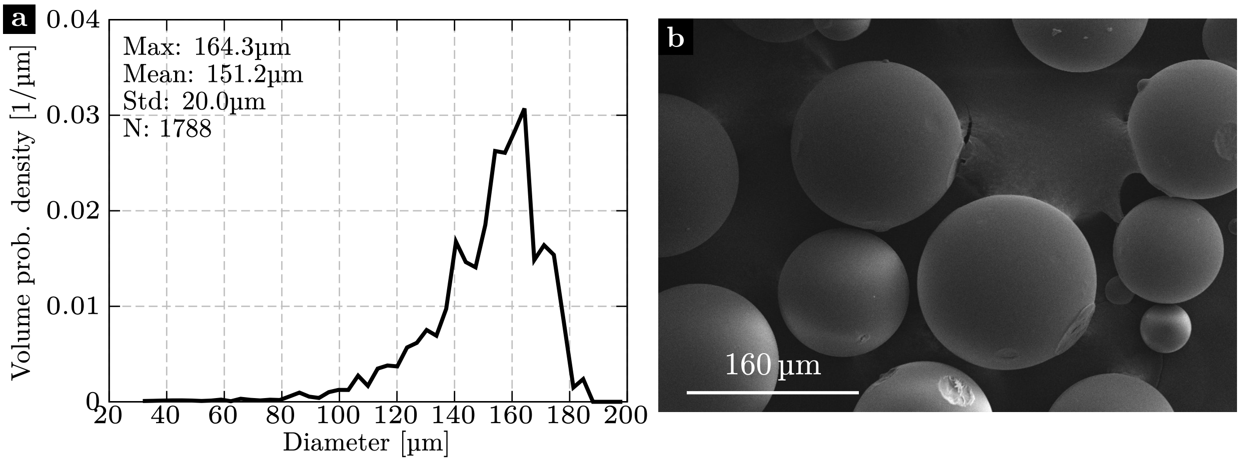

Figure 2.4: Arkema spheres, sieved between 150 and 160 µm. a) Size distribution by volume. b) SEM image.

In this thesis, we will present results for the range $80 - 90\,\mu\text{m}$, since they have the most convenient size ratio with the available channel gaps $2b$. Regrettably, we could not fully characterize them due to the very small quantity obtained ($\approx 20\,\text{g}$ from $1\,\text{Kg}$ of unsieved spheres), but experimental images (like those shown in Fig. 2.9) display disks of the expected sizes within the experimental uncertainty. From now on, we will refer to them simply as the $85\,\mu\text{m}$ particles.

When these spheres were mixed with the fluid to make a suspension, a large amount of bubbles were trapped inside, and attempting to remove them in a vacuum chamber did not produce the desired result in a reasonable amount of time. Finally, we found that adding a small amount of a surfactant to the fluid solved the problem. It is possible that these spheres have hydrophobic surfaces. Furthermore, these spheres do not absorb rhodamine on their surfaces, like those from Microbeads, making them easier to visually separate in experiments with this dye in the fluid.

2.2. Fluids

We worked with two sets of solutions: one made from water (H_2O), glycerine ($C_3H_8O_3$) and ammonium thiocyanate (NH_4SCN); and another made from water, zinc chloride ($ZnCl_2$) and Triton X-100 (a polymeric fluid commonly used as detergent in laboratories). For the sake of brevity, we will call the first *thiocyanate-based* and the second, *triton-based.*

2.2.1. Thiocyanate-based solutions

These solutions can match the density and refractive index of PMMA, and they are Newtonian over a wide range of temperatures (Dijksman et al. 2012). Their density and refractive index vary depending on the temperature and the proportions of the total weight corresponding to each of the three components (Bailey and Yoda 2003). We performed extensive tests in order to obtain the best visualization possible with negligible particle sedimentation at the temperature of our laboratory.

For these tests, we prepared several solutions with different proportions and then measured their density ρ_f and refractive index n_f. Afterward, we added particles to each candidate solution and introduced the resulting suspensions into the complete experimental setup, one at a time. Then, we took images to evaluate qualitatively the index matching (see examples in Fig. 2.5). The density matching was evaluated taking images two minutes apart and observing if the particles showed any significant displacements. Remember that our particles are non-colloidal and should remain static if the buoyancy force is zero.

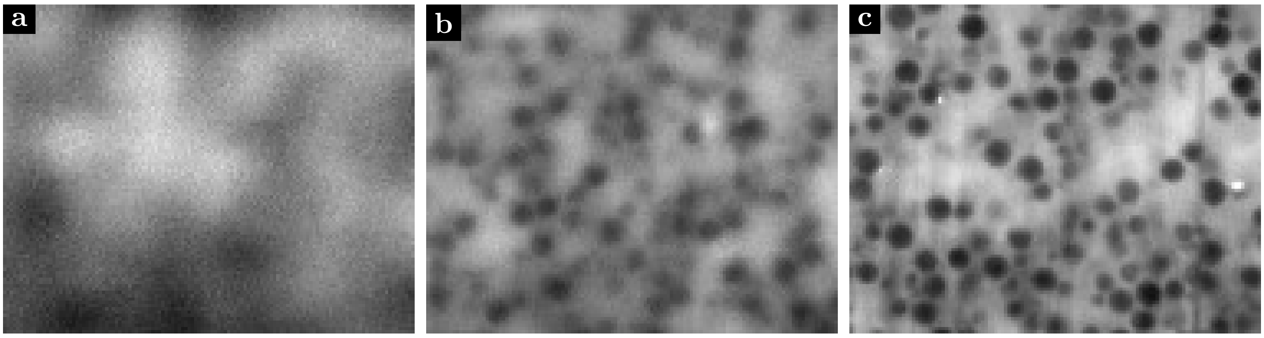

Figure 2.5: Images of 85 µm spheres suspended in different thiocyanate-based solutions. The accuracy of the index matching improves from left to right by varying the proportions of the suspending solution.

Finally a solution with 23.0 % of water, 38.9 % of glycerine, and 38.1 % of ammonium thiocyanate (all by weight) was used at a temperature 22 ± 1ºC. This solution has estimated values of density $\rho_\mathrm{f} \approx 1.19\,\mathrm{g/cm^3}$, refractive index $n_\mathrm{f} \approx 1.49$, and viscosity $\eta_\mathrm{f} \approx 7.6\,\mathrm{mPa\,s}$.[2]

For some experiments, we added ≈ 6.5 µm of rhodamine per gram of fluid to make it shine under the laser light and allow for the visualization of the spheres. This was achieved using water with an appropriate amount of rhodamine previously diluted.

2.2.2. Triton-based solutions

The thiocyanate-based solution has a viscosity larger than water, but not as large as other fluids used in previous studies of suspensions at negligible Reynolds numbers. To completely rule out inertial effects in our experiments, especially those related to unstable flows, we performed experiments using a solution composed of 11.89 % of water, 14.19 % of zinc chloride, and 73.91 % of Triton X-100 (Pham, Butler, and Metzger 2016). This solution gave an acceptable visualization of the particles at 21 ± 1ºC, and we estimate that its viscosity ranges between 2.4 and 4.6 Pa s, from measurements reported in the literature (Snook, Butler, and Guazzelli 2016; Sarabian et al. 2019).

---

[2] Density measured with an *Anton Paar DMA 35M* density meter. Refractive index measured with an *Anton Paar Abbemat WR MW* refractometer. Viscosity measured with a *Anton Paar Physica MCR 501* rheometer with a CC27 head (cone-plate) and shear rates between 5 and $50\,\mathrm{s^{-1}}$.

The reduction of Re by a factor ~ 500 is of scientific interest, but it was accompanied by several experimental difficulties. First, when a suspension is prepared, particles are added to the fluid and then, mixed with a spoon. This process introduced bubbles that took a few days to ascend and evacuate. Afterward, during the experiments, we had to reduce the flow rates by a factor of ~ 8, otherwise the observed velocities during injection and retraction of the syringe were different, probably due to limitations of the syringe pump. This reduction in the flow rate had the side advantage of further reducing Re.

In short, we had to take greater care during the preparation and equivalent experiments took longer to perform. This is why we used this solution only in a few experiments intended to validate the inertialess nature of our results by comparing with those performed with the less-viscous solution.

2.3. Channels

We studied the suspension flow inside straight channels with rectangular cross sections and, mostly, with large aspect ratios. The channels were made by cutting a slit of the desired gap thickness $2b$ in a block of PMMA using a disk saw, down to the desired width W. Afterwards, the open side is covered with a glued PMMA plate or with adhesive tape. In either case, we never looked through this side, nor made any measurements with the laser sheet near it. To connect the channel with the pumping system (see Sec. 2.4), we used 3d-printed caps glued at both ends of the channels, allowing the connection of flexible silicon tubes. The caps have cavities inside which provide a gradual transition from the channel cross section to a circular one appropriate for connecting the tubes. See a diagram and pictures in Fig. 2.6.

After a channel is prepared, we characterized it by filling it with water. First, we support the channel with its length vertical, and connect it to a syringe with water. The water is injected at a constant flow rate with the help of a syringe pump, and we record the water level in the channel with a video camera. Processing the video, we determine the water height as a function of time and its average velocity. The ratio between the flow rate and this velocity is the channel cross-sectional area $S = 2bW$. Using visual measurements of W ($> 2b$, usually), we determine $2b$. Table 2.1 lists the channels used, along with their measurements. We used mostly channels of width $W \approx 10\,\mathrm{mm}$ and thickness $2b \approx 1$ or $2\,\mathrm{mm}$, though others were

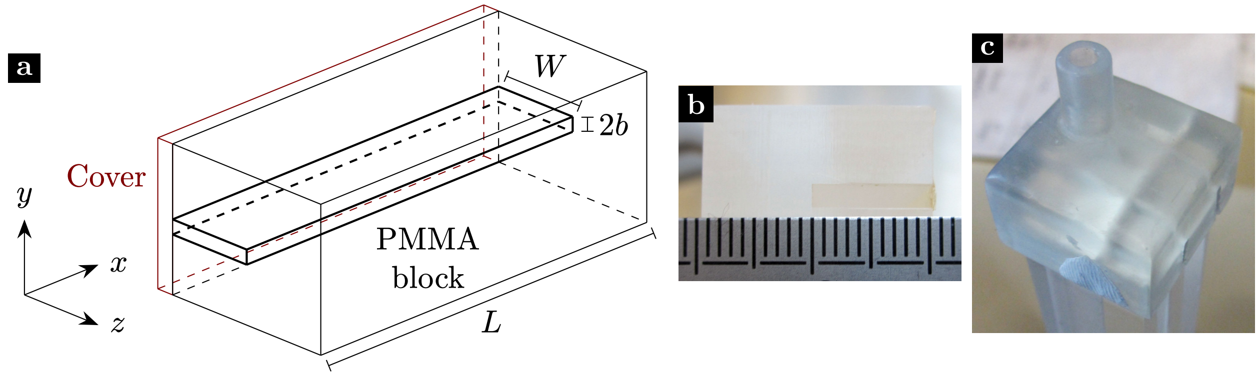

Figure 2.6: a) Diagram of a channel with dimensions $L \times W \times 2b$ cut into a block of PMMA and covered. b) Photograph of the cross section of a channel with $L = 150\,\mathrm{mm}$, $W = 10\,\mathrm{mm}$, and $2b = 2\,\mathrm{mm}$. c) Photograph of the 3d-printed channel cap.

$2b$	W	$W/(2b)$	S	
2.08	10.0	4.8	20.8	
2.03	5.05	2.5	10.2	
2	2	1	4	(nominal)
1.05	10.5	10.0	11.0	
1.05	5.8	5.5	6.1	
1.05	6.0	5.7	4.3	
1.05	3.6	3.4	3.7	
1.05	3.0	2.9	3.2	
1.05	2.6	2.5	2.7	
0.51	10.0	19.5	5.1	

Table 2.1: Channels utilized and their measurements ($S = 2bW$). In all cases, $L = 150\,\mathrm{cm}$.

constructed to investigate the influence of the aspect ratio $W/(2b)$.

2.4. Flow setup

After preparation, the suspension was transferred to a “large” syringe (capacity between 10 and 60 ml) which was connected to the channel inlet through plastic tubes. A smaller syringe (1 ml) was also connected to the channel for a finer control of the imposed flow. Both syringes were attached to syringe pumps and controlled from a computer using a program written in the *Python* programming language. The smaller syringe was always connected to a *Nemesys NEM-B101-02 E* low pressure module made by *Cetoni GmbH*, while the larger one could be either connected to a second identical module or to a *Harvard Apparatus model 22* pump, depending on the availability of equipment. See the diagrams in Fig. 2.7.

To set up an experiment, the large syringe is first used to inject the suspension until the channel is completely saturated. The channel outlet is connected to an extension tube to

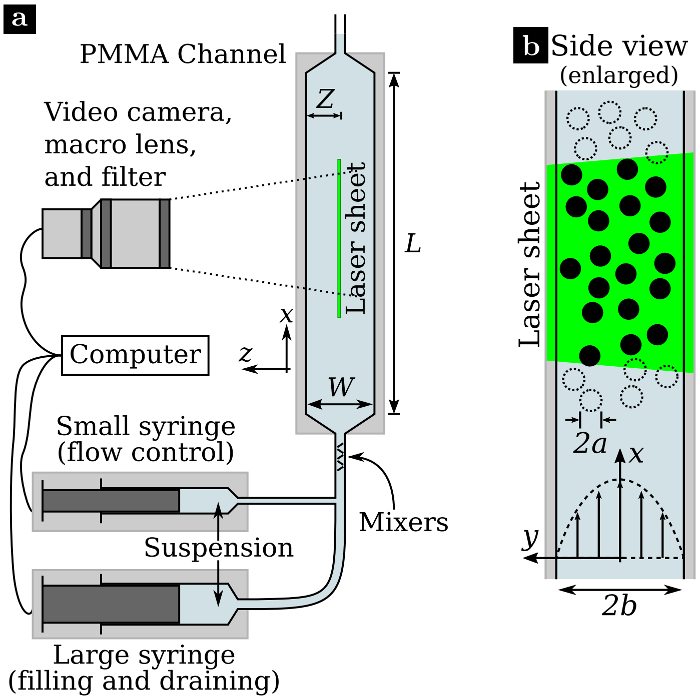

Figure 2.7: Schematic view of the experimental setup (a) and the visualization inside the gap (b).

prevent overflows. During this process, the channel must be vertical to prevent the entrapment of large bubbles. We performed most experiments keeping the channel in this position, and a few with the channel rotated by 90º to demonstrate the independence of the results from the direction of gravity. After the system (syringes, tubes and channel) is completely saturated with suspension, the pump with the small syringe is programmed to generate the desired flow, usually symmetric square wave oscillations with periods T between 1 and 20 s, and maximum flow rates such that the average particle velocity is of the order of 1 mm/s.

Several experiments with the same suspension and channel, but different flow parameters, could be performed sequentially. Between each, the channel is drained and filled again with the large syringe to ensure similar starting conditions. If the suspension always enters the channel in a well-mixed state, the subsequent results should be statistically equivalent. However, we found some small differences in the initial particle velocity profiles across the gap in sequential experiments with the same parameters. To remedy this situation, we added five plastic "mixers" in the tube just before the inlet (see Fig. 2.7a). These mixers have a helical shape with a diameter similar to that of the tube (≈ 4 mm), and force the suspension to follow non-straight paths, enhancing its homogenization.

2.5. Particle visualization

During the preparation of a suspension, we dye with rhodamine 6G either some particles or the fluid. Rhodamine 6G is a fluorescent dye that absorbs light with a wavelength of $\approx 530\,\mathrm{nm}$ (green) and emits with a peak wavelength $\approx 590\,\mathrm{nm}$ (orange). With this in mind, we used a $80\,\mathrm{mW}$ laser with a wavelength $\lambda_{\mathrm{laser}} = 532\,\mathrm{nm}$ to illuminate the suspension inside the channel, and optical filters in front of the camera to partially reject light from sources other than the fluorescence. We tested with two different filters: a high-pass filter that lets the orange light pass, and a notch filter that filters out the green light. Both resulted in much cleaner images than the unfiltered ones, without any significant difference between the filters except, maybe, for the intensity of the observed light.

2.5.1. Laser sheet

The laser beam is shaped into a plane sheet by the system of lenses described in Appendix A. The resulting laser sheet has a thickness S_{sheet} which is roughly uniform over a distance $\pi S_{\mathrm{sheet}}^2/(2\lambda_{\mathrm{laser}})$ inside the channel gap. Then, S_{sheet} can be no smaller than $\approx 26\,\mathrm{\mu m}$ while remaining uniform over the whole span of the largest channel gap used in our experiments, $2b = 2\,\mathrm{mm}$. This limits our ability to visualize the particles located only in one plane when their diameter $2a$ is similar to S_{sheet}.

Figure 2.8 shows schematically pairs of spheres illuminated by laser sheets which are thin (a) o thick (b) with respect to the sphere diameter $2a$. Assuming that we have dyed the fluid, the volume illuminated by the laser sheet will shine due to the fluorescence everywhere except in the shaded regions where the spheres and the laser sheet intercept.[3] When viewed by a camera located above, each sphere will be viewed as a dark disk of radius $\tilde{a} \leq a$, depending on the distance $|z|$ of its center to the laser sheet (see left figure). If the laser sheet is thick (right), two nearby spheres may be viewed as overlapping disks by the camera. In the following section, we will see images with examples of disks with different sizes or overlapping and how this affects the visualization of the particles.

---

[3] If the dye is in the spheres instead of the fluid, then, the shaded regions are the ones shinning, while the rest of the volume remains dark. In either case, we will observe the particles as disks, or as rings if they only shine on their surface.

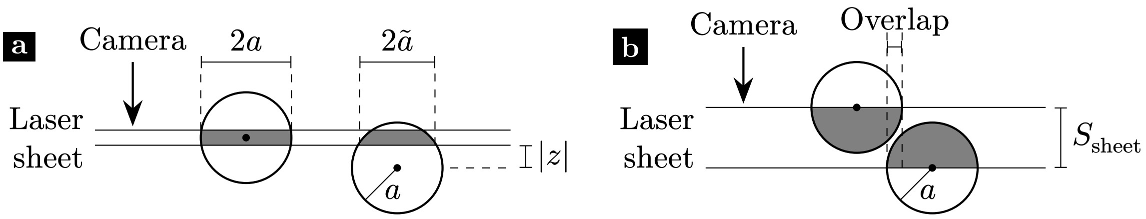

Figure 2.8: Pairs of spheres illuminated by laser sheets that are either thin (a) or thick (b) relative to the sphere diameter $2a$. A camera looks from above. a) Two identical spheres are seen by the camera as disks with different radii $\tilde{a}$, depending on their vertical distance $|z|$ with respect to the thin laser sheet. b) Two spheres seen as overlapping disks when the laser sheet is too thick.

2.5.2. Camera

A video camera connected to a computer looks at the plane illuminated by the laser sheet, as previously shown in the diagrams of Fig. 2.7. Two camera models were used alternatively, both with similar characteristics: a *Basler* acA1920-155um (1936 px × 1216 px) or an *IDS uEye* UI337xCP-M (2048 px × 2048 px). The captured images show a region of ≈ 20 mm by $2b$ which occupies the whole width of the sensor, and a height between 100 and 200 px. We usually work with 48 fps, and never exceeded 200 fps. Attached to the camera, we used a 55 mm adjustable macro lens to put into focus the observed plane.

Figure 2.9 displays examples of images where spherical particles can be seen as either disks or rings, depending on whether the fluorescent dye was put in the fluid or on spheres, and whether the spheres can absorb it from the fluid. During the experiments, the particles move mostly horizontally (x direction, channel length). Images (e-g) show experiments with dyed fluid and all the particles in the plane visible. In this case, the larger spheres [85 µm, see image (e)] do not present significant overlaps, while the smaller ones [40 µm, see image (g)] can be difficult to separate visually. Image (f) with 60 µm-diameter particles is an intermediate case which is still challenging to analyze. The particles manufactured by *Microbeads* [images (f,g)] have the appearance of shining rings because they absorb at their surface the rhodamine in the fluid.[4] On the other hand, the particles from *Arkema* in image (e) show clean contours implying no significant absorption of the dye from the fluid. In this image, dark disks with different radii can be seen, of which the smallest have roughly half the radius of the largest ones. As explained before, this is a natural consequence of the illumination by

---

[4] This was verified later by retrieving the particles from the liquid using a cloth filter, washing and drying them in the process, and illuminating them with the laser: they shined orange as proof of their fluorescence.

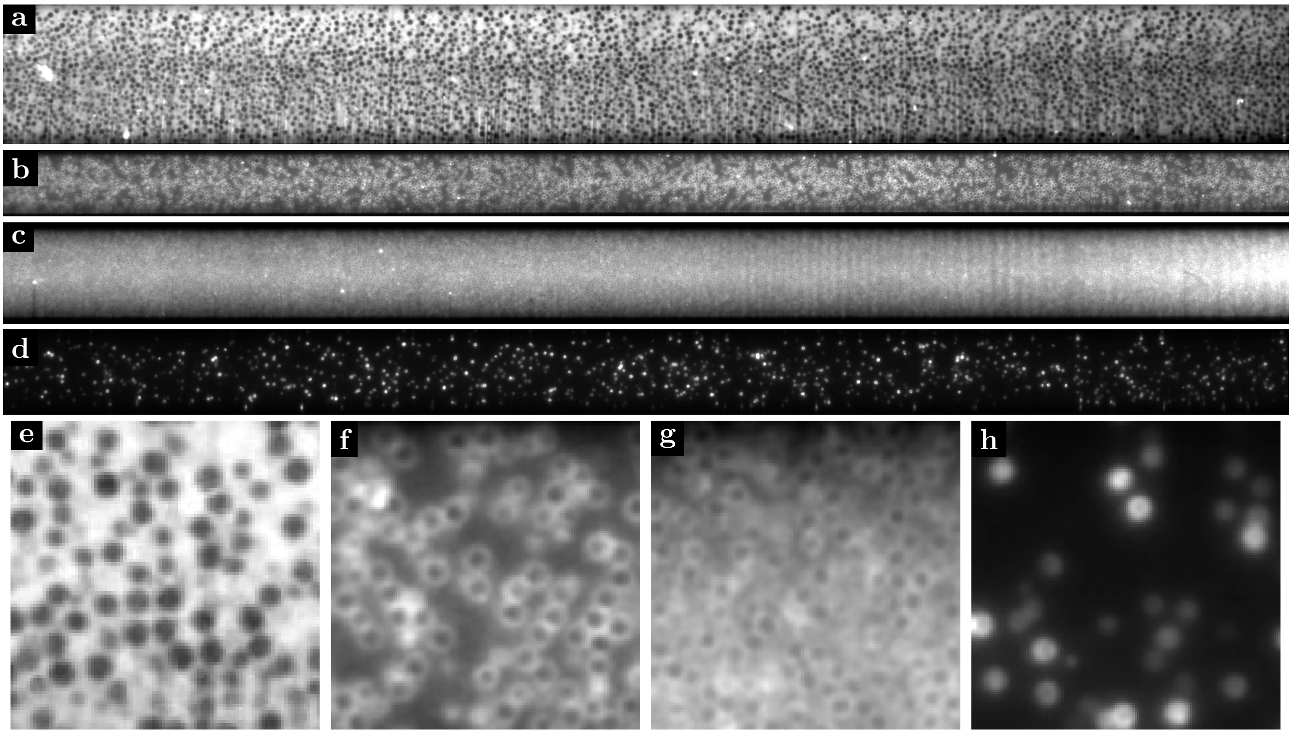

Figure 2.9: Example images. The contrast was increased to aid the eye. The top four images (a-d) show the full captured region, while the bottom four (e-h) are enlargements of small regions of the same images. The relevant parameters are: (a,e) 85 µm Arkema spheres in dyed fluid, $\phi_{\text{bulk}} = 0.40$, $2b \approx 2\,\text{mm}$; (b,f) 60 µm Microbeads spheres in dyed fluid, $\phi_{\text{bulk}} = 0.30$, $2b \approx 1\,\text{mm}$; (c,g) 40 µm Microbeads spheres in dyed fluid, $\phi_{\text{bulk}} = 0.40$, $2b \approx 1\,\text{mm}$; (d,h) dyed 40 µm Microbeads spheres in clean fluid, $\phi_{\text{bulk}} = 0.40$, $2b \approx 1\,\text{mm}$, 1% of the spheres dyed.

a laser sheet (see Fig. 2.8a).

Finally, we performed experiments using only the configurations for which the particles could be clearly distinguished: 85 µm particles in a dyed fluid and dyed 40 µm particles in a clear fluid. Although some experiments with dyed 60 µm particles were also performed, their results were similar enough to those with the 40 µm particles so that we decided to omit them from this thesis.

2.5.3. Supporting structure

The channel, the laser system and the camera were attached to a structure made from metallic profiles as shown in Fig. 2.10. The relative positions of every element could be adjusted. In particular, by moving the channel laterally, it was possible to change the observed plane, although we mostly performed experiments looking at a plane in the middle of the width, as sketched in Fig. 2.7.

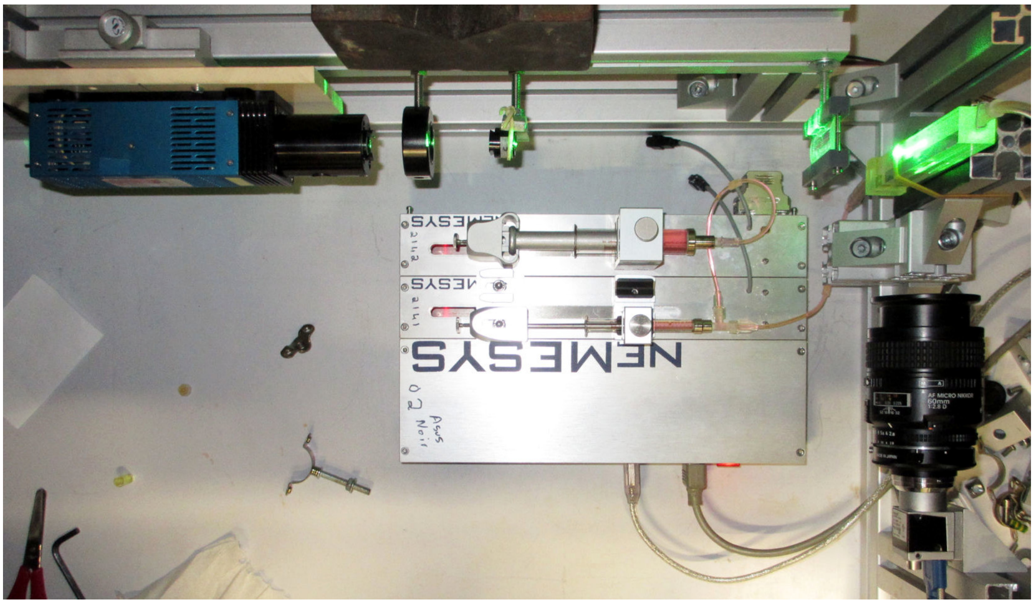

Figure 2.10: View from above of the working experimental setup. Elements in view: laser and lenses (top), pump with two syringes (middle), camera with macro lens (right), PMMA channel (top right).

2.6. Image analysis

After the suspension is prepared and fills the channel, and we have a good visualization of the particles through the camera, we can perform experiments with the desired flows. The process control is fully automated: using a *Python* script, the camera and pump operations are coordinated. First, the camera starts recording and, then, the pump starts the desired flow, for example, a number of square wave oscillations. When the programmed flow finishes, the camera stops recording. Afterward, the resulting video records are processed in the computer to detect and track the particles present. The video acquisition, storage, and particle tracking is done with a computer program developed during this thesis using the *C* programming language.

2.6.1. Particle detection

Each video is composed of a sequence of images like those presented in Fig. 2.9. To identify the particles in each image, we use a process similar to *template matching* where we define a template to find (i.e. the shape of the particles), perform a convolution between the image and the template, and finally extract the particle positions by looking for local maxima.

Each experimental image is a two-dimensional array of values proportional to the light intensity captured at the corresponding cell of the camera sensor. The template is also an image, but with its values generated artificially to match an idealized vision of the particles we look for. Our particle detection process is based on the convolution operation that, given an image I and a template T, is defined as

$$(I * T)(x, y) = \int\int I(x-u, y-v)\, T(u, v)\, \mathrm{d}u\, \mathrm{d}v. \tag{2.1}$$

The advantage of using convolutions to find occurrences of the template in the image is that their calculation can be greatly accelerated by the use of the fast Fourier transform (FFT).

Before processing a video, we select a number M of different disk radii a_i ($i = 1..M$) that we want to find in each image. Then, we generate corresponding templates P_i using the shape of either a disk or a ring depending of the appearance of the particles in the image. For example, Figure 2.11a-d shows four disks of different sizes generated to process images like that shown in Fig. 2.9a,e.

These templates can be detected more precisely in the images if we use instead templates $T_i = P_i * L$ which result from the convolution with a Laplacian kernel

$$L = \begin{bmatrix} 0 & -1 & 0 \\ -1 & 4 & -1 \\ 0 & -1 & 0 \end{bmatrix}. \tag{2.2}$$

Figure 2.11e-h displays the resulting templates T_i for the previous example disks. The convolution with the Laplacian kernel produces templates where the inner edge of the disks has positive values (blue) and the outer edge, negative ones (red). These templates T_i will result in large values of the integral in Eq. (2.1) when there is a disk of radius a_i centered at the

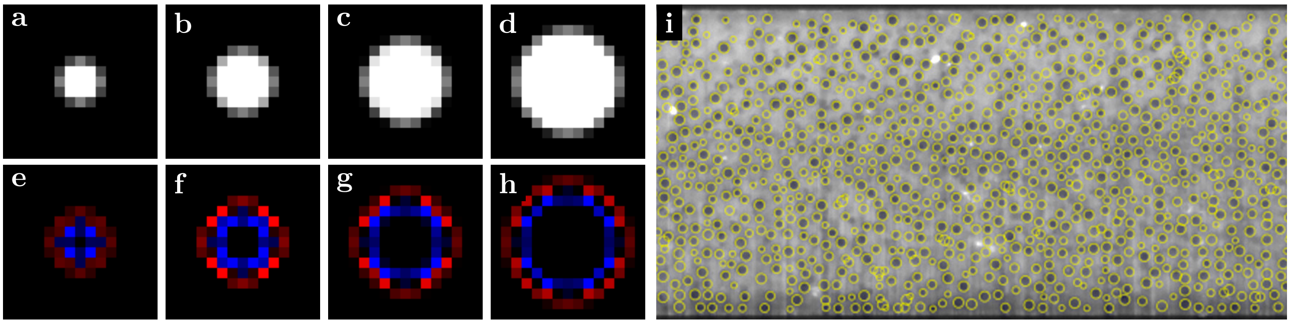

Figure 2.11: Templates P_i (a-d) and T_i (e-h) used for the detection of disks with radii $a = 2$, 3, 4, and 5 pixels. Blue and red correspond to positive and negative values, respectively. i) Experimental image with the detected disks marked by yellow circles.

position (x, y) in the image and the surrounding area is clear of other disks.

After the initial preparation, we process each image I of the video by computing accumulator images $A_i = I * T_i$ for $i = 1..M$, and locating the local maxima that surpass a threshold value in each accumulator. Each of such positions (x, y) corresponds to a candidate for a detected disk, with its radius a taken to be equal to the radius a_i of the accumulator with the largest value in that position.

The resulting list of candidates is further trimmed by removing candidates overlapping (we keep the one with the largest value in the accumulator) and those with a very uneven intensity distribution inside, usually artifacts near the walls at the top and bottom. An example of the resulting detection is shown in Fig. 2.11i.

Finally, the precision of the positions is improved to subpixel resolution by fitting neighboring values in the corresponding accumulator A_i to a Gaussian curve along each direction. For example, if a disk of radius a_i was detected at position (x, y), then, $A_i(x, y)$ is a local maximum and the refined x position is

$$x + \frac{[B(x+1, y) - B(x-1, y)]/2}{2B(x, y) - B(x-1, y) - B(x+1, y)} \tag{2.3}$$

where $B(x, y) = \log[A_i(x, y)]$, and x and y are always integer values corresponding to the position in measured in pixels.

2.6.2. Particle tracking

After we locate the particles in each image, we want to track their movements during the video to obtain trajectories and velocities. Given two consecutive images I_t and I_{t+1}, where t is a discrete time variable, we seek to establish a correspondence between the particles detected in both images such that we can determine whether a disk found in I_t and another one found in I_{t+1} correspond to the same physical particle that was displaced in the interval between the images.

The procedure is simple: for each disk centered at $\boldsymbol{x}_t = (x_t, y_t)$ in an image I_t, we find the disk which is closest in the next image I_{t+1} and, if their separation is below a threshold, we consider them to be the same particle. Repeating this process for each successive pair of images, we obtain trajectories of the particles as sequences of points in time. For this process to work reasonably well, the time lapse between images must be small enough to prevent any confusion over the identity of a particle (usually the disks in successive images must overlap). In view of this, we configured the camera frames per second (fps) to scale approximately as the maximum particle velocity, which is proportional to the pump flow rate and inversely proportional to the area of the channel cross section.

Several improvements can be brought to the previous procedure. First, using the instantaneous velocity of a particle at time t, $\boldsymbol{v}_t = (\boldsymbol{x}_t - \boldsymbol{x}_{t-1})/2$, we may predict its position at time $t+1$ as $\boldsymbol{x}_t + \boldsymbol{v}_t$. Then, the distance between the predicted position and the detected one can be used to make the process less sensitive to the frame rate (fps), but this can backfire if there are sudden changes in the velocities, like a flow reversal, in which case this procedure must be temporarily disabled. Furthermore, these predictions can be extended to more than one step in the future, allowing for the continuation of trajectories when a particle is temporarily lost due, for instance, to an imperfection in the illumination.

Smoothing the trajectories

The trajectories obtained by the tracking procedure are noisy, and this can be especially problematic for the analysis of displacements in the direction transversal to the main flow. To improve the signal to noise ratio, we use a smoothing procedure that takes into account particle positions several time steps before and after the current one.

Given a dynamic variable X, for example the longitudinal position x of a particle, we apply a linear filter to obtain

$$\hat{X}_t = \sum_{i=-r}^{r} \alpha_i \, X_{t+i}, \tag{2.4}$$

where r is a smoothing radius (a positive integer), and α_i are fixed coefficients calculated using the procedure proposed by Savitzky and Golay (1964). This filter is equivalent to fitting a polynomial of order p to the data in the window $[t-r, t+r]$ and taking its value at time t. It is also possible to calculate coefficients to obtain smooth numerical derivatives of any order, something we use to calculate the instantaneous velocity $\boldsymbol{v}_t$ of a particle from its past and future positions.

Figure 2.12 displays the coordinates, velocity components and their smoothed values for one example trajectory. The smoothing was done with $p = 2$ and $r = 8$. The particle

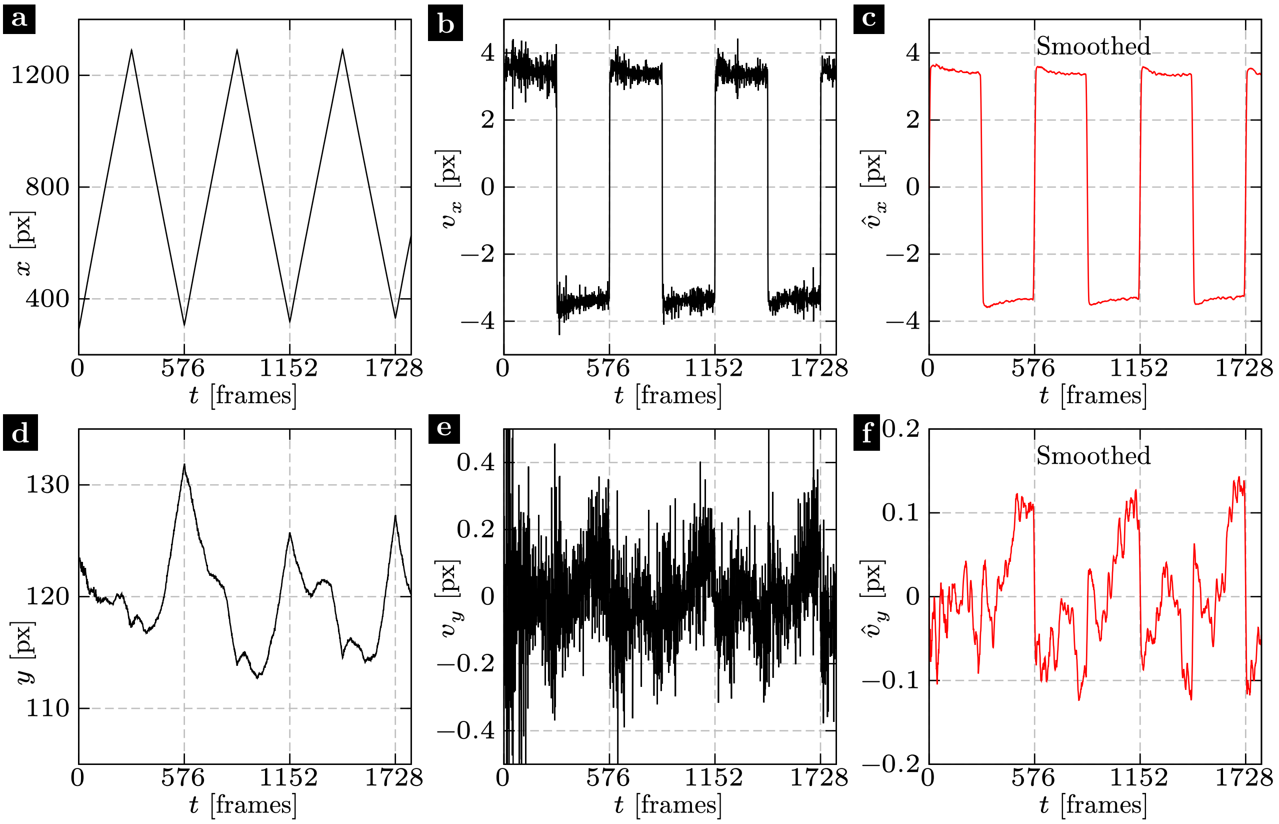

Figure 2.12: Dynamic variables of one example tracked particle: position (a,d), velocity (b,e), smoothed velocity (c,f).

undergoes an oscillatory motion in the x direction, as evidenced by the top row of plots, and it may be possible to perceive a modulation of the transverse motion in plots (d) and (e), but a clear periodicity can be seen only in plot (f) with the smoothed transversal velocity $\hat{v}_y$.

From now on, we will drop the hat notation ("ˆ") for smoothed variables and present further results already smoothed unless otherwise stated.

2.7. Data analysis

In this section, we explain the further data analysis performed on the results of the particle tracking. At a given time t, we know the positions $\boldsymbol{x}^p = (x^p, y^p)$, velocities $\boldsymbol{v}^p = (v_x^p, v_y^p)$, and apparent radii a_p of N tracked particles in the observed slice, where the index $p = 1...N$ identifies each particle. Then, we obtain spatial averages by subdividing the xy plane into rectangular bins with dimensions $\Delta x \times \Delta y$ and calculating statistics for the particles inside each one.

2.7.1. Concentration, velocity and velocity fluctuations fields

The sum of the area occupied by the particles in a bin centered at (x, y) divided by the bin area gives the particle area fraction

$$\phi_{2\mathrm{D}}(x, y) = \frac{1}{\Delta x \Delta y} \sum_{p \in \mathrm{bin}} \pi a_p^2, \tag{2.5}$$

which is statistically equal to the volume fraction ϕ, a fact know as the Delesse principle in stereology theory (Delesse 1847; Mayhew and Orive 1974). This calculation requires an accurate detection of all the particles in a thin slice and a determination of their sizes, something we only have for the experiments with the 85 µm particles in a dyed fluid, where we see clearly all the particles in a slice with a thickness much smaller than the particles. On the other hand, in the experiments with 40 µm particles, we only see $\approx 2\%$ of the particles present and the thickness of the slice allows for some overlap between the observed disks. In this latter case, the above calculation underestimates the value of ϕ and we corrected it by introducing a multiplicative factor that makes the average value of $\phi_{2\mathrm{D}}$ equal to the bulk volume fraction ϕ_{bulk} known from the suspension preparation. This correction assumes that we detect particles inside any given bin (x, y) in proportion to their concentration there, but it is possible that detection errors occur more frequently in zones where the concentration is large and overlapping disks are more common. For this reason, our analysis of the local values of ϕ will be only qualitative for the experiments with the smaller particles.

In some cases, we are also interested in the two-dimensional particle number density

$$n_{2\mathrm{D}}(x, y) = \frac{N_{\mathrm{bin}}(x, y)}{\Delta x \Delta y} = \frac{1}{\Delta x \Delta y} \sum_{p \in \mathrm{bin}} 1, \tag{2.6}$$

where $N_{\mathrm{bin}}(x, y)$ is the number of detected particles whose centers are inside the bin centered at (x, y).

Furthermore, we can calculate the particle velocity field $V(x, y)$ using the average velocity of the particles detected inside each bin:

$$\boldsymbol{V}(x, y) = \frac{1}{N_{\mathrm{bin}}(x, y)} \sum_{p \in \mathrm{bin}} \boldsymbol{v}^p. \tag{2.7}$$

Note the uppercase V for the average, and the lowercase v for the individual particle velocities. Similarly, we may estimate a velocity fluctuations tensor

$$T_{ij}(x,y) = \frac{1}{N_{\text{bin}}(x,y)} \sum_{p\in\text{bin}} [v_i^p - V_i(x,y)][v_j^p - V_j(x,y)], \tag{2.8}$$

where the indices i, j correspond to the dimensions x, y, z.

During the beginning of each experiment, the flow is mostly laminar and the only significant variations of the above fields are in the direction y. For this reason, we use bins that extend across the full width of the images to analyze this situation, obtaining *profiles* that depend only on y, e.g. $\phi(y)$, $V_x(y)$. The bin size Δy is set to one pixel ($\approx 10\,\mu\text{m}$), and we rely on the time-averaging procedures described in Sec. 2.7.3 in order to collect enough statistical data inside each bin.

To analyze the flow during the instability, when variations in both directions are important, we divide the observed plane in a rectangular grid with bins of equal size $\Delta x \approx 580\,\mu\text{m}$ by $\Delta y \approx 133\,\mu\text{m}$. As a reference, we detect on average 4000 particles in each image of the experiments using the 85 µm particles, resulting in roughly 8 particles per bin.

2.7.2. Pair correlations

The previous statistical quantities consider each particle individually, but to understand the interactions between particles, it is useful to have information on the relative positions and velocities of nearby particles. In Sec. 1.5, we established the pair distribution function (pdf) as the preferred tool for such a purpose. Here, we describe our procedure for its calculation, which is similar to that used by Blanc, Lemaire, et al. (2013).

- First, we exclude detected particles whose apparent radius is less than $0.8a$, where a is an estimation of the real spherical radius. This ensures that all the particles considered are roughly in the same plane ($z \approx 0$ in Fig. 2.8a) and the observed two-dimensional relative positions match the real ones.
- For each particle p with its center inside a bin centered at (x, y), we consider all other particles q up to a distance $6a$ and make a list of pairs. The particle q does not need to be in the same bin as particle p.

- The relative positions $\boldsymbol{r}^{qp} = \boldsymbol{x}^q - \boldsymbol{x}^p$ and velocities $\boldsymbol{v}^{qp} = \boldsymbol{v}^q - \boldsymbol{v}^p$ are computed for each pair.
- The space (r_x, r_y) of relative positions is subdivided into bins of size $\Delta r_x \times \Delta r_y$ with $\Delta r_x = \Delta r_y \approx 2.5\,\mu\mathrm{m}$.
- Inside each of these bins we count the number of pairs $N_{\mathrm{pair}}(x, y, r_x, r_y)$ and calculate the average relative velocity $\boldsymbol{V}_{\mathrm{pair}}(x, y, r_x, r_y)$.

Summarizing, a pair of particles p and q contribute to the bin labeled (x, y, r_x, r_y) if

$$\begin{gathered} |x^p - x| < \tfrac{1}{2}\Delta x, \quad |y^p - y| < \tfrac{1}{2}\Delta y, \\ |x^q - x^p - r_x| < \tfrac{1}{2}\Delta r_x, \text{ and } \quad |y^q - y^p - r_y| < \tfrac{1}{2}\Delta r_y. \end{gathered} \tag{2.9}$$

With this information, we may estimate the probability density $P(x, y, r_x, r_y)$ of finding a particle in a position $(x + r_x, y + r_y)$, given that a reference particle is present at (x, y), as

$$P(x, y, r_x, r_y) = \frac{N_{\mathrm{pair}}(x, y, r_x, r_y)}{N_{\mathrm{bin}}(x, y)\,\Delta r_x \Delta r_y}, \tag{2.10}$$

where $N_{\mathrm{bin}}(x, y)$ is the number of particles inside bin (x, y) (see Eq. 2.6). As explained in Sec. 1.5, P is equal to the particle number density n if the particles are randomly distributed everywhere, and $g = P/n$ is called the *pair distribution function.* In our case, we calculate g at different positions (x, y) by replacing n by $n_{\mathrm{2D}}(x, y)$ from Eq. (2.6):

$$g(x, y, r_x, r_y) = \frac{P(x, y, r_x, r_y)}{n_{\mathrm{2D}}(x, y)}. \tag{2.11}$$

It is also possible to represent the relative pair position in polar coordinates as $(r_x, r_y) = [r\cos(\theta), r\sin(\theta)]$. Then, binning only along r we may calculate the radial pair distribution

$$g(x, y, r) = \frac{N_{\mathrm{pair}}(x, y, r)}{n_{\mathrm{2d}}(x, y)\, N_{\mathrm{bin}}(x, y)\, 2\pi r \Delta r}. \tag{2.12}$$

Here, $2\pi r \Delta r$ is the area of the bin in the space of the variables (r, θ), with $\Delta r \approx 2.5\,\mu\mathrm{m}$. We are also interested in the angular distribution of pairs almost in contact. For its calculation, we include only the pair that have $|r - r_{\mathrm{peak}}| < \frac{1}{2}\Delta r_{\mathrm{peak}}$, with $r_{\mathrm{peak}} \approx 1.9\,a$ and $\Delta r_{\mathrm{peak}} \approx 0.3\,a$.

The last two values were estimated from the radial distribution, and will be explained in more detail when the corresponding results are discussed. Then, we subdivide the space of the variable $\theta \in [-\pi, \pi)$ into 48 segments of size $\Delta\theta$, and compute the angular pair distribution as

$$g(x, y, \theta) = \frac{N_{\mathrm{pair}}(x, y, \theta)}{n_{\mathrm{2d}}(x, y)\, N_{\mathrm{bin}}(x, y)\, r_{\mathrm{peak}} \Delta\theta \Delta r_{\mathrm{peak}}}. \tag{2.13}$$

A large amount of particle pairs is required to correctly calculate g due to the double binning involved. For that reason, we use averages in time and across multiple experiments (as explained in the following section), and we usually bin the image space only in y, obtaining in effect $g(y, r_x, r_y)$, $g(y, r)$ and $g(y, \theta)$. For the sake of simplicity, we will refer to them without the explicit dependence on y from now on, e.g. $g(r_x, r_y)$.

2.7.3. Temporal averaging

All the previously presented quantities are instantaneous, that is, they are functions of time t even if not explicitly shown before, and we may take their averages over multiple times to improve the quality of the results (reduce noise). Most of our experiments use oscillatory flows without a net displacement, where the flow direction is periodically reversed as sketched in Fig. 2.13. In these experiments, there are two time scales of interest: the time between two consecutive reversals, when the suspension experiences a transient reorganization, and the long-term evolution of the system.

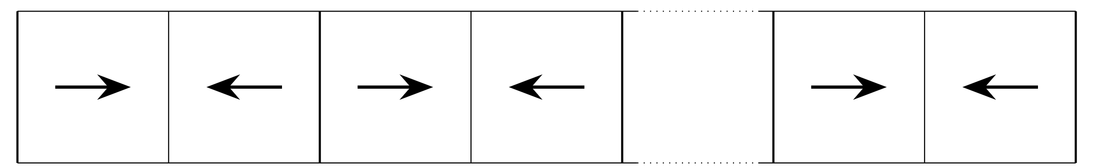

Figure 2.13: Diagram showing different times of interest during an experiment with oscillatory flow. Each oscillation is divided in two halves of identical duration, but opposite mean flow direction (arrows).

To study the short-term variations, we perform ensemble averages over multiple oscillations. Given a dynamic variable $X(t)$, for example $X(t) = V_x(y, t)$ for some y, the ensemble average over M oscillations is calculated as

$$\tilde{X}(t) = \frac{1}{M} \sum_{i=0}^{M-1} X(t_i + t), \tag{2.14}$$

where t_i is the time when the oscillation $i + 1$ starts (see Fig. 2.13). The M oscillations selected for the average do not encompass whole experiments; instead, different averages $\tilde{X}$ are obtained during each stage of the development of the instability, as explained in the next chapter.

To study the long-term evolution, we determine first the lapse Δt_{qss} required to reach a *quasi steady state (qss)* after each flow reversal. We consider that the suspension is in quasi steady state when some key dynamic variables no longer change significantly with time, the exact criteria will be made explicit along with the results in the next chapter. Then, for each period between consecutive reversals, we calculate the average value of X (a variable of interest) between a time Δt_{qss} since the last reversal and until the next one, obtaining $2M$ values for an experiment with M oscillations.

From each oscillation i we obtain two values, lets say X_{i+} and X_{i-}, corresponding to the halves of oscillation with the suspension going forward (+) and backward (−). For variables that do not change sign, like the local particle volume fraction ϕ, we average both to obtain M values $X_i = (X_{i+} + X_{i-})/2$. On the other hand, for variables like the longitudinal velocities V_x which have sign inversions after each flow reversal, the result of the sum would be roughly zero. Instead, we use $X_i = (X_{i+} - X_{i-})/2$ in those cases to retain the information of interest. Something similar is done for the averaging of the pair distribution function g, since the particle reorganization processes occurring during each half of the oscillations are similar, but with microstructures mirrored along the x direction compared to one another. Therefore, we invert the signs of the relative longitudinal positions r_x and velocities v_x of the pairs during the backward flow (−), before proceeding with averaging.

Finally, we also average the results from different experiments with physically equivalent parameters. The procedure is the same as the ensemble average of Eq. (2.14), but using multiple experiments instead of multiple oscillations.

2.7.4. Auto- and cross-correlations

In our experiments, we observe an instability that introduces spatially-periodic patterns in the particle concentration and velocity fields (see Chapter 4 for details). In order to characterize the time evolution of one of these patterns we will use correlations between its values at different positions and at different times.

The correlation between two function $f(x)$ and $g(x)$ defined for $x \in [x_1, x_2]$ is

$$C_{fg}(\delta x) = \frac{1}{x_2 - x_1} \int_{\max(x_1, x_1 - \delta x)}^{\min(x_2, x_2 - \delta x)} [f(x) - \mu_f]\,[g(x + \delta x) - \mu_g]\;\mathrm{d}x, \tag{2.15}$$

where δx is called the *lag*, and μ_f and μ_g are respectively the mean values of f and g, taken to be both zero for the functions that interest us.

As a concrete example, we show in Fig. 2.14a the transverse velocity along the channel center line, $V_{y,\mathrm{cen}}(x,t)$, for a typical experiment with the instability fully developed. The blue curve corresponds to a time t_1, and the red curve, to a later time $t_2 \approx t_1 + 1\,\mathrm{s}$. Observe that both curves are roughly periodic along x, with a wavelength $\lambda \approx 3.5\,\mathrm{mm}$, and the curve at time t_2 is displaced $\approx 1\,\mathrm{mm}$ to the right with respect to other curve. Our objective here is to obtain an amplitude $A_{V_y}(t)$ and a wavelength $\lambda_{V_y}(t)$ for each curve, and a travel velocity V_{V_y} between them.

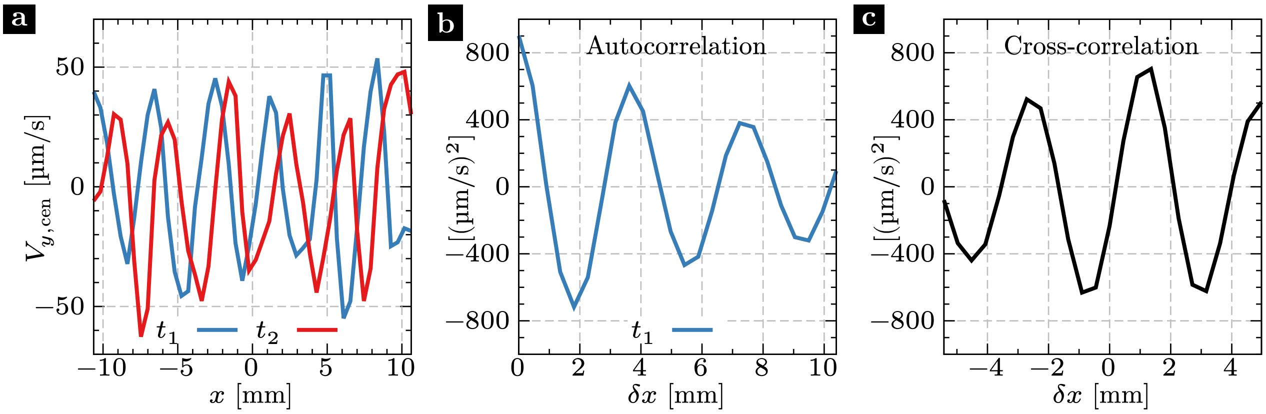

Figure 2.14: a) Function $V_{y,\mathrm{cen}}(x,t)$ plotted against x for two specific times t_1 (blue) and $t_2 \approx t_1 + 1\,\mathrm{s}$ (red), when the instability is fully developed in a typical experiment (40 μm particles, 1 mm channel gap, $\phi_{\mathrm{bulk}} = 0.40$). b) Autocorrelation of the curve for time t_1. c) Cross-correlations between both curves from (a).

The autocorrelation of $V_{y,\mathrm{cen}}(x,t_1)$ is shown in Fig. 2.14b. Observe that it has the same periodicity as the curves on the left, with a maximum at $\delta x = 0$ and a second peak at

$\delta x_{\text{peak}} \approx 3.5\,\text{mm}$. For a perfectly periodic variable, e.g. $f(x) = A_f \sin(2\pi x/\lambda)$, with an integer number of oscillations inside the range $[x_1, x_2]$, the following relations can be demonstrated:

$$\lambda = \delta x_{\text{peak}}, \quad A_f = \sqrt{2\frac{x_2 - x_1}{x_2 - x_1 - \lambda}\, C_{ff}(\delta x_{\text{peak}})}, \tag{2.16}$$

where $C_{ff}(\delta x)$ is the autocorrelation of $f(x)$. In our analysis of the experimental data, we assume that only one wavelength is relevant and use the above relations to estimate the wavelengths and the amplitudes of relevant variables at each time during the experiment.

To determine the travel velocity V_{V_y}, we use the cross-correlation between $f(x) = V_{y,\text{cen}}(x, t_1)$ and $g(x) = V_{y,\text{cen}}(x, t_2)$ shown in Fig. 2.14c. The maximum value at $\delta x_{\text{max}} \approx 1\,\text{mm}$ corresponds to the lag at which both curves are most similar, then, it is clear that $V_{V_y} = \delta x_{\text{max}}/(t_2 - t_1) \approx 1\,\text{mm/s}$.

Finally, using the value δx_{max} from the cross-correlation between two different variables f and g measured at the same time t and with the same wavelength λ, we may calculate a phase relation $\phi_{fg} = 2\pi \delta x_{\text{max}}/\lambda$. For example, $\phi_{fg} = \pi/2$ means that g is displaced to the right of f by a quarter of wavelength.

Chapter 3

Presentation of the instability and reference quasi-steady state

In the previous chapter, we described our experiments with suspensions undergoing oscillatory channel flow. From our observations, and those of Roht (2017), we know that each of these experiments can be divided into roughly two stages: a first one where the flow is laminar and shear-induced migration may be observed in some cases, and a second stage where a velocity component transverse to the main flow becomes significant and the particles get organized into a pattern periodic along the main flow direction.

We begin this chapter with an overview of a typical experiment, making explicit the distinctions between those two stages. Then, we restrict our attention to the state of the suspension just before the beginning of the second stage, in order to understand the situations that give rise to the unstable flow occurring afterward. We delay a thorough description of the instability until Chapters 4 and 5.

3.1. Development of the instability in a typical experiment

Figure 3.1 displays a series of images captured during a typical experiment using a bulk particle volume fraction $\phi_{\text{bulk}} = 0.40$, particles with diameter $2a \approx 85\,\mu\text{m}$, and a channel of thickness $2b = 2.08\,\text{mm}$ and width $W = 10.0\,\text{mm}$. During the experiment, a syringe pump induced a symmetric square-wave flow with a period $T = 12\,\text{s}$ and a maximum flow rate $Q_0 = 24\,\text{mm}^3/\text{s}$ that, given a channel cross section $S = 20.8\,\text{mm}^2$, resulted in an absolute average velocity of the suspension $V_\mathrm{s} = Q_0/S \approx 1.15\,\mathrm{mm/s}$ and a Reynolds number $\mathrm{Re} = V_\mathrm{s} b \rho_\mathrm{f}/\eta_\mathrm{f} \approx 0.2$. Following the notation introduced in Sec. 1.8, we will present temporal variations as functions of either the characteristic accumulated strain $\bar{\gamma} = tV_\mathrm{s}/b$ or the number of oscillations t/T. Between two flow reversals (a half oscillation), the suspension travels a distance $A_0 = V_\mathrm{s}T/2 \approx 6.92\,\mathrm{mm}$ on average and, from now on, we will characterize the oscillation amplitudes by the characteristic strain $\bar{\gamma}_0 = A_0/b = V_\mathrm{s}T/(2b)$ which is ≈ 6.66 in this case.

The images in Fig. 3.1 show views at successive times t of a plane parallel to the channel length (x direction) and thickness (y direction), and located at the middle of the width ($W/2 = 5\,\mathrm{mm}$ from the lateral walls). The particles intersected by the plane can be seen as black disks in a white background corresponding to the suspending fluid.

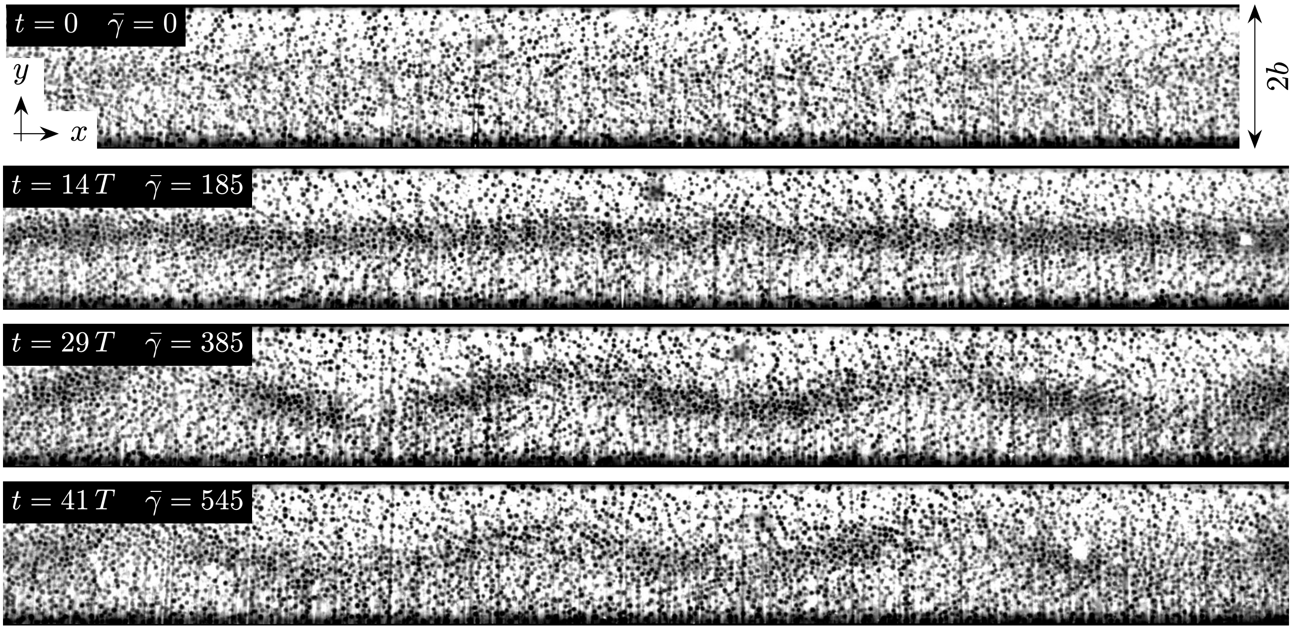

Figure 3.1: Sequence of images taken at different times t from an experiment with a oscillatory flow in the x direction. Parameters: $\phi_\mathrm{bulk} = 0.40$, $2a \approx 85\,\mathrm{\mu m}$, $2b \approx 2.1\,\mathrm{mm}$, $V_\mathrm{s} = 1.15\,\mathrm{mm/s}$, $T = 12\,\mathrm{s}$, $\bar{\gamma}_0 = T\,V_\mathrm{s}/(2b) = 6.66$.

The first image ($t = 0$) presents the initial state of the suspension just after the channel was filled and before any oscillations. The particle concentration is slightly larger near the center of the thickness, probably due to shear-induced migration occurring when the channel was being filled. The suspension might enter the channel in a well-mixed state, but this view was obtained at a distance of $\approx 70\,\mathrm{mm}$ from the inlet, long enough to induce a partial migration with $\phi_\mathrm{bulk} = 0.40$, as shown in Fig. 1.13. The migration process continues as the suspensions oscillates, increasing the particle concentration in the center line, as shown the second image ($t = 14\,T$), taken when the maximum concentration there was reached.

Around this time, this central band of high particle concentration began to destabilize, eventually forming the wave-like pattern displayed in the third image ($t = 29\,T$). During this process, the particles move in the y direction, transverse the main flow along the x direction, but, as we will see in Chapter 4, this process is more complex since the whole pattern is being convected longitudinally by the oscillatory main flow. Afterward, the pattern becomes less clear, as shown in the fourth image ($t = 41\,T$) but, then, it remains without significant changes until the experiment is finished.

Figure 3.2a displays the local volume fraction $\phi(y, t)$ as a function of y, for times t corresponding to the first three images. The initial migration (from $t/T = 0$ to 14) increases ϕ near the center ($y = 0$) and decreases it near the walls ($y = \pm 1$). With the instability onset, the wave-like pattern starts to form and the particles move out of the center line, resulting in a profile at $t/T = 29$ that looks similar to the initial one, although we know from the images that the configuration is different.

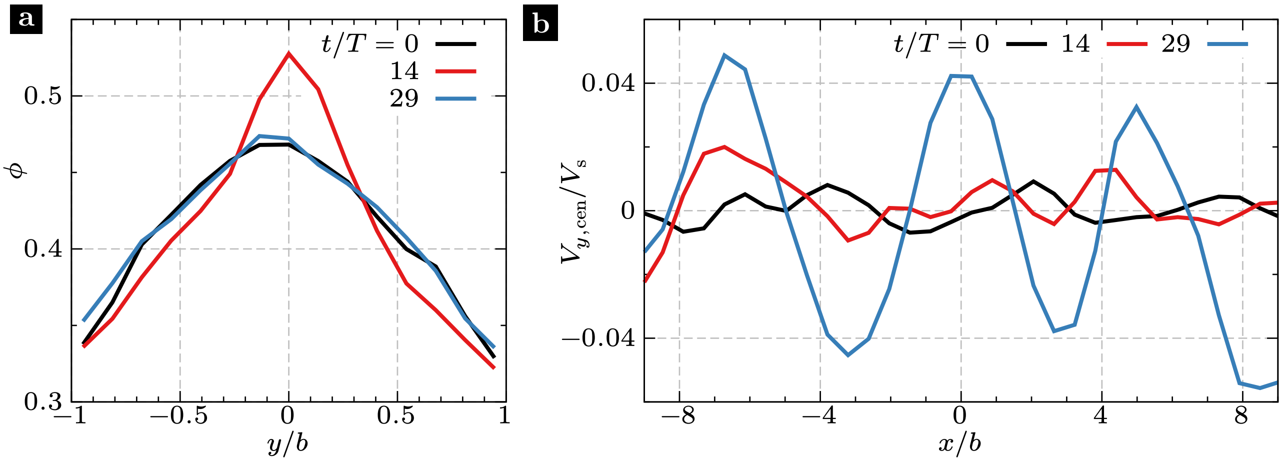

Figure 3.2: a) Local particle volume fraction ϕ across the channel thickness (y direction). Walls at $y/b = \pm 1$. b) Transverse velocity in the center of the thickness $V_{y,\mathrm{cen}}$ as a function of the coordinate x, normalized by $V_\mathrm{s} = 1.15\,\mathrm{mm/s}$. Each plot has three curves corresponding to the times of the first three images of Fig. 3.1.

During the unstable flow, the velocity field presents variations along both x and y. The temporal variations of the transverse velocity component $V_y(x, y, t)$ are especially useful to track the development of the instability because the magnitude of its values increases sharply after the instability onset. Figure 3.2b shows $V_{y,\mathrm{cen}}(x, t) = V_y(x, 0, t)$ along x for the same three times t as plot (a). The velocities are normalized by V_s. During the migration ($0 \leq t/T \leq 14$), $V_{y,\mathrm{cen}}$ does not have any discernible structure and its values are small (compared with later times). At $t/T = 29$, we see that $V_{y,\text{cen}}$ has become periodic along x with a period of $\approx 5\,b$ like the particle distribution observed in the image of Fig. 3.1c.

The curves shown here correspond to times shortly before a flow reversal. After the reversal occurs, both velocity components V_x and V_y change sign. For this reason, the pattern formed by the particles is not simply the result of them moving steadily with the transverse velocity shown here, instead, it must be an irreversible consequence of each oscillation. We will continue this analysis in Chapter 4.

The temporal variations described above can be tracked for each oscillation using Fig. 3.3. There, we see two curves plotted versus the number of oscillations t/T and the accumulated strain $\bar{\gamma}$: the volume fraction in the center of the thickness, $\phi_{\text{cen}}(t) = \phi(0,t)$, and the root mean square (rms) of the $V_{y,\text{cen}}(x,t)$:

$$V_{y,\text{cen,rms}}(t) = \sqrt{\frac{1}{x_2 - x_1}\int_{x_1}^{x_2} V_{y,\text{cen}}^2(x,t)\ \mathrm{d}x}, \tag{3.1}$$

with $x_2 = -x_1 \approx 9\,b$ in this example. When the migration is occurring ($0 \leq t/T \leq 14$), ϕ_{cen} (green line) increases from ≈ 0.46 to ≈ 0.53, while $V_{y,\text{cen,rms}}$ remains approximately constant at a initial value of $\approx 0.005\,V_\text{s}$. Then, the effects of the instability become clear: $V_{y,\text{cen,rms}}$ increases until it reaches at $t/T \approx 30$ a maximum value of $\approx 0.03\,V_\text{s}$ and, almost simultaneously, ϕ_{cen} decreases until it reaches a value ≈ 0.45. Afterward, both curves remain almost constant.

During the analysis of our experiments, we used curves like the above ones to determine

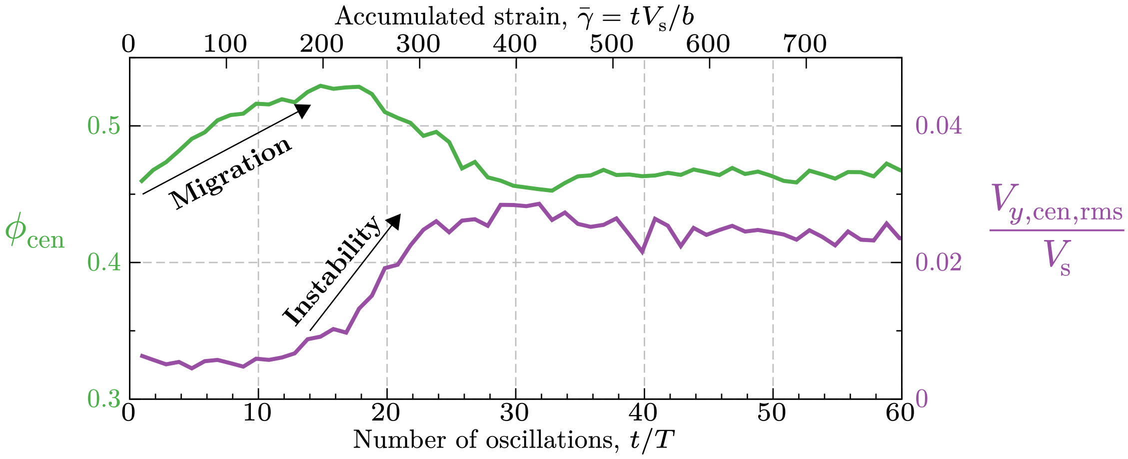

Figure 3.3: Temporal evolution of ϕ_{cen} (volume fraction ϕ at $y = 0$, left axis) and $V_{y,\text{cen,rms}}$ (root mean square of $V_{y,\text{cen}}$, right axis) as functions of the number of oscillations t/T (bottom axis) and the accumulated strain $\bar{\gamma} = tV_\text{s}/b$ (top axis). Same experiment as Fig. 3.1.

the time t_{onset} after which the effects of the instability become important (here $t_{\text{onset}}/T \approx 14$). In the remainder of this chapter, we study the flow and particle distributions found just before this onset time, while a complete characterization of the instability will be deferred to Chapter 4.

3.2. Quasi-steady flow before the instability

Before the onset of the unstable behavior, the flow and particle distribution are roughly invariant along the x direction. As such, we focus on the variations across the gap (y direction) in this section, and present profiles of the volume fraction $\phi(y,t)$, longitudinal velocity $V_x(y,t)$ and velocity fluctuations $T_{ij}(y,t)$ calculated using the particle positions and velocities as described in Sec. 2.7.

During our experiments the flow direction is periodically reversed, producing transient variations in the flow after each reversal. These variations are a consequence of the microstructure reorganization (see Sec. 1.5.2) and will be discussed in more detail in Secs. 3.3 and 3.5. In the following subsections, we will show results averaged during the *quasi-steady state* (qss) reached after a strain $\Delta\bar{\gamma}_{\text{qss}}$ is accumulated since the last reversal.

In order to determine $\Delta\bar{\gamma}_{\text{qss}}$, we look at the instantaneous longitudinal velocity profiles $V_x(y,t)$ and calculate the ratio between the velocity in the center $V_{\text{cen}}(t) = V_x(0,t)$ and the average over y, $V_{\text{avg}}(t)$. For very dilute suspensions ($\phi < 0.01$), with the particles acting as tracers, we see the expected parabolic velocity profiles where $V_{\text{cen}}/V_{\text{avg}} \approx 1.5$, as displayed in Fig. 3.4a. As the average volume fraction ϕ_{bulk} increases, we observe the blunting of the velocity profiles described in Sec. 1.6.2, and a decrease of the quotient $V_{\text{cen}}/V_{\text{avg}}$. Furthermore, after each flow reversal, there is a transient rise of this quotient as a result of inhomogeneous variations of the suspension viscosity (see Sec. 3.3), with an amplitude that increases with ϕ_{bulk}. Figure 3.4b illustrates both effects during one oscillation of representative experiments. From these plots, we conclude that, after a strain $\Delta\bar{\gamma}_{\text{qss}} = 5$ (see the top axis), the velocity profiles no longer present significant effects from the reversal and we can consider them as representative of a quasi-steady state.

There are also the long-term variations induced by the particle migration and the instability mentioned in the previous section. The migration has been the topic of previous studies,

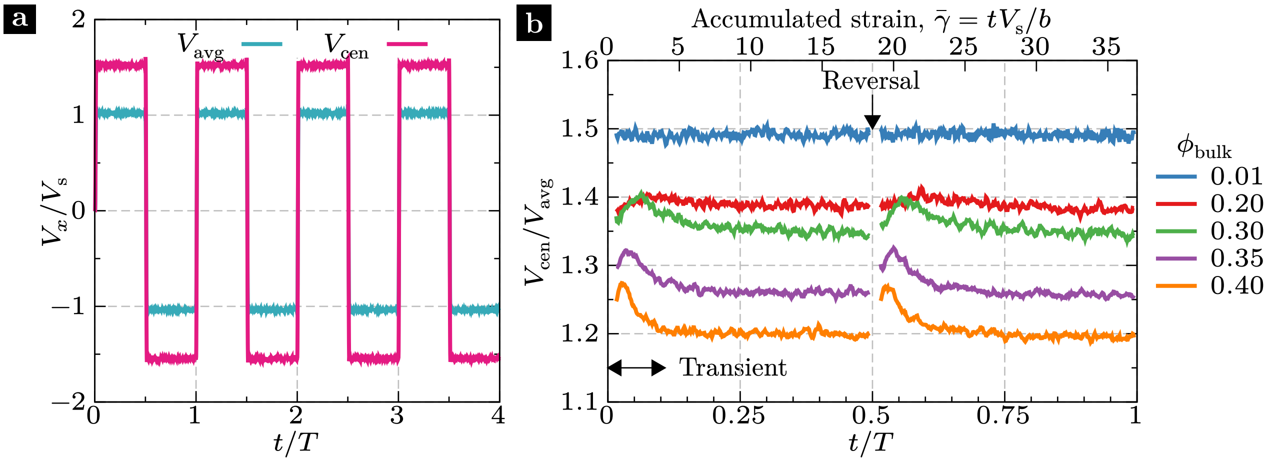

Figure 3.4: a) Average and central longitudinal velocity during four oscillations of a calibration experiment with $\phi_{\text{bulk}} < 0.01$. b) Quotient between central and average velocities during one oscillation at the beginning of experiments with different volume fractions (increasing from top to bottom). For both graphs: $2a \approx 40\,\mu\text{m}$, $2b = 1.0\,\text{mm}$, $V_s = 1.16\,\text{mm/s}$, $T = 16\,\text{s}$, $\bar{\gamma}_0 = T\,V_s/(2b) = 18.6$.

and the instability will be studied in detail in the following chapters. Our objective here is to characterize the base state just before the onset of the instability occurring after t_{onset}/T oscillations. For the present analysis, we define t_{onset}/T as the last cycle when $V_{y,\text{cen,rms}}$ was below 10% between its initial and maximum value.

Following the time-averaging procedures explained in Sec. 2.7.3, from each experiment, we take the six half oscillations before t_{onset}/T and, from each of them, we take the quasi-steady part after a time Δt_{qss}. Finally, we make a temporal average leaving only the dependence on y. For V_x, which alternates signs, we invert the sign every two half oscillations before the averaging. Finally, the profiles from different experiments with the same parameters are averaged together (between two to four experiments in each case).

3.2.1. Longitudinal velocity

Figure 3.5 shows the longitudinal velocity profiles $V_x(y)$ corresponding to the quasi-steady state observed before the onset of the instability. Each profile is normalized by its average across y, V_{avg}.

On plot (a), the bulk volume fraction ϕ_{bulk} varies while particle and channel sizes ($2a \approx 40\,\mu\text{m}$, $2b = 1.0\,\text{mm}$) remain fixed. We observe that the profiles become progressively more blunted as ϕ_{bulk} increases, like those of Rashedi et al. (2020) shown in Fig. 1.12. This is a consequence of the shear-induced migration of particles toward the center ($y = 0$).

On plot (b), the volume fraction is fixed at $\phi_{\text{bulk}} = 0.4$ and we compare experiments with

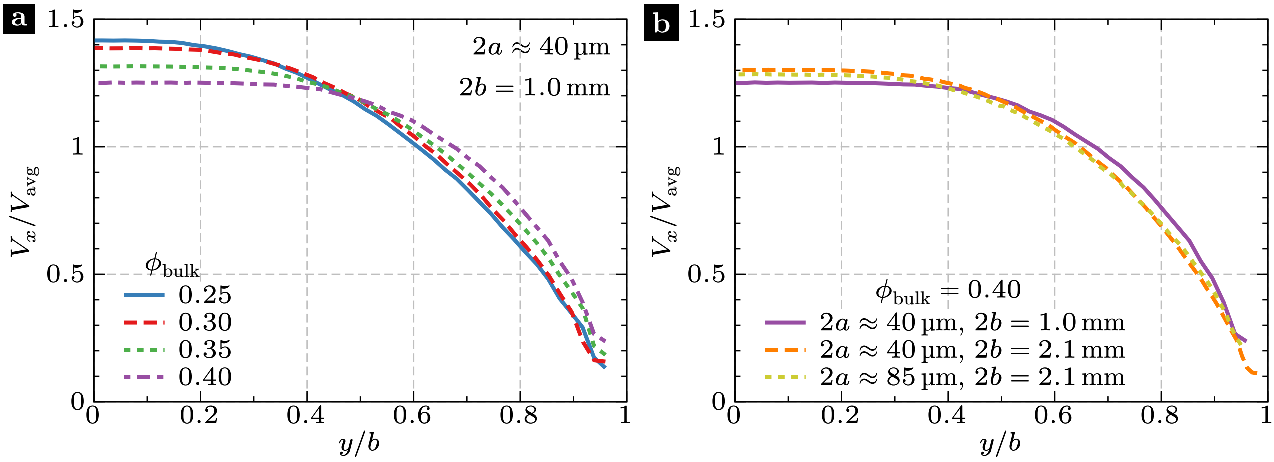

Figure 3.5: Longitudinal velocity profiles for experiments with different volume fractions (a) and geometric parameters (b). Oscillation amplitude $\bar{\gamma}_0 \approx 18$, no significant differences for other values.

different particles and channel sizes. The profiles are similar, with the violet curve being slightly blunter, but it is unclear whether this is significant.

It is important to note that each profile is normalized by the corresponding measured average velocity V_{avg} and not by a fixed value determined from the parameters. We have to do this to make them comparable, since variations of up to 5% were observed between the average velocities of different experiments, even consecutive ones. These discrepancies may result from variations of the initial conditions, particularly, the particle distribution inside the channel.

3.2.2. Volume fraction

Figure 3.6 shows the particle volume fraction profiles corresponding to the previous velocity profiles. In all cases, the values increase from the wall ($y/b = 1$) to the center ($y/b = 0$). This trend is consistent with the shear-induced migration and the curves from Rashedi et al. (2020) shown in Fig. 1.12a, although the latter presents sharper variations of ϕ around $y/b \approx 0.1$. Since these profiles occurs shortly before the onset of the instability, one possibility is that the mechanism responsible for it is partially counteracting the particle migration. In the case of the 40 µm particles, limitations in the visualization technique may also play a role since those particles can overlap visually due to their small size in relation to the thickness of the laser plane (see Sec. 2.5.1 and 2.7.1).

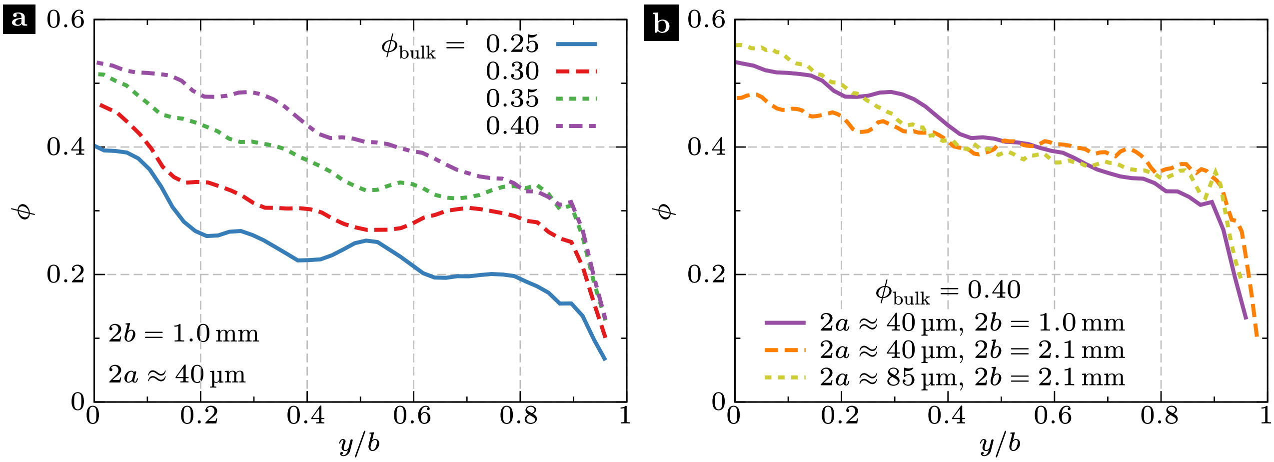

Figure 3.6: Particle volume fraction profiles for experiments with different volume fractions (a) and geometric parameters (b). Same experiments as Fig. 3.5.

3.2.3. Transverse velocity fluctuations

Although the average transverse velocities across the gap are negligible, $|V_y(y)/V_{\mathrm{avg}}| < 0.002$, interactions between particles can result in non-zero velocity fluctuations as a consequence of their finite size. This was illustrated in Sec. 1.4.2 for the case of two particles approaching with a local shear rate $\dot{\gamma}$: if their transverse separation is small enough ($\Delta y \lesssim 2a$), the pair will have to separate transiently a distance of the order of a. Then, we may expect transverse velocity fluctuations to be proportional to $a\,\dot{\gamma}$ and increase with ϕ.

Figure 3.7 shows the transverse velocity fluctuations profile $T_{yy}^{1/2}(y)$ normalized by $V_{\mathrm{avg}}a/b$. As expected, the fluctuations grow with ϕ and $\dot{\gamma} = |\partial V_x/\partial y|$ (see inset), with exceptions in two extreme regions. Near the wall ($y/b \gtrsim 0.9$), its influence reduces the fluctuations, and near the center ($y/b \lesssim 0.25$), the shear rate is almost zero but finite fluctuations are observed. In plot (a), we see that simulations of steady channel flow done by Yeo and Maxey (2011) (black lines) have characteristics similar to our measurements. In particular, they predict non-zero values near the center ($y = 0$), although smaller than ours. It is possible that some of the fluctuations observed in our measurements come from small errors in the particle tracking process, affecting more severely regions of higher particle concentration.

Plot (b) displays results for experiments with different particle diameters $2a$ and channel thicknesses $2b$. The curves for experiments with $b/a \approx 25$ (violet and yellow curves) are similar, but the experiments with $b/a \approx 50$ (orange) have significantly larger values than the other two, using our chosen normalization. These specific experiments with smaller beads

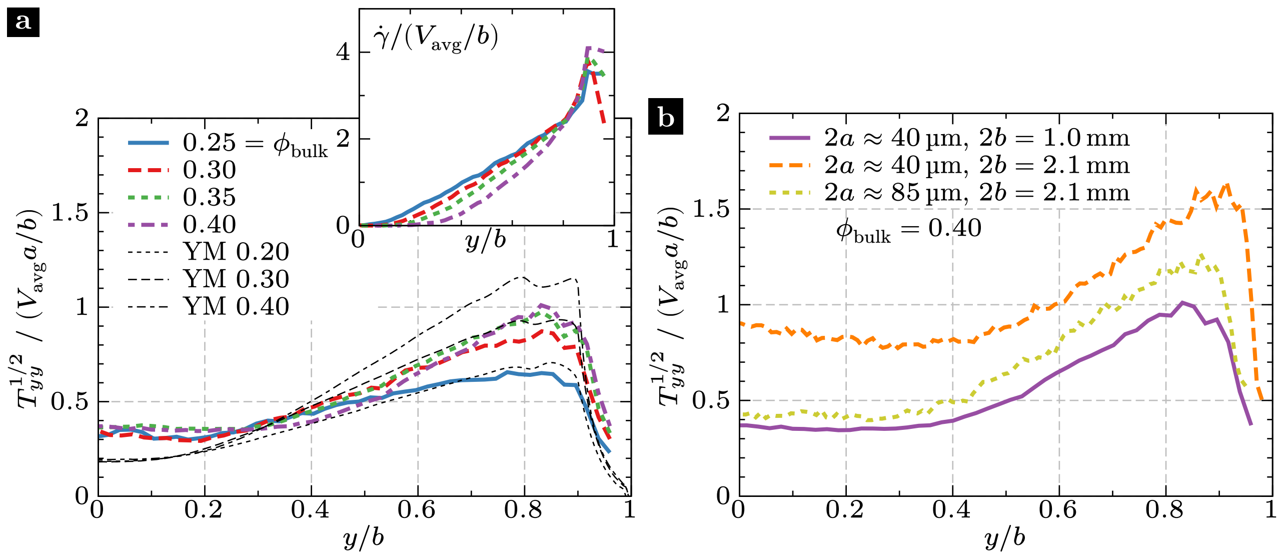

Figure 3.7: Particle velocity fluctuation profiles for experiments with different volume fractions (a) and geometric parameters (b). The black curves in (a) were taken from Yeo and Maxey (2011). Inset in (a): local shear rate across the gap for the same experiments. Same experiments as Fig. 3.5.

($2a = 40\,\mu\mathrm{m}$) used a larger proportion of dyed particles (2.5% vs 1%), possibly increasing the overlap between them and the spurious fluctuations.

3.3. Macroscopic variations after a flow reversal

In Fig. 3.4b, we saw that the ratio $V_{\mathrm{cen}}/V_{\mathrm{avg}}$ increased after a flow reversal and, then, relaxed to a steady value. In this section, and onward, we will consider variations as a function of the characteristic strain $\Delta\bar{\gamma} = \Delta t V_{\mathrm{s}}/b$ accumulated after a flow reversal, where Δt is the time elapsed since the reversal. To continue our description, we show in Fig. 3.8 the instantaneous profiles for one set of parameters[1] at two different times: when $V_{\mathrm{cen}}/V_{\mathrm{avg}}$ is maximum ($\Delta\bar{\gamma} = 0.9$ in this case), and just before the next reversal ($\Delta\bar{\gamma} \approx \bar{\gamma}_0$), when a quasi-steady state (qss) has been reached. Like in the previous section, these results come from averaging several cycles before the onset of the instability, but using instead the ensemble averages described in Sec. 2.7.3 to study the transient changes between reversals.

Shortly after reversal, the profiles of the longitudinal velocity V_x (plot a) and transverse fluctuations $T_{yy}^{1/2}$ (plot c) resemble those corresponding to a smaller bulk volume fraction ϕ_{bulk}, but the volume fraction profile (plot b) itself remains unchanged. Moreover, these effects become more noticeable as ϕ_{bulk} increases, like it was shown in Fig. 3.4b, suggesting

---

[1] With other parameters (ϕ_{bulk}, a, b) we see qualitatively similar results, but the ones chosen here correspond to experiments where a larger number of particles are tracked at each instant, and thus provide better statistical quality for the analysis of transient changes.

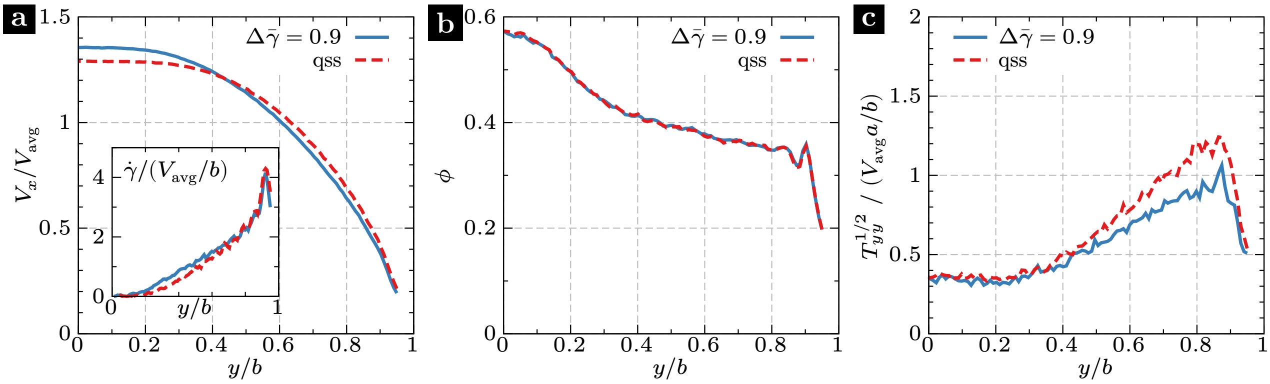

Figure 3.8: Profiles across the channel gap shortly after a flow reversal (solid blue line) and just before the next one (dashed red line) for the longitudinal velocity (a), the shear rate (a inset), volume fraction (b), and transverse fluctuations (c). In (b), both curves overlap almost perfectly. Parameters: $\phi_\mathrm{bulk} = 0.4$, $2a \approx 85\,\mu\mathrm{m}$, $2b = 2.1\,\mathrm{mm}$, $V_\mathrm{s} = 1.15\,\mathrm{mm/s}$, $\bar{\gamma}_0 = T\,V_\mathrm{s}/(2b) = 13.3$. Average of three experiments.

as an explanation changes in the average interactions between particles.

Ruling out inertial effects (see Sec. 5.4 for a justification), and knowing that the carrier fluid is Newtonian and the particles are rigid (then, there are no additional time scales from those), the only simple explanation for the above observations is a transient change in the microstructure. In Sec. 1.5, we have shown that sphere suspensions get organized into an asymmetric microstructure under shear flows as a consequence of solid contacts between the particles, and that these contacts account for a large fraction of the suspensions stresses and, particularly, of its viscosity. When the shearing direction is reversed, the microstructure has to reach a new equilibrium and, transiently, the viscosity decreases due to the loss of most contacts between particles (Blanc, Peters, and Lemaire 2011).

Modeling the suspension as a continuous fluid, we can use the classical relation for the shear stress in a laminar channel flow:

$$\eta_\mathrm{s}(y,t)\,\dot{\gamma}(y,t) = \tau_\mathrm{w}(t)\,y/b, \tag{3.2}$$

where η_s is the suspension viscosity, τ_w is the shear stress on the wall ($y = b$) which is proportional to the pressure gradient along the flow direction (see Eq. 1.24). In our experiments, the flow rate is constant between reversals and τ_w adjust itself. In uniform shear flows (i.e. with $\dot{\gamma}$ and ϕ independent of y), η_s decreases shortly after a flow reversal in a proportion that increases with the volume fraction ϕ (see Sec. 1.5.2). Extrapolating this result to our case, we can expect a decrease of the suspension viscosity all across the gap, but in a larger proportion toward the center ($y = 0$), where ϕ is larger. This makes the viscosity across the gap less inhomogeneous and, in turn, the velocity and shear rate profiles approach (but do not become) those of a uniform Newtonian fluid. This is indeed what we see in Fig. 3.8a.

Transient variations of the viscosity and the shear rate with the strain after a reversal

In a Stokesian (Re $=$ 0) non-Brownian suspension, all variations occur as a result of the cumulative effect of irreversible interactions (e.g. contacts) which happen as a strain γ is induced in the suspension. In our case, this strain varies across the gap and we may estimate its local value as

$$\gamma(y, \Delta t) = \int_0^{\Delta t} \dot{\gamma}(y, t')\ \mathrm{d}t'. \tag{3.3}$$

Here, $t' = 0$ corresponds to the reversal and γ measures the strain imposed locally on the suspension after a time Δt since the reversal. In what follows, we will compare a local estimation of the viscosity with previous measurements obtained in uniform conditions in order to determine if the latter explains the temporal variations of the velocity profile shown in Fig. 3.8a. In Sec. 3.5, we will continue this discussion with the aid of measurements related to the microstructure.

Using Eq. (3.2), we may estimate the variations of the local viscosity $\eta_\mathrm{s}(y, t)$ even though $\tau_\mathrm{w}(t)$ is not known in our experiments. From Eq. (3.3), it is clear that a given value of γ is reached much faster near the wall ($y = b$), where the shear rate is largest (see Fig. 3.8 inset), than near the center ($y = 0$). Then, assuming that the variations of τ_w are driven mainly by the local strain (remember that τ_w is the shear stress on the wall), we may consider that $\tau_\mathrm{w}(t)$ reaches a constant value $\tau_\mathrm{w}^\mathrm{qss}$ a relatively short time after the reversal, when the viscosity in regions nearer to the center ($y = 0$) is still evolving at much slower rate (again, we assume here that the main driver of these changes is the local strain γ). With this in mind, we divide Eq. (3.2) term-by-term by its qss values and obtain, after a rearrangement,

$$\frac{\eta_\mathrm{s}(y,t)}{\eta_\mathrm{s}^\mathrm{qss}(y)} = \frac{\tau_\mathrm{w}(t)}{\tau_\mathrm{w}^\mathrm{qss}} \frac{\dot{\gamma}_\mathrm{qss}(y)}{\dot{\gamma}(y,t)} \approx \frac{\dot{\gamma}_\mathrm{qss}(y)}{\dot{\gamma}(y,t)}. \tag{3.4}$$

In Fig. 3.9, we show $\dot{\gamma}_\mathrm{qss}/\dot{\gamma}$ for different positions y across the gap as functions of both the local strain γ (plot a) and the characteristic strain $\Delta\bar{\gamma} = \Delta t\, V_{\rm s}/b$ (plot b), which we may call also the *global strain*. Plot (a) is reminiscent of the measurements of $\eta_{\rm s}(\gamma)$ shown in Fig. 1.8a: in each curve, there is a discontinuous decrease at $\gamma = 0$, followed by a further decrease until a minimum is reached and, then, an asymptotic relaxation toward a steady value. Each curve here corresponds to different positions y, but also to different local volume fractions $\phi(y)$ (see the profiles in Fig. 3.8b). Then, further similarities between $\dot{\gamma}_{\rm qss}/\dot{\gamma}$ and $\eta_{\rm s}$ can be seen: the minima of both variables decrease relative to the corresponding steady value as ϕ increases, while the strain γ needed to reach these minima also decreases with ϕ.

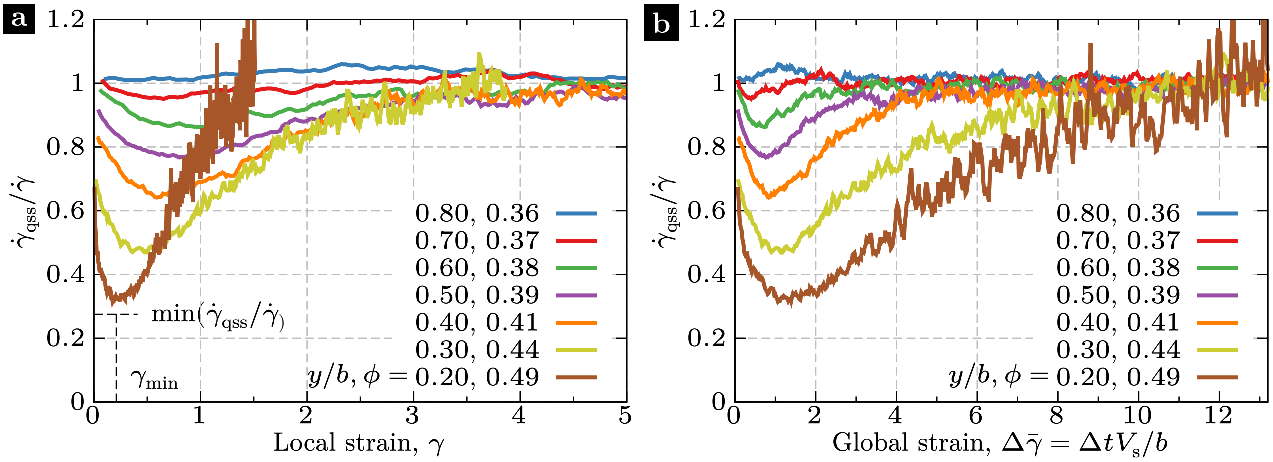

Figure 3.9: Variations of $\dot{\gamma}_{\rm qss}/\dot{\gamma}$ for different positions y across the gap as functions of the local strain γ (a) and of the global strain $\Delta\bar{\gamma}$ (b) after a flow reversal at zero strain. Same experiments as in Fig. 3.8.

In Fig. 3.10a, we show the fractions $1 - \min(\dot{\gamma}_{\rm qss}/\dot{\gamma})$ (from our measurements) and $1 - \min(\eta_{\rm s}/\eta_s^{\rm ss})$ (from previous works, $\eta_s^{\rm ss}$ is the steady-state value equivalent to our qss value) as functions of the local volume fraction ϕ. As the volume fraction increases, a larger fraction of the steady viscosity is lost shorty after a flow reversal. This is consequence of the loss of particle contacts and the fact that the largest contribution to the steady viscosity comes from these contacts (Peters et al. 2016). The trend in our estimation (red symbols) is similar to that of the measurements in uniform shear (black symbols), but our values vary more sharply with ϕ, possibly due to the unaccounted for influence of the variations of τ_w.

In Fig. 3.10b, we show the local strains $\gamma_{\rm min}$ and $\gamma_{0.5}$ need to reach, respectively, the minimum viscosity and the average between this value and the steady one. In all cases, the characteristic strains decrease with the volume fraction ϕ, with a good agreement between our estimation using the shear rate (red symbols) and previous measurements in uniform

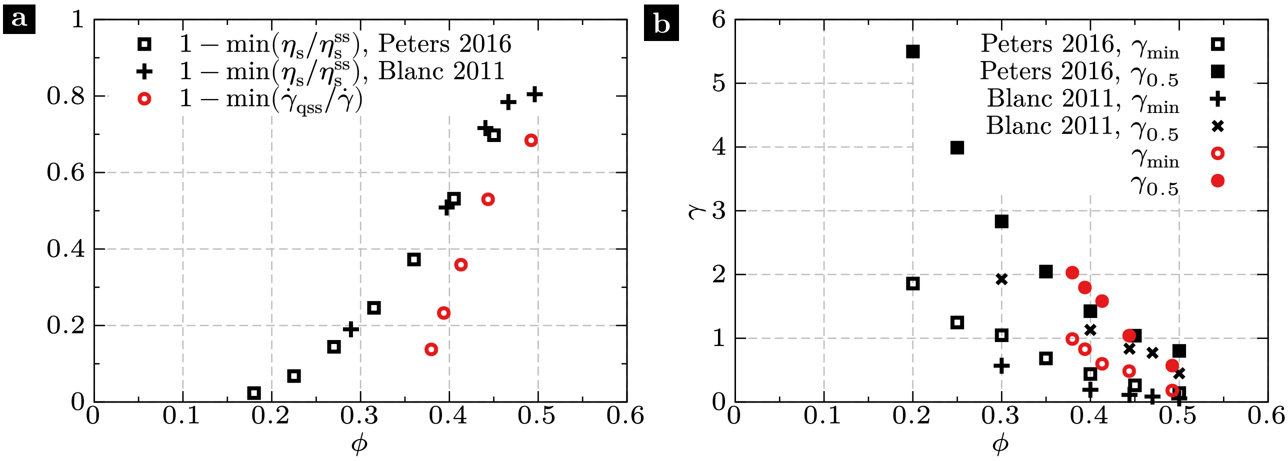

Figure 3.10: a) Fraction of the steady viscosity lost shortly after a reversal as a function of the volume fraction ϕ. b) Strain required to reach the minimum and a 50% relaxation in the viscosity after reversal. In both plots, the red symbols correspond to our estimation using the curves in Fig. 3.9a, and the black symbols reproduce values obtained in experiments by Blanc, Peters, and Lemaire (2011) and in simulations by Peters et al. (2016).

shear flows (black symbols). From the above observation, we can conclude that the local variations of the viscosity are mainly driven by the local strain felt by the suspension. Then, a quasi-steady state may be recovered locally after a strain of the order of $\gamma_{0.5}$ is accumulated at a given position y across the gap, with $\gamma_{0.5}$ decreasing with $\phi(y)$, that is, toward the center at $y = 0$.

The previous observation may be misinterpreted as suggesting that the qss is recovered sooner near $y = 0$, but this not the case: in Fig. 3.9b, we see clearly that $\dot\gamma(y,t)$ becomes $\approx \dot\gamma_{qss}(y)$ for smaller global strains $\Delta\bar\gamma$ (i.e. times) as y increases (toward the wall). A possible explanation is the fact that, although both the local shear rate $\dot\gamma$ and the local value of $\gamma_{0.5}$ increase with y, the first presents a larger relative increase and, as such, the suspension is able to reach the strain needed to reach its qss faster near the walls, even though this strain is also larger there.

Finally, comparing the curves for variations near the center ($y \leq 0.3$) to those in the middle region ($0.3 \leq y \leq 0.6$) in Fig. 3.9b, we could infer that the relaxation process does not reach its steady value before the next reversal in the first case. Although this may be true, bear in mind that the values of $\dot\gamma$ near the center are almost zero (see inset of Fig. 3.8a) and that the influence of their variations on the flow should be minimal.

3.4. Microstructure in the quasi-steady state

The results presented up to this point suggest that shearing a suspension induces an organization of the particles that depends on the flow direction, and occurs at a scale small enough so that the local volume fraction does not change. Such an organization has been observed and extensively studied in the suspension literature under the name of microstructure, mostly for steady uniform shear flows (see Sec. 1.5 for a summary).

In this section, we will characterize the microstructure in the flow-gradient plane $(x - y)$ by the means of the bidimensional pair distribution function (pdf) $g(r_x, r_y)$, calculated from the experimental data as explained in Sec. 2.7.2. The function g is proportional to the probability density of finding a particle at a position $(x + r_x, y + r_y)$ given the presence of another particle at (x, y), and it is normalized such that a value of one everywhere would result for a statistically homogeneous distribution of particles. This removes the direct influence of the local volume fraction (otherwise a larger ϕ implies a larger probability), and will allow us to concentrate in the spatial organization. The calculation is performed independently in twelve non-overlapping strips between $y = 0$ and $y = b$, each one small enough so that ϕ and $\dot{\gamma}$ do not have large variations, but large enough to accumulate sufficient statistics to obtain clean plots.[2]

3.4.1. Pair distribution in the flow-gradient plane

Figure 3.11 shows pdf's in the quasi-steady state, that is, long enough after a reversal and just before the next one and, globally, before onset of the instability. Plots (b-h) corresponds to different strips across the gap, going from the center (plot b) to the wall (plot h). Calculations were performed so that the local shear rate is always positive, that is, on the top half, particles are going from left to right with respect to a particle at the center, and the opposite is true on the bottom half, as illustrated in plot (a).

First of all, we see that large pair probabilities are clustered in a ring with $r = \sqrt{r_x^2 + r_y^2} \approx 2$ (colors red and black), corresponding to pairs in contact or near contact. This can be

---

[2] The pair distribution was calculated only on the top half of the channel ($y > 0$) due to limitations of the visualization technique: the laser light is distorted as it goes from top to bottom due to imperfections of the index matching, especially after it crosses the central band of high particle concentration. This can be seen as a vertical banding in images like those shown in Fig. 3.1.

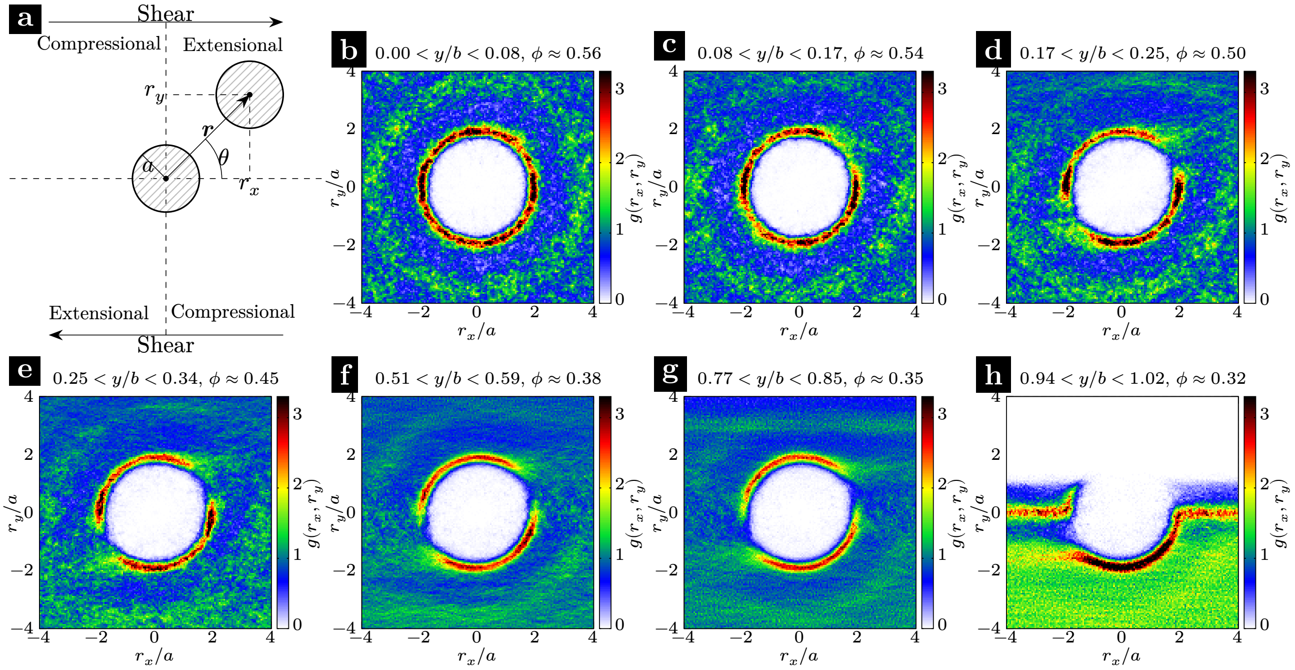

Figure 3.11: a) Diagram showing a pair of particles with the coordinates, quadrants and shear directions. b-h) Pair distribution functions calculated at different positions across the gap, during the quasi-steady state, and normalized such that a uniform distribution would have a unit value everywhere. Parameters: $\phi_{\text{bulk}} = 0.4$, $2a \approx 85\,\mu\text{m}$, $2b = 2.1\,\text{mm}$, $V_\text{s} = 1.15\,\text{mm/s}$, $\bar{\gamma}_0 = T\,V_\text{s}/(2b) = 13.3$. Average of six experiments.

understood as a consequence of the lubrication interactions (see Sec. 1.4.1) which tend to make particles stick together. A partial exception is the strip on the wall (plot h) where the probability for $r_y/a > 1$ is negligible and for $r_y = 0$ is increased. The first difference is due to the wall confinement and the fact that the strip has a width of approximately one particle. The second may be a consequence of a tendency of the particles to align on the walls and form layers, as shown in many other studies (Yeo and Maxey 2011; d'Ambrosio, Blanc, and Lemaire 2023).

Another important characteristic is the fore-aft asymmetry (i.e. with respect to inversion in the flow direction, r_x) seen in most strips, except in the center (plot b). In plots (d-g), we observe two regions relatively depleted of particles in the extensional quadrants ($r_x r_y > 0$) where the probability of pairs in near contact (red ring, $r \approx 2$) is significantly lower (green-blue colors) than in the rest of the ring (red color). As explained in Sec. 1.5.1, this is a consequence of irreversible interactions between the particles, most commonly, through solid contacts. The angular symmetry in the center (plot b) may occur because the accumulated shear between reversals is not large enough ($\gamma < 0.7$) to induce the formation of a fore-aft asymmetric structure. Observe that, in plot (c), corresponding to a strip located above the one from plot (b), we see both behaviors: on the bottom half ($r_y < 0$) the distribution is almost independent of the angle, while on the top, the depletion is present. In this case, a large inhomogeneity of both the shear rate and the volume fraction in the region covered by the strip may be a relevant factor. Also, the other intermediate strips (plots d-g) have slight top-bottom asymmetries which are possibly related to the volume fraction gradient as will be discussed later in this section.

3.4.2. Radial pair distribution

Figure 3.12a shows the radial pair distributions $g(r)$ for different strips. The curves for all the strips have a peak and global maximum at $r_{\text{peak}}/a \approx 1.9$, with widths at half-height $\Delta r_{\text{peak}}/a \approx 0.3$. As the concentration increases (toward $y = 0$), the height of the peak (i.e. the fraction of pairs nearly in contact) increases, while a second peak at $r/a \approx 3.6$ becomes more pronounced and a depletion $[g(r) < 1]$ becomes apparent in between. Figure 3.12b shows the magnitudes of the peaks versus the local volume fraction of the corresponding strip; a linear trend can be observed. It is important to note that g is already normalized by the local particle concentration ϕ, so, this variation of the peak value cannot be explained simply by the change of ϕ between the strips but, instead, it indicates differences in the spatial distribution of the pairs.

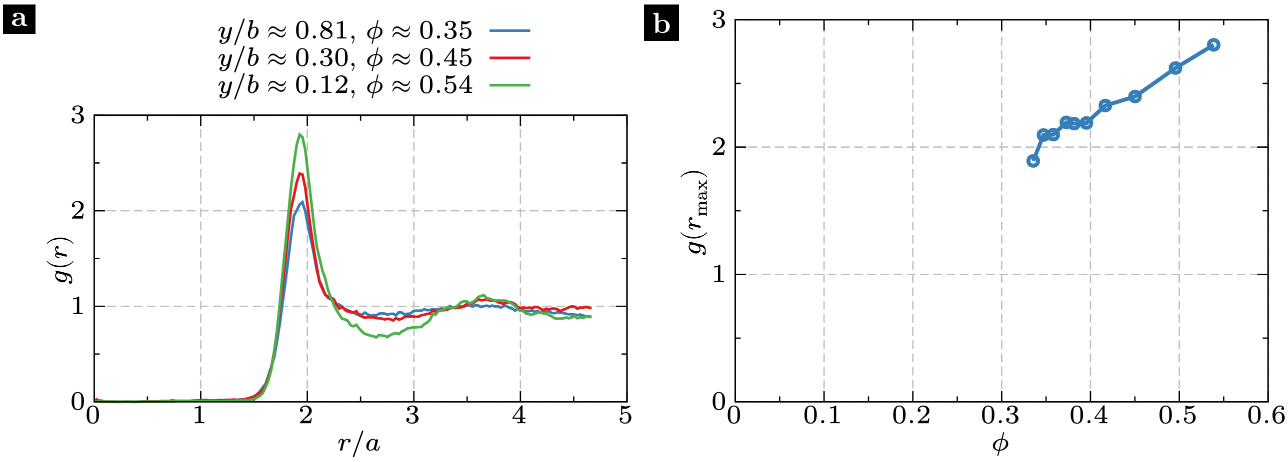

Figure 3.12: a) Radial pair distribution function calculated at different positions across the gap, during the quasi-steady state. b) Maximum value $g(r_{\text{max}})$ as a function of the local volume fraction (i.e. position across the gap). Same experiments as in Fig. 3.11.

3.4.3. Angular pair distribution

Now, we will restrict our analysis to pairs in near contact ($|r - r_{\text{peak}}| < \frac{1}{2}\Delta r_{\text{peak}}$), and look at angular pair distributions $g(\theta)$ since those contain the most important information about the microstructure. Figure 3.13 shows $g(\theta)$ for different strips across the gap. In order to account for possible effects of the gradients, we display separately the pair probabilities above ($r_y > 0$, $\theta > 0$, blue curves) and below ($r_y < 0$, $\theta < 0$, red curves) the reference particle at the origin. For comparison, we include measurements performed by Blanc, Lemaire, et al. (2013) in simple shear flows (black dashed lines). In general, all the curves display a dip around $\theta = 0.2\,\pi$, corresponding to the depletion of pairs in the extensional quadrants observed in the pdf's of Fig. 3.11. Also, a secondary and shallower dip can be seen around $\theta = 0.75\,\pi$.

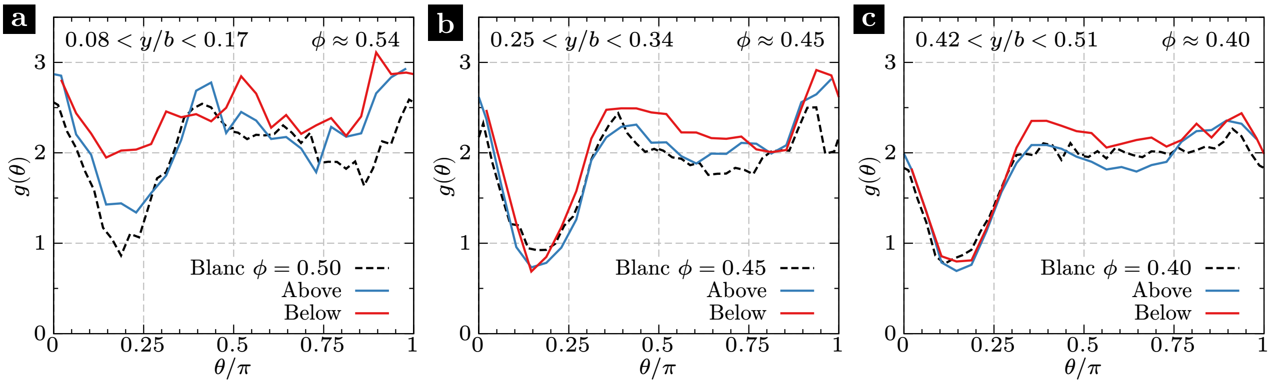

Figure 3.13: Angular distribution $g(\theta)$ of pairs nearly in contact for three different strips. The blue and red curves correspond respectively to the probabilities above ($r_y > 0$, $0 < \theta < \pi$) and below ($r_y < 0$, $-\pi < \theta < 0$) the reference particle, with the later curve displaced by π to allow for comparisons. Same experiments as in Fig. 3.11. The black dashed lines display measurements performed in simple shear flows by Blanc, Lemaire, et al. (2013).

In regions far from the center and the walls ($0.2 \lesssim y/b \lesssim 0.8$), of which plots (b-c) are representative examples, our measurements are in good agreement with those of simple-shear experiments (black dashed curves). Going into the details, the probability of pairs below (red curves) tends to be always higher than for pairs above (blue curves), specially near $\theta = 0.5\,\pi$ on the plot, that is, immediately above and below the reference particle located at the origin in Fig. 3.11. Since the particle concentration grows toward the center (below), one simple explanation is that the pair probability is modulated by the gradient of ϕ. A similar observation is made by Yeo and Maxey (2011) in relation to their pdf's obtained in simulations of channel flow.

Regarding plot (a), it corresponds to the pdf shown in Fig. 3.11c, for which the fore-aft asymmetry is clear only in the top part ($r_y > 0$) while, below ($r_y < 0$), it is approximately symmetric in the angular direction (θ). In Fig. 3.13a, we observe that $g(\theta)$ displays dips at $\theta \approx 0.2\,\pi$ for both curves (above and below the reference particle), but its minimum value is much smaller for the blue curve (above), which is also more similar to uniform-shear measurements (black dashed).

In Fig. 3.14a, a comparison between curves $g(\theta)$ for multiple strips can be seen. The values tend to increase at almost all angles as the volume fraction ϕ increases (and y/b decreases), in agreement with our observations for the peak of $g(r)$ shown in Fig. 3.12. The change is particularly large in the fore ($\theta = 0$) and aft ($\theta = \pm\pi$) positions. Furthermore, the positions of the dips near $\theta = 0.2\,\pi$ and $-0.8\,\pi$ also change with ϕ. We estimate the angular position of the dip on the right ($\theta > 0$) by a parabolic fit around the corresponding local minima of in each curve $g(\theta)$. In Fig. 3.14b, the resulting angles are plotted versus the local volume fraction (red dots), along with the results of Blanc, Lemaire, et al. (2013) for uniform volume fractions and shear rates (black circles). Again, both sets of results are in good agreement, within the experimental uncertainties. The roughly linear increase of θ_{min} with ϕ can be interpreted as a sort of rotation of the pdf's that occurs as the irreversible interactions responsible for the fore-aft asymmetry (and the dip) become more significant (Drazer et al. 2002).

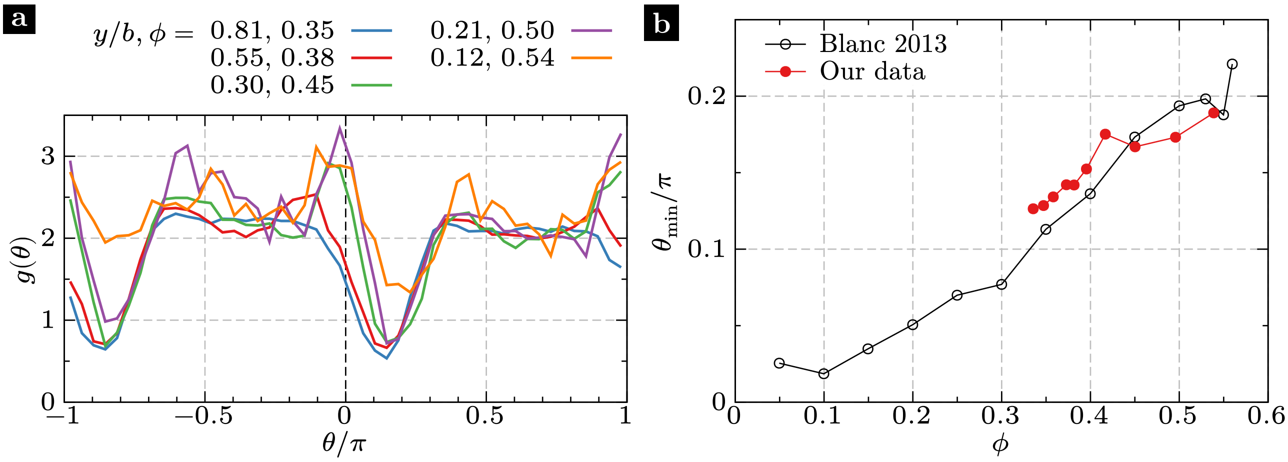

Figure 3.14: a) Angular distribution of pairs in near contact at different positions across the gap, during the quasi-steady state. b) Angle of minimum probability θ_{min} as a function of ϕ. Black symbols correspond to uniform shear measurements from the literature (Blanc, Lemaire, et al. 2013). Same experiments as in Fig. 3.11.

So far, we can conclude that away from the walls and the center, the observed quasi-steady pair distributions can be accounted almost exclusively by the local volume fraction, with a small effect from its gradient. In Sec. 1.6.2, we have seen that the equilibrium reached following the shear-induced migration results in a volume fraction ϕ increasing from the walls at $y = \pm b$ to the center at $y = 0$, and a shear rate $\dot{\gamma}$ with the opposite trend. At the scale of one particle, we observe that it is more probable to find a second particle nearly in contact toward the center ($r_y < 0$) than toward the wall ($r_y > 0$), in qualitative agreement with the gradient of ϕ. On the other hand, the gradient of $\dot{\gamma}$ results in particles that move, on average, faster above ($r_y > 0$) than below ($r_y < 0$) the reference particle, as we show in the following section.

3.4.4. Pair relative velocity distribution

The information presented up to this point comes from counting the occurrence of pairs with relative position vectors (r_x, r_y) within specific ranges of values (i.e. bins), but we can also compute statistics using the pair relative velocity (see Sec. 2.7.2). Figure. 3.15a shows the average pair relative velocity $(\delta v_x, \delta v_y)$ in the space (r_x, r_y), for one example strip (position across the gap), while plots (b) and (c) show the angular dependence of both components for pairs in near contact ($r \approx 2a$). Other strips are similar, except those on the extremes.

Broadly, the particles surrounding the reference one follow the imposed shear: they move from left to right in the top, and opposite in bottom. The magnitude of the longitudinal component δv_x is larger above than below (see plot b), in agreement with the macroscopic shear rate gradient which increases toward the wall (above). Pairs with $r \approx 2a$ will interact strongly due to geometrical restrictions (i.e. a collision) and can have transverse velocities δv_y of a magnitude comparable to δv_x (see plot c) while, outside this region and far enough from $r_y = 0$, δv_y is almost negligible (horizontal arrows in plot a).

In general, the velocity arrows in plot (a) suggest trajectories like those shown in Sec. 1.4.2: particles on the top half come from the left, move up and, then, down to pass the reference particle in the center, while a similar but horizontally-mirrored situation occurs on the bottom. There seems to be an interesting exception: particles coming from the left (right) very near the $r_y = 0$ axis would seem to go down (up), and then back to the left (right). See also that the sign changes in plot (c) near $\theta \approx 0.15\,\pi$ and $\theta \approx 0.90\,\pi$. Such trajectories are not predicted for pairs of particles interacting, so it is possible that this is a result of three or more nearby particles interacting simultaneously, a situation that may be very common at

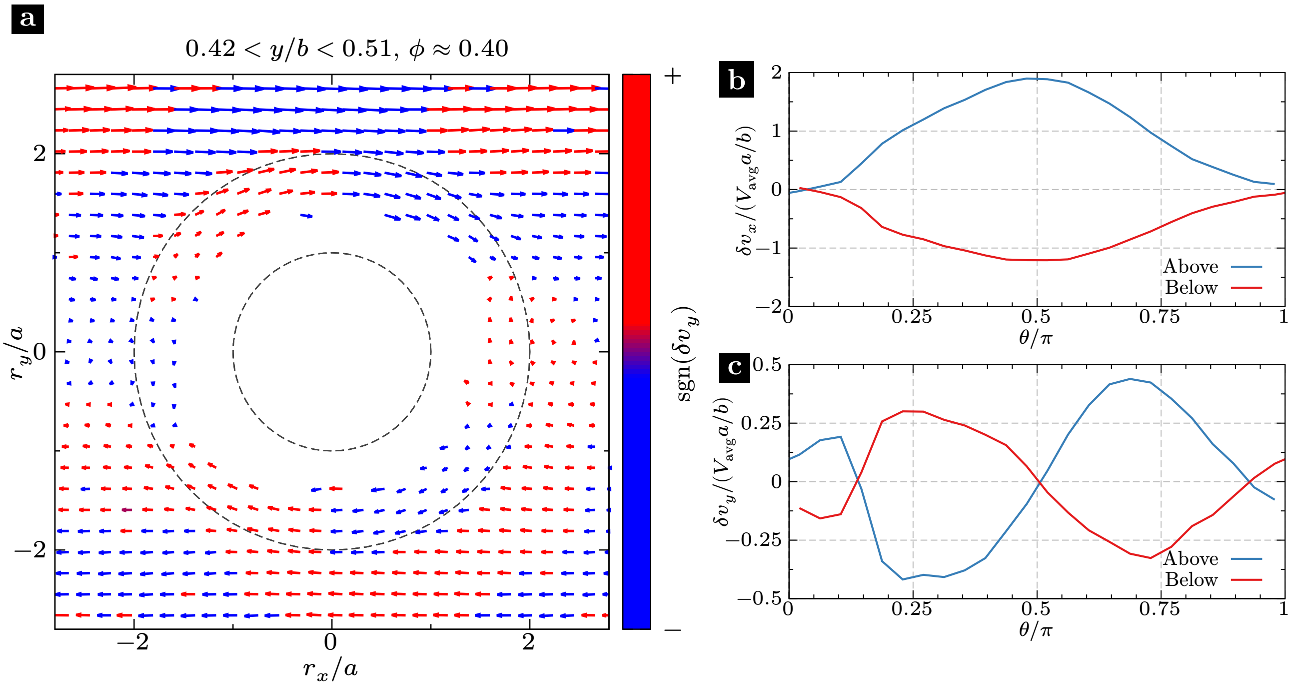

Figure 3.15: a) Particle velocity field relative to a reference particle in the center in one strip across the gap. The arrows indicate the directions and their lengths, the magnitudes. Red and blue colors indicate the sign of the transverse component, up and down, respectively. b-c) Angular dependence of both velocity components for particles in near contact ($r \approx 2a$). Shown separately are the parts of the curves that correspond to above the reference particle ($r_y > 0$, $0 < \theta < \pi$, blue) and below ($r_y < 0$, $-\pi < \theta < 0$, red), with the latter shifted by π to make the comparison between both easier.

high particle concentrations like the ones we are studying.

3.5. Transient variations of the microstructure after a flow reversal

After seeing the fore-aft asymmetry in the pair distribution functions shown in Figs. 3.11, it is clear that changing the shear direction will prompt a reorganization of the particles to reach a distribution matching the new direction. Such a reorganization has been previously characterized by its end result (the steady microstructure) or from the variations in some stress tensor components and the viscosity (see Sec. 1.5.2). Here, we will show explicitly the variations of the pair distribution after a flow reversal and across the channel thickness.

3.5.1. Pair distribution in the flow-gradient plane

Figure 3.16a shows a sequence of pair distribution functions (pdf) that we obtained before ($\gamma < 0$) and after ($\gamma > 0$) a flow reversal, inside one example strip. Each plot results from averages over shorter times than the ones shown in Fig. 3.11, making them nearly instantaneous, but with a lower spatial resolution and noisier. The first one ($\gamma = -0.05$) shows the state shortly before the reversal and is a horizontally mirrored version of the map show in Fig. 3.11e for the same strip, since here the shearing is occurring in the opposite direction. The next five plots show the situation at progressively larger accumulated strains γ after the reversal. Interestingly, the first map after reversal ($\gamma = 0.30$) does not present significant differences. It is only after enough shearing ($\gamma \geq 0.57$) that the expected reorganization becomes apparent, eventually reaching a mirrored version of the first pdf.

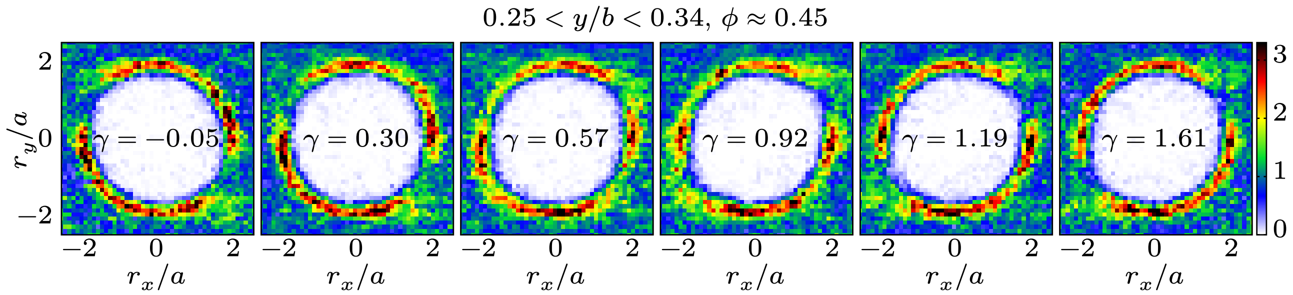

Figure 3.16: Pair distribution functions at different local strains γ before and after a flow reversal at $\gamma = 0$. Same experiments as Fig. 3.11.

3.5.2. Angular pair distribution

It is clear from the previous maps that the most important changes occur in the angular distribution of pairs in near contact (red ring close to $r \approx 2$). Figure 3.17(a-c) shows angular pair distributions for three strips and at three different moments: when the reversal occurs, midway during the reorganization, and after it became roughly steady. Here, the mirroring in the r_x direction seen in Fig. 3.16 corresponds to transformation into a π-complementary distribution, that is, depletions at $\theta \approx 0.8\,\pi$ and $\theta \approx -0.2\,\pi$ change to depletions at $\theta \approx 0.2\,\pi$ and $\theta \approx -0.8\,\pi$, respectively. Notice that midway in this process (middle plot of each row), both sets of depletions are present and the distribution is roughly symmetric with respect to rotations by $\pi/2$.

In order to capture a more detailed picture of the reorganization process, we show in Fig. 3.17(d-f) color maps representing the evolution of $g(\theta)$ with the accumulated shear γ (horizontal axis). The same color scale as for the pdf's is used here, where blue represents a small probability and red, a high one, with green and yellow for intermediate values. Like in Fig. 3.16, it is clear that, for small enough deformations, the distributions do not change

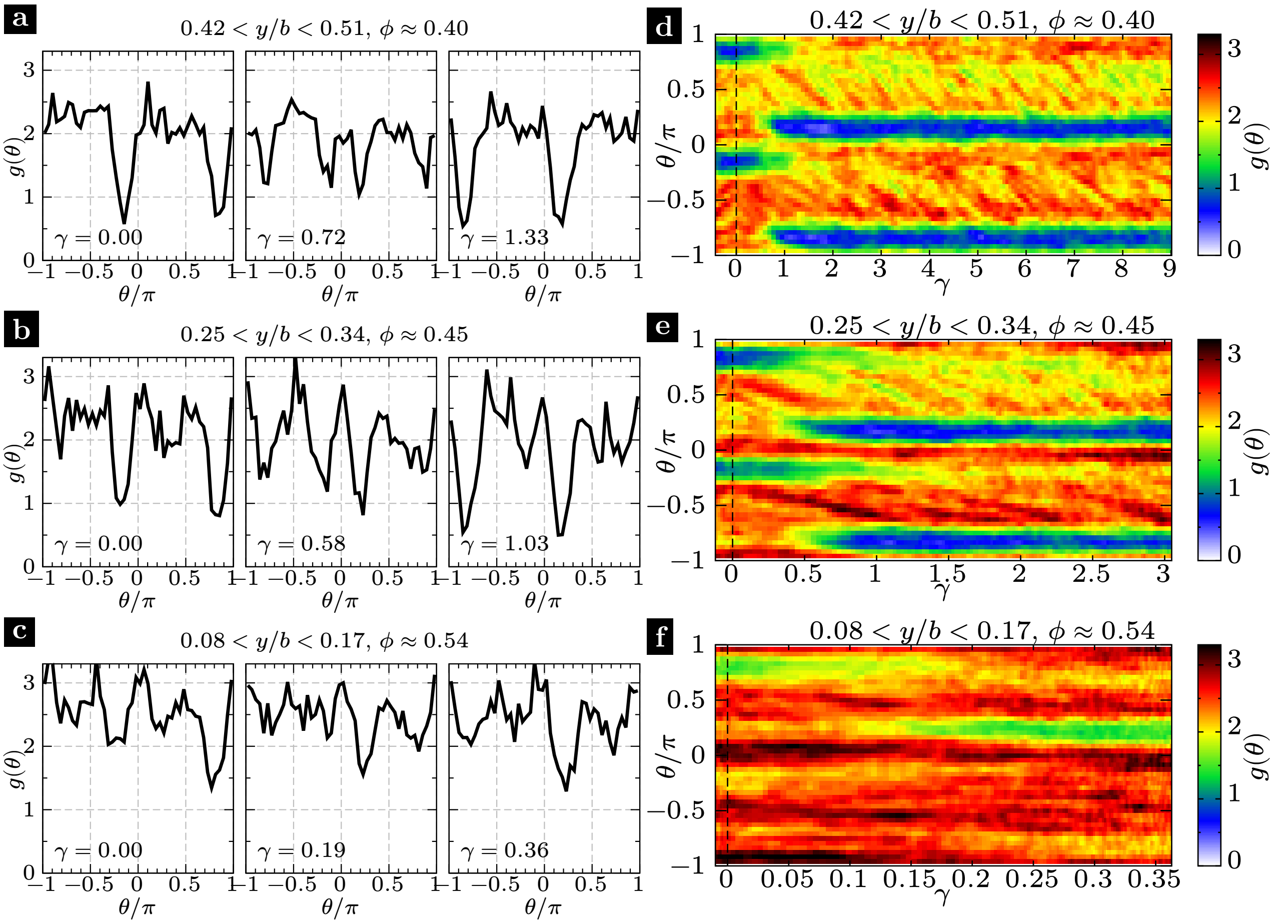

Figure 3.17: a-c) Angular pair distribution for particle pairs in near contact ($r \approx 2a$) at three different times (columns) before and after a flow reversal, and in three different strips across the channel gap (rows). d-f) Color maps showing the angular pair distribution $g(\theta)$ as a function of the accumulated shear γ (horizontal axis). Each row corresponds to the same strips as in (a-c).

significantly and, then, a marked transition starts with four simultaneous angles of depletion (colors blue and green).

Plot (f) is a little different with the bottom part ($\theta < 0$) displaying much softer variations than the top part ($\theta > 0$). This is probably a result of the inhomogeneous shear rate since this strip is in an intermediate position between the center, where the accumulated shear may be too small to form the asymmetric structure, and the rest of the channel, where it does form. Finally, we observe that the transition requires less shearing as the local volume fraction ϕ increases (top to bottom), but since each plot shows the same time lapse (one half oscillation), it is clear that the transition is faster toward the wall (bottom to top) due to a sharp increase of the local shear rate.

3.5.3. Temporal evolution of the fore-aft asymmetry

In order to study quantitatively the characteristic times (and deformations) of the reorganization process observed above, we use the parameter

$$A_{xy} = \left\langle \frac{r_x r_y}{r_x^2 + r_y^2} \right\rangle_{\text{pairs}} = \frac{1}{2} \left\langle \sin(2\theta) \right\rangle_{\text{pairs}}, \tag{3.5}$$

where the averaging is done over the pairs in near contact, using the same criterion as for the angular distributions ($|r - r_{\text{peak}}| < \frac{1}{2}\Delta r_{\text{peak}}$). This parameter is one component of the bidimensional projection of the tensor used by J. Gillissen and H. Wilson (2018) to model the suspension microstructure and its evolution, but, for our current purposes, it is a variable that quantifies the anisotropy seen in the angular distributions. Specifically, after reversal, it displays a smooth transition from positive to negative values of equal magnitude, as shown in Fig. 3.18.

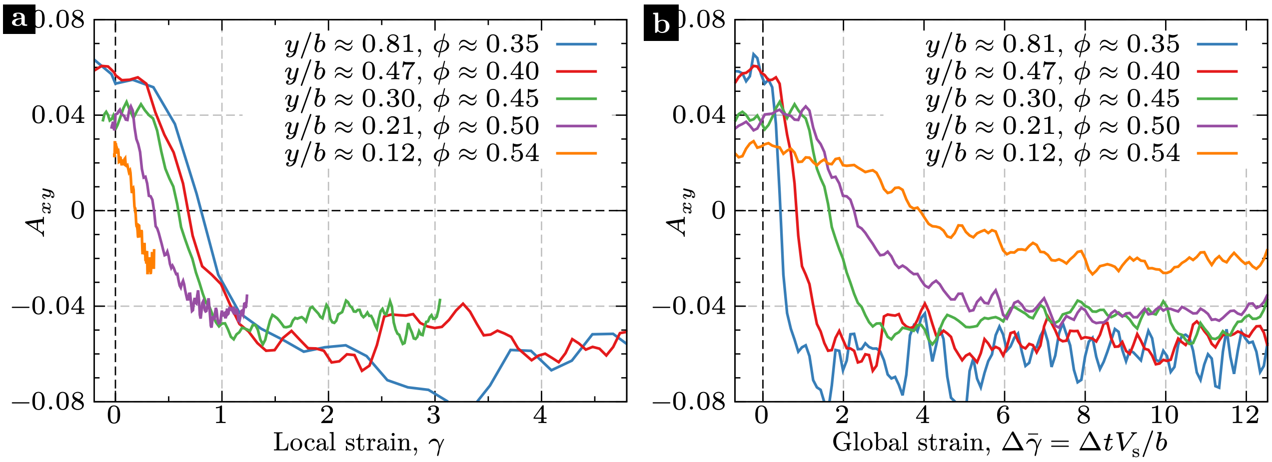

Figure 3.18: Microstructure anisotropy parameter A_{xy} as a function of local (a) and global (b) strains accumulated after a reversal, for different strips across the channel thickness (y direction).

Following the discussion started in Sec. 3.3 for the transient variations of the viscosity, we plot the variations of A_{xy} for different position y across the gap as functions of both the local strain (defined in Eq. 3.3, Fig. 3.18a) and the global strain $\Delta\bar{\gamma} = \Delta t\, V_s/b$ ($\Delta t = 0$ at reversal, Fig. 3.18b) accumulated after a reversal (at zero for both strains). The transition of A_{xy} from positive to negative values tracks the changes seen in Fig. 3.17 from angular pair distributions with minima at $\theta/\pi \approx -0.2$ and 0.8 to ones with minima at -0.8 and 0.2. As functions of $\bar{\gamma}$ (plot b), these transitions occur faster toward the wall ($y = b$), where $\dot{\gamma}$ is maximum, while, as functions of γ (plot a), they are “faster” toward the center ($y = 0$), where ϕ is maximum.

Those are the same trends observed for $\dot{\gamma}_{\text{qss}}(y)/\dot{\gamma}(y,t)$ in Fig. 3.9, emphasizing the connection between the microstructure and macroscopic variables like the shear rate and the viscosity.

In order to do a more direct comparison, we choose one representative strip and show in Fig. 3.19a both $A_{xy}/A_{xy}^{\text{qss}}$ (red) and $\dot{\gamma}_{\text{qss}}/\dot{\gamma}$ (blue) as functions of γ. Here, A_{xy}^{qss} is the value reached by A_{xy} just before the next reversal (toward the right side of the plot) and, since it is negative, the curve looks inverted with respect to those shown in Fig. 3.18a. Observe that A_{xy} reaches a value similar to its qss one with a strain $\gamma \sim 1$, while $1/\dot{\gamma}$ is still far from its qss value near that strain. Since $1/\dot{\gamma}$ is a proxy for the viscosity here, a possible interpretation is that the viscosity fully recovers its steady value only when enough contacts form between nearby particles, introducing additional forces between them, while A_{xy} changes with the reorganization of pairs without taking into account whether they are touching or just nearby, something which is very difficult to determine from just visual observations like ours.

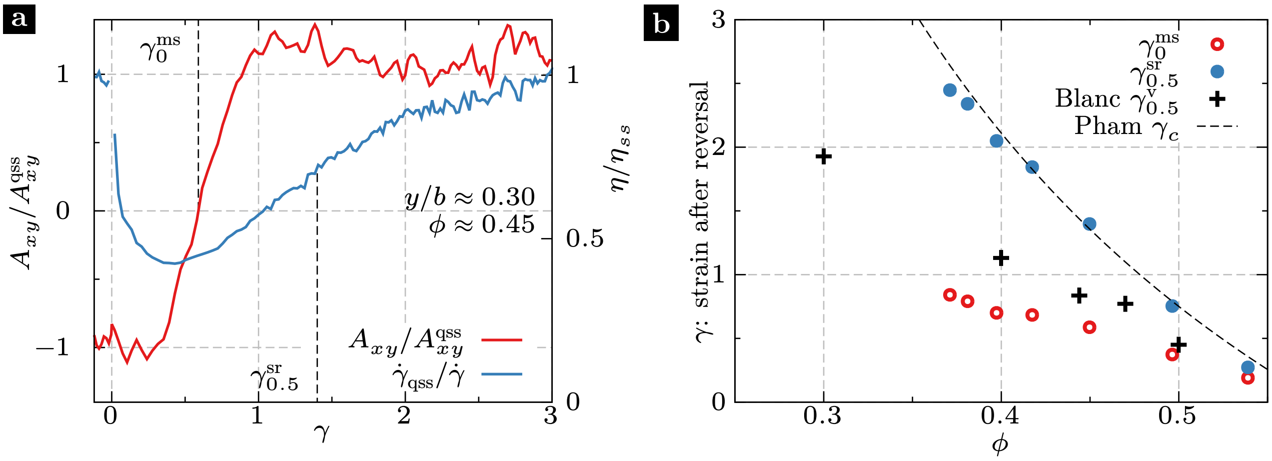

Figure 3.19: a) Comparison of A_{xy} and $1/\dot{\gamma}$ as functions of the strain γ after a flow reversal (at $\gamma = 0$), both normalized by their quasi-steady-state (qss) values, for one representative strip. b) Characteristic strains γ_0^{ms} and $\gamma_{0.5}^{\text{sr}}$ versus the local volume fraction ϕ, obtained from curves like those of (a). Black crosses: characteristic strain obtained from viscosity measurements in uniform shear flows, from Blanc, Peters, and Lemaire (2011). Black dashed line: Eq. (1.27) with $\epsilon/a = 0.002$, from Pham, Butler, and Metzger (2016).

From the previous curves we calculate two characteristic strains: γ_0^{ms} corresponding to $A_{xy} = 0$ and $\gamma_{0.5}^{\text{sr}}$ corresponding to $1/\dot{\gamma} = (1/\dot{\gamma}_{\text{max}} + 1/\dot{\gamma}_{\text{qss}})/2$ (50% between the minimum and qss value of $1/\dot{\gamma}$). Figure 3.19b displays both characteristic strains, along with the strain $\gamma_{0.5}^{\text{v}}$ obtained from viscosity measurements in simple shear flows (Blanc, Peters, and Lemaire 2011). These three characteristic strains mark approximate midpoints in the temporal evolution of the corresponding parameter measured after reversal. In the figure, we observe a decreasing trend with the local volume fraction ϕ for the three sets of points.

In Sec. 3.3, we already discussed $\gamma_{0.5}^{\mathrm{sr}}$ and $\gamma_{0.5}^{\mathrm{v}}$ (without the superscripts), observing that the differences between them may steem from differences in physical properties of the particles that affect their interactions, like their surface roughness. That said, our previous observation that A_{xy} relaxes faster toward its qss value as a function of the strain still stands here: γ_0^{ms} is always smaller than the other two characteristic strains.

As a final comparison, we show with a black dashed line the critical strain amplitude γ_{c} from Eq. (1.27) (taken from Pham, Butler, and Metzger 2016). This strain is different to the others since it is obtained from experiments changing the oscillation amplitude, and it marks a transition from reversible to irreversible particle trajectories (see Sec. 1.7.1). The black line matches our values of $\gamma_{0.5}^{\mathrm{sr}}$, though this may be a coincidence. The important conclusion here is that for strains of the order of one after a flow reversal, and decreasing with the local volume fraction, the suspension undergoes a reorganization with clear effects on the microstructure, the viscosity, the velocity profile, and the trajectories of the particles.

3.5.4. Non-uniformity of the variations after a flow reversal

Up to this point, we have shown that, locally, the microstructure behaves more or less as expected, but in non-uniform shear flows like ours, this expected behavior may have some interesting consequences. Figure 3.20 shows several profiles of A_{xy} across the channel gap, each corresponding to a different global strain $\Delta\bar{\gamma} = \Delta t\, V_{\mathrm{s}}/b$ before and after a flow reversal. Just before the reversal ($\Delta\bar{\gamma} = -0.65$, blue), A_{xy} has positive values everywhere and, after the reversal at $\Delta\bar{\gamma} = 0$, it evolves into a profile roughly symmetrical with respect to the initial one ($\Delta\bar{\gamma} = 12$, orange). In between, we see that the transition is inhomogeneous, progressing faster near the wall ($y/b = 1$) than near the center ($y/b = 0$). This is a consequence of the inhomogeneous shear rate, as previously discussed. Now, remember that the normal stress σ_{yy} across the gap should be at equilibrium (i.e. uniform) in a fully migrated suspension under steady flow (see Eq. 1.26 in Sec. 1.6.2). If we assume this to be the case before a reversal, then, after it, the inhomogeneous variations of the microstructure should lead to a transient non-equilibrium situation which might explain some of the unexpected behavior seen in oscillating suspensions, like the inverse migration (Butler, Majors, and Bonnecaze 1999), or the instability seen in our experiments after the quasi-steady state discussed in the

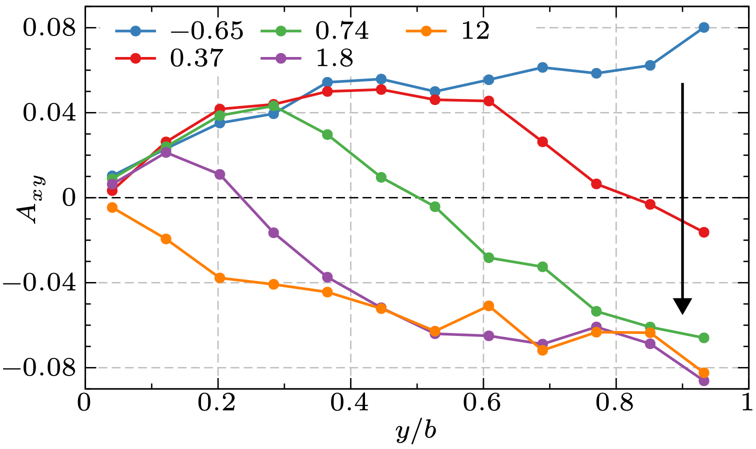

Figure 3.20: Microstructure anisotropy parameter A_{xy} across the channel thickness, at different global strains $\Delta\bar{\gamma} = \Delta t\, V_{\mathrm{s}}/b$ after a flow reversal (the numbers shown in the legend).

present Chapter.

In the following two chapters, we will characterize the latter instability and its dependence the experimental parameters. Finally, in Chapter 6, we will use the present approach and results to discuss the kind of mechanism which may account for the unstable behavior.

Chapter 4

Instability of oscillatory channel flows of suspensions for different oscillation amplitudes

In Sec. 3.1, we have shown that the evolution of the suspension in our experiments can be roughly divided in two stages. During the first oscillations, the flow is mostly laminar with a macroscopic particle distribution that varies only across the channel gap (y direction). In this stage, we observe two well-known suspension phenomena: the shear-induced migration and the formation of an anisotropic microstructure due to the shearing flow. Afterwards, a velocity component transversal to the main flow direction (x) increases, corresponding to a secondary flow which deforms the previous particle distribution into a wave-like pattern periodic along the x direction (see the images in Fig. 3.1). The smooth growth of this additional flow and its spatial periodicity prompts us to consider it as a flow instability. Within this framework, we will devote the present chapter to describe precisely this instability and its consequences in experiments using the 85 µm particles in the 2 mm-thick channel and with bulk particle volume fraction of 0.4, since those experiments provide the most informative description of the particle distribution.

As for the influence of experimental parameters, we focus here only on variations in oscillation amplitude, delaying a comprehensive analysis of the influence of volume fraction, particle size, and channel dimensions to the next chapter.

4.1. Particle distribution and secondary velocity field in the flow-gradient plane

In the previous chapters, we studied only variations across the gap direction (y), but here we need to consider arbitrary spatial variations of the volume fraction and the velocity field in the flow-gradient plane (xy). We do this by dividing this plane into a regular grid (32×15) and estimating variables of interest inside each subspace, as described in Sec. 2.7.1. The size of the grid is a compromise between having enough spatial resolution to describe the patterns of interest and reducing unwanted fluctuations (noise). Here, we present results from one example experiment which is representative of our observations when the oscillation strain amplitude $\bar{\gamma}_0 = T\,V_\mathrm{s}/(2b)$ is large enough. Later, we will show that as the amplitude decreases, some characteristics change and eventually the instability disappears.

The color maps of Fig. 4.1 display the particle volume fraction ϕ as a function of x and y, and at different global strains $\bar{\gamma} = tV_\mathrm{s}/b$ accumulated since the begin of the experiments at $t = 0$, in all cases, just before flow reversals. These plots illustrate the progression in the state of the suspension. Comparing plots (a) and (b), we see that the particles have become more concentrated in the central band around $y/b = 0$ in the latter plot, clearly as a result of the shear-induced migration, but the general distribution remains more or less invariant with x. Afterwards, the central band of high ϕ starts to become distorted into a wave-like pattern periodic along x. Plot (c) shows the state midway in this process while, in plot (d), we see it at its maximum amplitude (by a criterion to be made clear later). Later, in plots (e) and (f), the particles are less concentrated in a band, but the spatial periodicity of the pattern remains.

In order to track the deformation of the high concentration band seen in Fig. 4.1, we estimated the coordinate $y_{\phi\mathrm{max}}(x,t)$ where ϕ is maximum inside each column x of the maps $\phi(x,y,t)$. Due to the noisy nature of the data, we estimate each value from a third-order polynomial fitted to the values of ϕ in each column x at a given time t. The resulting curve $y_{\phi\mathrm{max}}(x,t)$ is shown over the maps of Fig. 4.1 using black lines. Later, we will use this information to track the evolution of the instability in time.

The previously-discussed pattern in ϕ influences the particle velocity field (V_x, V_y) mea-

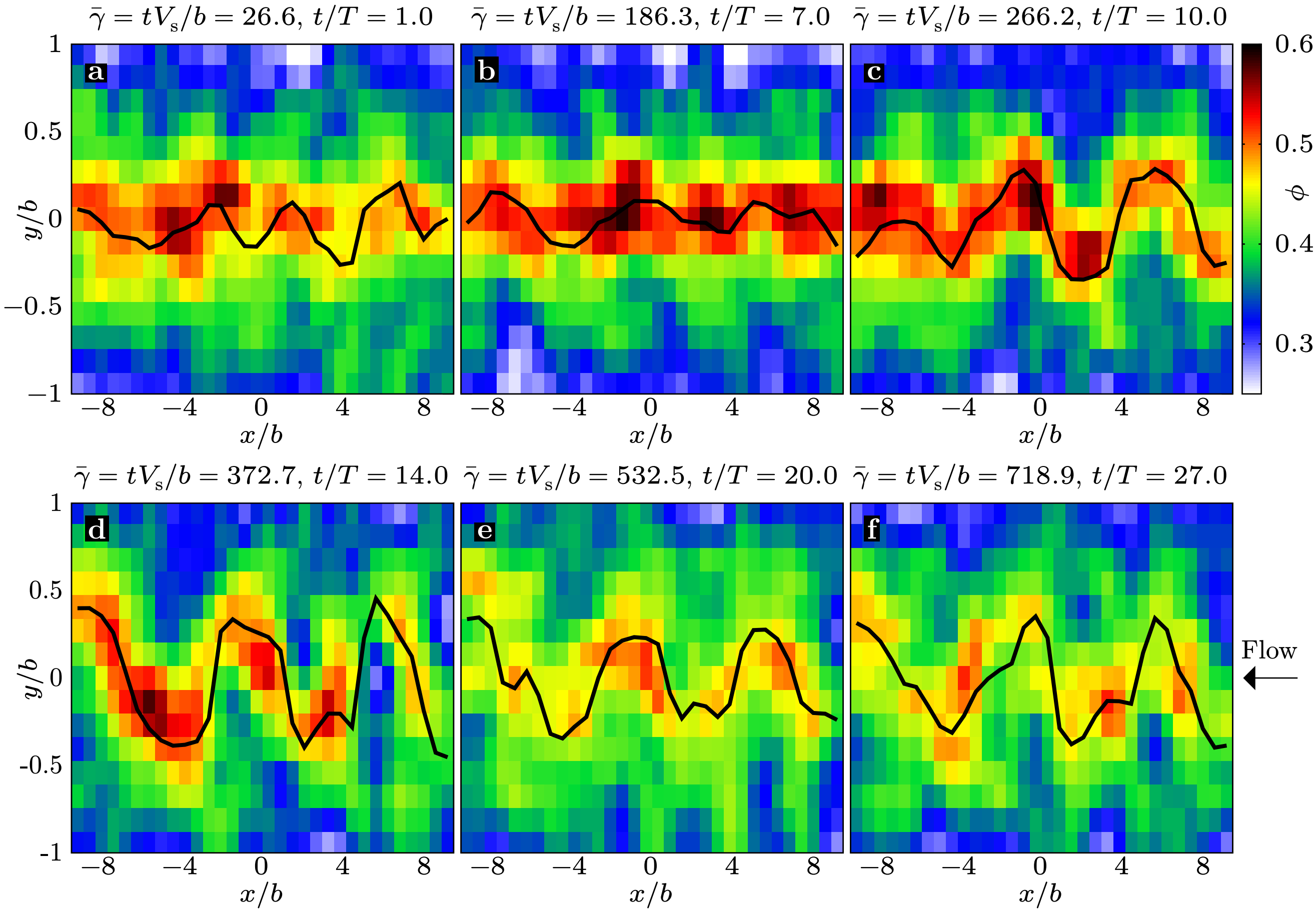

Figure 4.1: Particle volume fraction ϕ in the observation plane (xy) at different times t just before a flow reversal, in an example experiment. Main flow toward the left. The colors indicate ϕ values. The black lines correspond to the curves $y_{\phi\max}(x, t)$, for each t. Parameters: $\phi_{\text{bulk}} = 0.4$, $2a \approx 85\,\mu\text{m}$, $2b = 2.1\,\text{mm}$, $V_s = 1.15\,\text{mm/s}$, $\bar{\gamma}_0 = T\,V_s/(2b) = 13.3$.

sured simultaneously and, in particular, it induces an x-periodic component with the same wavelength. Globally, the velocity field is still dominated by the Poiseuille-like flow found before the onset of the instability (see Sec. 3.2), and we may decompose it as[1]

$$\begin{aligned} V_x(x, y, t) &= \overline{V}_x(y, t) + \delta V_x(x, y, t), \\ V_y(x, y, t) &= 0 \qquad\qquad + \delta V_y(x, y, t). \end{aligned} \tag{4.1}$$

On the right hand side of both equations, the first term is the dominant laminar flow which is characterized by velocity profiles like those shown in Fig. 3.5, while the second term corresponds to any secondary flow present. In Sec. 3.1, we have already shown that, with the

---

[1] Here we assume that the flow is roughly symmetrical against translations in the z direction (normal to the observed plane). Then, we neglect any dependence with z and consider $V_z \approx 0$. This is based on the fact that the stripes observed by Roht et al. 2018 exhibit this symmetry over the width of the cell, except near the side walls ($z = \pm W/2$). Moreover, the observation plane is positioned in the center of the width ($z = 0$), where the secondary flows proposed by Ramachandran and D. T. Leighton 2008 are null.

instability, $V_y(x,0,t)$ becomes x-periodic like ϕ and averages to zero. The same characteristics can be expected of δV_x, if we assume that the flow out of the plane is negligible ($V_z \approx 0$) and the incompressibility of the fluid ($\nabla \cdot \boldsymbol{V} = 0$). Then, we may estimate $\overline{V}_x$ as the average of V_x along x, and separate the secondary flow in our measurements.

Figure 4.2a shows the secondary velocity field $(\delta V_x, V_y)$ corresponding to Fig. 4.1d, when the magnitude of the secondary flow and the deformation of the central band are both maximum. The plot clearly captures a cross-section of recirculation rolls, similar to those observed in other hydrodynamic instabilities. The transverse velocity V_y reaches its maxima near $y/b = 0$ and is negligible near the walls ($y/b = \pm 1$), while the opposite is true for δV_x. Near the center, the particles alternate between upward and downward motions, with stagnation zones in between, where the velocity perturbation is zero. Near the walls, δV_x also alternates signs but is out of phase with V_y. The wavelength is roughly $7\,b$. On top of the velocity field, we also display the curve $y_{\phi\mathrm{max}}(x,t)$ marking where the volume fraction ϕ is maximum. Note that this curve crosses $y/b = 0$ where $V_y(x,0)$ is approximately maximum. Later, we will see that this changes for smaller oscillation amplitudes.

Figure 4.2b shows the transverse velocity along the gap center, $V_{y,\mathrm{cen}}(x,t) = V_y(x,0,t)$, and the longitudinal perturbation near the wall, $\delta V_{x,\mathrm{nw}}(x,t) = \delta V_x(x, 0.8b, t)$. As expected, both curves are out of phase by a quarter of wavelength. We observe that the amplitude of $\delta V_{x,\mathrm{nw}}$ is roughly twice that of $V_{y,\mathrm{cen}}$. Comparing with $y_{\phi\mathrm{max}}(x,t)$, we see that it crosses zero at roughly the same positions x as $\delta V_{x,\mathrm{nw}}$, and where $|V_{y,\mathrm{cen}}|$ is maximum. We will consider the implications of this fact further in this chapter.

The fields presented up to this point (ϕ, δV_x, V_y) correspond to times after a significant strain $\bar{\gamma}$ has accumulated since the last flow reversal. Thus, the state of the suspension can be considered to be momentarily in a sort of quasi-steady state. Between reversals, the perturbations in ϕ and $\boldsymbol{V}$ are dragged by the main flow, although at a longitudinal velocity slightly slower, and when the pump reverses is motion, all components of the velocity field (main and secondary) change sign.

These two facts can be seen in the spatiotemporal diagram of Fig. 4.3. There, $V_{y,\mathrm{cen}}(x,t)$ is represented with colors (blue, negative; red, positive) in a plot where the time is on the horizontal axis, and the longitudinal coordinate, on the vertical one. Initially (on the left),

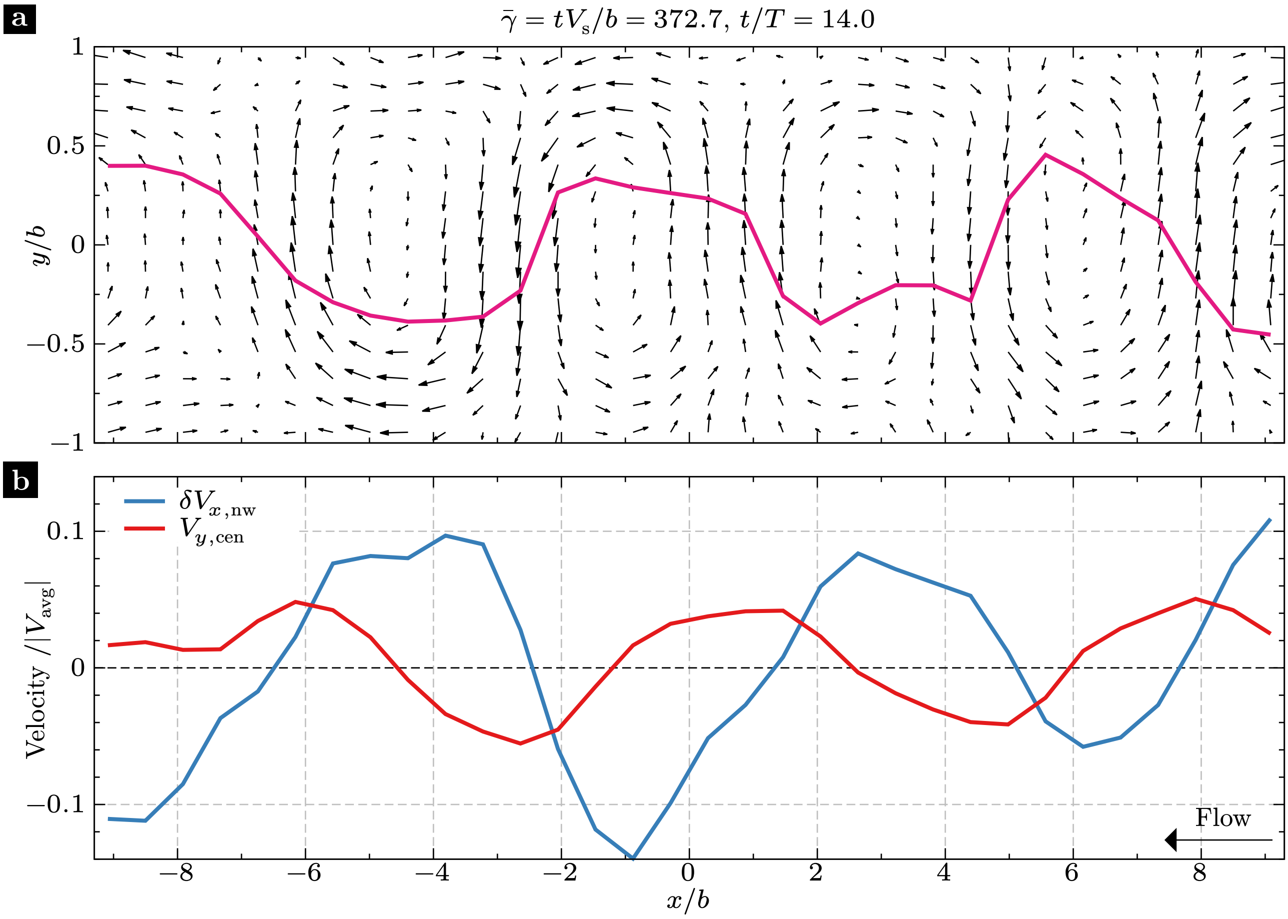

Figure 4.2: a) Secondary velocity field $(\delta V_x, V_y)$ in the observation plane (xy). The black arrows indicate the direction and relative magnitude of field at each position. The magenta curve denotes $y_{\phi\max}(x,t)$ versus x and marks the positions where the volume fraction is maximum along x. Notice that this representation is compressed horizontally with respect to the images shown previously, enlarging the transverse variations. b) $V_y(x,0)$ and $V_x(x,0.8b)$ versus x. Both are normalized by the absolute value of the instantaneous average velocity V_{avg} (average of $\overline{V}_x$, $\approx V_s$). Both plots correspond to the volume fraction field shown in Fig. 4.1d, when the instability is fully developed, and at a time just before a flow reversal.

the values are smaller (white or light colors) and no structure is discernible. Around $\bar{\gamma} = 250$, the structure corresponding to Fig. 4.2 starts to appear as a pattern periodic in x and $\bar{\gamma}$. The herringbone form of the pattern means that the curves seen in Fig. 4.2b move to the right and then, to the left, following the main flow direction. At the times when the flow direction changes (integer and half-integer values of t/T on the top), $V_{y,\mathrm{cen}}$ changes sign, i.e. colors blue and red exchange.

It is important to note that the particle fluxes induced during both halves of an oscillation cannot compensate each other, otherwise the particles would not rearrange irreversibly, like we see with the initial migration and later, with the deformation produced by the instability. We will postpone further analysis of the variations between reversals until Sec. 4.3, and

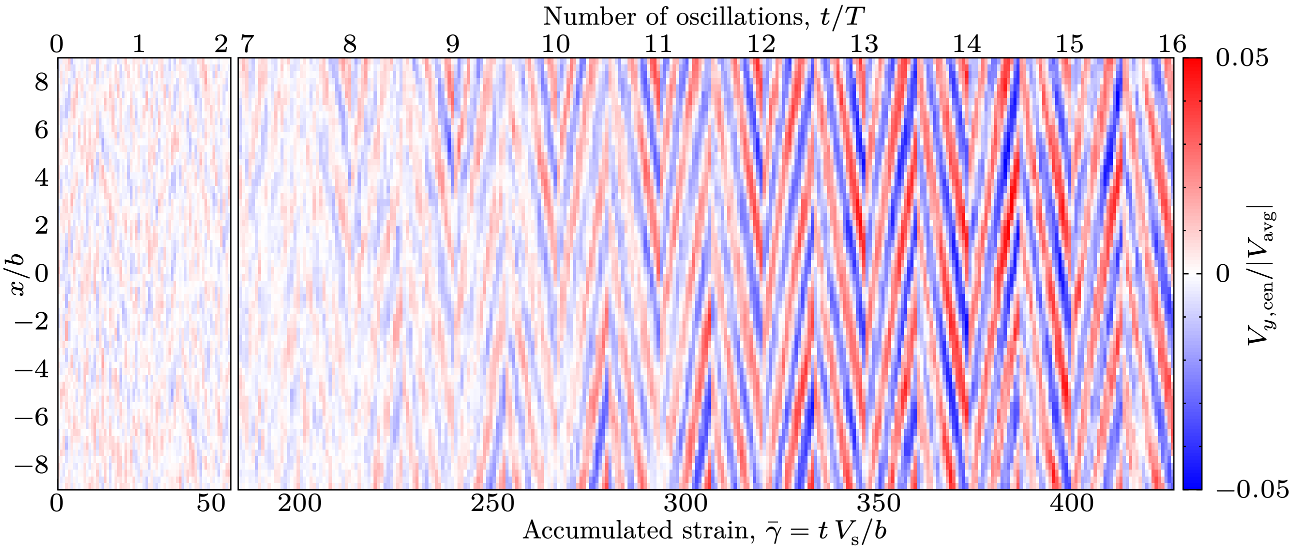

Figure 4.3: Spatiotemporal diagram of $V_{y,\mathrm{cen}}(x,t)$ normalized by $|V_\mathrm{avg}|$. The horizontal direction corresponds to time t, shown as an accumulated strain $\bar{\gamma} = t\,V_b/b$ below, and as the number of oscillations t/T, above. The vertical direction marks the coordinate x/b. The color blue indicates the negative values and, red, positive ones. The plot is divided two parts, with the first two oscillations on the left, and oscillations 7 through 15, on the right. Same experiment as in Fig. 4.1.

concentrate now in growth of the instability across multiple oscillations.

4.2. Instability growth and long-term variations

In this section, we quantify the temporal variations of the volume fraction ϕ and the secondary flow $(\delta V_x, V_y)$ fields. For this purpose, we calculate instantaneous quantities that capture the state of the suspension and average them in time to obtain one value per oscillation cycle, as explained in Sec. 2.7.3. The temporal averages are include only the times corresponding to the quasi-steady state to exclude the transient variations occuring after each reversal, as explained in Sec. 3.2. The transient variations between reversals will be reported in Sec. 4.3. In Sec. 4.4.1, we will consider smaller oscillation amplitudes with strains shorter than those needed to reach the qss, in this case, we perform the temporal averages during a strain $\bar{\gamma} = 1$ just before each reversal.

Figure 4.4a displays as function of the accumulated strain $\bar{\gamma} = tV_s/b$ the average volume fraction $\phi_\mathrm{avg}(t) = \langle \phi(x,y,t) \rangle_{x,y}$, the average in the center line $\phi_\mathrm{cen}(t) = \langle \phi(x,0,t) \rangle_x$, and the average of the volume fraction in the positions tracked by the curve $y_{\phi\mathrm{max}}(x,t)$ (see Fig. 4.1), $\phi_\mathrm{max}(t) = \langle \phi(x, y_{\phi\mathrm{max}}(x,t), t) \rangle_x$. Observe that ϕ_cen initially increases as particles migrate toward the gap center, and then decreases as they move out of it due to the secondary flow.

One may wonder whether the decrease is just a consequence of the way the averaging is performed, and the central band of high particle concentration (dark red in Fig. 4.1) is just deformed without a reduction in its concentration. From Fig. 4.1(c-e), it is clear that this may be the case at the start of the deformation (plot c) but, eventually, the suspension reaches a more spread out particle distribution (plot e). This observation is reflected in Fig. 4.4a: the curve $\phi_{\max}(t)$ remains at a value near its maximum for a longer time than $\phi_{\text{cen}}(t)$, but eventually decreases too.

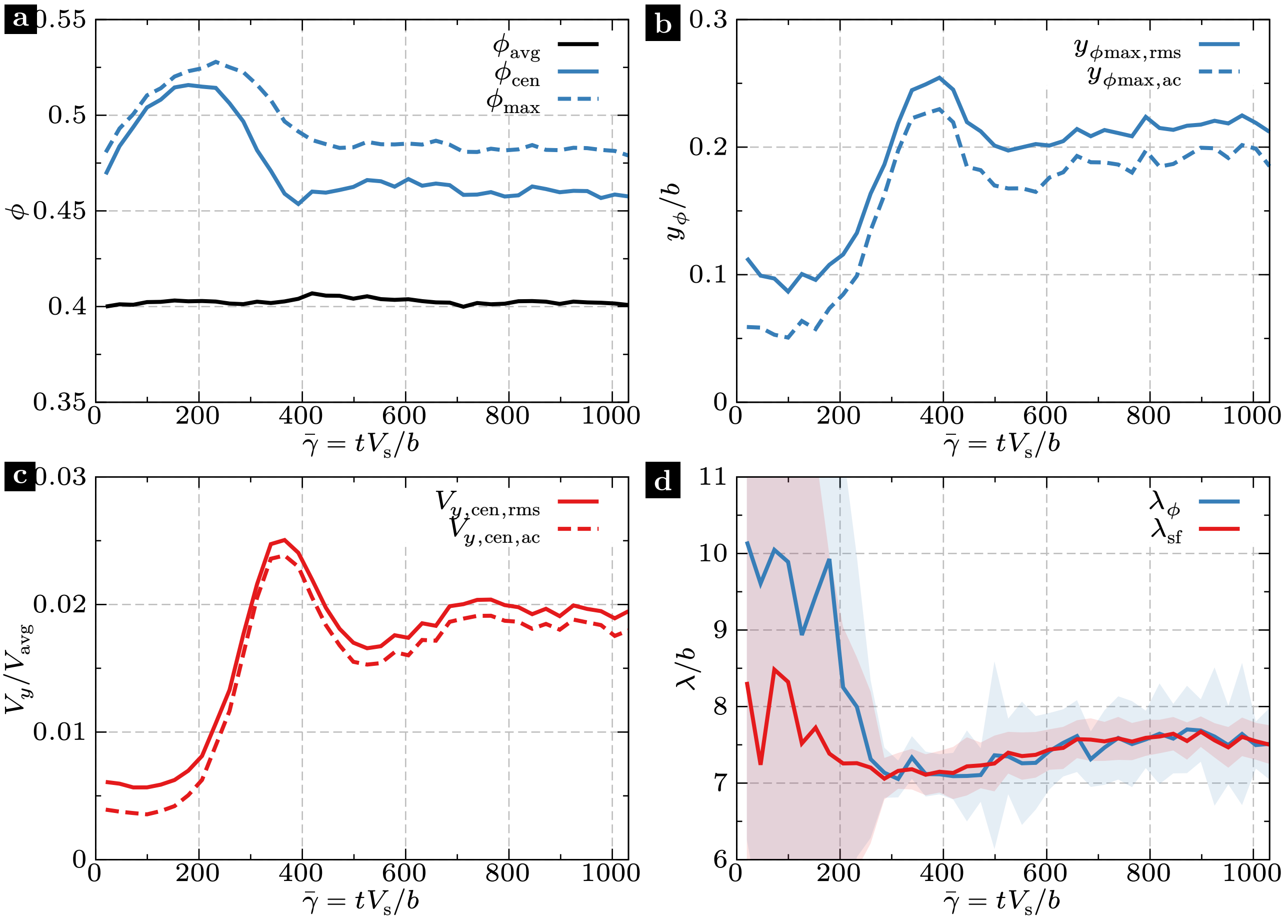

Figure 4.4: Variations as a function of accumulated strain $\bar{\gamma}$ of quantities that characterize the state of the suspension and its flow during one example experiment. a) Volume fraction averages: global (ϕ_{avg}), in the gap center (ϕ_{cen}), and peak value at $y_{\phi\max}$ ($\phi_{\max}$). b) Amplitude of the transverse deformation of ϕ calculated from $y_{\phi\max}$ using the rms ($y_{\phi\max,\text{rms}}$) and the autocorrelation ($y_{\phi\max,\text{ac}}$). c) Amplitude of the instantaneous transverse velocities calculated from $V_{y,\text{cen}}$ using the rms ($V_{y,\text{cen,rms}}$) and the autocorrelation ($V_{y,\text{cen,ac}}$). d) Wavelengths λ_ϕ and λ_{sf} calculated from the autocorrelations of $y_{\phi\max}$ and $V_{y,\text{cen}}$, respectively. The shading denotes the standard deviation of each time-averaged value. All: same parameters as in Fig. 4.1, averages of three experiments.

From the curve $y_{\phi\max}(x,t)$, we can also obtain an amplitude of the transverse deformation induced in the particle distribution. In Fig. 4.4b, we show two estimations of its amplitude: the root mean square (rms), $y_{\phi\max,\text{rms}}(t) = \langle y^2_{\phi\max}(x,t)\rangle_x^{1/2}$, and $y_{\phi\max,\text{ac}}(t)$, calculated from the first maximum of the autocorrelation as explained in Sec. 2.7.4. The second measure is more selective toward periodic patterns. Nonetheless, both quantities have similar trends and values during the whole experiment, suggesting that the pattern have a more or less pure spectrum.[2] Both curves are initially constant, with non-zero values due mostly to the noisy nature of the base data. Around $\bar{\gamma} = 150$, they start to increase until they reach maximum values at $\bar{\gamma} \approx 400$. Then, both partially decrease and remain with roughly constant values. During this last stage, the wave-like pattern in ϕ is not so well defined (see Fig. 4.1e-f), and our estimations of the amplitude may be less reliable.

Taking together Figs. 4.4a and 4.4b, it is clear that, when the band of high particle concentration starts to deform (see the increase of $y_{\phi\text{max,ac}}$ at $\bar{\gamma} \approx 150$), the accumulation of particles in the gap center stops (see ϕ_{cen}) and, then, decreases until the deformation reaches its maximum amplitude around $\bar{\gamma} \approx 400$. Therefore, it is natural to wonder whether there are two competing processes, the shear-induced migration and the instability, and if there is a causal relation between them, e.g. enough particles must migrate to the gap center for the suspension to become unstable. We do not have definitive answers to these questions currently, but we will try to shed some light into them in the following sections.

Now, we will turn our attention to the secondary flow (i.e. the perturbation in the velocity field) and, in order to characterize its temporal variations, we calculate the amplitude of $V_{y,\text{cen}}(x,t) = V_y(x,0,t)$ by the rms and the autocorrelation methods used before. Figure 4.4c shows both curves as a function of the accumulated strain $\bar{\gamma}$. Again, both curves are similar between them, suggesting that the variations of $V_{y,\text{cen}}$ with x have a roughly sinusoidal form, and they are also similar to those seen in Fig. 4.4b for the amplitude of transverse deformation observed in ϕ. A comparable calculation was done for the longitudinal velocity perturbation using $\delta V_{x,\text{nw}}(x,t) = \delta V_x(x, 0.8b, t)$, resulting in curves with similar shapes, but with values about 2.5 times larger than those obtained from $V_{y,\text{cen}}$. The previous observations, and the fact that the transverse and longitudinal velocity components are related by the continuity equation (i.e. mass conservation), suggests that $V_{y,\text{cen,ac}}$ is a good indicator of the amplitude of the secondary flow as a whole and, more generally, of the instability.

In summary, the onset and growth of the instability can be simultaneously detected in

---

[2] Bear in mind that the division of the xy plane into a grid also functions as a high-pass filter that excludes fluctuations at very small scales (particle size), but those are not of interest here.

the particle distribution (looking at $y_{\phi\max,\mathrm{ac}}$) and the secondary flow (looking at $V_{y,\mathrm{cen,ac}}$). To make this point even more clear, Fig. 4.4d displays the wavelengths λ_ϕ and λ_{sf} calculated using the autocorrelations (details in Sec. 2.7.4) of $y_{\phi\max}(x,t)$ and $V_{y,\mathrm{cen}}(x,t)$, respectively. The shared regions represent the pointwise standard deviation. Remember that each point in this section is the average during short lapses just before reversals. Initially ($\bar{\gamma} < 300$) the values are not reliable due to their large fluctuations (large shaded regions), and the difference between λ_ϕ and λ_{sf} may be meaningless. Afterward ($\bar{\gamma} \approx 300$), both curves settle on $\lambda/b \approx 7$, showing that both ϕ and the secondary flow are similarly modulated along x. Then, after the peak in the instability amplitudes ($\bar{\gamma} \approx 400$), the wavelengths start to increase until $\lambda/b \approx 7.5$ is reached.

The figures of this section present a consistent scenario where the evolution of the oscillating suspension can be divided in three well-defined stages. The first stage is before the onset of the instability, when the transverse velocities are small and the particle are migrating toward the center of the gap. The second stage corresponds to the simultaneous growth of periodic perturbations in the volume fraction (the wave-like pattern shown in Fig. 4.1) and in the velocity field (the secondary flow shown in Fig. 4.2). Both perturbations are periodic along x, with a similar wavelength that becomes well defined during this stage. The final stage corresponds to a long-term, probably non-linear, evolution of the perturbations.

4.3. Short-term variations after reversal

The previous sections focused primarily on the long-term evolution of the perturbations introduced by the instability into the volume fraction and velocity fields. In this section, we present the transient variations that occur between two flow reversals in the oscillatory flow, revealing a more complex relationship between the two perturbations than previously suggested. The results presented here correspond to “large” oscillation amplitudes ($\bar{\gamma}_0 \gtrsim 11$), while Section 4.4.2 will show notable differences at smaller amplitudes ($\bar{\gamma}_0 \lesssim 7$).

Continuing our analysis of the same experiment from previous sections ($\bar{\gamma}_0 = 13.3$), Fig. 4.5 displays the variations of the particle volume fraction ϕ and secondary velocity field ($\delta V_x, V_y$) after a flow reversal occurring at $\bar{\gamma} = 372.8$, when $V_{y,\mathrm{cen,ac}}$ is roughly maximum. We choose a time near the maximum amplitude of the perturbations because they are then

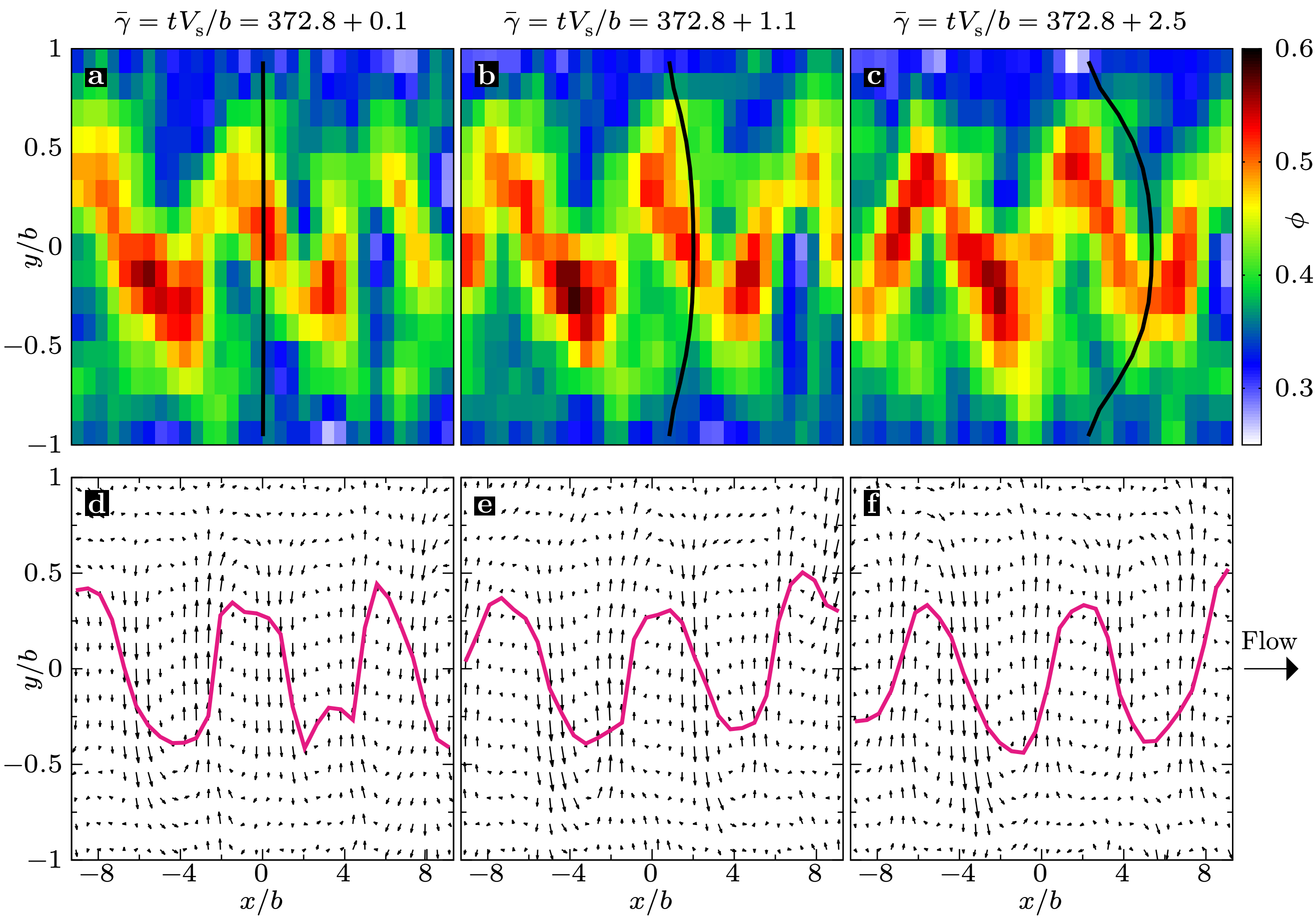

Figure 4.5: a-c) Particle volume fraction ϕ in the xy plane at three different accumulated strains $\bar{\gamma}$ after a flow reversal occurring at $\bar{\gamma} = 372.8$. The black curves show the deformation produced by the main flow [time integral of $\overline{V}_x(y,t)$]. d-f) Secondary velocity field $(\delta V_x, V_y)$ in the same plane and strains as above. The magenta curve marks the positions of maximum ϕ inside each column ($y_{\phi\max}$). Main flow from left to right. Same experiment as in Fig. 4.1.

easier to follow, but the following description applies also at any other time (before and after) when the instability is apparent as x-periodic perturbations in ϕ and $(\delta V_x, V_y)$.

Shortly after reversal (Fig. 4.5a,d), ϕ is indistinguishable from before (Fig. 4.1d), while the secondary velocity has changed sign (compare with Fig. 4.2a), but it is otherwise similar. In the figure here, the main flow is from left to right ($\overline{V}_x > 0$), and looking carefully at the next plots (b,c,e,f), it is possible to notice that the pattern in both fields is being dragged to the right. To make a direct comparison, superimposed over the map of ϕ, we show how a hypothetical black vertical line would deform under the effect of the main flow $\overline{V}_x$. Observe that the sinusoidal pattern in ϕ is being left behind by the black curve, especially in the center. This means the pattern does not moves like a solid block: the particles forming it have to be constantly rearranging in other to move as suggested by $\overline{V}_x$, while keeping the general form of the pattern in ϕ. Regarding the secondary flow (plots d-f), it seems to move with the pattern in ϕ at all times (compare with the superimposed magenta curve showing $y_{\phi\mathrm{max}}$ versus x). At longer times (not shown), the same characteristics remain valid.

In order to validate our impressions from the previous plots, we use the cross-correlations along x between successive curves to calculate the travel velocities of both patterns. For this purpose we choose the quantities $y_{\phi\mathrm{max}}(x,t)$ and $V_{y,\mathrm{cen}}(x,t)$, respectively, and followed the procedures described in Sec. 2.7.4. The resulting travel velocities have large fluctuations in time due to limitations in the procedure,[3] but on average both are $\approx 0.8\,V_{\mathrm{avg}}$ (curves shown in Sec. 4.4.2), confirming our observation that the pattern induced by the instability lags behind the main flow.

Turning our attention to the amplitude of the perturbations, there is a sharp drop of $V_{y,\mathrm{cen,ac}}$ immediately after a reversal, as shown by the blue curve in Fig. 4.6a, while $y_{\phi\mathrm{max,ac}}$ is roughly unchanged (red curve). The value of $V_{y,\mathrm{cen,ac}}$ remains at a plateau up to $\Delta\bar{\gamma} \approx 4$ and, then, it slowly increases until it reaches the value from before the reversal (the quasi-steady value) at $\Delta\bar{\gamma} \approx 10$. It is important to note that the variations of $V_{y,\mathrm{cen,ac}}$ are representative of the secondary flow over the whole plane, not just in the center line ($y = 0$) where V_y is measured to make the calculation.

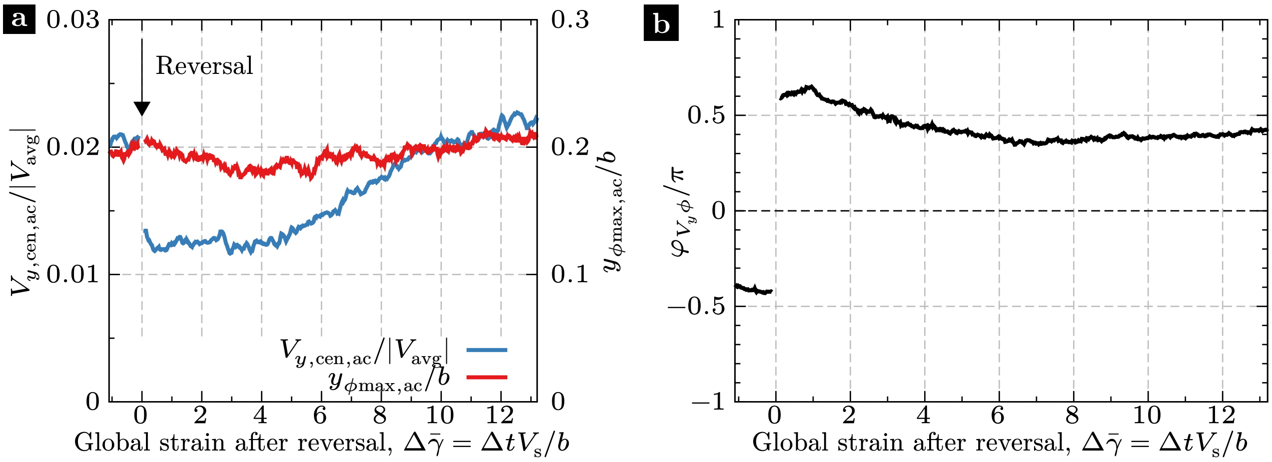

Figure 4.6: Variations after flow reversal ($\Delta\bar{\gamma} = 0$). a) Amplitudes of the perturbations in the velocity field (blue) and volume fraction (red). The former is characterized by $V_{y,\mathrm{cen,ac}}$ normalized by $|V_{\mathrm{avg}}|$ (roughly constant, $\approx V_{\mathrm{s}} = 1.15\,\mathrm{mm/s}$) and, the latter, by $y_{\phi\mathrm{max,ac}}$ normalized by the channel half gap b. b) Phase of the $V_{y,\mathrm{cen}}$ relative to $y_{\phi\mathrm{max}}$. Same experiment as in Fig. 4.1.

The lack of significant changes of $y_{\phi\mathrm{max,ac}}$ after reversal is to be expected since this variable tracks a macroscopic arrangement of the particles and those cannot change suddenly. On the

---

[3] Here, we are working with almost instantaneous results (one video frame). All the curves have fluctuations from one frame to the next, and the cross-correlation procedure is sensitive to them.

other hand, the sudden drop of $V_{y,\mathrm{cen,ac}}$ is clearly connected with the loss of particle contacts after reversal. In Fig. 3.9b, we have shown that the viscosity (by proxy) drops and, then, recovers its quasi-steady value as the contacts between the particles are recovered all over the channel gap after a strain $\Delta\bar{\gamma} \approx 10$, while the microstructure parameter A_{xy} changes sign across the gap as shown in Fig. 3.18b. Those two figures and the ones in this section correspond to the same experiments. Given the similarity in the strain scale for the changes of $V_{y,\mathrm{cen,ac}}$ compared with those other two variables, the most plausible explanation for the post-reversal variations of $V_{y,\mathrm{cen,ac}}$ is, likewise, the loss of contacts and their subsequent recovery as the microstructure reorganizes.

Finally, using the cross-correlation along x between $y_{\phi\mathrm{max}}(x,t)$ and $V_{y,\mathrm{cen}}(x,t)$, we estimated a phase relation $\varphi_{V_y\phi}$ between both perturbations induced by the instability. Figure 4.6b shows that $\varphi_{V_y\phi}$ changes sign after reversal, this is normal since the secondary flow does so, but also increases its absolute value from $\approx 0.4\,\pi$ to $\approx 0.6\,\pi$ and, then, relaxes slowly over a timescale similar to $V_{y,\mathrm{cen,ac}}$. In Sec. 4.4.2, we will see that the temporal variations of the phase relationship after reversal exhibit qualitative differences in experiments with smaller oscillation amplitudes.

4.4. Influence of the oscillation amplitude

We performed experiments with oscillation strain amplitudes $\bar{\gamma}_0 = T\,V_\mathrm{s}/(2b)$ between 4.4 and 15.5 using the same channel and suspension as in the experiment shown before ($\bar{\gamma}_0 = 13.3$). This variation was induced by changing only the oscillation period T, while keeping $V_\mathrm{s} = 1.15\,\mathrm{mm/s}$ and the Reynolds number $\mathrm{Re} = V_\mathrm{s} b \rho_\mathrm{f}/\eta_\mathrm{f} \approx 0.2$. In Sec. 5.4, we will show that variations of Re do not influence significantly the development of the instability.

4.4.1. On the development of the instability

Figure 4.7 shows the evolution of ϕ_cen (plot a), $y_{\phi\mathrm{max,ac}}$ (plot b), $V_{y,\mathrm{cen,ac}}$ (plot c), and λ_sf (plot d) for different oscillations amplitudes $T\,V_\mathrm{s}/b$. Each curve corresponds to the pointwise average of two or three experiments with the same parameters. In each plot, all the curves mostly overlap, except only for the following differences.

The experiments with $\bar{\gamma}_0 = 8.9$ are slightly delayed with the respect to the others. The

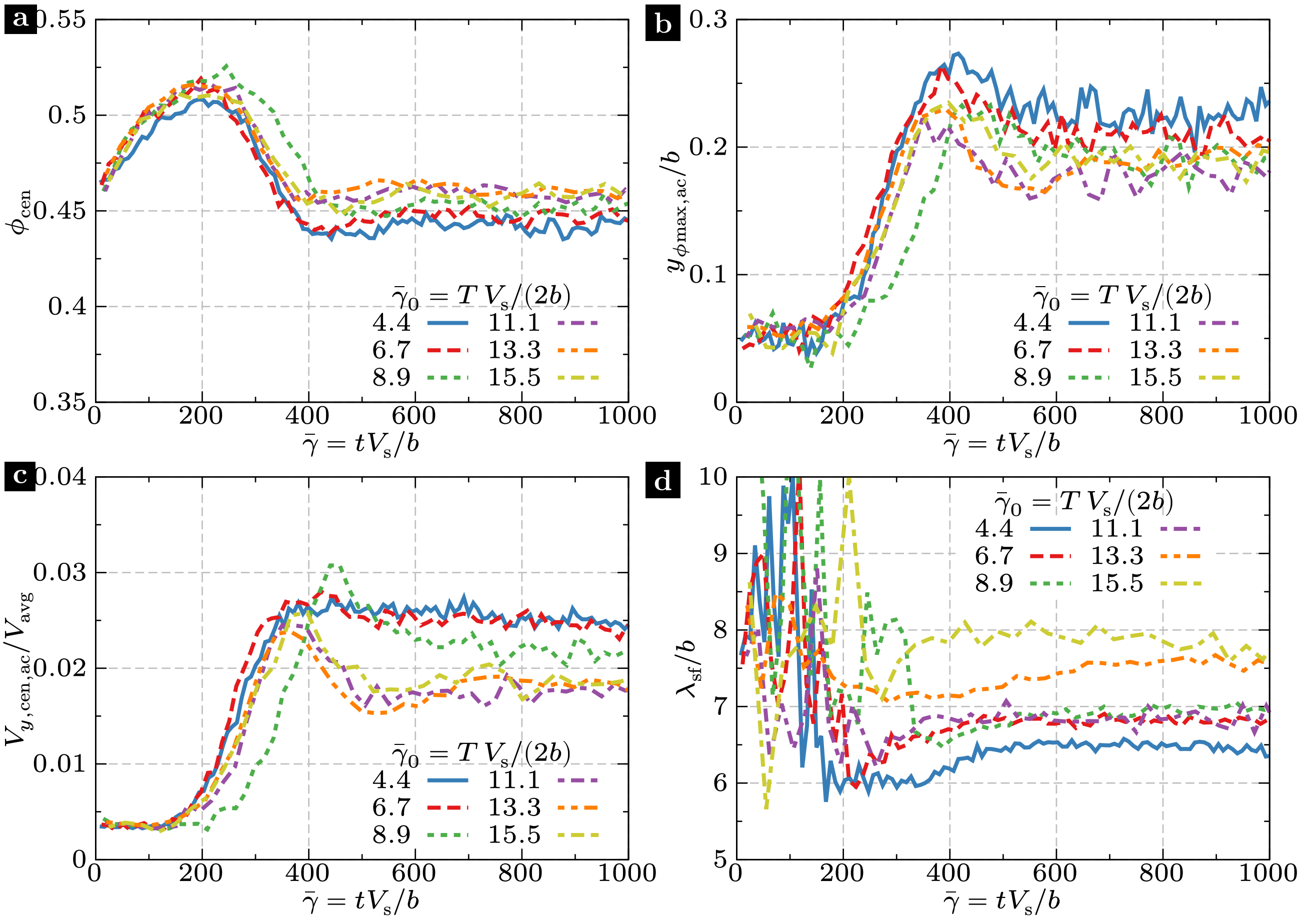

Figure 4.7: Variations as a function of the accumulated strain $\bar{\gamma}$ of quantities that characterize the state of the suspension and its flow during experiments with different oscillation strain amplitudes $\bar{\gamma}_0$. a) Volume fraction average in the gap center. b) Amplitude of the transverse deformation of ϕ, calculated from $y_{\phi\max}$ using the autocorrelation. c) Amplitude of the instantaneous transverse velocities, calculated from $V_{y,\rm cen}$ using the autocorrelation. d) Wavelengths calculated from the autocorrelation of $V_{y,\rm cen}$. All: the parameters beside $\bar{\gamma}_0$ (and T) are the same as in Fig. 4.1. Each curve is the pointwise average of two or three experiments.

curves shown correspond to the average of two experiments performed one after the other, both with very similar temporal evolutions. It is unknown to us whether this delay is just a fluctuation in the experimental conditions or there is physical meaning in it. Nonetheless, the difference with respect to the other curves is not large enough to weaken our following conclusions.

A more clear dependence on $\bar{\gamma}_0$ arises after $V_{y,\rm cen,ac}$ reaches its maximum, around $\bar{\gamma} = 400$ in Fig. 4.7c. The two curves with smaller oscillations (blue and red) retain values consistently larger than the three curves with larger oscillations, which have pronounced decreases. A similar observation can be made in plot (b) for the amplitude of the volume fraction perturbation, although the variations between curves are weaker in this case.

On the other hand, in plot (d), we see that in all cases the wavelength starts with larger values and large fluctuations, and reaches a roughly constant value after the instability is developed enough ($\bar{\gamma} \approx 250$). These final values are spread between $6\,b$ and $8\,b$, and increase with the oscillation amplitude.

To conclude, we observe that the growth of the perturbations depend essentially on the accumulated deformation induced by the flow, with little influence of the oscillation amplitude. In the next chapter, we will show that the development of the instability can be delayed for oscillations amplitudes outside of the range reported here. Although those observations were made using the 40 µm particles, we believe that they deserve a mention here. For very large amplitudes $\bar{\gamma}_0$, more strain $\bar{\gamma}$ is accumulated before the onset of the instability, suggesting that steady flows ($\bar{\gamma}_0 \to 0$) are stable, in agreement with previous works (Lyon and Leal 1998a; Rashedi et al. 2020). On the other hand, for amplitudes below a threshold of the order of one, the flow is stable and the perturbations shown in this chapter do not appear, suggesting the kind of reversible behavior showing in Sec. 1.7.2 (Morris 2001; Guasto, Ross, and Gollub 2010).

4.4.2. Between reversals

In Sec. 4.3, we discussed the variations of the perturbations in the volume fraction and the velocity field for an experiment with $\bar{\gamma}_0 = 13.3$, which is near the upper bound of amplitudes tested using the 85 µm particles. For smaller amplitudes, we observe some qualitative differences in the relation between both perturbations.

Figure 4.8 shows a sequence of secondary velocity maps before and after a flow reversal, during one example experiment with $T\,V_\mathrm{s}/b = 8.9$. Plot (a) shows the situation before a reversal when the instability is fully developed. Looking at the centerline ($y/b = 0$), we see that $y_{\phi\mathrm{max}}$ (magenta curve), which tracks where ϕ is maximal, is in phase with $V_{y,\mathrm{cen}}$: the magenta curve has positive values where the particles are going up, negative where they go down, and its zeros coincide with the regions of null velocity perturbation. This is in contrast with the equivalent plot for oscillations of larger amplitude (Fig. 4.2a), where both perturbations are out of phase by roughly a quarter of wavelength.

Immediately after the flow reverses, in plot (b), the secondary flow field changes signs, while the perturbation in ϕ remains unchanged. Now, both perturbations are out of phase by

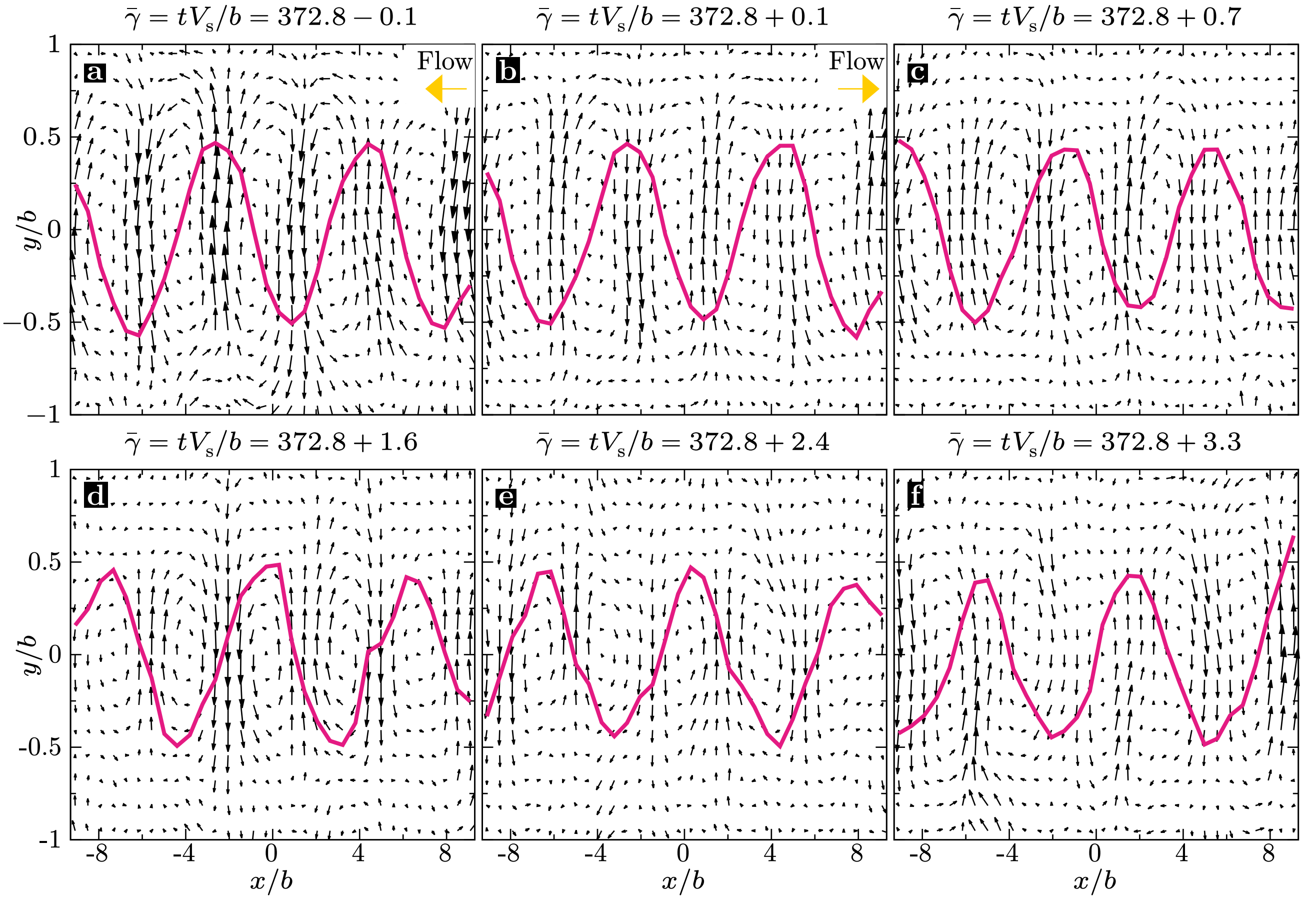

Figure 4.8: Secondary velocity field $(\delta V_x, V_y)$ in the xy plane at six different strains (i.e. times) after a flow reversal in an experiment with small oscillations. The magenta curve marks the positions of maximum ϕ inside each column ($y_{\phi\mathrm{max}}$ versus x). Main flow direction indicated by the yellow arrows. Parameters: $\phi_{\mathrm{bulk}} = 0.4$, $2a \approx 85\,\mu\mathrm{m}$, $2b = 2.1\,\mathrm{mm}$, $V_s = 1.15\,\mathrm{mm/s}$, $\bar{\gamma}_0 = T\,V_s/(2b) = 4.4$.

half a wavelength. This situation is apparently out of equilibrium since in the following plots (c-e), the perturbation in ϕ (tracked by the magenta curve) seems to move faster to the right (direction of the main flow) than the perturbation velocity field, resulting in a progressive change in the relative phase between both, until it is fully "corrected" in plot (f).

We calculate again the travel velocities of both perturbations using the cross-correlations between successive curves $y_{\phi\mathrm{max}}$ and $V_{y,\mathrm{cen}}$. Figure 4.9 shows both travel velocities (V_{V_y} and V_ϕ), along with the velocity V_{cen} of the main flow in the gap center, all three normalized by the instantaneous average velocity of the main flow, V_{avg}. The left plot corresponds to experiments with a small oscillation amplitude ($\bar{\gamma}_0 = 4.4$), while the right one, to large oscillations ($\bar{\gamma}_0 = 13.3$). In both plots, V_ϕ fluctuates around constant values: $0.9\,V_{\mathrm{avg}}$, on the left and $0.8\,V_{\mathrm{avg}}$, on the right. On the other hand, V_{V_y} has a value similar to V_ϕ for large oscillations (right), but is much smaller for small oscillations (left). In this later case, V_{V_y} is nearly zero up to $\Delta\bar{\gamma} \approx 1$ and then, fluctuates about $0.4\,V_{\mathrm{avg}}$. This is consistent with

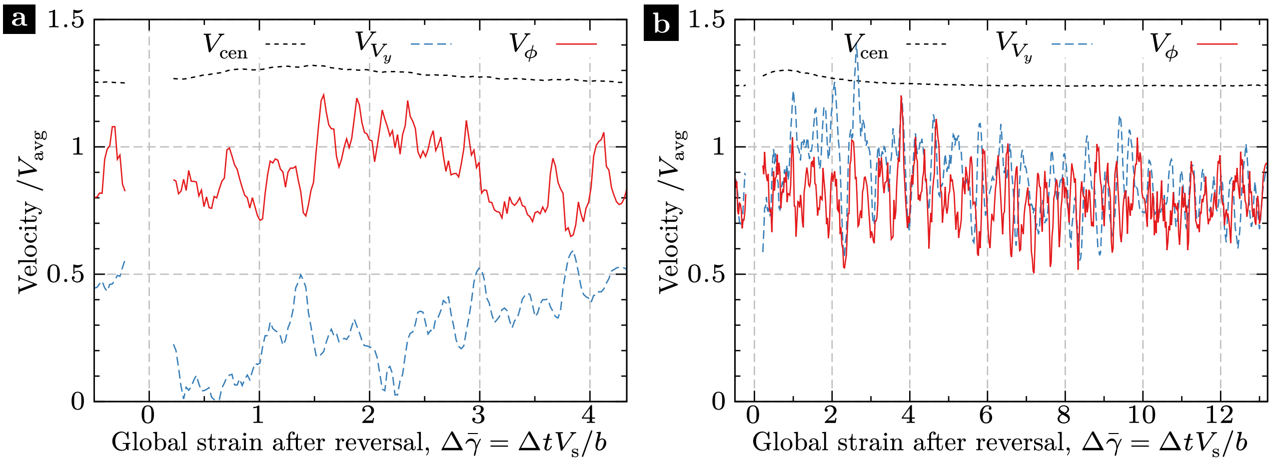

Figure 4.9: Travel velocities V_{V_y} (dashed blue lines) and V_ϕ (solid red line) as functions of the accumulated strain $\Delta\bar{\gamma}$ after a flow reversal. For reference, V_{cen} is also shown (dashed black line). All three velocities are normalized by V_{avg}. a) Small oscillations [$\bar{\gamma}_0 = T\,V_{\text{s}}/(2b) = 4.4$]. b) Large oscillations [$\bar{\gamma}_0 = T\,V_{\text{s}}/(2b) = 13.3$].

our previous observation, in Fig. 4.8, that the velocity perturbation lags behind the volume fraction one, allowing it to recover the phase relation present before the reversal.

In order to do a more complete comparison between oscillation amplitudes, Fig. 4.10 displays for $V_{y,\text{cen}}$, its amplitude (plot a) and its phase relative to $y_{\phi\max}$ (plot b). In plot (b), we see that the relative phase for large oscillations ($11.1 \le \bar{\gamma}_0 \le 15.5$) varies from $\approx 0.6\,\pi$ to $\approx 0.4\,\pi$ after reversal, while for small oscillations ($4.4 \le T\,V_s/b \le 6.7$), it continuously increases starting from $\approx 0.8\,\pi$ immediatelly after reversal and finishing at $\approx 0.2\,\pi$ when $\Delta\bar{\gamma} \approx 6$.[4] This later variation agrees with our observations in Fig. 4.8 where the relative phase changes from nearly zero before reversal to a half wavelength ($\varphi_{V_y\phi} = \pi$) after reversal and, then, it progressively goes back zero before the next reversal.

In Fig. 4.10a, we observe that the amplitude of the transverse velocities ($V_{y,\text{cen,ac}}$) sharply decreases immediately after reversal and, eventually, recovers its previous value, but with some differences in its evolution depending on the oscillation amplitude. For large oscillations ($11.1 \le \bar{\gamma}_0 \le 15.5$), the curves remain more or less constant and then increase linearly. For intermediate oscillation amplitudes ($6.7 \le \bar{\gamma}_0 \le 8.9$), it decreases until it reaches a non-zero minimum and, then, increases. And finally, for the smallest oscillations ($\bar{\gamma}_0 = 4.4$), the curve presents a much smaller range of values, with some oscillations after reversal, before a final increase.

---

[4] The discontinuity for $\varphi_{V_y\phi} = \pm\pi$ is just a consequence of the way we represent a 2π-periodic variable on the plot.

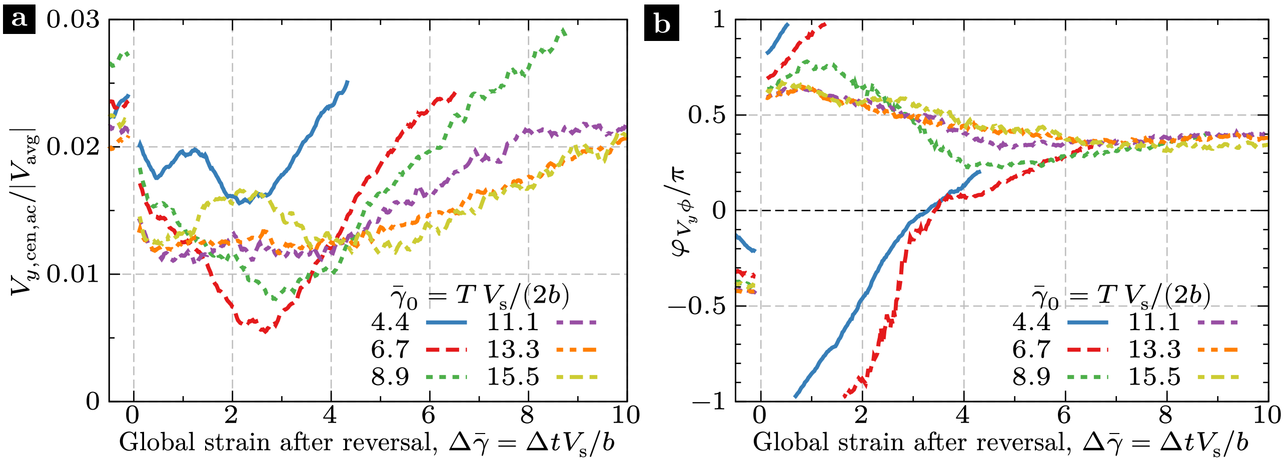

Figure 4.10: Comparison for difference oscillation amplitudes $\bar{\gamma}_0$ of the transverse velocity perturbation amplitude (a) and the phase relative to the volume fraction perturbation (b), before and after a flow reversal occurring at $\Delta\bar{\gamma} = 0$.

The differences between oscillation amplitudes discussed in this section are puzzling in the face of how similar all the curves for the long-term variations are in Fig. 4.7. In the following chapter, we will continue the characterization of the instability using experiments performed with the 40 µm particles. In those experiments, the particles sometimes overlap inside the laser plane, limiting our ability to characterize the volume fraction in the observed plane. Instead, we will rely on measurements of the velocity field and the intuitions built up in these previous sections in order to compare both sets of experiments.

Chapter 5

Study of the influence of the experimental parameters

In the previous chapter, we characterized an instability that has been the focus of our studies, using experiments with our largest beads ($2a \approx 85\,\mu\mathrm{m}$). Those experiments provide quantitative information on the particle distribution and velocities, allowing us to see clearly that the instability perturbs the particle volume fraction ϕ in the observation plane (xy) and introduces a secondary velocity field ($\delta V_x, V_y$). Both perturbations are equally periodic along the channel length and increase in amplitude simultaneously as the suspension oscillates. These observations allow us to establish a close connection between the perturbation of ϕ and the increase of transverse velocities V_y. In the present chapter, we will take advantage of this connection to continue our characterization of the instability using smaller beads ($2a \approx 41\,\mu\mathrm{m}$), where limitations in the visualization technique do not allow for a precise measurement of ϕ, but V_y remains a good indicator of the unstable behavior.

We will start by comparing the experiments of Chapter 4 with new ones using smaller particles in a channel with the thickness scaled down to keep most length ratios approximately equal. After confirming that we observe the same phenomenon (the instability) in both cases, we will proceed with a study of the instability growth rate for different oscillation amplitudes and bulk particle volume fractions, making connections with shear-induced migration and the particle self diffusivity from previous studies. Then, we discuss experiments in which the Reynolds number varies by several orders of magnitude down to values for which inertial effects are ruled out. Finally, we will consider the influence of the geometry: first by changing the channel thickness and, then, the aspect ratio of the cross section.

5.1. Comparison of experiments with different particle sizes

In this section, we report experiments using spheres of diameter $2a \approx 41\,\mu\text{m}$, a channel with thickness $2b = 1.0\,\text{mm}$, a surface average velocity $V_\text{s} = 1.16\,\text{mm/s}$, and a bulk particle volume fraction $\phi_\text{bulk} = 0.4$. The values of the first two parameters are approximately half of those used in the Chapter 4, effectively scaling down the experiments, while keeping the ratio b/a and other parameters similar. The Reynolds number $\text{Re} = V_s b\rho/\eta_f \approx 0.1$ is now half of the previous one, but in Sec. 5.4 we will see that this does not have any influence on the results. Another dimensionless number which varied is the aspect ratio $W/(2b)$: since we keep the channel width W roughly constant (10.5 mm here, 10.0 mm in Chapter 4), the ratio $W/(2b)$ approximately doubles (10.5 here, 4.8 in Chapter 4). In Sec. 5.7, we will see that no significant differences were found for ratios above 5, but important ones were observed at lower values.

Figure 5.1 shows a spatiotemporal diagram of $V_{y,\text{cen}}(x,t)$, comparable to the one shown in Fig. 4.3. The horizontal axis corresponds to time (as an accumulated strain $\bar{\gamma}$ or a number of oscillations t/T) and the vertical one, to the coordinate x along the channel length. The

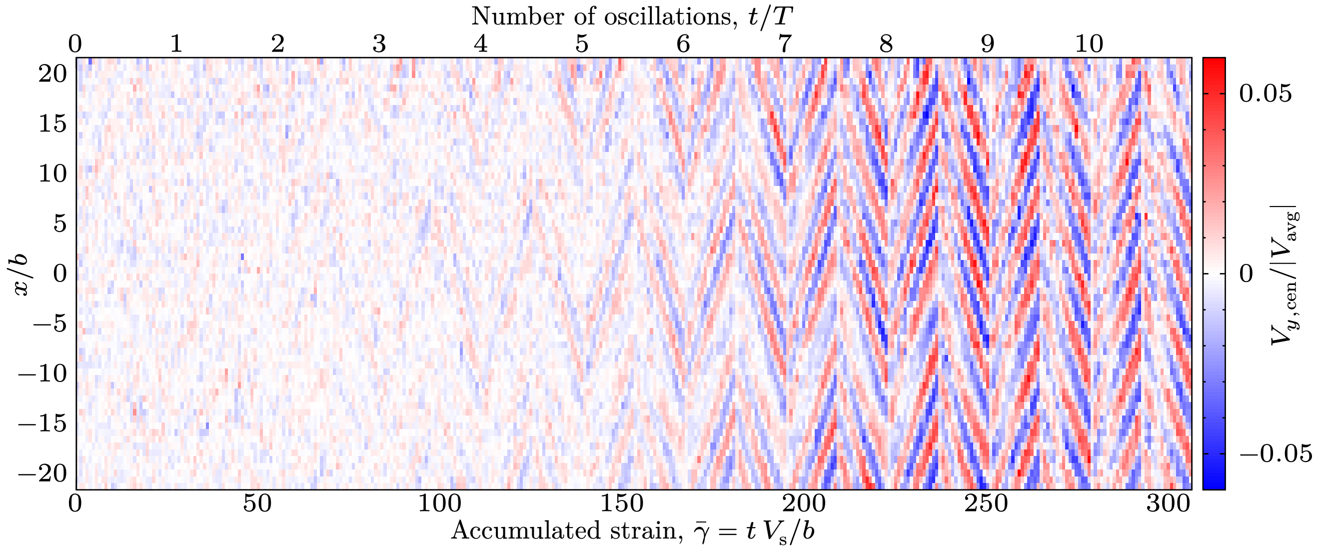

Figure 5.1: Spatiotemporal diagram of $V_{y,\text{cen}}(x,t)$ normalized by $|V_\text{avg}|$. The horizontal direction corresponds to time t, shown as an accumulated strain $\bar{\gamma} = t\,V_b/b$ below, and as the number of oscillations t/T, above. The vertical direction marks the coordinate x/b. The color blue and red indicate the negative and positive values, respectively. Parameters: $\phi_\text{bulk} = 0.4$, $2a \approx 41\,\mu\text{m}$, $2b = 1.0\,\text{mm}$, $V_\text{s} = 1.16\,\text{mm/s}$, $\bar{\gamma}_0 = T\,V_\text{s}/(2b) = 13.9$.

colors blue, white, and red codify negative, null, and positive values of $V_{y,\mathrm{cen}}$, respectively. Qualitatively, this graph is very similar to the one shown in Fig. 4.3 for the larger beads: a herringbone pattern appears after a number of oscillations, periodic both in x and $\bar{\gamma}$. In this case, the pattern appears earlier (around $\bar{\gamma} = 150$ instead of 250), a difference that we will study in the following section.

Selecting the time of maximum amplitude of $V_{y,\mathrm{cen}}$ ($\bar{\gamma} \approx 250$), we plot in Fig. 5.2 the secondary velocity field in the xy plane. Inside the band $-0.7 < y/b < 0.7$, we see recirculation cells similar to those seen in Fig. 4.2a. Outside, the velocity could not be estimated with the required spatial resolution due to the compounded effect of lower particle concentration near the walls and not all of them being visible in these experiments. The wavelength measured in units of b is also similar ($\lambda \approx 7\,b$). In Sec. 5.5, we will see that λ is roughly proportional to b (channel half thickness).

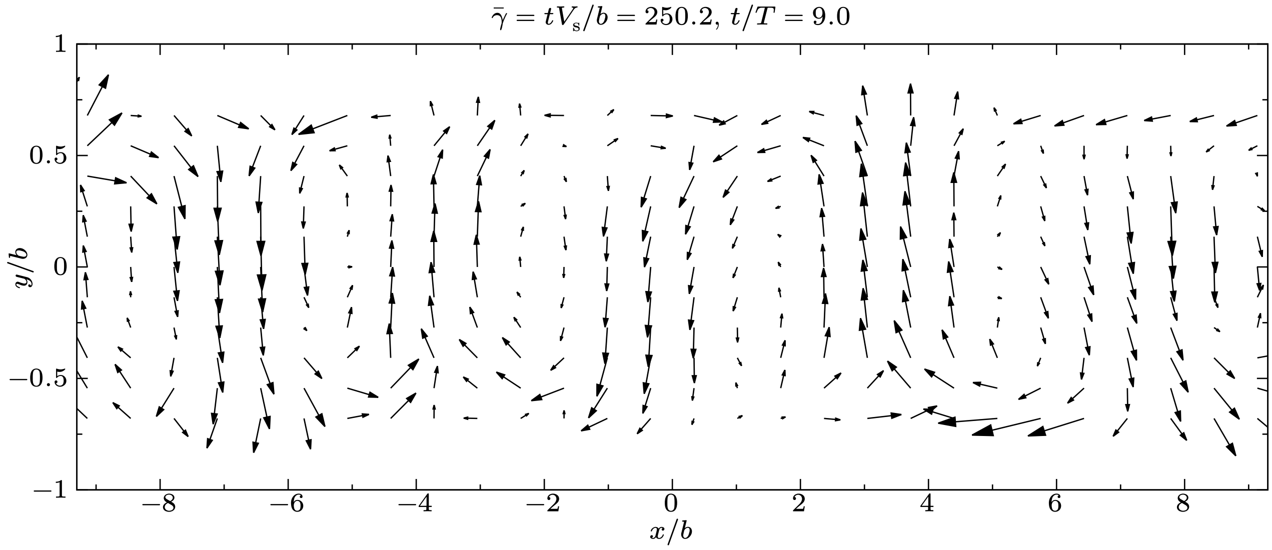

Figure 5.2: Secondary velocity field ($\delta V_x, V_y$) in the observation plane (xy) at the time of maximum amplitude. The black arrows indicate the direction and relative magnitude of the field at each position. Notice that this representation is horizontally compressed with respect to the real images, enlarging the transverse variations. Main flow toward the left. Same experiment as in Fig. 5.1.

From the previous observations, we conclude that both sets of experiments (beads of diameter ≈ 41 µm and ≈ 85 µm) present instabilities characterized by similar perturbations to the velocity field. In the following section, we will study the influence of the oscillation amplitude on the development of the instability, comparing between the results with both kinds of particles.

5.2. Influence of the oscillation amplitude on the growth of the instability

Following the same procedure as in Sec. 4.2, we estimate here the amplitude of the velocity perturbation as a function of time using $A_{V_y}(\bar{\gamma}) = V_{y,\mathrm{cen},ac}(\bar{\gamma})/V_{\mathrm{avg}}(\bar{\gamma})$, and study this variable for experiments with different oscillation amplitudes $\bar{\gamma}_0 = T\,V_\mathrm{s}/(2b)$. In this case, we vary both the period T and surface average velocity V_s: we performed first a set of experiments with $2 \leq T \leq 20\,\mathrm{s}$ and $V_\mathrm{s} = 1.16\,\mathrm{mm/s}$ and, then, a set with periods T twice longer and half the velocity V_s. Both sets produced similar results (within our experimental uncertainty) for plots as a function of the accumulated strain $\bar{\gamma}$ (i.e. times normalized by b/V_s) and with the velocities normalized by measured average longitudinal velocity V_{avg} (which is proportional to V_s). Here we present directly averages of experiments with the same amplitude $\bar{\gamma}_0$. A more thorough study performed by varying V_s can be read in Sec. 5.4. The other parameters (ϕ_{bulk}, a, b) are the same as in the experiment of the previous section. Figure 5.3 shows that the resulting curves are qualitatively similar to the ones shown in Fig. 4.7c for the larger beads, but there are some differences as detailed below.

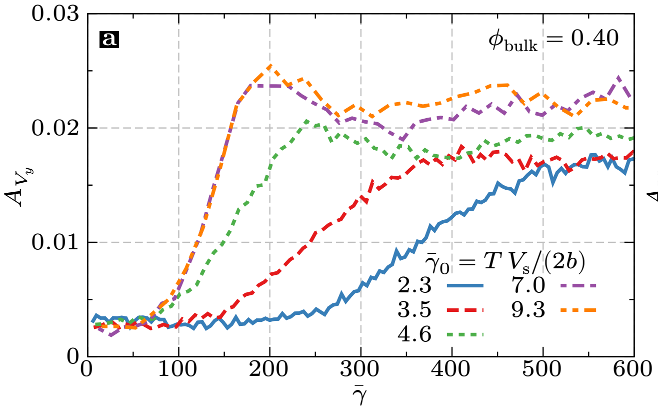

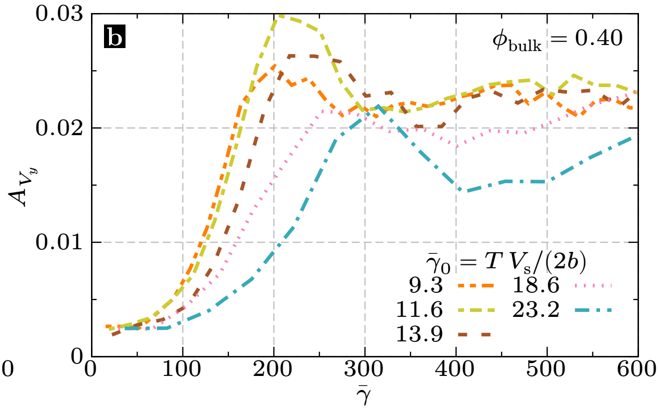

Figure 5.3: Variation of $A_{V_y} = V_{y,\mathrm{cen},ac}/V_{\mathrm{avg}}$ as a function of accumulated strain $\bar{\gamma} = t\,V_\mathrm{s}/b$. Results from experiments with different oscillation amplitudes $\bar{\gamma}_0$ are shown, with the smaller amplitudes on the left (a), and the largest, on the right (b). Other parameters: $\phi_{\mathrm{bulk}} = 0.4$, $2a \approx 41\,\mu\mathrm{m}$, $2b = 1.0\,\mathrm{mm}$.

For intermediate oscillation amplitudes ($7.0 \leq \bar{\gamma}_0 \leq 11.6$), there is little influence of $\bar{\gamma}_0$, like in Fig. 4.7c, but here the transverse velocities start to increase around $\bar{\gamma} = 75$, and reach a maximum around 200, for roughly half of the strain needed by the larger particles. It is important to remember that the beads (larger and smaller) do not differ only in their sizes, but they also come from different manufacturers (Sec. 2.1), and differences in the surface roughness might account for the difference in the rate at which the system evolves under strain (see Sec. 1.7.1 and Pham, Metzger, and Butler 2015, for instance).

Outside the range $7.0 \leq \bar{\gamma}_0 \leq 11.6$ in Fig. 5.3, the curves $A_{V_y}(\bar{\gamma})$ have similar shapes, but the accumulated strains required for a growth to be visible and to reach the maximum value, both increase as the oscillation amplitude decreases ($\bar{\gamma}_0 \leq 9.3$ in plot a) or increases ($\bar{\gamma}_0 \geq 9.3$ in plot b).

In order to quantify the characteristic strains for the growth of the instability, we show in Fig. 5.4 a semi-log plot of A_{V_y} as a function of the accumulated strain $\bar{\gamma}$ for one example experiment. Using plots like this one, we identify for each experiment an interval $[\bar{\gamma}_{\text{onset}}, \bar{\gamma}_{\text{sat}}]$ where there is an exponential growth (linear on the plot), and obtain a growth rate σ from a linear fit (read a full explanation in Appendix B.1). Notice that mathematically,

$$\sigma = \frac{\log[A_{V_y}(\bar{\gamma}_{\text{sat}})/A_{V_y}(\bar{\gamma}_{\text{onset}})]}{\bar{\gamma}_{\text{sat}} - \bar{\gamma}_{\text{onset}}}, \tag{5.1}$$

and that we can interpret σ as the inverse of the strain needed for the transverse velocity perturbation to grow by a factor e ≈ 2.7.

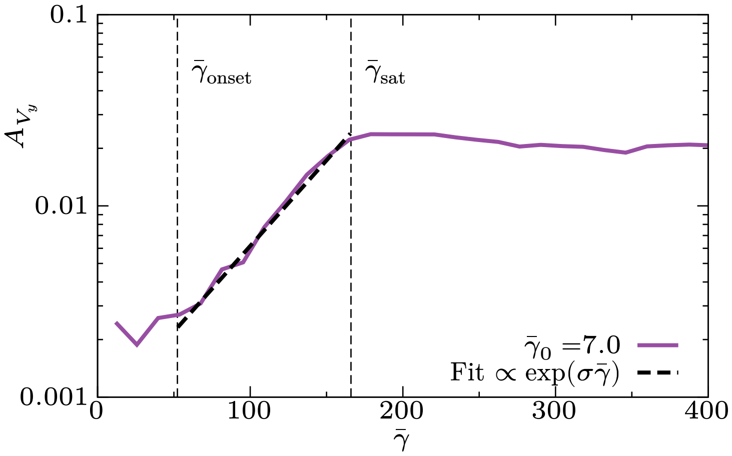

Figure 5.4: Curve $\bar{\gamma}_0 = 7.0$ from Fig. 5.3a, but using a logarithmic vertical scale. Due to the scale, the “overshoot” seen in the other figure is less pronounced here, while the small variations near the beginning are enlarged.

The fact that we do not observe an exponential growth from the beginning (i.e. $\bar{\gamma}_{\text{onset}} > 0$) could be due to another physical process that needs to happen before (e.g. shear-induced migration of particles to the gap center), but it could also be affected by a base noise level in our measurements that the perturbation needs to overcome to be detectable. On the other hand, $\bar{\gamma}_{\text{sat}}$ marks the accumulated strain at which the perturbation growth starts to saturate, usually reaching the maximum value of $V_{y,\mathrm{cen},ac}$ shortly after.

Figure 5.5 shows the parameters $\bar{\gamma}_{\mathrm{onset}}$, $\bar{\gamma}_{\mathrm{sat}}$, and σ versus the oscillation amplitude $\bar{\gamma}_0$ for the experiments using the small beads (from this chapter), and the large ones (from Chapter 4). Observe that the three parameters are roughly constant for $\bar{\gamma}_0$ between 5 and 15, in both cases. The experiments with large beads fall almost completely inside this range and do not show any significant variations with the oscillation amplitude. On the other hand, the experiments with smaller beads show clearly that outside this range, the growth of the perturbation is slower, with larger characteristic strains, and a smaller growth rate. This is specially clear for $\bar{\gamma}_0 < 5$, where the strains required for instability onset and saturation may diverge as the oscillation amplitude decreases, and the growth rate seems to decrease toward zero.

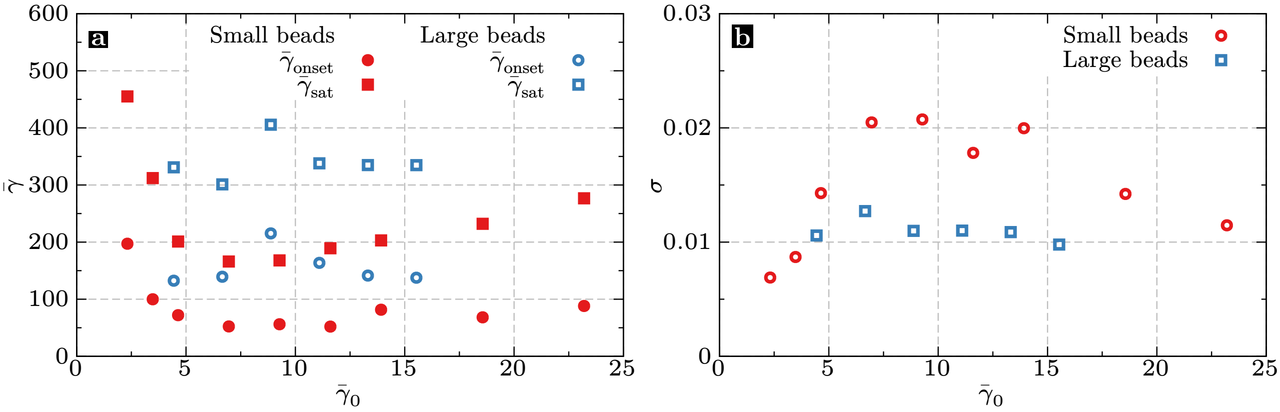

Figure 5.5: a) Parameters $\bar{\gamma}_{\mathrm{onset}}$ and $\bar{\gamma}_{\mathrm{sat}}$ for experiments with different oscillation amplitudes (horizontal axis) and beads types. b) Same for parameter σ. The small beads experiments are the same as in Fig. 5.3, and the large beads ones, correspond to Fig. 4.7.

5.2.1. A simple interpretation of the influence of the oscillation amplitude on the growth rate

In Sec. 1.7, we reviewed previous works showing that there is a critical amplitude for shearing oscillations in suspensions, below which the particles return to their initial positions after each oscillation, and above which the particles positions randomly change in a diffusive motion. Furthermore, we have seen in Sec. 1.5.2 and Sec. 3.5 that, after flow reversal, the particle microstructure undergoes a reorganization with a transient loss of most contacts and a sharp reduction of the viscosity. Particle contact interactions were identified as the main reason for irreversible processes in suspensions (Lemaire et al. 2023), such as shear-induced migration, and are most probably the driving mechanism of the instability studied here. Therefore, it is reasonable to consider that during a small strain $\bar{\gamma}_c$ after reversal, the perturbations induced by the instability do not grow in amplitude (i.e. zero growth rate), and it is only after this much strain has taken place during one half oscillation, that the perturbations develop. This view is partly supported by Fig. 4.6a where we have shown that A_{V_y} decreases after reversal and recovers its previous value only after a certain accumulated strain, although this interpretation is complicated by the fact that the curves corresponding to different oscillation amplitudes start to increase after different amounts of strains have accumulated (see Fig. 4.10a).

We propose here a simplified interpretation where a half oscillation that strains the suspension by an amount $\bar{\gamma}_0$ in total, only contributes to the perturbation growth by a strain $\bar{\gamma}_0 - \bar{\gamma}_c$. In particular, we will assume a step-like variation of the growth rate between reversals, with no growth up to a strain $\bar{\gamma}_\mathrm{c}$ and, after that, an intrinsic growth rate σ_i which does not depends on the oscillation amplitude $\bar{\gamma}_0$. Then, the growth rate we measure by observing the increase of A_{V_y} from one oscillation to the next one will be

$$\sigma = \frac{\bar{\gamma}_0 - \bar{\gamma}_c}{\bar{\gamma}_0}\sigma_\mathrm{i}. \tag{5.2}$$

Figure 5.6 displays $\sigma\bar{\gamma}_0$ versus γ_0. For experiments with small beads, it shows indeed that $\sigma\bar{\gamma}_0$ increases linearly with $\bar{\gamma}_0$ for small oscillations ($\bar{\gamma}_0 < 15$) and tends to zero as $\bar{\gamma}_0$ approaches a non-zero critical strain $\bar{\gamma}_c \approx 2$. On the other hand, for large oscillation

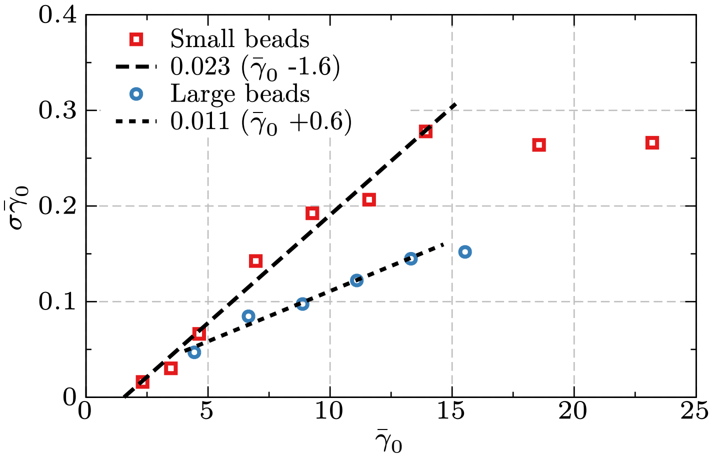

Figure 5.6: Plot of $\sigma\bar{\gamma}_0$ versus oscillation amplitude $\bar{\gamma}_0$ for the same experiments as in Fig. 5.5. Fitting linear functions to the points with $\bar{\gamma}_0 < 15$, we can estimate the parameters of Eq. (5.2).

amplitudes ($\bar{\gamma}_0 > 15$), $\sigma\bar{\gamma}_0$ seems to saturate, suggesting that for long strains after the reversal, the development of the perturbations induced by the instability becomes hindered again. For the larger beads, the plot is also linear, but the lack of experiments with small and large enough oscillation amplitudes prevents us from reaching any strong conclusions.

5.2.2. Comparison of the onset strain to a characteristic migration strain

In the experiments using the larger beads (Chapter 4), we have seen that the instability onset occurs roughly when the volume fraction reaches a maximum in the center of the channel thickness, after increasing for some time (see Figs. 4.4 and 4.7). In the experiments with the smaller beads, we do not have access to precise information about the particle concentration, but it is reasonable to expect some sort of particle redistribution to be occurring, because that is the only way for the system to change irreversibly, ruling out any deformation of the particles, variations in the fluid composition, and inertial effects (see Sec. 5.4 for the latter)

To obtain a characteristic strain for this process, we will consider that it involves the migration of particles across the gap, and that we can model it as a diffusive process, as done by Nott and Brady (1994).[1] Then, given a particle self-diffusivity D and channel thickness $2b$, we can calculate a characteristic time $t_{\mathrm{sim}} = b^2/(4D)$ for the shear-induced migration (sim). In Sec 1.6.1, we have seen that $D = \hat{D}(\phi)\,\dot{\gamma}\,a^2$, where $\dot{\gamma}$ is the local shear rate, a is the particle radius, and $\hat{D}$ is an increasing function of the local volume fraction ϕ. Then, we may estimate a characteristic strain taking $\phi \approx \phi_{\mathrm{bulk}}$ and $\dot{\gamma} \approx 1.5V_{\mathrm{s}}/b$, to obtain:[2]

$$\bar{\gamma}_{\mathrm{sim}} = t_{\mathrm{sim}}\,V_{\mathrm{s}}/b = \frac{1}{6\hat{D}}\left(\frac{b}{a}\right)^2 . \tag{5.3}$$

The previous equation is valid for steady flows but, like we said before, after a flow reversal the particles transiently lose contacts and, as a simple approximation, we may consider that the irreversible behavior is “paused” until the particles reorganize after an accumulated strain $\bar{\gamma}_{\mathrm{c}}$.

---

[1] We neglect any particle redistribution along the channel length because it would require much more accumulated strain to occur due to diffusion, and also because we do not have any evidence of it before the onset of the instability.

[2] For a Newtonian fluid in Poiseuille flow with average velocity V_{s} and a channel with gap $2b$, the average shear rate is $1.5V_{\mathrm{s}}/b$.

Then, each half oscillation contributes a strain $\bar{\gamma}_0 - \bar{\gamma}_c$ to the migration process, and

$$\frac{\bar{\gamma}_0}{\bar{\gamma}_{\rm sim,osci}} = \frac{\bar{\gamma}_0 - \bar{\gamma}_c}{\bar{\gamma}_{\rm sim}}, \tag{5.4}$$

where $\bar{\gamma}_{\rm sim,osci}$ is an estimation of the accumulated strain needed with oscillations to reach a state equivalent to that reached after a strain $\bar{\gamma}_{\rm sim}$ in steady flows. Next, we will analyze whether $\bar{\gamma}_{\rm onset}$ is equal to $\bar{\gamma}_{\rm sim,osci}$ or, at least, partly explained by it.

In Fig. 5.7, we plot $\bar{\gamma}_0/\bar{\gamma}_{\rm onset}$ as a function of the oscillation amplitude $\bar{\gamma}_0$, that is, we plot the inverse of the number of half oscillations (i.e. reversals) before the onset. This plot is very similar to that of Fig. 5.6, and the conclusions are almost identical: the variation of $\bar{\gamma}_0/\bar{\gamma}_{\rm onset}$ is linear with $\bar{\gamma}_0$ for small enough oscillations ($\bar{\gamma}_0 < 12$). For the small beads a linear fit crosses the horizontal axis at a positive value $\bar{\gamma}_c = 1.8$, similar to the one found in the previous section. On the other hand, the large beads do not seem to agree with this interpretation, but additional experiments with smaller oscillation amplitudes would be required to reach more definitive conclusions.

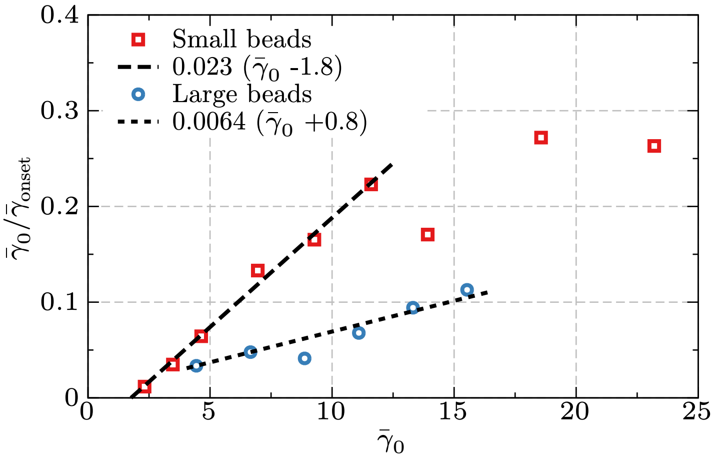

Figure 5.7: Plot of $\bar{\gamma}_0/\bar{\gamma}_{\rm onset}$ versus oscillation amplitude $\bar{\gamma}_0$ for the same experiments as in Fig. 5.5. Fitting linear functions to the points with $\bar{\gamma}_0 < 12$, we can estimate the parameters of Eq. (5.4).

Assuming that $\bar{\gamma}_{\rm onset}$ is equal to $\bar{\gamma}_{\rm sim,osci}$, from the slopes of the linear fits we can estimate $\bar{\gamma}_{\rm sim} \approx 50$ and ≈ 150 for the small and large beads, respectively. If these values are conditioned by the shear-induced migration of particles toward the gap center, then we must also add the strain induced in the suspension as it was injected into the channel for first time. As explained in Sec. 2.4, there are some mixers before the channel inlet that should ensure a well mixed suspension entering the channel. Then, the suspension must reach the position at half the channel length L, where the observation is performed. The experiments with the small particles were performed using a channel of dimensions $L = 200\,\text{mm}$ and $2b = 1\,\text{mm}$, and for the large particles, $L = 150\,\text{mm}$ and $2b = 2\,\text{mm}$. Adding a strain $(L/2)/b$ to each estimation, we obtain $\bar{\gamma}_{\text{sim}} \approx 250$ and ≈ 225 for the small and large beads, respectively. The values are similar now, but a more thorough validation of this correction will require experiments with different bulk volume fractions for both particle types.

On the other hand, while both values are similar, they are significantly below what can be estimated from the literature. For example, from the experiments with steady channel flow of Rashedi et al. (2020), we may estimate $\bar{\gamma}_{\text{sim}} \approx 2000$ (see Sec. 1.6.2 for our discussion), from the experiments with oscillatory pipe flow of Snook, Butler, and Guazzelli (2016), $\bar{\gamma}_{\text{sim}} \approx 850$, and from measurements of $\hat{D}$ of D. Leighton and Acrivos (1987a), $\bar{\gamma}_{\text{sim}} \approx 1150$. One simple explanation is that $\bar{\gamma}_{\text{onset}}$ actually corresponds the onset of the instability, which might occur before the suspension reaches its steady state after a strain $\bar{\gamma}_{\text{sim,osci}}$, as assumed by the previous examples. In the following section, we will investigate the dependence of these parameters on the mean particle volume fraction.

5.3. Influence of the particle volume fraction

Besides the previously introduced experiments with bulk volume fraction $\phi_{\text{bulk}} = 0.40$, we also performed other sets of experiments varying both the oscillation amplitude and the bulk volume fraction, while keeping the same type of particles ($2a \approx 41\,\mu\text{m}$) and the same channel ($2b = 1\,\text{mm}$). Figure 5.8 shows plots of A_{V_y} versus $\bar{\gamma}$ for different oscillation amplitudes $\bar{\gamma}_0$ (inside each plot), and for different ϕ_{bulk} (changes with the plot). The first plot shows the same curves as Fig. 5.3 for completeness. All of them are qualitatively similar in the sense that A_{V_y} starts to increase significantly above a certain strain ($\bar{\gamma}_{\text{onset}}$), until it reaches a maximum at another accumulated strain. Notice that the strains required for this process to develop increase significantly as the volume fraction decreases (look at the horizontal axes). This is natural if we consider that as the particle concentration decreases, the rate of particle interactions will also decrease, slowing down all the processes driven by them. In all these curves, A_{V_y} has a similar initial value (≈ 0.003), but its maximum depends on both the oscillation amplitude and the bulk volume fraction ϕ_{bulk}, generally decreasing for

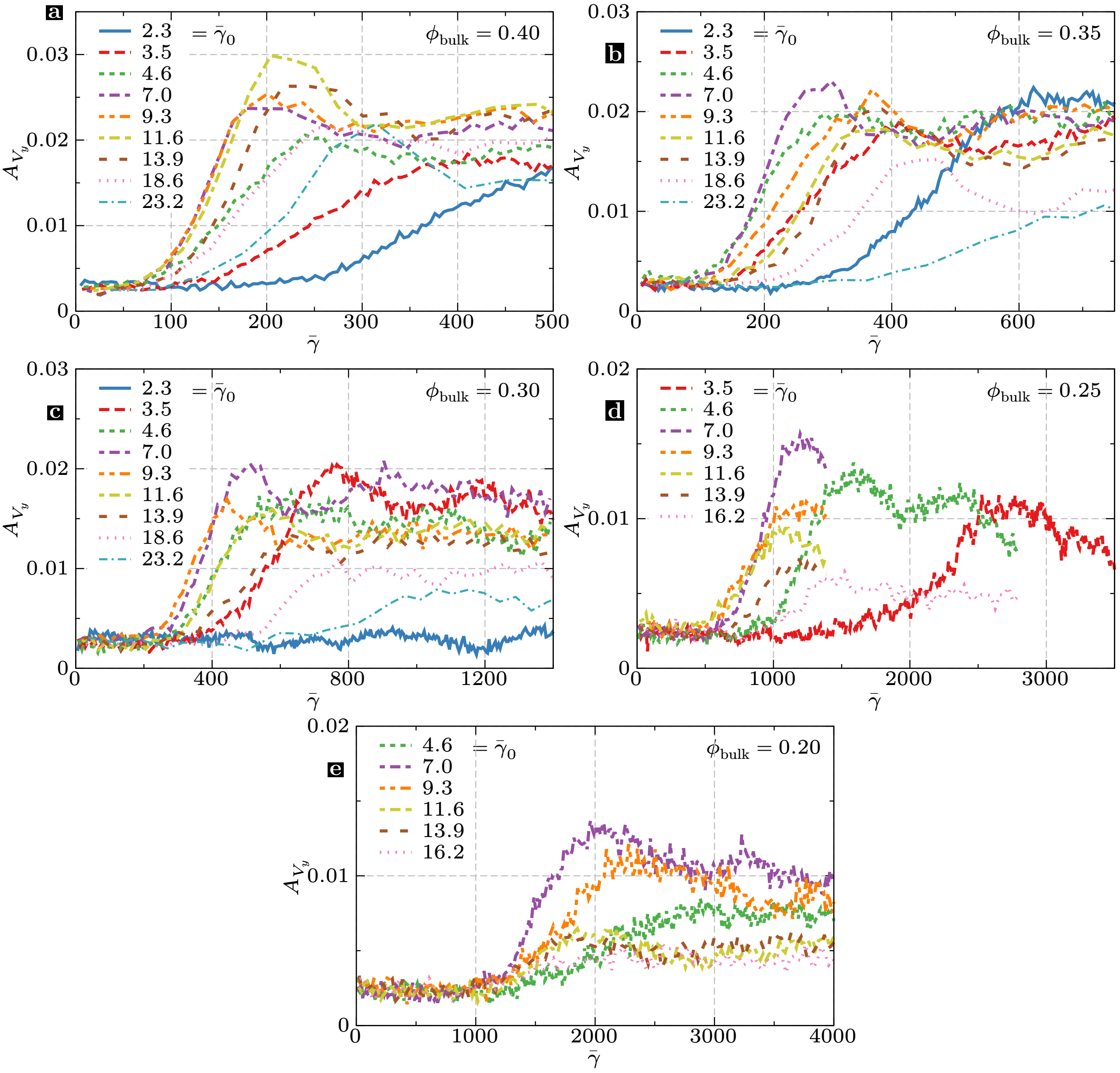

Figure 5.8: Variation of $A_{V_y} = V_{y,\mathrm{cen},ac}/V_{\mathrm{avg}}$ as a function of accumulated strain $\bar{\gamma} = t\,V_{\mathrm{s}}/b$. Each plot corresponds to a different bulk volume fraction ($0.2 \leq \phi_{\mathrm{bulk}} \leq 0.4$) and, inside each, curves for experiments with different oscillation amplitudes $\bar{\gamma}_0$ are shown. Other parameters: $2a \approx 41\,\mathrm{\mu m}$, $2b = 1.0\,\mathrm{mm}$.

smaller ϕ_{bulk}'s.

Figure 5.9(a,b) shows the accumulated strain $\bar{\gamma}_{\text{onset}}$ required for the onset of the instability as a function of the oscillation amplitude $\bar{\gamma}_0$ for each set of experiments (different ϕ_{bulk}). For each set of points, we see again that the onset strains display a minimum in the amplitude range $5 < \bar{\gamma}_0 < 15$, and increase outside this range, except for $\phi_{\text{bulk}} = 0.20$ (orange points), where we do not have enough measurements outside this range to validate the tendencies. It is also clear that the onset strain increases greatly as the volume fraction decreases. For example, at $\phi_{\text{bulk}} = 0.25$, the onset strain is at least ≈ 500, while for $\phi_{\text{bulk}} = 0.40$ all tested oscillation amplitudes already saturated after this much accumulated strain (see Fig. 5.8a). For these reasons, experiments with small volume fractions and/or oscillations amplitudes must have very long durations (sometimes several hours), and before an increase in the transverse velocities is observed, it is impossible to know when (or if) the flow will become unstable.

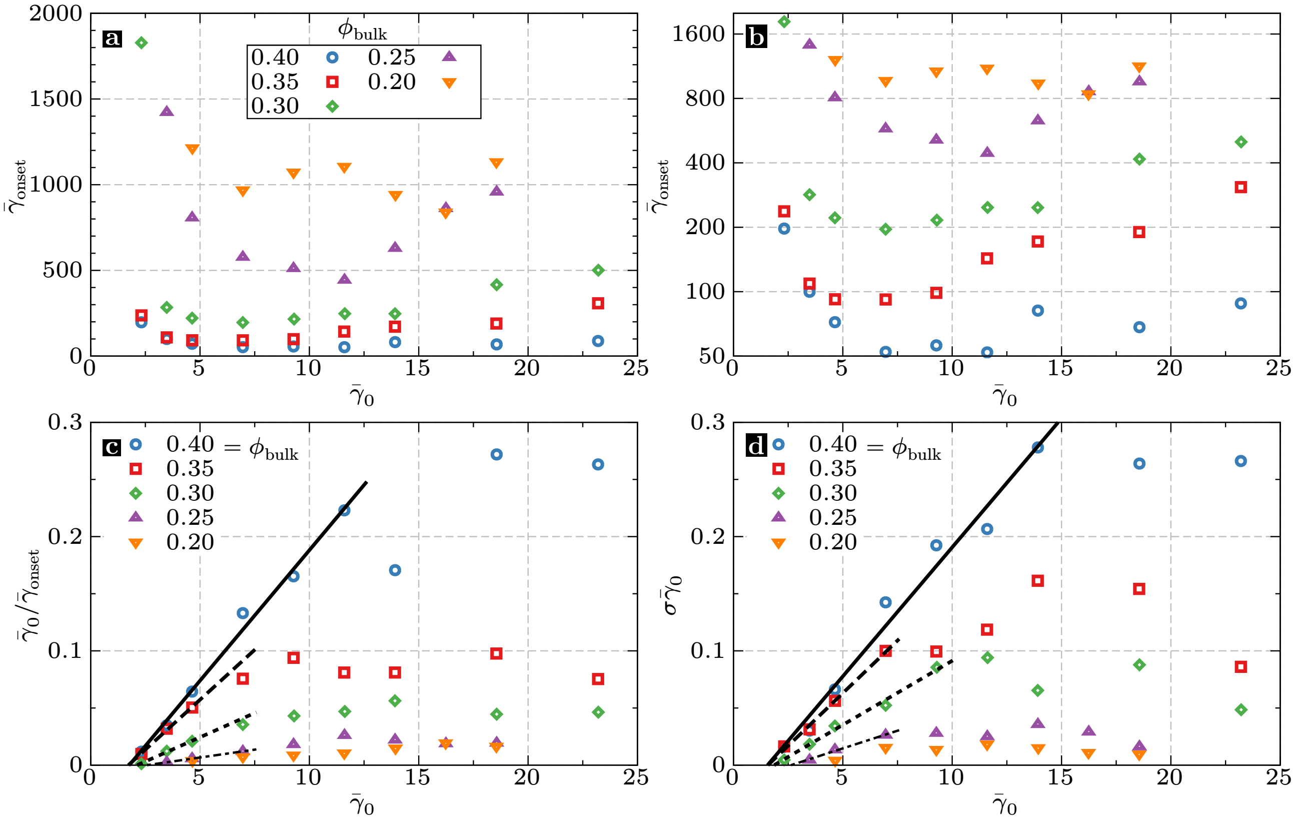

Figure 5.9: Parameters estimated from the curves in Fig. 5.8 to characterize the instability growth versus the oscillation amplitude $\bar{\gamma}_0$ (horizontal axis) and versus the bulk volume fraction ϕ_{bulk} (different symbols and colors). a) $\bar{\gamma}_{\text{onset}}$ with a linear vertical scale. b) $\bar{\gamma}_{\text{onset}}$ with a logarithmic vertical scale (same symbols). c) $\bar{\gamma}_0/\bar{\gamma}_{\text{onset}}$ and linear fits for small oscillations. d) $\sigma\bar{\gamma}_0$ and linear fits for small oscillations.

Figures 5.9(c,d) show $\bar{\gamma}_0/\bar{\gamma}_{\mathrm{onset}}$ and $\sigma\bar{\gamma}_0$ versus $\bar{\gamma}_0$ for the same experiments. Both figures are very similar to each other, and the trends in the sets of points for $\phi_{\mathrm{bulk}} \geq 0.25$ are all qualitatively similar to those for $\phi_{\mathrm{bulk}} = 0.40$ (blue circles), already discussed in the previous section. The main difference between them is the scale of the values, which decreases as ϕ_{bulk} decreases. From the linear fits (black lines), we obtain again values for $\bar{\gamma}_{\mathrm{c}}$, σ_{i}, and $1/\bar{\gamma}_{\mathrm{sim}}$.

In Fig. 5.10a, we show $\bar{\gamma}_{\mathrm{c}}$ as a function of ϕ_{bulk}, obtained from linear fits of $\bar{\gamma}_0/\bar{\gamma}_{\mathrm{onset}}$ (Fig. 5.9c) and $\sigma\bar{\gamma}_0$ (Fig. 5.9d) versus $\bar{\gamma}_0$. Both sets of points have similar values and tendencies. The values are of the order of one and decrease with the volume fraction, similar to the local strains required for the reorganization of the microstructure and also to the critical oscillation amplitude observed in previous works (see Sec. 1.7), both shown in Figs. 3.19b. A more direct comparison with those values is complicated by the fact that the local strain in our system is inhomogeneous across the channel gap, and $\bar{\gamma}$ is a global measure of accumulated strain, proportional to the average one. That being said, in Fig. 3.20 we have seen, for experiments with $\phi_{\mathrm{bulk}} = 0.40$ and the larger particles, that the reorganization of the microstructure is almost complete across the gap after a global strain $\bar{\gamma} \approx 2$ is applied. The similarity of this value with $\bar{\gamma}_{\mathrm{c}}$, agrees with our previous interpretation that the evolution of the instability (onset and growth) occurs mostly after the particle microstructure has built up again following each flow reversal. If the linear fits shown in Figs. 5.9(c,d) truly model the underlying dynamic of the suspension, then $\bar{\gamma}_{\mathrm{c}}$ can be interpreted as a critical strain that must be surpassed between flow reversals for the suspension to evolve irreversibly and the instability to develop.

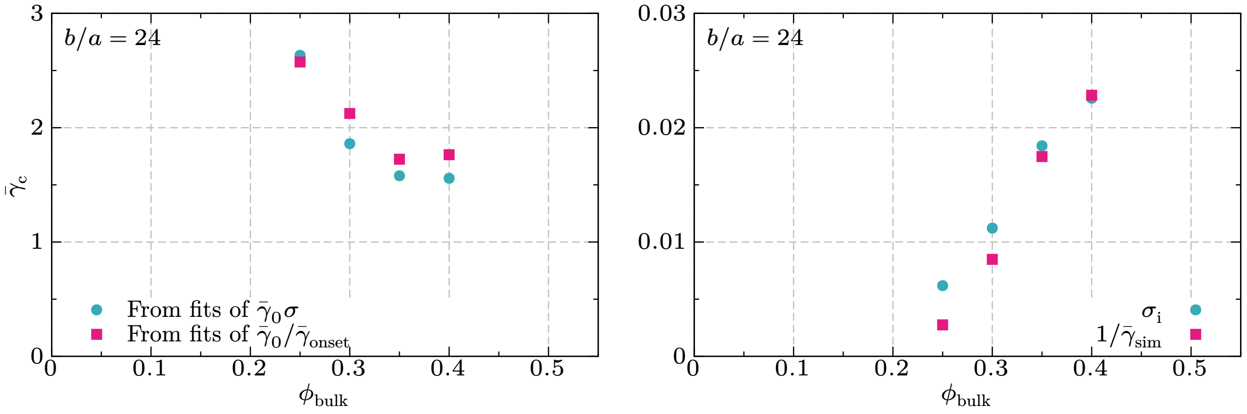

Figure 5.10: Parameters obtained from the linear fits in Figs. 5.9(c,d) as functions of the bulk particle volume fraction ϕ_{bulk}. a) Critical oscillation amplitude $\bar{\gamma}_{\mathrm{c}}$. b) Intrinsic growth rate σ_{i} and parameter $1/\bar{\gamma}_{\mathrm{sim}}$ possibly related to the shear-induced migration.

Figure 5.10b, shows σ_i and $1/\bar{\gamma}_\mathrm{sim}$ as a function of ϕ_bulk, each point having been obtained from the fitted slopes in Figs. 5.9(c,d). The first variable is an effective growth rate after a strain $\bar{\gamma}_\mathrm{c}$ has occurred since the last flow reversal (see Sec. 5.2.1). The second, although not strictly a growth rate, provides information about the rate at which the process(es) occurring before the onset of the instability develop (see Sec. 5.2.2). The fact that both sets of values are similar could be coincidental, but the approximately linear dependence of both with the ϕ_bulk is probably indicative of the influence of particles interactions in the overall development of the instability.

To conclude, we have seen that the perturbations induced by the instability become apparent above a global strain $\bar{\gamma}_\mathrm{onset}$ and, then, grow by a factor σ per unit of strain, until there is a saturation. If we consider that $\bar{\gamma}_\mathrm{onset}$ and $1/\sigma$ are characteristic strain scales for processes happening respectively before and after the onset, then, Figs. 5.9(c,d) makes clear that both scales are similar in their values and variations with respect to ϕ_bulk and $\bar{\gamma}_0$. This is logical given that all irreversible processes in non-Brownian suspensions at $\mathrm{Re} \approx 0$ seem to be driven by same microscopic mechanism: contact interactions between particles. When the particle concentration (i.e. ϕ_bulk) is increased, the frequency of these interactions increases and the instability develops faster (smaller $\bar{\gamma}_\mathrm{onset}$, larger σ). On the other hand, after each flow reversal and until a strain $\bar{\gamma}_c \approx 2$ is accumulated, the effects of contacts may be negligible (or greatly reduced) and the system is stable (no transverse motions of the particles) if the strain between reversals $\bar{\gamma}_0$ is below $\bar{\gamma}_c$. At large oscillation amplitudes ($\bar{\gamma}_0 \gtrsim 14$), the number of reversals $\bar{\gamma}_\mathrm{onset}/\bar{\gamma}_0$ before the onset of the instability seem to more or less plateau, suggesting that each reversal (or oscillation) makes a similar contribution the development of the instability, regardless of the how much straining each oscillation induces. Accordingly, in the limit of a steady flow ($\bar{\gamma}_0 \to \infty$), the system should be stable since no reversals occur.

5.4. Influence of the Reynolds number

In this section, we vary the Reynolds number of the channel flow, $\mathrm{Re} = V_\mathrm{s}\, b\, \rho_f/\eta_f$, by changing different experimental parameters. First, we performed experiments for different surface average velocities V_s, while simultaneously adjusting the period T to keep the oscillation amplitude $\bar{\gamma}_0 = T\, V_\mathrm{s}/(2b)$ constant. Second, we changed the suspending fluid to a Triton-based solution with a much larger viscosity η_f (see a description of the fluid in Sec. 2.2.2). We also modified the channel thickness $2b$, but those experiments will be discussed in Sec. 5.5 as b has an influence on the instability's wavelength and growth rate.

Figure 5.11a displays the curves $A_{V_y}(\bar{\gamma})$ corresponding to experiments with different values of V_s. While the Reynolds number changes by more than an order of magnitude (from 0.05 to 0.8), the curves present a good overlap, confirming that the normalization of the transverse velocities and the time by the mean velocity is appropriate.[3] There are some small differences between the curves, but they do not display any trend and they are similar in scale (along both axes of the plot) to those seen between repetitions of experiments with the same parameters.

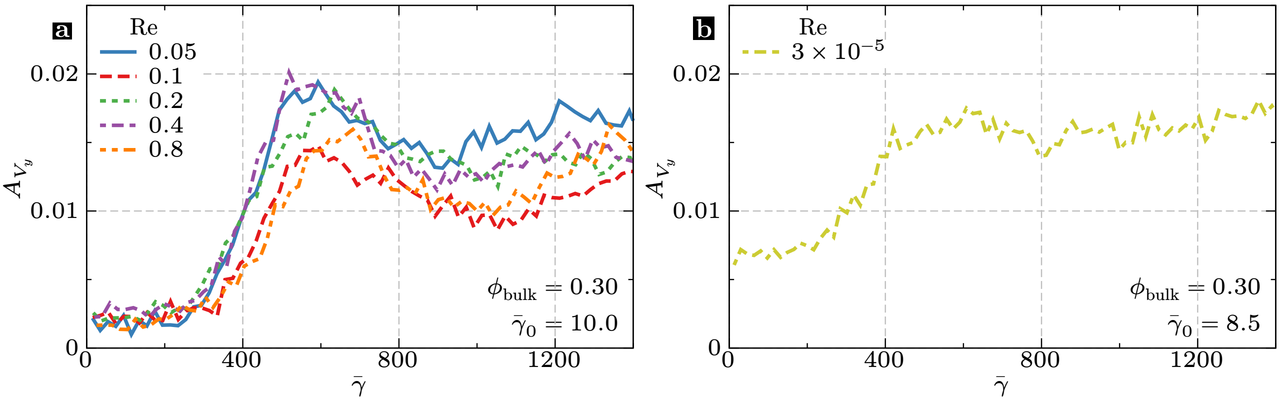

Figure 5.11: Amplitude A_{V_y} of the transverse velocity perturbation as a function of the accumulated strain $\bar{\gamma}$ for experiments with different Reynolds numbers, but similar regarding oscillation amplitude, particle concentration, and channel and particle size. a) $\eta_f \approx 7.6\,\mathrm{mPa\,s}$, $0.31\,\mathrm{mm/s} \le V_\mathrm{s} \le 5.0\,\mathrm{mm/s}$, $\bar{\gamma}_0 = 10.0$, $\phi_\mathrm{bulk} = 0.3$, $2b = 1\,\mathrm{mm}$, $2a \approx 41\,\mu\mathrm{m}$. b) $\eta_f \approx 3.5\,\mathrm{Pa\,s}$, $V_\mathrm{s} = 0.12\,\mathrm{mm/s}$, $\bar{\gamma}_0 = 8.5$, $\phi_\mathrm{bulk} = 0.3$, $2b = 0.84\,\mathrm{mm}$, $2a \approx 41\,\mu\mathrm{m}$.

In order to do a more stringent test, we performed experiments using a Triton-based solution with ≈ 500 times the viscosity of the previous thiocyanate-based one. In Fig. 5.11b, we present one experiment with Re three orders of magnitude smaller that the smaller one in the previous figure (left). Again, we see a clear increase of the transverse velocities (characterized by A_{V_y}) reaching a maximum value $A_{V_y} \approx 0.017$ similar to the previous one after an accumulated strain $\bar{\gamma} \approx 600$, also similar. The only notable difference is the larger initial value of A_{V_y} (0.007 vs 0.002). The images from this experiment display the particles as blurry dots because we could not match the index of refraction between the particles and the Triton mixture as well as with the thiocyanate one used in the previous experiments. This mismatch probably

---

[3] All the velocities are normalized by the average longitudinal velocity V_avg, measured at each time from the velocity profile $V_x(y,t)$. Although this average velocity has some slight variations with time (see Sec. 5.6), it is proportional to $V_\mathrm{s} = Q_0/S$, where Q_0 is the flow rate configured for the pump and S is the area of the channel cross section.

resulted in a less precise detection of the particles, and introduced artificial fluctuations that increase the noise level in our measurements of the transverse velocities.

Besides the amplitude, we also verified that the transverse velocities form a periodic pattern, alternating in sign along the channel length. This pattern has a wavelength λ between $6\,b$ and $8\,b$, similar to the previously shown results.

In summary, we have seen that even when the Reynolds number is reduced by four orders of magnitude (respect to the experiments in the previous sections), a periodic secondary flow structure with similar properties is still observed, thus, we conclude that this flow instability is not driven by inertial effects.

5.5. Influence of the channel thickness

In our experiments, the only length scales seemly relevant are the particle radius a and the channel half thickness b, making b/a an important nondimensional parameter. Previous works have shown that particle diffusion and particle fluxes are expected to be proportional to the square of the particle radius a (see Sec. 1.6). Then, changes in the macroscopic particle distribution induced by shearing the suspension, should develop with characteristic strains proportional to $(b/a)^2$, as proposed for the onset of the instability in Sec. 5.2.2. Somewhat to our surprise, in Fig. 5.5 we have seen that experiments with our larger beads ($2a \approx 85\,\mu\text{m}$) have characteristic deformations for the development of the instability significantly larger than the smaller beads ($2a \approx 41\,\mu\text{m}$), even though both sets of experiments have similar values of b/a (≈ 24). As mentioned before, one possible explanation is that the larger particles have a smaller surface roughness (relative to their sizes) or that short range repulsive forces make direct contacts between them less frequent. Both propositions have in common the introduction of an additional length scale which may differ between the particle types, but which would be too small to be observed in our experimental device. In this section, we study the influence of the variations of b while using only the smaller ($2a \approx 41\,\mu\text{m}$) beads.

Larger channel thickness

We performed experiments with $\phi_{\text{bulk}} = 0.4$ and a channel with a thickness $2b = 2.1\,\text{mm}$ (width $W = 10\,\text{mm}$), roughly twice the size of that used in Secs. 5.1 and 5.2. The flow rate was doubled in order to keep the surface average velocity similar at $V_s = 1.30\,\mathrm{mm/s}$. In general, we observe the same behavior: after a number of oscillations a secondary velocity field with recirculation rolls appears. The wavelengths measured in units of b, remain similar around $7\,b$.

Figure 5.12a shows the wavelength λ divided by b versus the oscillation amplitude $\bar{\gamma}_0$ for three sets of experiments: small beads and $b/a = 24$ (Sec. 5.2), small beads and $b/a = 51$ (this section), and large beads and $b/a = 24$ (Chapter 4). All of them with $\phi_{\mathrm{bulk}} = 0.40$. The points collapse quite well, with a trend toward larger wavelengths as the oscillation amplitude increases. Plots for the experiments with smaller particle concentrations ($0.20 \leq \phi_{\mathrm{bulk}} \leq 0.35$, not shown here) display similar values and trends.

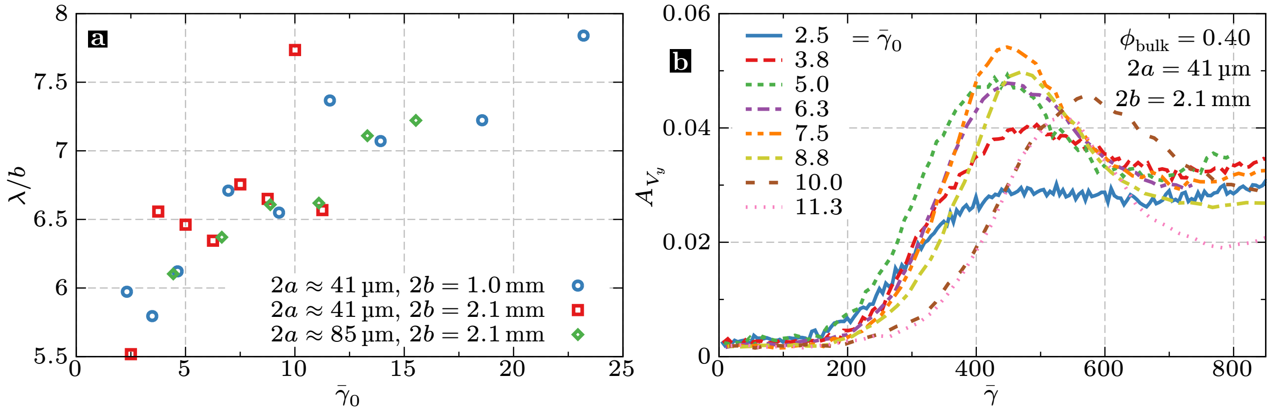

Figure 5.12: a) Normalized wavelength λ/b as a function of the oscillation amplitude $\bar{\gamma}_0$ for three sets of experiments with different particle diameters $2a$ or channel thicknesses $2b$. b) Amplitude $A_{\mathrm{V_y}}$ of the transverse velocity perturbation as a function of the accumulated strain $\bar{\gamma}$ for experiments with different oscillation amplitudes $\bar{\gamma}_0$ with ratio $b/a = 51$ (red squares in plot a).

In Fig. 5.12b, we see the plots of $A_{V_y}(\bar{\gamma})$ for $b/a = 51$. There, the peak values of A_{V_y} and the strains $\bar{\gamma}$ at which those are reached are about twice as large as those seen in Fig. 5.3, using a channel with $2b = 1.0\,\mathrm{mm}$ ($b/a = 24$) and all other parameters equal. From these curves, we estimated the accumulated strain $\bar{\gamma}_{\mathrm{onset}}$ required for the onset of the instability, and its growth rate σ, following the same procedure used in Sec. 5.2.

In Fig. 5.13a, we see that $\bar{\gamma}_{\mathrm{onset}}$ is between three and four times larger for $b/a = 51$ than for $b/a = 24$, except for oscillation amplitudes smaller than $\bar{\gamma}_0 \approx 6$, where the trends is unclear. From the discussion at the beginning of this section, we expected $\bar{\gamma}_{\mathrm{onset}}$ to scale as $(b/a)^2$, and although the results are not too far from that [$(b/a)^2$ changes by a factor 4.5], it is unclear why the points for $b/a = 51$ show a tendency to increase with $\bar{\gamma}_0$ in a range where the points for $b/a = 24$ remain more or less flat.

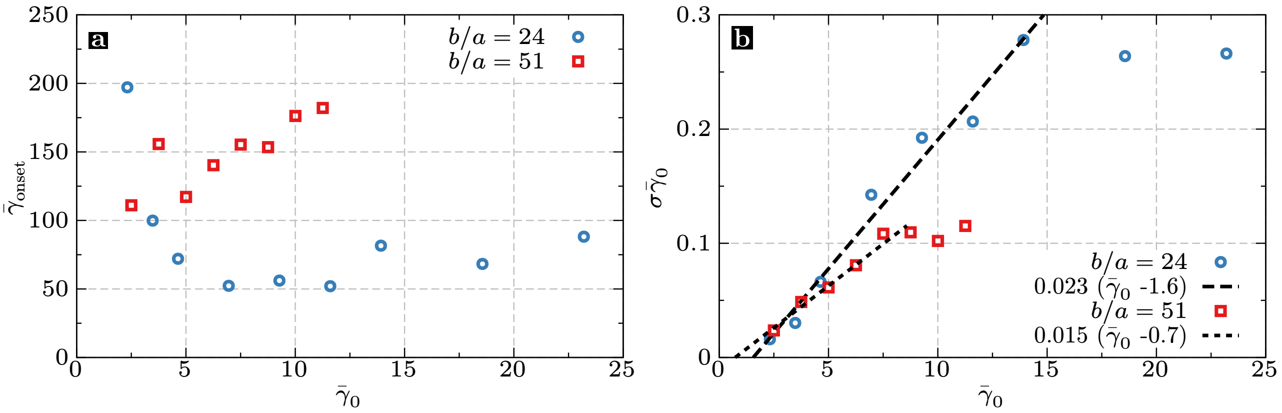

Figure 5.13: Comparison of results between experiments with $b/a = 51$ and $b/a = 24$, for particles with the same diameter $2a \approx 41\,\mu\mathrm{m}$. a) Strain $\bar{\gamma}_{\mathrm{onset}}$ for the onset of the instability as a function of the oscillation amplitude $\bar{\gamma}_0$. b) $\sigma\bar{\gamma}_0$ as a function of the oscillation amplitude $\bar{\gamma}_0$. The linear fits for low oscillation amplitudes correspond to Eq. (5.2).

Figure 5.13b shows $\sigma\bar{\gamma}_0$ versus $\bar{\gamma}_0$, and the corresponding linear fits for small enough oscillations ($\bar{\gamma}_0 < 14$ for $b/a = 24$, $\bar{\gamma}_0 < 7.5$ for $b/a = 51$). As explained in Sec. 5.2.1, the slopes of these fits allow us to estimate an intrinsic growth rate σ_{i}, which is independent of the oscillation amplitude, while the position on the horizontal axis where the line crosses estimates $\bar{\gamma}_{\mathrm{c}}$, the minimal oscillation amplitude required for the suspension to behave irreversibly, and thus, for the flow to become unstable. Both sets of points present similar qualitative tendencies: a linear increase at small amplitudes with plateau starting from a particular amplitude (≈ 14 for $b/a = 24$, and ≈ 7.5 for $b/a = 51$). In general, the plots give the impression that they would overlap better if we multiplied $\bar{\gamma}_0$ by a factor two in both axes and only for $b/a = 51$, or almost equivalently, if we replaced $\bar{\gamma}_0 = T\,V_{\mathrm{s}}/b$ by just $T\,V_{\mathrm{s}}$. But then, one may wonder is there is another, more appropriate, length scale to normalize macroscopic distances instead of b. Like for the left figure, more experiments with different particle and channel sizes will be required to better understand the scaling laws of these experiments.

Smaller channel thickness

We also performed experiments in a channel with a smaller thickness $2b = 0.51\,\mathrm{mm}$ (same width $W = 10\,\mathrm{mm}$) using the small beads ($2a \approx 41\,\mu\mathrm{m}$). To our surprise, experiments with $\phi_{\mathrm{bulk}} = 0.4$ and $10.5 \leq \bar{\gamma}_0 \leq 42.1$ did not show clear signs of the instability, that is, A_{V_y} does not increase significantly with the oscillations, and no periodic pattern is apparent in the velocity field. This was so even after the suspension reached accumulated strains > 2000, an order of magnitude larger than the values of $\bar{\gamma}_{\mathrm{onset}}$ observed with larger channel gaps (see

Fig. 5.9(a,b) for $2b \approx 1\,\mathrm{mm}$, and Fig. 5.13a for $2b \approx 2\,\mathrm{mm}$). On the other hand, experiments with $\phi_{\mathrm{bulk}} = 0.3$ and $7.9 \leq \bar{\gamma}_0 \leq 13.2$ did show the characteristic increase of A_{V_y}, but with very small peak values of A_{V_y}, as displayed in Fig. 5.14.

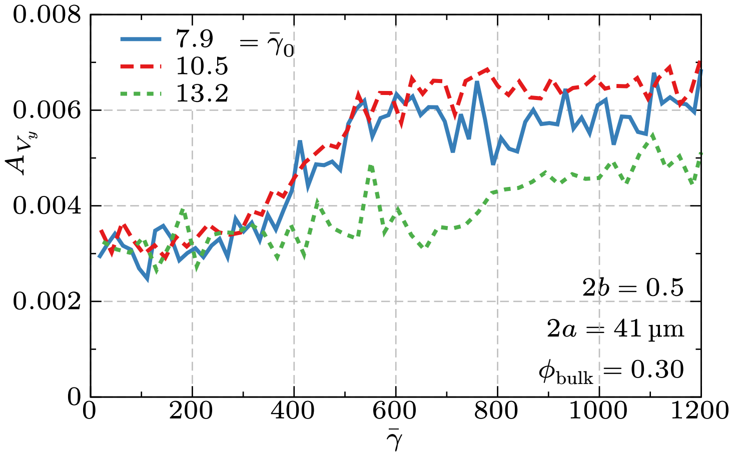

Figure 5.14: Amplitude A_{V_y} of the transverse velocity perturbation as a function of the accumulated strain $\bar{\gamma}$ for experiments with a small channel thickness ($2b = 0.5\,\mathrm{mm}$) and different oscillation amplitudes $\bar{\gamma}_0$.

One possible interpretation of these results is that at high confinements (small b/a) and large concentrations (large ϕ_{bulk}) the process responsible for the instability is hindered, possibly as a consequence of particle layering (Snook, Butler, and Guazzelli 2016) or some other form of strong ordering which prevents the deformation of the central band into the wavy pattern observed in Fig. 4.1.

5.6. Influence of the position of the observation plane across the channel width

All the previous experiments were performed with the observation plane (the one illuminated by the laser) near the center of the channel width W (see Fig. 2.7). In order to test if our results were influenced by the plane position, we performed a few experiments in other positions. In Fig. 5.15a, we present the amplitude A_{V_y} versus the accumulated strain $\bar{\gamma}$ for experiments that differ only by the distance z of the observation plane from the lateral wall. In the three cases, the instability appears and A_{V_y} reaches a peak value for similar accumulated strains, but the overall values of A_{V_y} decrease as the wall is approached (smaller z). One possible factor to consider here is a modulation of the longitudinal velocity, that is, the possibility of V_x changing significantly with z.

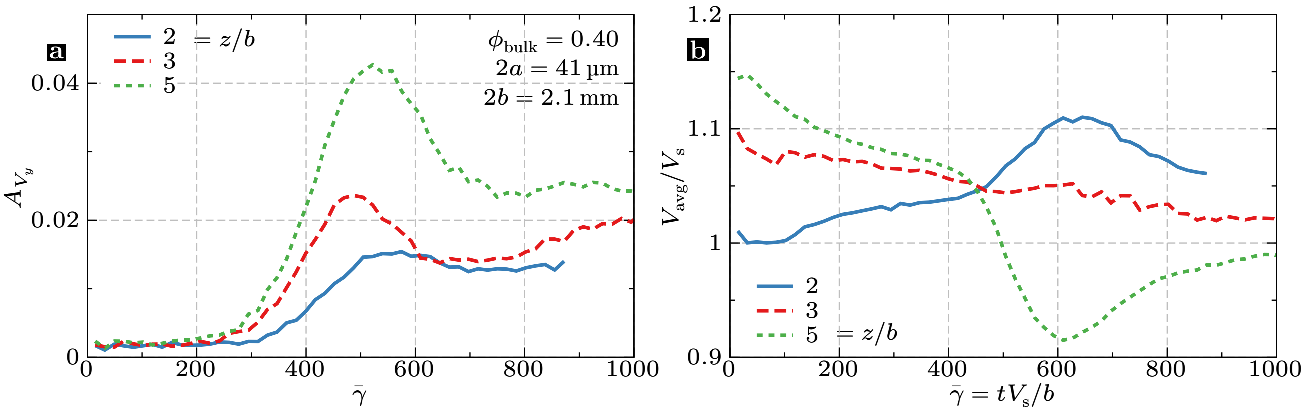

Figure 5.15: a) Amplitude A_{V_y} of the transverse velocity perturbation as a function of the accumulated strain $\bar{\gamma}$ for experiments with the observation plane at different distances z along the channel width, with $z = 0$ and $z = W = 10\,\text{mm}$ corresponding to the lateral walls. b) Average absolute longitudinal velocity V_{avg} as a function of the accumulated strain $\bar{\gamma}$ for the same experiments. Common parameters: $\phi_{\text{bulk}} = 0.4$, $2a \approx 41\,\mu\text{m}$, $2b = 2.1\,\text{mm}$, $V_{\text{s}} = 1.3\,\text{mm/s}$, $\bar{\gamma}_0 = 8.7$.

Figure 5.15b shows plots of the average absolute longitudinal velocity V_{avg} normalized by V_{s} (same value in all three experiments) versus the accumulated strain. We observe here that initially V_{avg} is slightly smaller toward the lateral wall ($z = 0$) and, more importantly, that the onset of the instability has a small but clear influence on V_{avg}, increasing it near the wall ($z = 2\,b$) and decreasing it near the center of the channel width ($z = 5\,b \approx W/2$). Note that the variations of V_{avg} with $\bar{\gamma}$ (i.e. time) are not significant enough to explain the much larger (in proportion) variations of A_{V_y} seen in Fig. 5.15a.

These variations of dynamic variables with the position across the channel width made us wonder if there are three-dimensional characteristics of the flow which influence the onset and development of the instability. In order to address this question, we proceeded to vary the channel width W as shown in the following section.

5.7. Influence of the channel cross-sectional aspect ratio

Zrehen and Ramachandran (2013) report experiments with a non-Brownian suspension steadily flowing through a channel with square cross-section. They observe that an element of suspension painted with dye follows a trajectory that departs from a straight line parallel to the walls. They explain this behavior as a consequence of normal stress differences which induce a secondary flow in the plane of the cross section (perpendicular to the main flow).

The above observations contrast with our secondary flow which is characterized by recirculation rolls in the flow-gradient plane, however, such effects could be simultaneously present in our experiments. Considering also our previous observation of a dependence of our transverse velocity perturbations on the position across the channel width, we wanted to know if the instability under study here is adequately described as a two-dimensional flow between two very large planes ($W \gg 2b$), or whether variations along the third dimension (width, z position) should be taken into account.

We started by doing experiments in a channel with a square cross section ($2\,\mathrm{mm} \times 2\,\mathrm{mm}$), observing no increase in the transverse velocities even after accumulating large strains (>3700, $\phi_{\mathrm{bulk}} = 0.3$ and 0.4, $2a \approx 41\,\mathrm{\mu m}$, $\bar{\gamma}_0 = 9.3$). Then, in order to better understand the effect of the channel cross sectional aspect ratio $W/(2b)$, we made channels with thickness $2b = 1\,\mathrm{mm}$ and a range of widths $2.7\,\mathrm{mm} \leq W \leq 11\,\mathrm{mm}$ (see Table 2.1), and performed experiments with $\phi_{\mathrm{bulk}} = 0.4$ and large oscillation amplitudes ($\bar{\gamma}_0 \gg \bar{\gamma}_c$, see Secs. 5.2.1 and 5.2.2) in each channel. Figure 5.16 shows the results: the curves $A_{V_y}(\bar{\gamma})$ on the left, and the accumulated strains $\bar{\gamma}_{\mathrm{onset}}$ required for instability onset obtained from the curves, on the right. Looking at the right plot, we see that the onset strain increases sharply as the aspect ratio is reduced, possibly diverging around $W/(2b) \approx 2$. On the other hand, for aspect ratios $\gtrsim 5$, changing the aspect ratio does not have any significant effect.

44

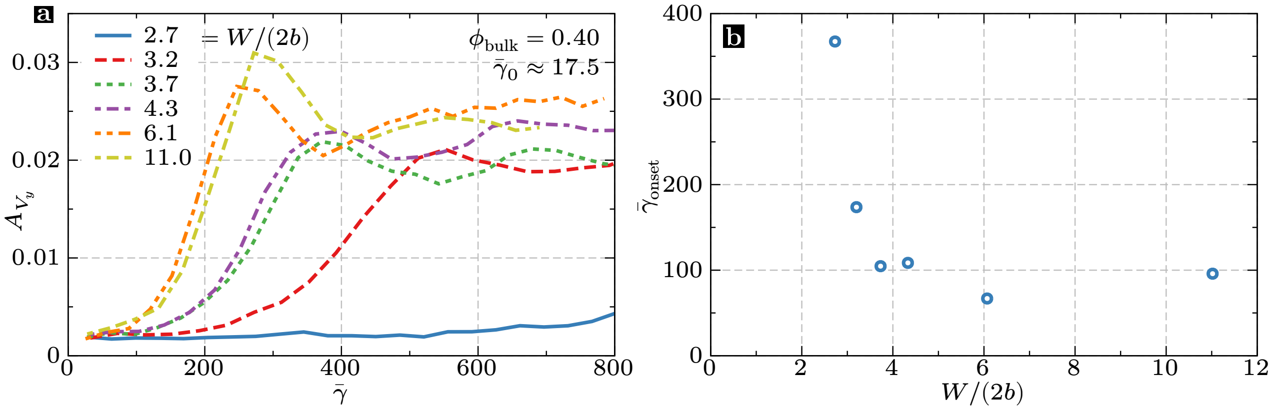

Figure 5.16: a) Amplitude $A_{\mathrm{V_y}}$ of the transverse velocity perturbation as a function of the accumulated strain $\bar{\gamma}$ for experiments with different channel aspect ratios $W/(2b)$ and similar oscillation amplitudes $15 < \bar{\gamma}_0 < 20$. b) Accumulated strain $\bar{\gamma}_{\mathrm{onset}}$ required for the onset of the instability as a function of the channel aspect ratio $W/(2b)$ for the same experiments as in plot a. Other parameters: $\phi_{\mathrm{bulk}} = 0.4$, $2a \approx 41\,\mathrm{\mu m}$, $2b = 1\,\mathrm{mm}$, $15 < \bar{\gamma}_0 < 20$.

We conclude from this that our instability is hindered by the proximity of the lateral walls (parallel to the observation plane), but may be described as a mostly two-dimensional effect in the flow-gradient plane when lateral walls are far enough [$W/(2b) > 5$].

To characterize better the effect of a reduction of the aspect ratio, we performed experiments varying the oscillation amplitude $\bar{\gamma}_0$ for one small aspect ratio $[W/(2b) = 3.2]$, and compared the results with our previous experiments with $W/(2b) = 11$. Figure 5.17 shows the results: the new curves $A_{V_y}(\bar{\gamma})$ on the left, and plots of $\sigma\bar{\gamma}_0$ versus $\bar{\gamma}_0$ comparing both sets of experiments, on the right. Remember that the linear fits of the right plot give us estimations of $\bar{\gamma}_c$, a critical or threshold amplitude for the instability, and of σ_i, its intrinsic growth rate (see Sec. 5.2.1). Comparing the experiments with $W/(2b) = 3.2$ to those with $W/(2b) = 11$, in Fig. 5.17b, we observe first that the intrinsic growth rate is reduced approximately in half (from 0.023 to 0.012) and, second, that the critical amplitude increases significantly from 1.6 to 4.4. Both effects make the instability weaker and more difficult to observe.

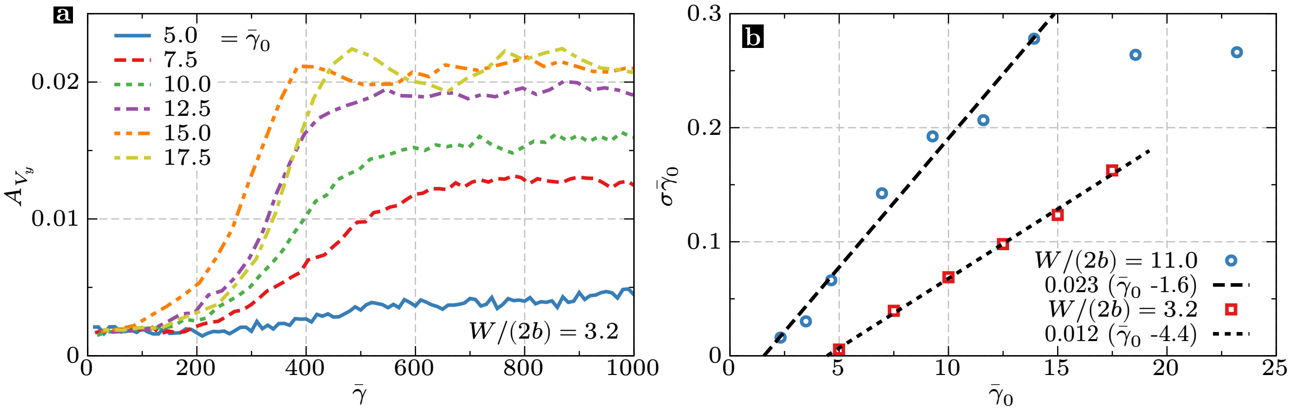

Figure 5.17: a) Amplitude A_{V_y} of the transverse velocity perturbation as a function of the accumulated strain $\bar{\gamma}$ for experiments with a small channel aspect ratio $[W/(2b) = 3.2]$ and different oscillation amplitudes $\bar{\gamma}_0$. b) Variation of $\sigma\bar{\gamma}_0$ as a function of the oscillation amplitude $\bar{\gamma}_0$. The linear fits for low-enough oscillation amplitudes correspond to Eq. (5.2). Other parameters: $\phi_{\text{bulk}} = 0.4$, $2a \approx 41\,\mu\text{m}$, $2b = 1\,\text{mm}$.

Chapter 6

Conclusions and perspectives

6.1. Summary

In this thesis, we performed experiments with concentrated suspensions of PMMA spheres in Newtonian fluids oscillating inside narrow channels, making observations at the particle scale in order to capture trajectories of a larger number of them and, then, using this information to infer both microscopic and macroscopic properties, such as the particle pair distribution, and concentration and velocity fields.

One of the main results of our work is a thorough characterization of a flow instability that arises during oscillations and induces a secondary flow superimposed on the primary oscillatory motion. The cumulative effect of this secondary flow can modulate the particle concentration along the channel into a periodic pattern of stripes orthogonal to the flow direction (see Fig. C.1), seen in experiments performed previously in our laboratories (Roht 2017).

In a typical experiment, the initial particle distribution is not uniform, instead the local

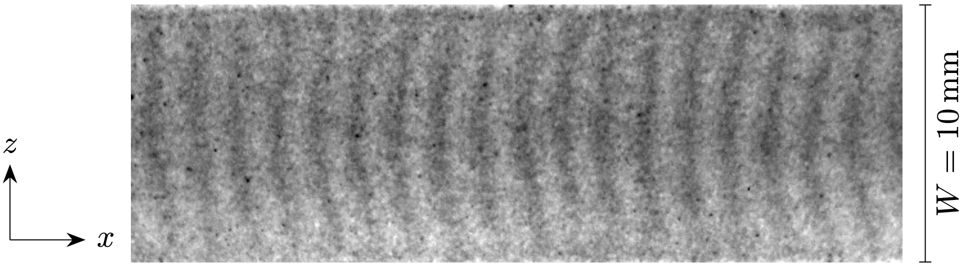

Figure 6.1: Typical pattern of stripes perpendicular to the main flow direction (x) observed in experiments with oscillatory flows of suspensions inside Hele-Shaw cells. The varying intensity corresponds to different particle concentrations. More details in Sec. 1.8.

volume fraction ϕ is larger in the center of the thickness ($y = 0$) than near the walls ($y = \pm b$), as a consequence of the shear-induced migration of particles occurring during the preliminary setup (e.g. filling the channel). The migration may continue during the first oscillations, increasing even more the volume fraction ϕ_{cen} in the center of the gap, as shown by the green curve in Fig. C.3. During this time ($\bar{\gamma} \lesssim 200$ in Fig. C.3), the local volume fraction ϕ varies only across the thickness (y direction) with profiles $\phi(y)$ that increase from the walls to the center, and the velocity field is mostly laminar ($V_y \approx 0$, V_x independent of x) with profiles $V_x(y)$ that become progressively more blunted in the center (compared to the parabolic profiles of a Newtonian fluid) as the bulk volume fraction ϕ_{bulk} is increased, in agreement with other authors (Lyon and Leal 1998a; Rashedi et al. 2020).

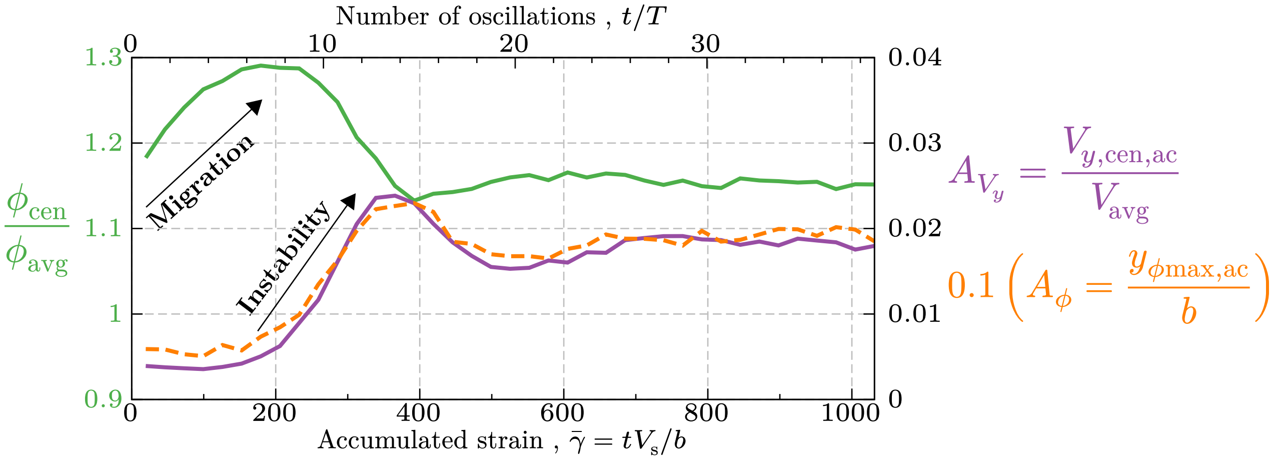

Figure 6.2: Temporal evolution of three important variables tracking the state of the suspension during the oscillations, for a typical experiment using the particles of diameter $2a \approx 85\,\mu\text{m}$. Green curve, left axis: ratio $\phi_{\text{cen}}/\phi_{\text{avg}}$ between particle volume fraction in the center of the channel gap and the average across it. Purple curve, right axis: amplitude $V_{y,\text{cen,ac}}$ of the perturbation in the transverse velocity component normalized by the average longitudinal velocity V_{avg} of the main flow. Dashed orange curve, right axis: amplitude $y_{\phi\text{max,ac}}$ of the deformation of the central band of high particle concentration, normalized by the channel half thickness b and multiplied by 0.1 to allow a direct comparison with the $V_{y,\text{cen,ac}}/V_{\text{avg}}$. Note that $\phi_{\text{avg}} \approx \phi_{\text{bulk}} = 0.4$, and $V_{\text{avg}} \approx V_{\text{s}} \sim 1\,\text{mm/s}$. More details in Sec. 4.2.

Afterward, we observe the onset of the unstable behavior: a secondary flow appears, characterized by recirculation cells of alternating directions along the channel length (x direction), with a wavelength $\lambda \approx 7\,b$ (see Fig. C.4). This secondary flow is present in addition to the main oscillatory one which convects it back and forth, making it change its directions each time the oscillatory flow reverses. We characterize its amplitude A_{V_y} from measurements of the transverse velocity component V_y near the center of the gap, and observe that it increases in time with an approximately exponential form until it saturates at values of the order of

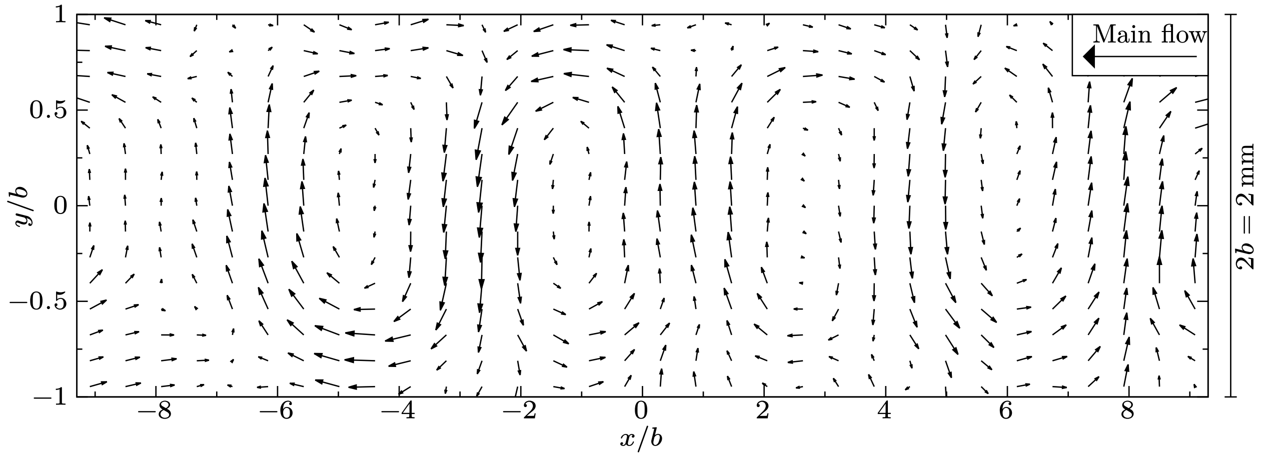

Figure 6.3: Velocity field corresponding to the secondary flow observed when the instability is fully developed. It is one of the two components into which we separate the total velocity field, together with the main laminar flow which points to the left at this time. More details in Sec. 4.1.

$0.02\,V_{\mathrm{avg}}$ (see the purple curve in Fig. C.3).

In time, the accumulated effect of this flow changes the particle distribution, moving particles out of the gap center (see the decrease of $\phi_{\mathrm{cen}}/\phi_{\mathrm{avg}}$ in Fig. C.3) and producing a wave-like pattern in the volume fraction ϕ with the same wavelength λ (see Fig. C.5), and which is also convected back and forth by the main flow. A study of the amplitude A_ϕ of this pattern (see the dashed orange curve in Fig. C.3) shows an evolution in time nearly identical (within a constant scale factor) to that of A_{V_y}, corresponding to the secondary flow. One difference can be observed shortly after a flow reversal: the pattern in ϕ is unaffected by it, while the secondary flow changes directions and abruptly decreases its amplitude, eventually, recovering its value from before the reversal after enough strain is accumulated. This latter behavior is similar to those observed for the microstructure and the local shear rate after a reversal.

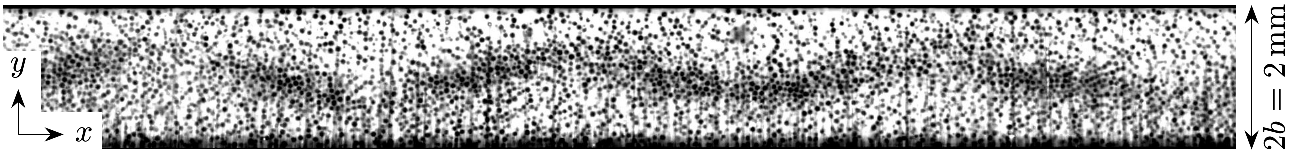

Figure 6.4: Wave-like pattern formed by particles (black disks) when the instability is fully developed. Image taken from the experiment described in Sec. 3.1.

Further studies varying the experimental parameters (mainly ϕ_{bulk} and $\bar{\gamma}_0$) showed that the instability grows faster with increasing bulk volume fraction ϕ_{bulk}, suggesting that the mechanism is related to irreversible particle interactions, almost certainly through solid contacts. On the other hand, as the strain amplitude $\bar{\gamma}_0$ decreases, the instability grows progressively more slowly, until a threshold amplitude $\bar{\gamma}_c \sim 1$ is reached. For $\bar{\gamma}_0 < \bar{\gamma}_c$, the flow is stable with no significant transverse velocities or variations of ϕ along x, in agreement with the previously observed reversibility in suspensions under oscillations of small amplitude (see Sec. 1.7.2). At the other extreme, for large enough amplitudes $\bar{\gamma}_0$, the characteristic accumulated strain $\bar{\gamma}_{\text{onset}}$ above which the instability becomes readily apparent increases with $\bar{\gamma}_0$, suggesting that steady flows ($\bar{\gamma}_0 \to \infty$) are also stable.

Irreversible interactions between neighboring particles are known to induce an anisotropic microstructure which has a strong influence in the suspension stresses and viscosity, and which gets reorganized after each flow reversal (see Sec. 1.5). Since the instability may be a consequence of the cumulative effect of such irreversible processes after several flow reversal, we characterized the microstructure just before the onset of the instability, between successive reversals and across the channel gap.

In the quasi-steady state reached before a reversal, we observed pair distribution functions $g(r_x, r_y)$ with a high probability of particle pairs nearly in contact ($r/a \approx 2$) except in the extensional quadrants where the pairs are separating on average (see the first plot of Fig. C.6). Our local measurements of $g(r_x, r_y)$ across the gap are in good agreement with measurements obtained in uniform conditions by Blanc, Lemaire, et al. (2013), except near the wall and near the gap center, where the respective effects of the confinement and of the very small shear rate take precedence. After a flow reversal, the extensional quadrants change positions and this structure gets reorganized into a horizontally mirrored one matching the new flow direction (see Fig. C.6). This process occurs as the suspensions is strained with a local strain

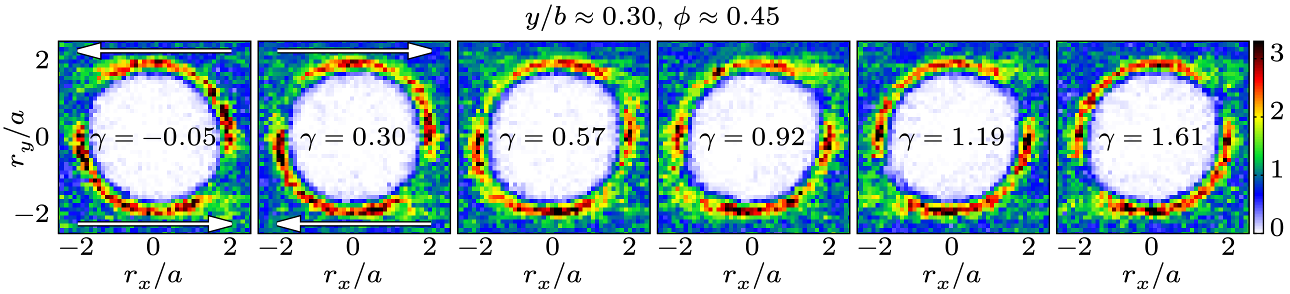

Figure 6.5: Pair distribution functions $g(r_x, r_y)$ at different instants before (first plot) and after (other five plots) a flow reversal occurring when $\gamma = 0$, where γ is the strain accumulated locally at the position y of the center of the strip under consideration across the channel gap. The white arrows indicate the local shear directions before and after the flow reversal. More details in Sec. 3.5.

rate $\dot{\gamma}$ which increases from zero, at the gap center ($y = 0$), to a maximum near the walls ($y = \pm b$).

Although the accumulated strain needed to reorganize the microstructure decreases with the local volume fraction ϕ, which in turns decreases toward the walls, the variations of the $\dot{\gamma}$ across the gap are much more important and, therefore, there is a transient state after a flow reversal when the microstructure has fully reorganized near the walls but, near the gap center, the process is still in progress. In the following section, we will discuss a possible mechanism for the instability, leaving for a future work the full development of the ideas.

6.2. Discussion on the possible causes of the instability

From our experiments, we have found that the most relevant time scale corresponds to the shearing of the suspension, with a characteristic time b/V_s. In Fig. 5.11a, we have shown that plots of A_{Vy} versus $\bar{\gamma} = tV_\mathrm{s}/b$ (tracking the development of the instability) are roughly invariant with respect to variations of V_s by a factor up to 16. The other time scale in our experiments is the oscillation period T: in this case, we have found that the characteristic strain amplitude $\bar{\gamma}_0 = TV_\mathrm{s}/(2b)$ is the relevant parameter that accounts for variations in the instability, when parameters other than T and V_s (e.g. ϕ_bulk) remain fixed. Therefore, mechanisms that rely on external forces (e.g. gravity), thermal diffusion or inertial effects are unlikely to explain our observations, as each would introduce a distinct time scale which does not scale with V_s and alter the good overlay seen in Fig. 5.11a. Given the possibility of remanent effects from inertia, the influence of the latter was tested specifically in experiments using a more viscous suspending fluid (Re $\sim 10^{-5}$ versus Re ~ 0.1), observing again a good overlay of the corresponding plots of $A_{Vy}(\bar{\gamma})$ with those from the previous experiments (see Fig. 5.11b).

A possible mechanism inspired by the co-extrusion of viscoelastic fluids

One important characteristic of our experiments is that the suspension viscosity η_s and normal stress differences (N_1 and N_2) vary across the gap. Such inhomogeneities in the properties of a fluid can be a source of instabilities and, in particular, flows where two different fluids are being co-extruded have been extensively studied (see, for instance, the review by Govindarajan and Sahu 2014).

Here, we will analyze the possible similarities between our experiments and pressure-driven flows through pipes or channels with a sharp interface between two distinct fluids: one at the core and, another, surrounding it and reaching to the walls, as illustrated by Fig. 6.6. This configuration serves as a simplified model of our suspension flow: the core represents the region where particle concentration approaches the jamming fraction and the shear rate is nearly zero, while, outside, the concentration is more moderate and the shear rate increases toward its maximum value near the walls. Now, we will consider under which conditions (always with Re → 0) a straight interface between those two fluids may be unstable and spontaneously acquire a form periodic in the flow direction (x).

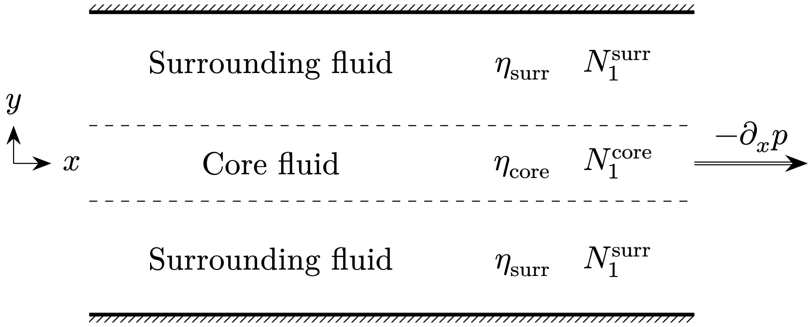

Figure 6.6: Representation of two fluids (core and surrounding) being co-extruded between the walls of either a circular pipe or a straight channel. The fluids may differ in their viscosities (η_{core} and η_{surr}) and first normal stress differences (N_1^{core} and N_1^{surr}).

Let us first consider instabilities induced purely by a jump in the viscosity. Both experimental and theoretical studies show that the interface between two Newtonian fluids that differ in their viscosity can be unstable (Hinch 1984; Than, Rosso, and Joseph 1987; d'Olce et al. 2008), but linear stability analysis shows that the growth rate is proportional to the Reynolds number (Re). As mentioned above, we did not observe significant variations in the amplitude A_{V_y} of the velocity perturbations as a function of the accumulated strain $\bar{\gamma}$ in experiments changing Re by several orders of magnitude, nor in the growth rates calculated from these curves. From this, we conclude that is is unlikely that inhomogeneities in the viscosity alone do explain our observations. Then, we will turn our attention to the effect of a jump in the first normal stress differences N_1 and show that it can induce an instability in the absence of inertia (Re = 0).

Hinch, Harris, and Rallison (1992) analyze an interfacial instability in the core-annular flow of two viscoelastic fluids being co-extruded through a circular pipe. The diagram of

Fig. 6.6 is also relevant here if we take x to be axial direction and y, the radial one. The reason to consider viscoelastic fluids is that they have a positive N_1 that increases with the elasticity and two different fluids may display a jump of N_1 at the interface, but the proposed mechanism also applies to other fluids with non-zero N_1, such as particle suspensions. These authors found that the interface is unstable if the core fluid is more elastic ($N_1^{\text{core}} > N_1^{\text{surr}}$) with a (real) growth rate that is unaffected by a jump in the viscosity ($\eta_{\text{core}} \neq \eta_{\text{surr}}$) when inertial effects are neglected ($\text{Re} = 0$). Moreover, they discuss both varicose and sinuous modes (see Fig. 6.7) and show that the sinuous mode is always more unstable (i.e. larger growth rate). This seems to agree qualitatively with our observations of a wave-like perturbation in the particle distribution, though caution must be exercised since our geometry is different (a straight channel instead of a circular pipe).

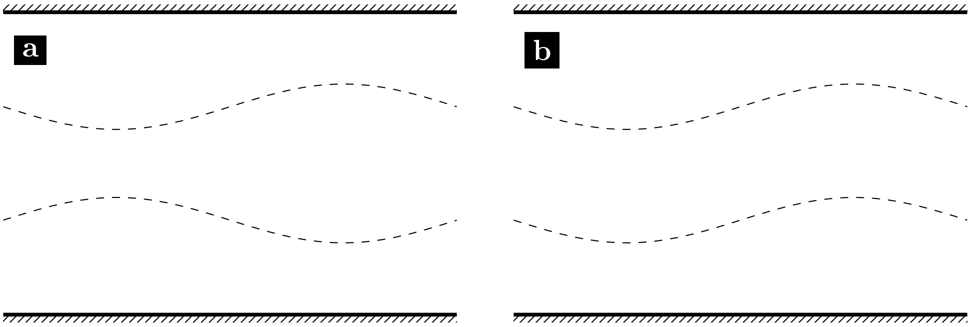

Figure 6.7: Varicose (a) and sinuous (b) perturbation modes corresponding to the situation show in Fig. 6.6.

For channel flows with a symmetric configuration like that show in Fig. 6.6, Khomami and Ranjbaran (1997) observed experimentally that the interface between two co-extruded polymer melts (which are viscoelastic) can be unstable with respect to small perturbations with wavelengths of the order of the gap thickness. This instability occurs for several combinations of experimental parameters and, of particular interest to us, when the core fluid is the more viscous and elastic ($N_1^{\text{core}} > N_1^{\text{surr}}$). Let us now consider when such a situation may arise in suspensions.

Stability of pressure-driven flows of suspensions

In steady flows with a fully migrated volume fraction profile, the suspension viscosity η_{s} will be larger in the core ($\eta_{\text{core}} > \eta_{\text{surr}}$) since η_{s} increases with the local particle volume fraction ϕ (and ϕ increases toward the core), while the first normal stress difference N_1 will be smaller there ($N_1^{\mathrm{core}} < N_1^{\mathrm{surr}}$) since N_1 is negative (far enough from the walls) and decreasing with ϕ (see Fig. 1.4a). The previous works with viscoelastic fluid suggest that this configuration should be stable, and that is indeed what is observed in the steady flow of suspensions through pipes and channels at low Reynolds numbers (Hampton et al. 1997; Rashedi et al. 2020).

On the other hand, we must remember that both the viscosity and N_1 depend on the local microstructure of the suspension and, after a flow reversal, the microstructure gets reorganized and the absolute values of both properties transiently decrease, with N_1 possibly becoming positive as shown in simulations (Bricker and Butler 2007; Chacko et al. 2018). One of our key observations is that this process of microstructure reorganization occurs inhomogeneously across the gap: after a characteristic strain $\bar{\gamma} \approx 2$ has accumulated since the reversal, the reorganization is essentially complete near the walls but remains incomplete near the gap center (see Fig. 6.8). This opens the possibility of an N_1 profile which is, transiently, larger (positive or less negative) near the "core" region of the gap than outside it.

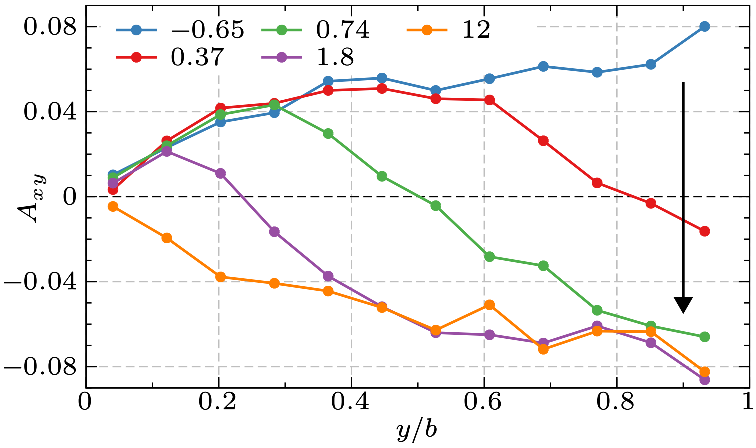

Figure 6.8: Microstructure anisotropy parameter A_{xy} from the center of the gap ($y/b = 0$) to the top wall ($y/b = 1$), for different accumulated strains $\bar{\gamma} = t\,V_{\mathrm{s}}/b$ after a flow reversal (the numbers shown in the legend). Reproduction of Fig. 3.20.

Then, we can imagine the following scenario for our experiments. After a reversal, the viscosity and the absolute value of the normal stress differences (NSD) decrease everywhere across the gap due to the particles losing contacts between them. In this state, the suspension is roughly reversible: if the flow is reversed again now, the particles will simply retrace their trajectories with negligible self-diffusivity (until new contacts form). This corresponds to our observation that the instability does not occur for strain amplitudes $\bar{\gamma}_0 < \bar{\gamma}_{\mathrm{c}} \sim 1$ (see Sec. 5.2.1 and Fig. 5.9). For larger strain amplitudes, the microstructure begins to get reorganized near the walls, where the shear rate is largest, inducing particle contacts and recovering the quasi-steady viscosity and NSD's there. It is during this transient state with a partially reorganized microstructure that we imagine the instability growing, possibly as a consequence of a value of N_1 larger in a core region than outside. In Sec. 5.2.1, we propose as a simple interpretation that the instability has an intrinsic growth rate σ_i which is constant after a strain $\bar{\gamma}_c$ has been applied since the reversal and up to the next reversal. Then, in Fig. 5.6, we see that this explains well our measured growth rate σ up to a strain amplitude $\bar{\gamma}_{0,\mathrm{sat}} \approx 15$ for experiments with $\phi_\mathrm{bulk} = 0.4$. It is possible then that this is the strain required for the quasi-steady state to be recovered all across the gap (or most of it), with the flow becoming stable again. Finally, we may conjecture that, for large strain amplitudes ($\bar{\gamma}_0 > \bar{\gamma}_{0,\mathrm{sat}}$), an unstable perturbation grows during a strain $\bar{\gamma}_{0,\mathrm{sat}} - \bar{\gamma}_\mathrm{c}$ and, then, the flow becomes stable again, with the shear-induced migration possibly counteracting the perturbation for very large strain amplitudes.

An additional factor to consider is the geometry of the channel, concretely, its cross section. Oscillatory-flow experiments performed by Snook, Butler, and Guazzelli (2016) in a circular pipe did not display any secondary flows or instabilities. Then, our experiments varying the aspect ratio $W/(2b)$ of the channel (Sec. 5.7) show that instability appears only when $W/(2b) \gtrsim 2$ and it is unaffected by the ratio when $W/(2b) \gtrsim 5$, in particular, a channel with a square cross seccion $[W/(2b) = 1]$ did not display any growth in the transverse velocities. Future studies will be needed to understand how the geometry of the channel affects the NSD profiles and the instability mechanism proposed here.

6.3. Future work

The previous discussion prompts us to know more about the rheological properties (e.g. η_s, N_1) of the suspension across the channel gap and in between flow reversals. Measurements of the normal stress differences (N_1 and N_2) can be very difficult to accomplish, even in uniform flows, but viscosity profiles $\eta_\mathrm{s}(y,t)$ may be calculated using simultaneous measurements of the pressure gradient and the shear rate profile, as pointed out in Sec. 3.3. Since in channel flows the pressure should vary mainly along the channel length, and in a roughly uniform way, we may estimate the longitudinal pressure gradient $\partial_x p$ using a differential pressure sensor connected by tubes near the inlet and outlet of the channel. Then, with access to $\eta_\mathrm{s}(y,t)$, we may study its relaxation after reversal to determine more precisely when new contacts between the particles are established. This is important since those contacts are the main contribution to the normal stress differences in non-Brownian suspensions. Furthermore, if a quantitative relation between η_s and the microstructure parameter A_{xy} (introduced in Sec. 3.5.3) can be established, knowledge of A_{xy} may be used to infer the suspension viscosity solely from visual measurements.

Experimental measurements might be complemented by calculations of the suspension stresses using one of the many suspension models which account for the microstructure and its variations. For instance, the model proposed by J. J. J. Gillissen and H. J. Wilson (2019) captures the influence of the microstructure in the suspension rheology with a second-order fabric tensor which varies in time depending on the components of the local strain-rate tensor. Their calculations show a transient decrease of the viscosity after reversal in qualitative agreement with experiments like those of Fig. 1.8a, and their model predicts normal stress differences N_1 and N_2 that also decrease in magnitude after reversal. A study of the oscillatory channel flow using such a model would allow us to estimate N_1 across the gap and in between reversals or, more ambitiously, to perform a linear stability analysis of the flow.

Finally, one of the original motivations for the current work was the study of solute dispersion in suspensions undergoing oscillatory flows (Roht 2017). In uniform oscillatory shear flows, Souzy, Pham, and Metzger (2016) found that both the diffusivity of a blob of dye and the self-diffusivity of the particles increase with the strain oscillation amplitude, with a threshold value ≈ 2 which separates a reversible regime with small diffusivities from an irreversible one with large diffusivities. However, in channel flows, inhomogeneities of shear rate and particle concentration are expected to produce spatial variations of both diffusivities. Furthermore, the onset of the instability introduces recirculation cells in the flow which can enhance the mixing of fluids at low Reynolds numbers, for instance, inside microchannels. Performing experiments with a blob of dye (or another inhomogeneous dye distribution) in the suspending fluid will enable us to determine the dye dispersion before and after the onset of the instability.

Appendix A

Optical system used to generate the laser sheet

We describe here the system of lenses used to shape the laser beam into a plane sheet with a thickness smaller than the particles. See Fig. A.1 for reference.[1]

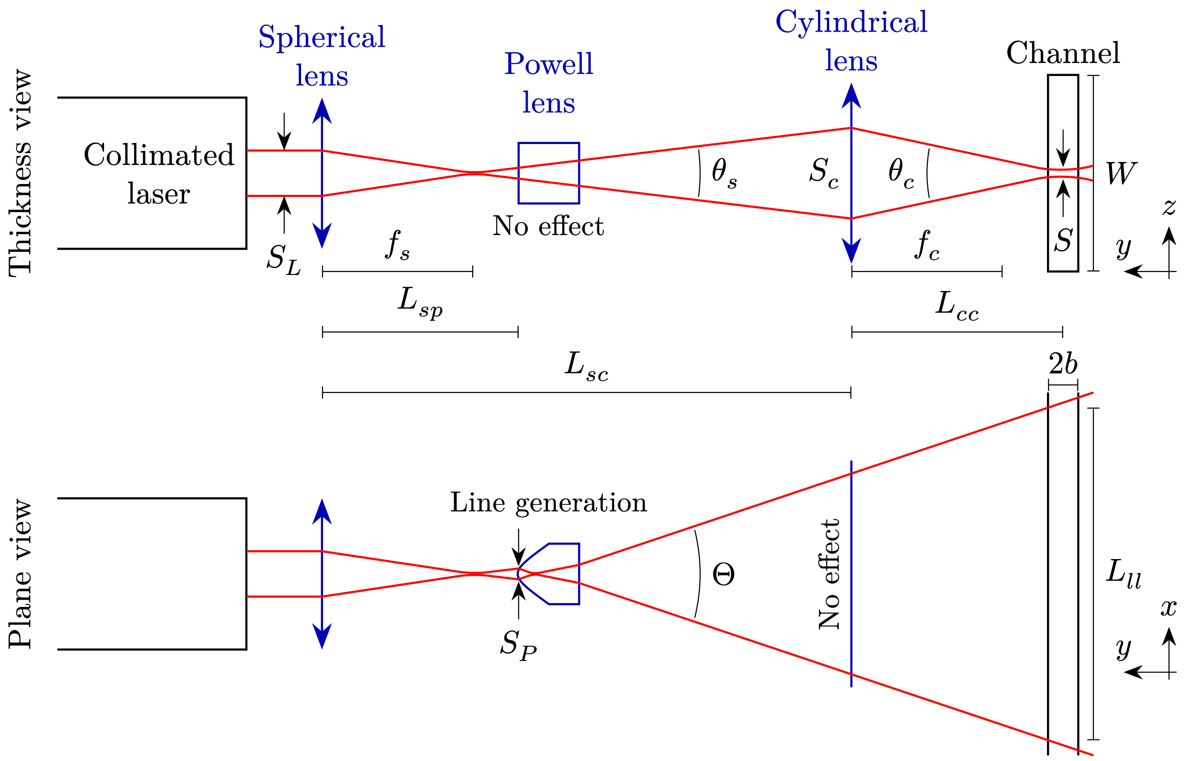

Figure A.1: Schematic view of the optics used to shape the laser beam into a plane sheet. The top part shows a view of the plane yz while, the bottom part, of the plane yx. Directions x, y, and z correspond respectively to the channel length, thickness, and width (see Fig. C.2). Both use the same scale, though some distances may be exaggerated with respect to the real ones.

---

[1] We thank F. Zaldivar from the *Laboratorio de Haces Dirigidos* (FI-UBA, Argentina) for the initial design that lead to this optical system.

First, the collimated laser beam of diameter $S_L \approx 3\,\text{mm}$ reaches a convergent spherical lens with a focal length $f_s = 25.4\,\text{mm}$. At a slightly larger distance L_{sp}, a Powell lens is placed. Powell lenses are laser line generators, designed to work with an incoming beam of diameter S_P (0.8 mm for our lens) and stretch them along one direction (x in this case) with a *fan angle* Θ (30^{o} in our case). The resulting line (as seen when projected on a wall) will have an approximately uniform intensity along its length. If the incoming beam has a diameter larger or smaller than S_p, the light intensity will be more concentrated near the extremes or the center, respectively. In our setup, we set the distance L_{sp} such that the divergent beam coming from the spherical lens reaches the Powell lens with the right diameter:[2]

$$\theta_s \approx \frac{S_L}{f_s} = \frac{S_P}{L_{sp} - f_s} \quad \Rightarrow L_{sp} = f_s(1 + S_P/S_L) \approx 32\,\text{mm}. \tag{A.1}$$

In practice, we adjusted the position of the Powell lens until the uniformity of the illumination was deemed optimal.

Going forward, the light reaches a cylindrical lens with focal length $f_c = 25.0\,\text{mm}$ that focuses it only along the direction z, reducing the laser sheet thickness to S. Due to diffraction, a beam cannot be focused to zero thickness, instead its minimum thickness S (at the focus point) is related to the *full-angular width* θ_c:[3]

$$\frac{4\lambda_{\text{laser}}}{\pi S} \approx \theta_c \approx \frac{S_c}{L_{cc}}, \tag{A.2}$$

where S_c is the thickness of the beam incident on the lens. The thickness S is approximately constant along a length two times the *Rayleigh range*

$$Z_R \approx \frac{\pi S^2}{4\lambda_{\text{laser}}}. \tag{A.3}$$

Since we desire a uniform thickness of the laser sheet over the span of the channel gap $2b$, we need $2Z_R \geq 2b$ and, consequently, the minimum thickness of the laser sheet is

$$S \approx \sqrt{4b\lambda_{\text{laser}}/\pi}. \tag{A.4}$$

---

[2] A more sophisticated setup would include two additional lenses before and after the Powell lens to ensure a collimated incoming beam of the right diameter, but this would make the setup far more complex and the possible advantages were deemed negligible.

[3] Eugene Hecht, "Optics", 4th edition, 2002. Chapter 13, section 13.1.3 .

Two important relations become evident from the previous equations. First, the size of the region we want to illuminate (in this case the channel gap $2b$) sets a lower bound on the sheet thickness S. Second, and maybe counterintuitively, we need to increase the thickness S_c of the beam incident on the cylindrical lens to reduce the final thickness S.

For a given thickness S, the required separations L_{sc} between the lens, and between the cylindrical lens and the channel L_{cc} can be calculated using

$$\theta_s \approx \frac{S_L}{f_s} = \frac{S_c}{L_{sc} - f_s}, \tag{A.5}$$

$$\frac{1}{f_c} = \frac{1}{L_{sc} - f_s} + \frac{1}{L_{cc}}, \tag{A.6}$$

and Eq. A.2, obtaining

$$L_{cc} \approx f_c(1 + \theta_s/\theta_c), \tag{A.7}$$

$$L_{sc} \approx f_s + f_c(1 + \theta_c/\theta_s), \tag{A.8}$$

$$\theta_c/\theta_s \approx \frac{4\lambda_{\text{laser}}}{\pi S}\frac{f_s}{S_L} = 2\sqrt{\frac{\lambda_{\text{laser}}}{\pi b}\frac{f_s}{S_L}} \tag{A.9}$$

Finally, with the channel positioned at a distance $L_{sc} + L_{cc} - L_{sp}$ from the Powell lens, the laser line will reach the first with a length

$$L_{ll} \approx \Theta(L_{sc} + L_{cc} - L_{sp}). \tag{A.10}$$

For a channel gap $2b = 2\,\mathrm{mm}$, the smallest thickness $S \approx 26\,\mu\mathrm{m}$ can be obtained with separations $L_{sc} \approx 56\,\mathrm{mm}$ and $L_{cc} \approx 140\,\mathrm{mm}$. Notice that these calculations require to know the beam diameter S_L of the laser utilized. In practice, we started from an estimation and then adjusted the distances L_{sc} and L_{cc} until the best visualization of the particles was achieved. For a gap $2b = 1\,\mu\mathrm{m}$, the smallest thickness is $S \approx 18\,\mu\mathrm{m}$. As explained in the main text, these values impose a lower limit to the particle size that can be visualized without excessive overlaps between them.

Appendix B

Details of the data analysis

B.1. Determination of the onset and saturation accumulated strains

We introduced in Chapter 4 the quantity A_{V_y}, defined as the ratio of $V_{y,\mathrm{cen,ac}}$ and V_{avg}. The first is a velocity perturbation amplitude calculated from the autocorrelation of the transverse velocities in the gap center (see Secs. 2.7.4 and 4.2), and the second is the average of the longitudinal velocity profile $V_x(y)$ (see Sec. 3.2.1). Both quantities are calculated instantaneously from the tracked particles in each video frame and, then, averaged in time during the last part of each half cycle, when dynamic quantities become approximately steady before the next reversal (see Secs. 3.2 and 4.3). Then, we average the values of successive half oscillations to obtain one value for each oscillation, taking care to use the absolute value of V_{avg} so that the values do not cancel out due to the oscillatory nature of the flow (see Sec. 2.7.3). This way we obtain positive values for $V_{y,\mathrm{cen,ac}}$ and V_{avg} for each oscillation, and use them to track the development of the instability. The ratio of both quantities gives us information about the magnitude of the perturbations introduced by the instability irrespectively of the main flow velocity, which as we have seen in Sec. 5.4, most likely acts just as a multiplier of all the velocities.

On the first row of Fig. B.1, we show a selection of plots of A_{V_y} versus the accumulated strain $\bar{\gamma}$ (blue solid lines). In Chapter 5, we compare such plots for a wide range of different experimental parameters and, in order to do so more effectively, we identify in each plot three stages: before the instability, instability growth, and saturation or non-linear behavior. Here we assume that like for other hydrodynamic instabilities, the process we study here involves a sustained amplification of perturbations already present in the system, but initially indistinguishable from noise. Usually a linearization of the corresponding equations leads to the calculation of a growth rate that depends on the harmonic mode considered for the initial perturbation, and the perturbation observed in practice corresponds to the mode with the largest positive growth rate. Our study being purely experimental, we do not have an analytic growth rate function to consider, but given that we observe a well-defined wave length for the perturbations (see Sec. 4.1) and that the plots $A_{V_y}(\bar{\gamma})$ present what looks like an exponential growth before the saturation, then we proceed with an analysis looking for intervals with constant growth rate.

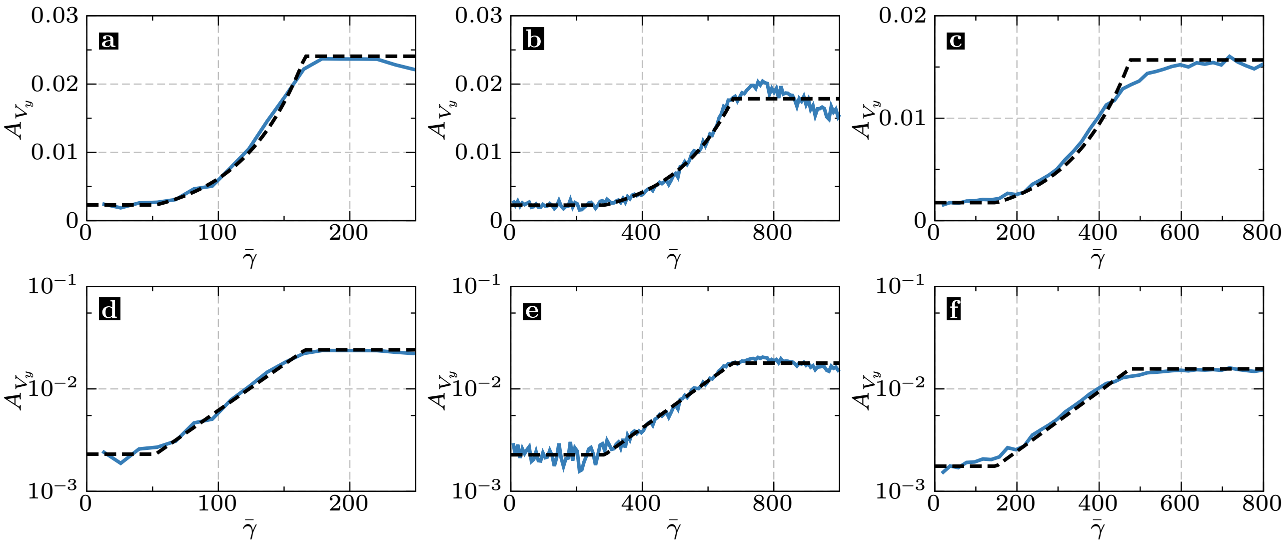

Figure B.1: Plots of $A_{V_y} = V_{y,\mathrm{cen,ac}}/V_{\mathrm{avg}}$ versus $\bar{\gamma} = t\,V_{\mathrm{s}}/b$ for three example experiments (each columns) in linear (top row) and logarithmic (bottom row) vertical scales. The experiments were chosen to give the reader a general idea of how well the function $\exp(f)$ (Eq. B.1, black dashed lines) fits the data (blue solid lines). a,d) Curve $\bar{\gamma}_0 = 7.0$ from Fig. 5.3a. b,e) Curve $\bar{\gamma}_0 = 3.5$ from Fig. 5.8c. c,f) Curve $\bar{\gamma}_0 = 10.0$ from Fig. 5.17a.

In order to identify the time intervals during which the growth is exponential, we look for a linear relation between A_{V_y} and $\bar{\gamma}$ in semilog plots likes the those shown in the second row of Fig. B.1 (blue solid lines). All the curves display roughly the same behavior: an initial lapse with more or less flat values, then a linear increase until the tendency changes, with the curve becoming flatter. To robustly separate these stages and obtain a growth rate, we perform a non-linear fit[1] of the following piecewise function to the data points of $\log(A_{V_y})$:

$$f(\bar{\gamma}) = \begin{cases} L_0 & \bar{\gamma} \leq \bar{\gamma}_{\text{onset}} \\ L_0 + \sigma(\bar{\gamma} - \bar{\gamma}_{\text{onset}}) & \bar{\gamma}_{\text{onset}} \leq \bar{\gamma} \leq \bar{\gamma}_{\text{sat}} \\ L_0 + \sigma(\bar{\gamma}_{\text{sat}} - \bar{\gamma}_{\text{onset}}) & \bar{\gamma} \geq \bar{\gamma}_{\text{sat}} \end{cases}, \tag{B.1}$$

where the fitted parameters are L_0, σ, $\bar{\gamma}_{\text{onset}}$, and $\bar{\gamma}_{\text{sat}}$. The function is not fitted over all the range of values but only up to the point where A_{V_y} reaches a maximum or a plateau, since the function f is not meant to capture the variations that occur after saturation. The dashed black lines in the figure show the resulting function $\exp(f)$ on top of the data (A_{V_y}, blue solid lines) using linear scale (top row) and semilog scale (bottom row). Looking at the bottom plots, the fits seems to obtain the correct slope for the linear part in all cases. The correctness of onset strain $\bar{\gamma}$, corresponding to the first inflection point in f, is difficult to evaluate but the values shown here are plausible and the tendencies shown in Chapter 5 for different experiments are consistent with our interpretations (see Sec. 5.2.2). The fitted strain $\bar{\gamma}_{\text{sat}}$ may be a little over estimated, but sufficient to provide a characteristic value, and also we do not rely too much this value on our analysis of the experiments.

Overall, the previous analysis of the experimental data allows us to obtain some characteristic values from the $A_{V_y}(\bar{\gamma})$ and use them to compare large sets of experiments.

---

[1] Using the Levenberg-Marquardt method for non-linear least square fitting.

Appendix C

Résumé étendu en français

Dans cette thèse, nous avons réalisé des expériences avec des suspensions concentrées de sphères de PMMA dans un fluide newtonien oscillant à l'intérieur de canaux étroits. Le but de ces expériences était de faire progresser notre compréhension des suspensions de particules dans des écoulements d'intérêt pratique, tout en travaillant avec un système modèle plus facile à manipuler, visualiser et interpréter que ses homologues naturels ou industriels. Nous avons fait des observations à l'échelle des particules, capturant les trajectoires d'un plus grand nombre d'entre elles, et avons utilisé ces informations pour déduire à la fois des propriétés microscopiques et macroscopiques, comme la distribution des paires de particules, et les champs de concentration et de vitesse.

L'un des principaux résultats de notre travail est une caractérisation approfondie d'une instabilité d'écoulement survenant pendant les oscillations, et induisant un écoulement secondaire en plus de l'écoulement principal oscillatoire. L'effet cumulatif de cet écoulement secondaire peut moduler la concentration des particules le long du canal en un motif périodique de bandes orthogonales à la direction de l'écoulement (voir Fig. C.1), observé dans des expériences réalisées précédemment dans nos laboratoires (Roht 2017).

Dans des espaces étroits, comme les canaux que nous avons utilisés, l'écoulement est généralement laminaire à moins qu'un obstacle ne soit présent, et l'écoulement secondaire induit par l'instabilité pourrait avoir des applications pratiques accélérant le mélange des particules et des solutés dans de tels espaces. De plus, une compréhension plus approfondie du mécanisme derrière l'instabilité pourrait contribuer à la modélisation de comportements transitoires plus généraux dans les suspensions.

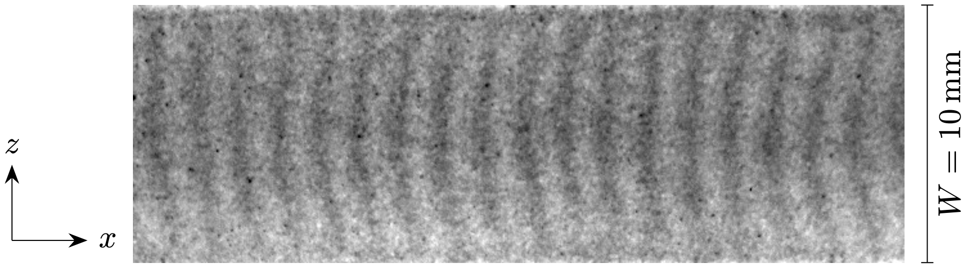

Figure C.1: Motif typique de bandes perpendiculaires à la direction principale de l'écoulement (x) observé dans des expériences avec des écoulements oscillatoires de suspensions à l'intérieur de cellules de Hele-Shaw. L'intensité variable correspond à différentes concentrations de particules.

C.1. Méthodes

Nous avons utilisé des fluides composés de mélanges d'eau et de deux autres composants, avec les proportions ajustées pour correspondre à la densité du fluide et à l'indice de réfraction avec ceux des particules. La correspondance de densité a rendu les particules neutres en flottabilité, évitant la sédimentation, tandis que la correspondance de l'indice de réfraction était nécessaire pour rendre la suspension transparente et permettre de voir à l'intérieur. Des particules de diamètres $2a$ de $40\,\mu\mathrm{m}$ et $85\,\mu\mathrm{m}$ ont été utilisées dans des expériences séparées, avec des résultats cohérents entre elles, bien que les plus grandes aient permis d'étudier la distribution des particules en beaucoup plus de détail. Les deux ensembles de particules étaient suffisamment grands pour être considérés comme non browniens et non colloïdaux, c'est-à-dire avec des effets négligeables du mouvement brownien et des forces interparticulaires à courte portée, en dehors de ceux médiés par le fluide ou les contacts solides. Dans les suspensions résultantes, la fraction ϕ_{bulk} du volume total occupé par les particules variait entre 0,2 et 0,4.

Les suspensions ci-dessus ont été utilisées pour remplir des canaux transparents de longueur $150\,\mathrm{mm}$, et de sections transversales rectangulaires de largeur W et d'épaisseur $2b$. La plupart des expériences ont été réalisées dans des canaux avec $W = 10\,\mathrm{mm}$ et $2b = 1\,\mathrm{mm}$ ou $2\,\mathrm{mm}$; les grands rapports d'aspect $W/(2b)$ font que la géométrie ressemble à deux plans infinis séparés par un petit espace $2b$, c'est-à-dire une cellule de Hele-Shaw. Nous avons également exploré d'autres tailles pour comprendre l'influence du rapport d'aspect $W/(2b)$ et du rapport b/a de l'espace aux dimensions des particules. Une fois tout mis en place, nous avons utilisé une pompe à seringue connectée au canal pour faire osciller la suspension en utilisant des formes d'onde carrées sans déplacement net après chaque cycle. Pendant la première moitié de chaque oscillation, la suspension parcourait une distance moyenne A, induisant une déformation caractéristique de $\bar{\gamma}_0 = A/b$ et, pendant la seconde moitié, la suspension retournait à sa position initiale. Habituellement, la vitesse de surface moyenne $V_\mathrm{s} = 2A/T$ restait constante à $\approx 1\,\mathrm{mm/s}$ ($\mathrm{Re} < 1$), et la période d'oscillation T était utilisée pour changer l'amplitude de déformation $\bar{\gamma}_0$ entre 2 et 24 dans différentes expériences.

Nous avons utilisé la fluorescence et une feuille laser pour observer les particules dans une fine tranche le long de la longueur et de l'épaisseur des canaux, la tranche étant située au milieu de la largeur. Ainsi, nous pouvions voir comment les particules oscillaient le long de la longueur (x direction) et également observer tout déplacement transversal dans la dimension la plus confinée (l'épaisseur $2b$, y direction). Pendant chaque expérience, nous avons enregistré des vidéos de cette vue et les avons traitées pour détecter et suivre les particules visibles dans les images. Par un traitement ultérieur, nous avons obtenu les champs de fraction volumique locale ϕ et de vitesse (V_x, V_y) pour les particules dans le plan d'observation (x, y). La figure C.2 montre un diagramme simplifié de la configuration expérimentale.

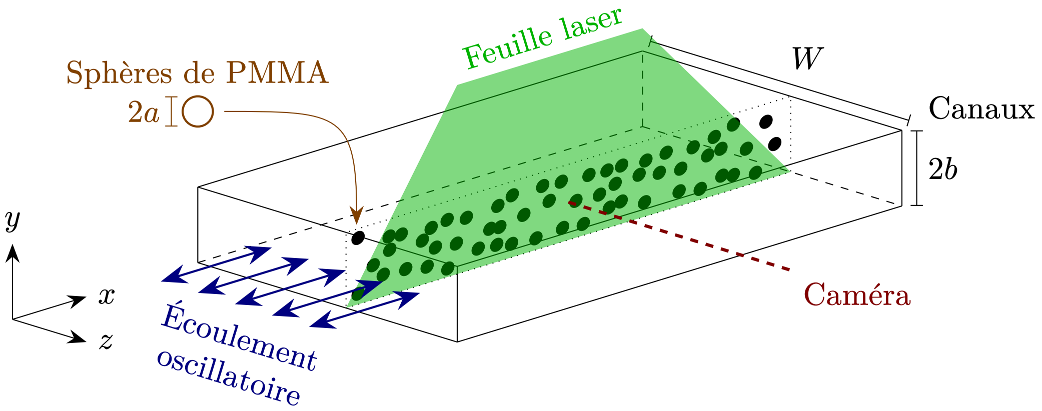

Figure C.2: Diagramme simplifié de la configuration expérimentale.

C.2. Résultats

Dans une expérience typique, la distribution initiale des particules n'est pas uniforme, au lieu de cela, la fraction volumique locale ϕ est plus grande au centre de l'épaisseur ($y = 0$) qu'à proximité des parois ($y = \pm b$), conséquence de la migration des particules induite par le cisaillement survenant lors de la mise en place préliminaire (par exemple, le remplissage du canal). La migration peut continuer pendant les premières oscillations, augmentant encore plus la fraction volumique ϕ_{cen} au centre de l'interstice, comme le montre la courbe verte dans la Fig. C.3. Pendant ce temps ($\bar{\gamma} \lesssim 200$ dans la Fig. C.3), la fraction volumique locale ϕ varie uniquement à travers l'épaisseur (y direction) avec des profils $\phi(y)$ qui augmentent des parois vers le centre, et le champ de vitesse est principalement laminaire ($V_y \approx 0$, V_x indépendant de x) avec des profils $V_x(y)$ qui deviennent progressivement plus émoussés au centre (par rapport aux profils paraboliques d'un fluide newtonien) à mesure que la fraction volumique en vrac ϕ_{bulk} est augmentée, en accord avec d'autres auteurs (Lyon and Leal 1998a; Rashedi et al. 2020).

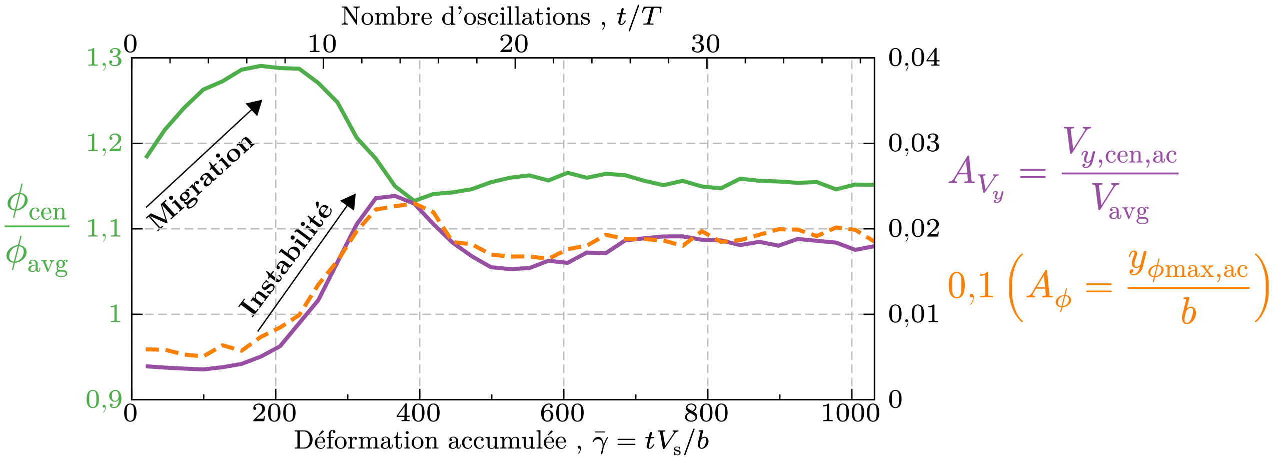

Figure C.3: Évolution temporelle de trois variables importantes suivant l'état de la suspension pendant les oscillations, pour une expérience typique utilisant les particules de diamètre $2a \approx 85\,\mu\text{m}$. Courbe verte, axe de gauche : rapport $\phi_{\text{cen}}/\phi_{\text{avg}}$ entre la fraction volumique des particules au centre de l'interstice du canal et la moyenne sur celui-ci. Courbe violette, axe de droite : amplitude $V_{y,\text{cen,ac}}$ de la perturbation dans la composante de vitesse transversale normalisée par la vitesse longitudinale moyenne V_{avg} du flux principal. Courbe orange en pointillés, axe de droite : amplitude $y_{\phi\max,\text{ac}}$ de la déformation de la bande centrale de haute concentration de particules, normalisée par la demi-épaisseur du canal b et multipliée par 0,1 pour permettre une comparaison directe avec le $V_{y,\text{cen,ac}}/V_{\text{avg}}$. Notez que $\phi_{\text{avg}} \approx \phi_{\text{bulk}} = 0{,}4$, et $V_{\text{avg}} \approx V_s \sim 1\,\text{mm/s}$.

Ensuite, nous observons l'apparition du comportement instable : un écoulement secondaire apparaît, caractérisé par des cellules de recirculation de directions alternées le long de la longueur du canal (x direction), avec une longueur d'onde $\lambda \approx 7\,b$ (voir Fig. C.4). Cet écoulement secondaire est présent en plus de l'écoulement oscillatoire principal qui le transporte d'avant en arrière, ce qui le fait changer de direction à chaque fois que l'écoulement oscillatoire s'inverse. Nous caractérisons son amplitude A_{V_y} à partir de mesures de la composante de vitesse transversale V_y près du centre de l'interstice, et observons qu'elle augmente avec le temps avec une forme approximativement exponentielle jusqu'à ce qu'elle sature à des valeurs de l'ordre de $0{,}02\,V_{\text{avg}}$ (voir la courbe violette dans la Fig. C.3).

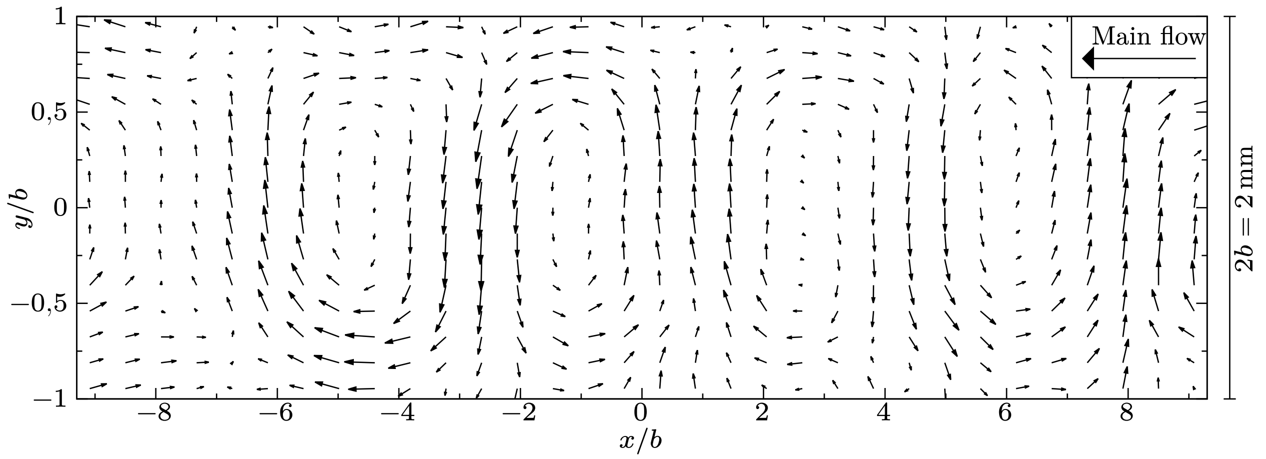

Figure C.4: Champ de vitesse correspondant à l'écoulement secondaire observé lorsque l'instabilité est pleinement développée. Il s'agit de l'une des deux composantes dans lesquelles nous séparons le champ de vitesse total, avec l'écoulement laminaire principal qui pointe vers la gauche à ce moment-là.

Au fil du temps, l'effet cumulatif de cet écoulement modifie la distribution des particules, déplaçant les particules hors du centre de l'interstice (voir la diminution de $\phi_{\text{cen}}/\phi_{\text{avg}}$ dans la Fig. C.3) et produisant un motif de type onde dans la fraction volumique ϕ avec la même longueur d'onde λ (voir Fig. C.5), et qui est également transporté d'avant en arrière par l'écoulement principal. Une étude de l'amplitude A_ϕ de ce motif (voir la courbe orange en pointillés dans la Fig. C.3) montre une évolution dans le temps presque identique (dans les limites d'un facteur d'échelle constant) à celle de A_{V_y}, correspondant à l'écoulement secondaire. Une différence peut être observée peu après une inversion de flux : le motif dans ϕ n'est pas affecté par celle-ci, tandis que l'écoulement secondaire change de direction et diminue brusquement son amplitude, pour finalement, retrouver sa valeur d'avant l'inversion après que suffisamment de déformation ait été accumulée. Ce dernier comportement est similaire à ceux observés pour la microstructure et le taux de cisaillement local après une inversion.

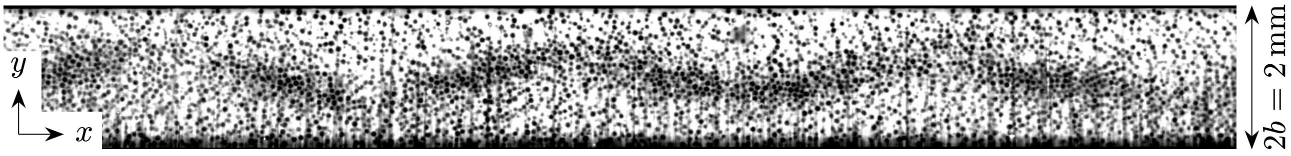

Figure C.5: Motif de type onde formé par les particules (disques noirs) lorsque l'instabilité est pleinement développée.

Des études supplémentaires en faisant varier les paramètres expérimentaux (principalement ϕ_{bulk} et $\bar{\gamma}_0$) ont montré que l'instabilité croît plus rapidement avec l'augmentation de la fraction volumique en vrac ϕ_{bulk}, suggérant que le mécanisme est lié aux interactions irréversibles des particules, presque certainement par des contacts solides. D'autre part, à mesure que l'amplitude de déformation $\bar{\gamma}_0$ diminue, l'instabilité croît de plus en plus lentement, jusqu'à ce qu'une amplitude seuil $\bar{\gamma}_c \sim 1$ soit atteinte. Pour $\bar{\gamma}_0 < \bar{\gamma}_c$, l'écoulement est stable sans vitesses transversales significatives ou variations de ϕ le long de x, en accord avec la réversibilité observée précédemment dans les suspensions sous oscillations de faible amplitude. À l'autre extrême, pour des amplitudes suffisamment grandes $\bar{\gamma}_0$, la déformation accumulée caractéristique $\bar{\gamma}_{\text{onset}}$ au-dessus de laquelle l'instabilité devient clairement apparente augmente avec $\bar{\gamma}_0$, suggérant que les écoulements stationnaire ($\bar{\gamma}_0 \to \infty$) sont également stables.

Les interactions irréversibles entre particules voisines sont connues pour induire une microstructure anisotrope qui a une forte influence sur les contraintes et la viscosité de la suspension, et qui se réorganise après chaque inversion de flux. Puisque l'instabilité peut être une conséquence de l'effet cumulatif de tels processus irréversibles après plusieurs inversions de flux, nous avons caractérisé la microstructure juste avant l'apparition de l'instabilité, entre les inversions successives et à travers l'interstice du canal.

Dans l'état quasi-stationnaire atteint avant une inversion, nous avons observé des fonctions de distribution de paires $g(r_x, r_y)$ avec une probabilité élevée de paires de particules presque en contact ($r/a \approx 2$) sauf dans les quadrants d'extension où les paires se séparent en moyenne (voir le premier graphique de la Fig. C.6). Nos mesures locales de $g(r_x, r_y)$ à travers l'interstice sont en bon accord avec les mesures obtenues dans des conditions uniformes par Blanc, Lemaire, et al. (2013), sauf près de la paroi et près du centre de l'interstice, où les effets respectifs de la confinement et du très faible taux de cisaillement prennent le dessus. Après une inversion de flux, les quadrants d'extension changent de position et cette structure se

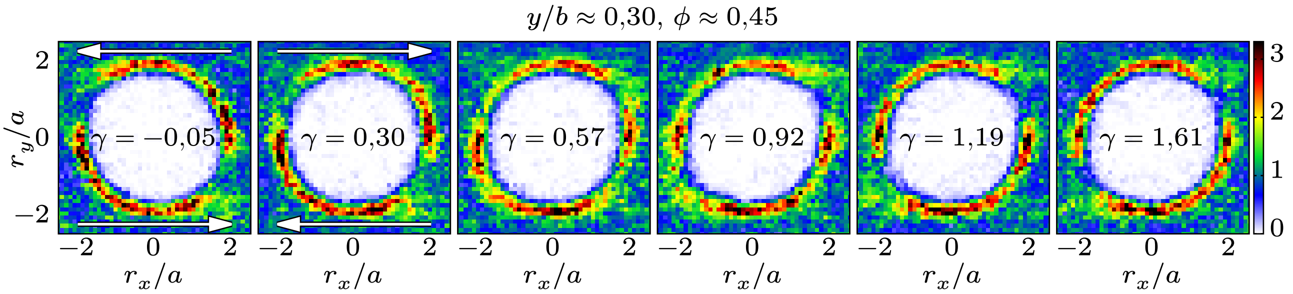

Figure C.6: Fonctions de distribution de paires $g(r_x, r_y)$ à différents instants avant (premier graphique) et après (cinq autres graphiques) une inversion de flux survenant lorsque $\gamma = 0$, où γ est la déformation accumulée localement à la position y du centre de la bande considérée à travers l'interstice du canal. Les flèches blanches indiquent les directions de cisaillement locales avant et après l'inversion de flux.

réorganise en une structure miroir horizontalement correspondante à la nouvelle direction de flux (voir Fig. C.6). Ce processus se produit alors que la suspension est soumise à une déformation avec un taux de déformation local $\dot{\gamma}$ qui augmente de zéro, au centre de l'interstice ($y = 0$), à un maximum près des parois ($y = \pm b$).

Bien que la déformation accumulée nécessaire pour réorganiser la microstructure diminue avec la fraction volumique locale ϕ, qui à son tour diminue vers les parois, les variations de $\dot{\gamma}$ à travers l'interstice sont beaucoup plus importantes et, par conséquent, il existe un état transitoire après une inversion de flux lorsque la microstructure s'est entièrement réorganisée près des parois mais, près du centre de l'interstice, le processus est encore en cours.

Bibliography

Bailey, B. C. and M. Yoda (2003). “An aqueous low-viscosity density- and refractive index-matched suspension system”. In: *Exp. Fluids* 35.123, pp. 1–3.

Barnes, H. (1989). “Shear-thickening (“Dilatancy”) in suspensions of nonaggregating solid particles dispersed in Newtonian liquids”. In: *Journal of Rheology* 33.2, pp. 329–366.

Baskurt, O. K. and H. J. Meiselman (2003). “Blood rheology and hemodynamics”. In: *Seminars in thrombosis and hemostasis.* Vol. 29. 05. Thieme Medical Publishers Inc., pp. 435–450.

Batchelor, G. (1967). *An Introduction to Fluid Dynamics.* Cambridge Mathematical Library. Cambridge University Press.

Batchelor, G. and J. Green (1972). “The determination of the bulk stress in a suspension of spherical particles to order c^2”. In: *Journal of Fluid Mechanics* 56.3, pp. 401–427.

Bird, R. B., R. C. Armstrong, and O. Hassager (1987). *Dynamics of polymeric liquids. Vol. 1: Fluid mechanics.* John Wiley and Sons Inc., New York, NY.

Blanc, F., F. Peters, and E. Lemaire (2011). “Local transient rheological behavior of concentrated suspensions”. In: *J. Rheol.* 55.4, pp. 835–854.

Blanc, F., E. Lemaire, A. Meunier, and F. Peters (2013). “Microstructure in sheared non-Brownian concentrated suspensions”. In: *J. Rheol.* 57.1, pp. 273–292.

Bougouin, A., B. Metzger, Y. Forterre, P. Boustingorry, and H. Lhuissier (2024). “A frictional soliton controls the resistance law of shear-thickening suspensions in pipes”. In: *Proceedings of the National Academy of Sciences* 121.17, e2321581121.

Brady, J. F. and G. Bossis (1988). “Stokesian dynamics”. In: *Annual review of fluid mechanics* 20.1, pp. 111–157.

Brady, J. F. and I. C. Carpen (2002). “Second normal stress jump instability in non-Newtonian fluids”. In: *J. Nonnewton. Fluid Mech.* 102.2, pp. 219–232.

Brady, J. F. and M. Vicic (1995). “Normal stresses in colloidal dispersions”. In: *J. Rheol.* 39.3, pp. 545–566.

Breedveld, V., D. van den Ende, M. Bosscher, R. J. J. Jongschaap, and J. Mellema (2001). “Measuring shear-induced self-diffusion in a counterrotating geometry”. In: *Physical Review E* 63, p. 021403.

Bricker, J. M. and J. E. Butler (2007). “Correlation between stresses and microstructure in concentrated suspensions of non-Brownian spheres subject to unsteady shear flows”. In: *J. Rheol.* 51.4, pp. 735–759.

Butler, J. E., P. D. Majors, and R. T. Bonnecaze (1999). “Observations of shear-induced particle migration for oscillatory flow of a suspension within a tube”. In: *Phys. Fluids* 11.10, pp. 2865–2877.

Chacko, R. N., R. Mari, S. M. Fielding, and M. E. Cates (2018). “Shear reversal in dense suspensions: The challenge to fabric evolution models from simulation data”. In: *Journal of Fluid Mechanics* 847, pp. 700–734.

Chapman, B. K. and D. T. Leighton Jr (1991). “Dynamic viscous resuspension”. In: *International journal of multiphase flow* 17.4, pp. 469–483.

d’Ambrosio, E., F. Blanc, and E. Lemaire (2023). “The characterization of the particle normal stresses of concentrated granular suspensions by local rheometry”. In: *Journal of Fluid Mechanics* 967, A34.

d’Olce, M., J. Martin, N. Rakotomalala, D. Salin, and L. Talon (2008). “Pearl and mushroom instability patterns in two miscible fluids’ core annular flows”. In: *Physics of Fluids* 20.2.

Da Cunha, F. R. and E. J. Hinch (1996). “Shear-induced dispersion in a dilute suspension of rough spheres”. In: *Journal of Fluid Mechanics* 309, pp. 211–223.

Dai, S.-C., E. Bertevas, F. Qi, and R. I. Tanner (2013). “Viscometric functions for noncolloidal sphere suspensions with Newtonian matrices”. In: *J. Rheol.* 57.2, pp. 493–510.

Davis, R. H. and A. Acrivos (1985). “Sedimentation of noncolloidal particles at low Reynolds numbers”. In: *Annual Review of Fluid Mechanics* 17.1, pp. 91–118.

Delesse, A. (1847). “Procede mecanique pour determiner la composition des roches. (Extrait)”. In: *C.r. hebd. sdanc. Acad. Sci., Paris* 25, p. 544.

Dijksman, J. A., F. Rietz, K. A. Lőrincz, M. van Hecke, and W. Losert (2012). "Invited Article: Refractive index matched scanning of dense granular materials". In: *Review of Scientific Instruments* 83.1, p. 011301.

Drazer, G., J. Koplik, B. Khusid, and A. Acrivos (2002). "Deterministic and stochastic behaviour of non-Brownian spheres in sheared suspensions". In: *Journal of Fluid Mechanics* 460, pp. 307–335.

Einstein, A. (1905). "Eine neue bestimmung der moleküldimensionen". PhD thesis. ETH Zurich.

Firouznia, M., B. Metzger, G. Ovarlez, and S. Hormozi (2018). "The interaction of two spherical particles in simple-shear flows of yield stress fluids". In: *Journal of Non-Newtonian Fluid Mechanics* 255, pp. 19–38.

Gadala-Maria, F. and A. Acrivos (1980). "Shear-Induced Structure in a Concentrated Suspension of Solid Spheres". In: *J. Rheol.* 24.6, pp. 799–814.

Gallier, S., E. Lemaire, L. Lobry, and F. Peters (2016). "Effect of confinement in wall-bounded non-colloidal suspensions". In: *Journal of Fluid Mechanics* 799, pp. 100–127.

Gallier, S., E. Lemaire, F. Peters, and L. Lobry (2014). "Rheology of sheared suspensions of rough frictional particles". In: *Journal of Fluid Mechanics* 757, pp. 514–549.

Gamonpilas, C., J. F. Morris, and M. M. Denn (2016). "Shear and normal stress measurements in non-Brownian monodisperse and bidisperse suspensions". In: *J. Rheol.* 60.2, pp. 289–296.

Gillissen, J. J. J. and H. J. Wilson (2019). "Effect of normal contact forces on the stress in shear rate invariant particle suspensions". In: *Phys. Rev. Fluids* 4 (1), p. 013301.

Gillissen, J. and H. Wilson (2018). "Modeling sphere suspension microstructure and stress". In: *Physical Review E* 98.3, p. 033119.

Govindarajan, R. and K. C. Sahu (2014). "Instabilities in viscosity-stratified flow". In: *Annual review of fluid mechanics* 46.1, pp. 331–353.

Guasto, J. S., A. S. Ross, and J. P. Gollub (2010). "Hydrodynamic irreversibility in particle suspensions with nonuniform strain". In: *Physical Review E* 81 (6), p. 061401.

Guazzelli, E. and O. Pouliquen (2018). "Rheology of dense granular suspensions". In: *Journal of Fluid Mechanics* 852, pp. 1–73.

Hampton, R. E., A. A. Mammoli, A. L. Graham, N. Tetlow, and S. A. Altobelli (1997). "Migration of particles undergoing pressure-driven flow in a circular conduit". In: *J. Rheol.* 41.3, pp. 621–640.

Hinch, E. J. (1984). "A note on the mechanism of the instability at the interface between two shearing fluids". In: *Journal of Fluid Mechanics* 144, pp. 463–465.

Hinch, E. J., O. J. Harris, and J. M. Rallison (1992). "The instability mechanism for two elastic liquids being co-extruded". In: *Journal of non-newtonian fluid mechanics* 43.2-3, pp. 311–324.

Hoffman, R. (1972). "Discontinuous and dilatant viscosity behavior in concentrated suspensions. I. Observation of a flow instability". In: *Transactions of the Society of Rheology* 16.1, pp. 155–173.

Ingber, M. and P. Vorobieff (2013). "Particle interactions in oscillatory Stokes flow". In: *WIT Transactions on Engineering Sciences* 79, pp. 147–155.

Khomami, B. and M. M. Ranjbaran (1997). "Experimental studies of interfacial instabilities in multilayer pressure-driven flow of polymeric melts". In: *Rheologica acta* 36.4, pp. 345–366.

Kostynick, R., H. Matinpour, S. Pradeep, S. Haber, A. Sauret, E. Meiburg, T. Dunne, P. Arratia, and D. Jerolmack (2022). "Rheology of debris flow materials is controlled by the distance from jamming". In: *Proceedings of the National Academy of Sciences* 119.44, e2209109119.

Leighton, D. and A. Acrivos (1986). "Viscous resuspension". In: *Chemical engineering science* 41.6, pp. 1377–1384.

Leighton, D. and A. Acrivos (1987a). "Measurement of shear-induced self-diffusion in concentrated suspensions of spheres". In: *Journal of Fluid Mechanics* 177, pp. 109–131.

Leighton, D. and A. Acrivos (1987b). "The shear-induced migration of particles in concentrated suspensions". In: *Journal of Fluid Mechanics* 181, pp. 415–439.

Lemaire, E., F. Blanc, C. Claudet, S. Gallier, L. Lobry, and F. Peters (2023). "Rheology of non-Brownian suspensions: a rough contact story". In: *Rheologica Acta* 62.5-6, pp. 253–268.

Lenoble, M., P. Snabre, and B. Pouligny (2005). “The flow of a very concentrated slurry in a parallel-plate device: Influence of gravity”. In: *Physics of Fluids* 17.7, p. 073303.

Létang, C., M. Piau, and C. Verdier (1999). “Characterization of wheat flour–water doughs. Part I: Rheometry and microstructure”. In: *Journal of Food Engineering* 41.2, pp. 121–132.

Lobry, L., E. Lemaire, F. Blanc, S. Gallier, and F. Peters (2019). “Shear thinning in non-Brownian suspensions explained by variable friction between particles”. In: *Journal of Fluid Mechanics* 860, pp. 682–710.

Lyon, M. K. and L. G. Leal (1998a). “An experimental study of the motion of concentrated suspensions in two-dimensional channel flow. Part 1. Monodisperse systems”. In: *J. Fluid.Mech.* 363, pp. 25–56.

Lyon, M. K. and L. G. Leal (1998b). “An experimental study of the motion of concentrated suspensions in two-dimensional channel flow. Part 2. Bidisperse systems”. In: *J. Fluid.Mech.* 363, pp. 57–77.

Mari, R., R. Seto, J. F. Morris, and M. M. Denn (2014). “Shear thickening, frictionless and frictional rheologies in non-Brownian suspensions”. In: *Journal of Rheology* 58.6, pp. 1693–1724.

Maron, S. H. and P. E. Pierce (1956). “Application of ree-eyring generalized flow theory to suspensions of spherical particles”. In: *Journal of colloid science* 11.1, pp. 80–95.

Mayhew, T. and L.-M. C. Orive (1974). “Caveat on the use of the Delesse principle of areal analysis for estimating component volume densities”. In: *Journal of Microscopy* 102.2, pp. 195–207.

Metzger, B., O. Rahli, and X. Yin (2013). “Heat transfer across sheared suspensions: role of the shear-induced diffusion”. In: *Journal of Fluid Mechanics* 724, pp. 527–552.

Miller, R. M. and J. F. Morris (2006). “Normal stress-driven migration and axial development in pressure-driven flow of concentrated suspensions”. In: *Journal of non-newtonian fluid mechanics* 135.2-3, pp. 149–165.

Moosavi, R., M. Maleki, M. R. Shaebani, J. C. Ruiz-Suárez, and E. Clément (2014). “Stripe formation in horizontally oscillating granular suspensions”. In: *EPL (Europhysics Letters)* 107.3, p. 34006.

Morris, J. F. (2001). “Anomalous migration in simulated oscillatory pressure-driven flow of a concentrated suspension”. In: *Phys. Fluids* 13.9, pp. 2457–2462.

Morris, J. F. and F. Boulay (1999). “Curvilinear flows of noncolloidal suspensions: The role of normal stresses”. In: *J. Rheol.* 43.5, pp. 1213–1237.

Ness, C., R. Mari, and M. E. Cates (2018). “Shaken and stirred: Random organization reduces viscosity and dissipation in granular suspensions”. In: *Science Advances* 4.3, eaar3296.

Nott, P. R. and J. F. Brady (1994). “Pressure-driven flow of suspensions: simulation and theory”. In: *Journal of Fluid Mechanics* 275, pp. 157–199.

Ovarlez, G., A. Vu Nguyen Le, W. J. Smit, A. Fall, R. Mari, G. Chatté, and A. Colin (2020). “Density waves in shear-thickening suspensions”. In: *Science Advances* 6.16, eaay5589.

Parsi, F. and F. Gadala-Maria (1987). “Fore-and-aft asymmetry in a concentrated suspension of solid spheres”. In: *J. Rheol.* 31.8, pp. 725–732.

Peters, F., G. Ghigliotti, S. Gallier, F. Blanc, E. Lemaire, and L. Lobry (2016). “Rheology of non-Brownian suspensions of rough frictional particles under shear reversal: A numerical study”. In: *J. Rheol.* 60.4, pp. 715–732.

Pham, P., J. E. Butler, and B. Metzger (2016). “Origin of critical strain amplitude in periodically sheared suspensions”. In: *Phys. Rev. Fluids* 1 (2), p. 022201.

Pham, P., B. Metzger, and J. E. Butler (2015). “Particle dispersion in sheared suspensions: Crucial role of solid-solid contacts”. In: *Phys. Fluids* 27.5, p. 051701.

Phan-Thien, N. (1995). “Constitutive equation for concentrated suspensions in Newtonian liquids”. In: *J. Rheol.* 39.4, pp. 679–695.

Phillips, R. J., R. C. Armstrong, R. A. Brown, A. L. Graham, and J. R. Abbott (1992). “A constitutive equation for concentrated suspensions that accounts for shear-induced particle migration”. In: *Phys. Fluids A: Fluid Dynamics* 4.1, pp. 30–40.

Pine, D. J., J. P. Gollub, J. F. Brady, and A. M. Leshansky (2005). “Chaos and threshold for irreversibility in sheared suspensions”. In: *Nature* 438.7070, pp. 997–1000.

Popova, M., P. Vorobieff, M. S. Ingber, and A. L. Graham (2007). “Interaction of two particles in a shear flow”. In: *Physical Review E—Statistical, Nonlinear, and Soft Matter Physics* 75.6, p. 066309.

Ramachandran, A. and D. T. Leighton (2008). “The influence of secondary flows induced by normal stress differences on the shear-induced migration of particles in concentrated suspensions”. In: *Journal of Fluid Mechanics* 603, pp. 207–243.

Rashedi, A. (2019). “The design and flow dynamics of non brownian suspension”. PhD thesis. University of Bordeaux and Ohio University.

Rashedi, A., M. Sarabian, M. Firouznia, D. Roberts, G. Ovarlez, and S. Hormozi (2020). “Shear-induced migration and axial development of particles in channel flows of non-Brownian suspensions”. In: *AIChE J.* 66.12, e17100.

Richardson, J. F. and W. N. Zaki (1954). “Sedimentation and fluidization: Part I”. In: *Trans. Inst. Chem. Eng.* 32, pp. 35–47.

Roht, Y. L., I. Ippolito, J. P. Hulin, D. Salin, and G. Gauthier (2018). “Stripes instability of an oscillating non-Brownian iso-dense suspension of spheres”. In: *Europhys. Lett.* 121.5, p. 54002.

Roht, Y. L. (2017). “Transporte y dispersión de un soluto en un flujo de suspensiones”. Tesis de doctorado, Facultad de Ingeniería, UBA.

Saint-Michel, B., T. Gibaud, and S. Manneville (2018). “Uncovering instabilities in the spatiotemporal dynamics of a shear-thickening cornstarch suspension”. In: *Physical Review X* 8.3, p. 031006.

Sarabian, M., M. Firouznia, B. Metzger, and S. Hormozi (2019). “Fully developed and transient concentration profiles of particulate suspensions sheared in a cylindrical Couette cell”. In: *Journal of Fluid Mechanics* 862, pp. 659–671.

Savitzky, A. and M. J. E. Golay (1964). “Smoothing and Differentiation of Data by Simplified Least Squares Procedures.” In: *Analytical Chemistry* 36.8, pp. 1627–1639.

Seto, R. and G. G. Giusteri (2018). “Normal stress differences in dense suspensions”. In: *Journal of Fluid Mechanics* 857, pp. 200–215.

Sierou, A. and J. F. Brady (2004). “Shear-induced self-diffusion in non-colloidal suspensions”. In: *Journal of Fluid Mechanics* 506, pp. 285–314.

Snook, B., J. E. Butler, and E. Guazzelli (2016). “Dynamics of shear-induced migration of spherical particles in oscillatory pipe flow”. In: *Journal of Fluid Mechanics* 786, pp. 128–153.

Souzy, M., P. Pham, and B. Metzger (2016). “Taylor’s experiment in a periodically sheared particulate suspension”. In: *Phys. Rev. Fluids* 1 (4), 042001(R).

Stickel, J. J. and R. L. Powell (2005). “Fluid mechanics and rheology of dense suspensions”. In: *Annu. Rev. Fluid Mech.* 37.1, pp. 129–149.

Stover, C. A., D. L. Koch, and C. Cohen (1992). “Observations of fibre orientation in simple shear flow of semi-dilute suspensions”. In: *Journal of Fluid Mechanics* 238, pp. 277–296.

Than, P., F. Rosso, and D. Joseph (1987). “Instability of Poiseuille flow of two immiscible liquids with different viscosities in a channel”. In: *International journal of engineering science* 25.2, pp. 189–204.

Varga, Z., V. Grenard, S. Pecorario, N. Taberlet, V. Dolique, S. Manneville, T. Divoux, G. H. McKinley, and J. W. Swan (2019). “Hydrodynamics control shear-induced pattern formation in attractive suspensions”. In: *Proceedings of the National Academy of Sciences* 116.25, pp. 12193–12198.

Wyart, M. and M. E. Cates (2014). “Discontinuous shear thickening without inertia in dense non-Brownian suspensions”. In: *Physical review letters* 112.9, p. 098302.

Yang, Y., W. Yuan, J. Hou, and Z. You (2022). “Review on physical and chemical factors affecting fines migration in porous media”. In: *Water Research* 214, p. 118172.

Yeo, K. and M. R. Maxey (2011). “Numerical simulations of concentrated suspensions of monodisperse particles in a Poiseuille flow”. In: *Journal of Fluid Mechanics* 682, pp. 491–518.

Yeo, K. and M. R. Maxey (2010). “Dynamics of concentrated suspensions of non-colloidal particles in Couette flow”. In: *Journal of Fluid Mechanics* 649, pp. 205–231.

Zarraga, I. E., D. A. Hill, and D. T. Leighton Jr (2000). “The characterization of the total stress of concentrated suspensions of noncolloidal spheres in Newtonian fluids”. In: *J. Rheol.* 44.2, pp. 185–220.

Zhang, H., D. I. Kopelevich, and J. E. Butler (2024). In: *Journal of Fluid Mechanics* 1001, A42.

Zhang, H., P. Pham, B. Metzger, D. I. Kopelevich, and J. E. Butler (2023). “Effect of particle roughness on shear-induced diffusion”. In: *Phys. Rev. Fluids* 8, p. 064303.

Zrehen, A. and A. Ramachandran (2013). "Demonstration of secondary currents in the pressure-driven flow of a concentrated suspension through a square conduit". In: *Physical review letters* 110.1, p. 018306.